Modelling of the 3D scattering of elastic waves by complex structures for specimen echoes calculation. Application to ultrasonic NDT simulation.

Samar Chehade

▶ **To cite this version:**

Samar Chehade. Modelling of the 3D scattering of elastic waves by complex structures for specimen echoes calculation. Application to ultrasonic NDT simulation.. Acoustics [physics.class-ph]. Université Paris Saclay (COmUE), 2019. English. NNT : 2019SACLS273 . tel-02329345

HAL Id: tel-02329345

https://theses.hal.science/tel-02329345

Submitted on 23 Oct 2019

HAL is a multi-disciplinary open access archive for the deposit and dissemination of scientific research documents, whether they are published or not. The documents may come from teaching and research institutions in France or abroad, or from public or private research centers.

L'archive ouverte pluridisciplinaire **HAL**, est destinée au dépôt et à la diffusion de documents scientifiques de niveau recherche, publiés ou non, émanant des établissements d'enseignement et de recherche français ou étrangers, des laboratoires publics ou privés.

NNT : 2019SACLS273

Thèse de doctorat

Modelling of the 3D scattering of elastic waves by complex structures for specimen echoes calculation. Application to ultrasonic NDT simulation.

Thèse de doctorat de l'Université Paris-Saclay
préparée à l'Université Paris-Sud

Ecole doctorale n°575 Electrical, Optical, Bio: Physics and Engineering (EOBE)
Spécialité de doctorat : Science des Matériaux

Thèse présentée soutenue à Gif-sur-Yvette, le 26 Septembre 2019, par

SAMAR CHEHADE

Thèse dirigée par Michel Darmon, expert CEA, HDR
co-dirigée par Gilles Lebeau, Professeur à l'Université de Nice Sophia Antipolis (Laboratoire J. A. Dieudonné) et membre de l'Académie des Sciences.

Composition du Jury :

Dominique Habault Directrice de recherche CNRS, HDR, LMA, Marseille	Rapportrice
Olivier Lafitte Professeur des Universités, Université Paris 13, Villetaneuse	Rapporteur
Larissa Fradkin Professeur émérite, London South Bank University, UK Directrice de recherche de Sound Mathematics Ltd., Cambridge, UK	Examinatrice
Frédéric Molinet Docteur d'état, ancien directeur de la société MOTHESIM	Examinateur
Daniel Bouche Directeur de Recherche CEA DAM, Arpajon et CMLA, ENS Cachan	Examinateur
Marc Deschamps Directeur de recherche CNRS, Institut de Mécanique et Ingénierie de Bordeaux (I2M), Talence	Président
Michel Darmon Expert CEA HDR, CEA LIST (DISC/LSMA), Gif-sur-Yvette	Directeur de thèse
Loïc De Roumilly Ingénieur EDF EDVANCE	Invité

Keywords: elastodynamics, diffraction, asymptotic methods

Mots clés : elastodynamique, diffraction, méthodes asymptotiques

This thesis has been prepared at

CEA LIST
CEA Saclay Digiteo Labs
Bât. 565
91191 Gif-sur-Yvette
France

☎ +33 (0)1 69 08 08 00
✉ info-list@cea.fr
Web Site http://www-list.cea.fr/

Modelling of the 3D scattering of elastic waves by complex structures for specimen echoes calculation. Application to ultrasonic NDT simulation.

Abstract

This thesis falls into the framework of model development for simulation of ultrasonic non-destructive testing (NDT). The long-term goal is to develop, using ray methods, a complete simulation tool of specimen echoes (input, back-wall surfaces...) or echoes of inner structures of inspected parts. The thesis aims more specifically to integrate the phenomenon of diffraction by wedges to an existing model derived from geometrical acoustics, which only accounts for reflections on the wedge faces.
To this end, a method called the spectral functions method, which was initially developed for immersed wedges, is developed and validated as a first step in the case of acoustic waves with Dirichlet or Neumann boundary conditions. The method is then extended to elastic wave diffraction by infinite stress-free wedges of arbitrary angles, for 2D and 3D incidences. This method is semi-analytic since the unknown solutions are expressed as the sum of a singular function, determined analytically using a recursive algorithm, and a regular function which is approached numerically.
The corresponding codes are validated by comparison to an exact solution in the acoustic case and by comparison to other codes (semi-analytic and numerical) in the elastic case. Experimental validations of the elastodynamic model are also proposed.

Keywords: elastodynamics, diffraction, asymptotic methods

CEA LIST
CEA Saclay Digiteo Labs – Bât. 565 – 91191 Gif-sur-Yvette – France

Modélisation de la diffusion 3D d'ondes élastiques par des structures complexes pour le calcul des échos de géométrie. Application à la simulation des CND par ultrasons.

Résumé

Le sujet de la thèse s'inscrit dans le cadre du développement de modèles pour la simulation du contrôle non-destructif (CND) par ultrasons. L'objectif à long terme est la mise au point, par une méthode de rayons, d'un outil complet de simulation des échos issus de la géométrie (surfaces d'entrée, de fond...) ou des structures internes des pièces inspectées. La thèse vise plus précisément à intégrer le phénomène de diffraction par les dièdres à un modèle existant dérivant de l'acoustique géométrique et qui prend uniquement en compte les réflexions sur les faces.
Pour cela, la méthode dite des fonctions spectrales, développée initialement pour le cas d'un dièdre immergé, est développée et validée dans un premier temps dans le cas des ondes acoustiques pour des conditions aux limites de type Dirichlet ou Neumann. La méthode est ensuite étendue à la diffraction des ondes élastiques par des dièdres infinis à faces libres et d'angles quelconques, pour une incidence 2D puis pour une incidence 3D. Cette méthode est semi-analytique puisque les solutions recherchées s'écrivent sous la forme d'une somme d'une fonction singulière, qui est déterminée analytiquement à l'aide d'un algorithme récursif, et d'une fonction régulière, qui est approchée numériquement.
Les codes correspondants sont validés par comparaison à une solution exacte dans le cas acoustique et par comparaison à d'autres codes (semi-analytiques et numériques) dans le cas élastique. Des validations expérimentales du modèle élastodynamique sont également proposées.

Mots clés : elastodynamique, diffraction, méthodes asymptotiques

Résumé de la thèse en français

Introduction

Le terme de Contrôle Non Destructif (CND) désigne l'ensemble des méthodes d'inspection de l'état d'une pièce qui préservent l'intégrité physique de celle-ci. Afin de prédire la faisabilité des inspections, mais également d'aider à l'analyse du signal reçu, le CEA LIST (Commissariat à l'Énergie Atomique et aux Énergies Alternatives - Laboratoire d'Intégration des Systèmes et Technologies) développe la plateforme logicielle de simulation d'inspections CIVA. Il existe de nombreuses techniques de CND et la présente thèse se focalise sur le contrôle par ultrasons. Lors d'un contrôle par ultrasons d'une pièce, cette dernière génère des échos issus de ses surfaces d'entrée, internes et de fond. Si ces faces contiennent des dièdres, il est alors nécessaire de modéliser correctement les interactions entre le faisceau ultrasonore et ces dièdres. Ces interactions sont liées à deux phénomènes : la réflexion par les faces du dièdre et la diffraction par l'arête.

Les inspections par ultrasons mettant en jeu des ondes haute fréquence ($f \approx 2-5$ MHz); les simulations par éléments ou différences finies peuvent s'avérer très couteuses numériquement et des méthodes semi-analytiques sont alors préférées pour traiter les problèmes haute fréquences. L'objectif de cette thèse est de développer et de valider un modèle générique et fiable de diffraction haute fréquence des ondes élastiques par les dièdres, valide pour tout angle de dièdre ainsi que pour les configurations 3D, en étendant une méthode semi-analytique appelée méthode des Fonctions Spectrales (SF en anglais).

Chapitre 1 : Revue des approximations hautes fréquences pour la diffraction par un dièdre

Dans le premier chapitre de ce manuscrit, une revue des modèles haute fréquence pour la diffraction d'ondes élastiques par un dièdre est effectuée. Cela commence par une description des deux principales méthodes asymptotiques non uniformes : l'élastodynamique géométrique, qui a donné lieu au développement d'un modèle appelé spéculaire dans CIVA et qui tient uniquement compte des rayons réfléchis et réfractés, et la Théorie Géométrique de la Diffraction (GTD en anglais), qui prend en compte la diffraction mais diverge dans des directions d'observation proches des réflexions spéculaires.

Dans un second temps, les principales solutions uniformes basées sur ces modèles sont présentées. L'approximation de Kirchhoff produit un champ diffusé uniforme mais modélise la diffraction de façon inexacte. La Théorie Physique de la Diffraction (PTD en anglais) fournit une bonne description du champ dispersé dans toutes les directions mais est coûteuse numériquement dans le cas de grands obstacles. La Théorie Asymptotique Uniforme (UAT en anglais) fournit également une bonne description du champ dispersé mais nécessite le tracé de rayons fictifs et est donc difficile à mettre en œuvre numériquement. Enfin, la Théorie Uniforme de la Diffraction (UTD en anglais), développée en élastodynamique par Audrey Kamta-Djakou [1] au cours de sa thèse, produit un résultat précis, est simple à mettre en oeuvre et peu couteuse numériquement. Pour ces raisons, l'UTD est le modèle asymptotique uniforme le plus adapté pour la diffraction par les arêtes de dièdre des grandes surfaces des pièces inspectées par ultrasons. Sa précision repose sur l'existence d'un modèle GTD fiable de diffraction par un dièdre.

Dans cette optique, les deux principaux modèles GTD existants de diffraction par l'arête d'un dièdre sont brièvement présentés. Il s'agit de la méthode dite de la Transformée de Laplace (LT en anglais) et de la méthode dite de l'Intégrale de Sommerfeld (SI en anglais). La méthode LT se fonde sur une formulation intégrale des composantes du champ de déplacement utilisant le tenseur de Green et valable dans tout l'espace pour obtenir un système d'équations fonctionnelles dont la transformée de Laplace du champ de déplacement est solution. La méthode SI se base sur l'expression exacte des potentiels élastodynamiques donnée par Sommerfeld sous forme d'intégrales dépendant de fonctions inconnues, appelées amplitudes de Sommerfeld, pour obtenir un autre système d'équations fonctionnelles, dont les solutions sont les amplitudes de Sommerfeld. Dans les deux méthodes, les systèmes d'équations fonctionnelles sont résolus en décomposant les solutions en une somme de deux termes : une fonction singulière qui est déterminée analytiquement et une fonction régulière qui est approchée

numériquement. A notre connaissance, aucune de ces deux méthodes n'a été développée pour une onde élastique incidente sur un dièdre d'angle supérieur à π, ou pour les configurations tridimensionnelles (c'est-à-dire lorsque le vecteur d'onde incident n'est pas contenu dans le plan normal à l'arête du dièdre).

Chapitre 2 : La méthode des fonctions spectrales pour la diffraction d'une onde acoustique par un dièdre

Le deuxième chapitre de ce manuscrit présente la première étape des développements menés au cours de la thèse. La méthode des Fonctions Spectrales (SF en anglais) y est développée dans le cas plus simple d'une onde acoustique diffusée par un dièdre mou (conditions aux limites de type Dirichlet) ou dur (conditions aux limites de type Neumann) et d'angle arbitraire.

Tout comme les méthodes LT et SI, la méthode SF se base sur une formulation intégrale de la solution pour en déduire un système d'équations fonctionnelles qui est ensuite résolu de manière semi-analytique en décomposant les solutions en la somme d'une fonction singulière et d'une fonction régulière. Toutefois, contrairement aux méthodes LT et SI, la méthode SF est valide pour tous les angles de dièdre, y compris les angles supérieurs à π. Cette généricité est obtenue grâce à la définition d'une nouvelle variable angulaire $\tilde{\varphi}$ qui est une fonction de l'angle du dièdre φ mais dont l'expression est différente lorsque $\varphi \leq \pi$ et lorsque $\varphi > \pi$. Dans la version acoustique de la méthode SF, la formulation intégrale susmentionnée est obtenue grâce à une transformée de Fourier de l'équation de Helmoltz. Cette intégrale est exprimée en fonction de deux fonctions inconnues appelées les fonctions spectrales. Une évaluation asymptotique en champ lointain de cette formulation intégrale à l'aide de la méthode de la plus grande pente conduit à une expression du coefficient de diffraction GTD dépendant des fonctions spectrales. La formulation intégrale de la solution est ensuite injectée dans les conditions aux limites du problème, menant à un système intégral d'équations fonctionnelles dont les fonctions spectrales sont la solution. Ce système est ensuite résolu de manière semi-analytique. Cela signifie que les fonctions spectrales sont décomposées en une somme de deux termes : une fonction singulière, qui est déterminée analytiquement grâce à un algorithme récursif, et une fonction régulière, qui est approchée numériquement grâce à une méthode de collocation de Galerkin. Enfin, la précision dans tout le plan complexe de l'approximation numérique de la partie régulière de la solution est améliorée grâce à une technique appelée "propagation de la solution".

La méthode des fonctions spectrales est validée avec succès en comparant les coefficients de diffraction GTD obtenus par celle-ci aux formules analytiques

des coefficients de diffraction GTD dérivés de la solution exacte exprimée par Sommerfeld. Les résultats obtenus avec la méthode des fonctions spectrales et ceux obtenus avec la GTD issue de la formule exacte donnée par Sommerfeld sont identiques, si ce n'est parfois pour certaines directions d'observation proches des faces du dièdre.

Chapitre 3 : La méthode des fonctions spectrales pour la diffraction 2D d'une onde élastique par un dièdre à faces libres

Dans le troisième chapitre du manuscrit, la méthode des fonctions spectrales est étendue au problème plus complexe de la diffraction des ondes élastiques par un dièdre d'angle arbitraire et à faces libres de contraintes.

Les principales étapes de la méthode sont les mêmes que dans le chapitre précédent, mais les calculs correspondants sont plus complexes, puisque les fonctions spectrales sont maintenant des vecteurs bidimensionnels et que les ondes incidentes, réfléchies et diffractées par les faces et l'arête peuvent être polarisées longitudinalement ou transversalement. Ces deux modes de propagation sont couplés par les conditions aux limites, ce qui signifie que des conversions de modes peuvent avoir lieu. Pour une configuration donnée, deux coefficients de diffraction sont donc calculés : un pour les ondes diffractées longitudinales et un pour les ondes diffractées transversales.

Pour les dièdres d'angle inférieur à π, les modules des coefficients de diffraction obtenus grâce à la méthode des fonctions spectrales sont comparés à ceux obtenus par la méthode de la Transformée de Laplace (LT en anglais) et les résultats sont extrêmement proches. Cependant, le code LT existant n'est valable que pour les dièdres d'angles inférieurs à π. Pour les dièdres d'angle supérieur à π, les modules des coefficients de diffraction calculés avec le code SF sont comparés aux modules de coefficients de diffraction extraits d'un code éléments finis. Dans les zones où l'onde diffractée n'interfère pas avec d'autres ondes et où l'approximation GTD est valable, les deux codes produisent des résultats très similaires. Enfin, les modules et phases des coefficients de diffraction calculés avec le code SF sont validés expérimentalement, à l'aide de mesures préexistantes qui avaient été effectuées pour valider le code LT et sont une fois de plus comparés aux résultats du code LT. Les résultats des deux codes sont identiques, à l'exception d'un léger décrochage près des faces du dièdre dans un des cas testés, et sont très proches des mesures expérimentales.

Chapitre 4 : La méthode des fonctions spectrales pour la diffraction 3D d'une onde élastique par un dièdre à faces libres

Dans le quatrième et dernier chapitre du manuscrit, la méthode des fonctions spectrales est étendue au cas 3D de la diffraction d'une onde élastique par un dièdre à faces libres, où le vecteur d'onde incident n'est pas nécessairement dans le plan normal à l'arête du dièdre. Dans ce cas, le rayon incident sur l'arête du dièdre produit une multitude de rayons diffractés pour chaque mode de propagation diffusé, formant des cônes appelés cônes de Keller. Le demi-angle au sommet de chacun de ces cônes est déterminé par la loi de Snell pour la diffraction. Selon cette loi, lorsque l'onde incidente est transversale et que l'angle d'obliquité du rayon incident (c'est-à-dire l'angle entre le vecteur d'onde incident et le plan perpendiculaire à l'arête du dièdre) est supérieur à un certain angle appelé angle critique, aucune onde longitudinale diffractée n'existe. Le champ diffracté présente alors des points de branchement imaginaires purs dont le traitement demande une attention particulière.

La méthode des fonctions spectrales est détaillée pour les cas 3D, pour tous les types d'incidences et pour les angles de dièdre supérieurs et inférieurs à π. Une approximation numérique supplémentaire est proposée pour calculer la partie régulière des fonctions spectrales dans le cas d'une onde incidente transversale dont l'angle d'obliquité est supérieur à l'angle critique. Les valeurs des coefficients de diffraction obtenus avec cette approximation sont raisonnables, mais n'ont pas été testées expérimentalement ou numériquement. Le code des fonctions spectrales en 3D est testé avec succès dans plusieurs cas particuliers. Il produit des résultats identiques à ceux du code 2D dans les cas particuliers d'incidences 2D (l'angle d'obliquité vaut 0) et à la GTD issue de la solution exacte fournie par Sommerfeld dans le cas de la "limite acoustique" (les vitesses d'onde longitudinale et transversale sont fixées pour simuler la propagation des ondes acoustiques). Dans le cas d'un plan infini, la partie régulière est bien évaluée (l'angle du dièdre est égal à π et aucune onde n'est diffractée), et ce notamment après l'angle critique lorsque l'approximation numérique mentionnée précédemment est appliquée.

Conclusion et perspectives

L'objectif de cette thèse est de développer et de valider un modèle générique et fiable de diffraction des ondes élastiques par les dièdres, valide pour tout angle de dièdre ainsi que pour les configurations 3D, en étendant une méthode

appelée méthode des Fonctions Spectrales (SF en anglais). Dans le premier chapitre, une revue bibliographique des modèles hautes fréquences existants est menée. Dans le deuxième chapitre, la méthode des fonctions spectrales est développée et validée numériquement pour le cas des ondes acoustiques. Dans le troisième chapitre, la méthode est étendue aux cas des ondes élastiques en 2D, puis validée numériquement et expérimentalement. Enfin, dans le quatrième et dernier chapitre, la méthode des fonctions spectrales est étendue aux cas des ondes élastiques en 3D et est validée numériquement pour certains cas particuliers.

Enfin, nous proposons certaines perspectives pour de futurs travaux. Ces perspectives sont :

- Dans le dernier chapitre de la thèse, les parties régulières des fonctions spectrales divergent dans le cas d'une onde transversale incidente avec une obliquité supérieure à l'angle critique. Il faut poursuivre les travaux afin de déterminer la cause de cette divergence et proposer une nouvelle méthode de calcul.

- Évaluer ou modéliser la contribution asymptotique de l'onde longitudinale évanescente générée dans le cas d'une onde transversale incidente avec une obliquité supérieure à l'angle critique.

- Mener une validation numérique et/ou expérimentale complète du code élastique 3D (travail actuellement en cours).

- Au cours de sa thèse, Audrey Kamta-Djakou [1] a développé le modèle UTD pour la diffraction des ondes élastiques par des dièdres, en utilisant l'algorithme de propagation des pôles de la méthode SI. Le modèle UTD doit donc être adapté à l'algorithme SF afin de pouvoir être appliqué aux incidences 3D. J'ai entamé les travaux d'intégration dans la plateforme logicielle CIVA du code SF 3D avec un modèle UTD. Afin de gérer l'extension finie des arêtes dans CIVA, une possibilité est d'utiliser un modèle incrémental tel que la Théorie Incrémentale de la Diffraction (ITD en anglais) ou le modèle de Huygens que j'ai aidé à développer et valider en élastodynamique [2].

- Proposer une modélisation rigoureuse de la contribution aux coefficients de diffraction élastodynamiques des ondes de tête, dans la continuité des travaux de Fradkin et al. [3] et de ceux de Darmon [4].

- Étendre la méthode des fonctions spectrales au traitement des interfaces diédrales entre deux solides. Ceci s'inscrirait dans la continuité des travaux du stage de Lucien Rochery, encadré par Michel Darmon et moi-même. Au

cours de ce stage, les développements théoriques concernant la diffraction des ondes acoustiques et élastiques par des dièdres impédants ont été initiés.

- Dans la continuité des travaux de Kamotskii [5], la méthode des fonctions spectrales pourrait être étendue au traitement des jonctions de dièdres (diffraction par deux dièdres adjacents) pour lesquelles d'autres méthodes [6, 7] pourraient également être étudiées.

Les résultats obtenus au cours de cette thèse ont mené à la publication de trois articles dans des journaux à comité de revue [2, 8, 9] ainsi qu'à deux communications dans des conférences internationales [10, 11].

Acronyms

C | **F** | **G** | **I** | **K** | **L** | **N** | **P** | **S** | **U**

C

CFL Courant-Friedrichs-Lewy. 89
CND Contrôle Non Destructif. ix
COD Crack Opening Displacement. 11

F

FE Finite Elements. 89, 90, 92

G

GE Geometrical Elastodynamics. 2, 5–9, 11, 13, 14, 16, 21, 24, 26, 27, 139
GTD Geometrical Theory of Diffraction. x–xiii, xix, 2, 5–14, 16, 17, 19, 21–23, 25–27, 29, 30, 36, 38, 90, 92–94, 98, 130, 137, 139–142

I

ITD Incremental Theory of Diffraction. 143

K

KA Kirchhoff Approximation. 2, 5, 6, 11–13, 26, 27, 139

L

LT Laplace Transform. x–xii, 2, 3, 5, 22, 27, 86, 87, 89, 92, 93, 95, 139–142

N

NDE Non Destructive Evaluation. 1

NDT Non Destructive Testing. 1, 5, 6, 11–13, 93, 143

P

PML Perfectly Matched Layers. 89
PO Physical Optics. 11
PTD Physical Theory of Diffraction. x, 2, 5, 6, 12, 13, 16, 27, 139

S

SF Spectral Functions. ix, xi, xii, xiv, 2, 3, 26, 27, 55, 86, 90, 92–94, 129, 132–134, 139–141, 143
SI Sommerfeld Integral. x, xi, xiv, 2, 3, 5, 18, 19, 24, 27, 139, 140, 142

U

UAT Uniform Asymptotic Theory. x, 2, 5, 6, 13, 14, 16, 27, 139
UTD Uniform Theory of Diffraction. x, xiv, 2, 5, 6, 14, 16, 27, 139, 142, 143

Table of Contents

Introduction

The term Non Destructive Testing (NDT), also known as Non Destructive Evaluation (NDE), regroups all the inspection techniques that preserve the inspected specimen's integrity. This is particularly useful in areas such as civil engineering, aeronautics, nuclear energy or the automobile and railway industries, as it enables users to test industrial components during their production phase or during the course of their lifetime. There exists a wide range of NDT methods, the most frequently used being visual testing, eddy-current, magnetic-particle, liquid penetrant, radiographic and finally ultrasonic testing.

This thesis focuses on ultrasonic testing, an approach in which ultrasounds are emitted into a specimen and the waves scattered inside the specimen are analyzed in order to detect anomalies. These waves, which propagate through solid mediums without causing structural damage or changes, are elastic waves. The signal collected by the receiving transducer, which corresponds to the wave scattered by the specimen's boundaries and inhomogenities, contains information about the component's state and must therefore be analyzed.

The feasibility of ultrasonic inspections is predicted using simulation and modeling. Simulation and modeling also helps with the analysis of the received signals. To this end, CEA-LIST (Commissariat à l'Énergie Atomique et aux Énergies Alternatives - Laboratoire d'Intégration des Systèmes et Technologies) offers an NDT simulation tool via the CIVA software platform. UT inspections deal with high frequency ($f \approx 2-5$ MHz) ultrasonic waves therefore, simulation of realistic inspections by finite elements and finite differences can be time consuming because such methods require a small mesh step for a precise description of the scattered wave (on the order of $1/5^{th}$ of the wavelength). Semi-analytical methods are consequently preferred for high frequency problems, in order to reduce computation time.

Ultrasonic inspection of a specimen generates echoes from the entry and back-wall surfaces of this specimen. If these surfaces contain dihedral corners,

it is then necessary to provide a correct model of the interaction between the ultrasonic beam and these wedges. These interactions may be linked to two different phenomena : reflection from the wedge faces and diffraction of the incident rays by the wedge edge. Both must be correctly taken into account by the model.

During the course of a previous thesis (Audrey Kamta-Djakou's PhD thesis [1]), the specular model, which models reflection but not diffraction and therefore is not spatially continuous, was combined to an edge-diffraction model. The resulting model is called the Uniform Theory of Diffraction (UTD) and provides a spatially uniform high frequency representation of the scattered field. This model presents the advantages of being computationally cheap (as opposed to finite elements or to the Kirchhoff Approximation (KA) which is currently implemented in CIVA) and of modeling diffraction correctly (as opposed to KA). In order for the UTD model to be valid, a preexisting trustworthy model is necessary to accurately predict diffraction from a wedge edge. A method called the Laplace Transform (LT) method [12] was also studied in Kamta-Djakou's thesis but has the disadvantage of only being developed for wedge angles lower than π.

The aim of this thesis is to propose and validate a generic and reliable elastodynamic wedge-diffraction model, valid for all wedge angles and for 3D incidences. So far, this has not yet been done in elastodynamics. This is done by extending a method called the Spectral Functions (SF) method and proposing the corresponding numerical resolution schemes.

This manuscript is divided into 4 chapters.

In chapter 1, a review of high frequency wedge scattering models is presented. The first section of this chapter describes non-uniform asymptotic methods (non-uniform in the sense that the resulting scattered field is not spatially continuous), namely Geometrical Elastodynamics (GE), which models specular reflection but not diffraction and is therefore discontinuous at shadow boundaries, and the Geometrical Theory of Diffraction (GTD), which models reflection and diffraction but diverges in observation directions of reflection and transmission. The second section presents uniform solutions based on these non-uniform models : the Kirchhoff Approximation (KA), the Physical Theory of Diffraction (PTD), the Uniform Asymptotic Theory (UAT) and finally the Uniform Theory of Diffraction (UTD). All these models (except for KA) require a reliable preexisting wedge-diffraction GTD solution in order to be accurate. The third and final section therefore presents the two main existing GTD wedge diffraction models : the Sommerfeld Integral (SI) method and the Laplace Transform (LT) method.

In chapter 2, the Spectral Functions (SF) method is developed as a first step for the simpler case of an acoustic wave scattered by a soft (Dirichlet boundary

conditions) or hard (Neumann boundary conditions) wedge. This is done by first, determining an integral formulation of the scattering problem. This formulation is given with respect to two unknown functions called the spectral functions. A system of functional equations of which these spectral functions are the solution is then determined using the problem's boundary conditions. This system permits the decomposition of the spectral functions into two terms : a singular function, determined analytically using a recursive algorithm and a regular function which is approached numerically using a Galerkin collocation method. The accuracy of this numerical approximation is improved by a method called "propagation of the solution". Finally, the solution computed using the Spectral Functions method is validated by comparison to the exact solution given by Sommerfeld.

Chapter 3 deals with extension of the Spectral Functions method to the 2D case of an elastic wave scattered by a stress-free wedge. The outline of the method is similar, but the unknown spectral functions are now two-dimensional vectors and the incident, reflected and diffracted waves can be longitudinal or transversal and mode conversion can occur. All of these phenomena are accounted for by the Spectral Functions method, which has the advantage of being valid for all wedge angles (as opposed to the previously existing Laplace Transform (LT) and Sommerfeld Integral (SI) methods). The resulting code is validated for wedge angles lower than π by comparison to the LT code and for wedge angles higher than π by comparison to a finite elements code. In addition, experimental validation is also carried out, thanks to previously made experimental measurements.

Finally, in chapter 4, the Spectral Functions method is developed for 3D cases, meaning for cases where the incident wave is no longer in the plane normal to the wedge edge. The spectral functions are now three-dimensional vectors and the possible wave polarizations are longitudinal, transverse horizontal and transverse vertical. An additional difficulty is created in the case of an incident transversal wave, when the skew angle (the angle between the incident ray and the plane normal to the edge) is higher than a certain angle called the critical angle (which depends on the propagation medium). Extra care must then be taken to deal with the branch points (for a multi-valued function, a branch point is a point where different definitions coincide) of the spectral functions, as some of them now lie on the imaginary axis (whereas up till now, the branch points were all real numbers) and can therefore be crossed by the complex contour deformations encountered in the method. Nevertheless, the method is developed in detail and for all wedge angles and tested numerically in various ways. In cases where imaginary branch points appear, an additional numerical approximation method is proposed.

CHAPTER 1

High frequency wedge diffraction models

Outline of the current chapter

Introduction

Non Destructive Testing (NDT) of industrial structures requires the modeling of specimen geometry echoes generated by the surfaces (entry, back-wall...)

of inspected blocks. If these surfaces contain wedges, it is then necessary to provide a correct model of the interaction between the ultrasonic beam and these wedges. These interactions may be linked to two different phenomena : reflection from the wedge faces and diffraction by the wedge edge. Both must be correctly taken into account by the model. For that purpose, the study of plane elastic wave scattering by a wedge is of great interest since surfaces of complex industrial specimen often include dihedral corners. These inspections often deal with high frequency ($f = 2 - 5$ MHz) ultrasonic waves. A study of the existing models for the problem of wedge diffraction shows that the Geometrical Elastodynamics (GE) model (a ray-tracing method based on geometrical optics), also called specular model, developed by CEA/LIST and partners in the NDT simulation platform CIVA [13] is much faster than other numerical models (finite elements or finite differences for example) because such methods require a fully numerical resolution with small mesh step (of the order of a third or a fifth of the wavelength) for a better description of the scattered wave. However, this specular model computes reflection by the wedge faces but not diffraction from the wedge edge. To complete this model, the Geometrical Theory of Diffraction (GTD) was developed by Keller [14] in optics and extended to elastic waves by Achenbach and Gautesen [15, 16] for a half plane scatterer. However, this model is not spatially uniform in the sens that it diverges in certain directions.

The Kirchhoff Approximation (KA) was first developed in optics [17] before being used for NDT applications [18, 19]. It is a high-frequency uniform scattering model but can be inaccurate far from directions of geometrical reflection. To overcome this shortcoming, the Physical Theory of Diffraction (PTD), introduced by Ufimtsev [20] in electromagnetics, has been extended to elastodynamics by Zernov et al. [21]. An ultrasonic system model based on the PTD was developed by Darmon et al. [22] and extended to mimic ultrasonics with some head waves by Fradkin et al. [3]. Nevertheless, this ultrasonic PTD model can be time consuming for large specimen surfaces. A third solution to this problem, called the Uniform Asymptotic Theory (UAT) was proposed for elastic waves by Achenbach et aL. [16]. This method models diffraction well but requires tracing of fictitious rays, which makes it difficult to implement for complex geometries. Finally, the Uniform Theory of Diffraction (UTD) was proposed in elastodynamics by Kamta Djakou et al. and developed for a half-plane scatterer [23] and for a wedge [1]. A system model based on the UTD is then proposed and combines the specular model with a diffraction model. To apply the aforementioned UTD method, a generic and trustworthy wedge edge diffraction model is necessary. The aim of this chapter is to present a review these high-frequency wedge scattering models, and to briefly recall the main existing GTD wedge diffraction models.

Section 1 of this chapter presents two non-uniform scattering models : the

GE model and the GTD model. Section 2 describes proposed uniform corrections of these models. The advantages and inconveniences of each of these models are also discussed. Finally, section 3 details two semi-analytical computation methods existing in the literature for the problem of 2D elastic wave diffraction by a stress-free wedge.

1.1 Non-Uniform asymptotic methods

There are various high-frequency approximations of the field echoed by the surfaces and interfaces of an inspected specimen. Some of these models lead to a discontinuous scattered field (which is not physical) and are therefore called non-uniform methods, as opposed to uniform models, which lead to continuous solutions.

1.1.1 Geometrical Elastodynamics (GE)

The first approximation that can be applied to the study of wave propagation in a complex isotropic medium is the Geometrical Elastodynamics (GE) model. It is a translation to elastodynamics of the geometrical optics theory. The field's propagation is described by ray tracing, each ray carrying a certain field value. At a given observation point, the field's value is the sum of the values carried by each of the rays passing through this point. In all this thesis, $\alpha = L, TH$ or TV represents the type of the incident wave (L for Longitudinal, TH for Transverse Horizontal and TV for Transverse Vertical) and β is the type of the reflected, transmitted or diffracted wave. In the GE theory, the incident, reflected and refracted rays are described. These rays are computed following Snell's laws of reflection and refraction :

$$\frac{1}{c_\alpha}\cos\theta_\alpha = \frac{1}{c_\beta}\cos\theta_\beta \tag{1.1}$$

where θ_α is the incident angle and θ_β is the reflection or refraction angle, measured with respect to the reflecting surface.

According to GE, when the incident plane wave meets a surface containing an edge (in the 2D representation of Fig. 1.1, this surface is the oblique wedge face $\mathcal{S}_2$), the propagation medium can be decomposed into four zones, see Fig. 1.1 :

- Zone I : the incident rays are "shadowed" by the scattering surface and therefore do not illuminate this zone, called the shadow zone. The boundary between zones I and II is called the incident shadow boundary.
- Zone II : only the incident rays propagate in this zone.

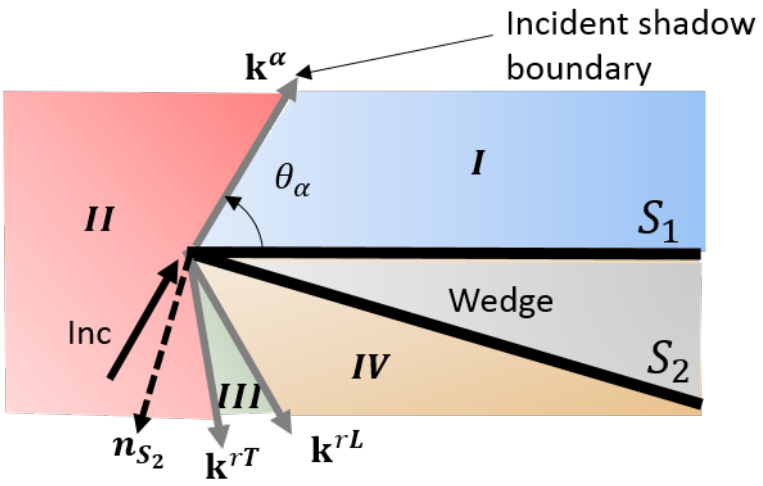

Figure 1.1 – Incident wave on an edge

- Zone III : the incident rays are reflected by the scattering surface and mode conversion occurs (following Snell's law of reflection (1.1)). This zone is illuminated by the incident rays and by the mode-converted reflected rays.

- Zone IV : the incident rays are reflected both with and without mode conversion. This zone is illuminated by incident rays and by L and T reflected waves.

The boundaries separating each of these zones are called the shadow boundaries. In the case where there is no mode conversion (when the incidence angle θ_{α} is after the critical angle θ_c determined by Snell's law of reflection (1.1)), there is no Zone III (and the space occupied by Zone III becomes part of Zone II).

The displacement fields carried by the reflected and refracted rays are proportional to the field incident on the reflecting or refracting interfaces. This proportionality is contained in multiplicative coefficients called reflection or transmission coefficients respectively, which depend on the properties of the propagation medium and on the directions of incidence and observation.

In reality, part of the incident wave is diffracted by the edge and propagates everywhere, including in Zone I. The GE model does not account for diffracted waves, as they can not be predicted by ray tracing. To complete the GE model, Keller [14] has developed the Geometrical Theory of Diffraction (GTD).

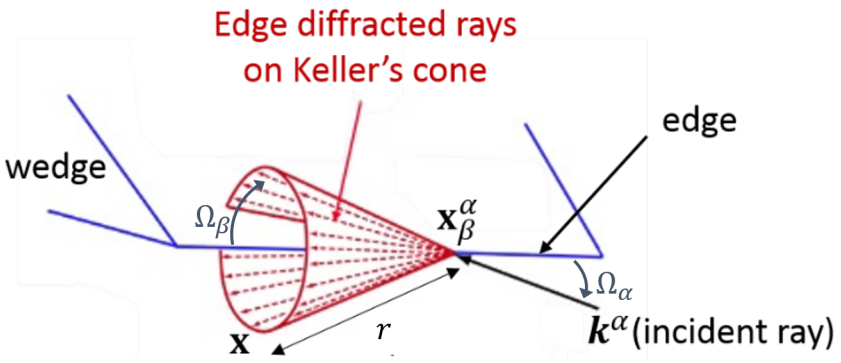

Figure 1.2 – Diffracted rays generated by an incident ray

1.1.2 Geometrical Theory of Diffraction (GTD)

The Geometrical Theory of Diffraction (GTD) was initially developed by Keller [14] for optical waves and adapted to elastodynamics by Achenbach and Gautesen [15, 16]. This theory postulates the existence of diffracted waves emanating from the edge of the scattering surface. An incident ray on an edge generates a cone of rays, called Keller's cone of diffraction [14], represented on Fig. 1.2. The cone's principal axis is the diffracting edge, its principal angle Ω_β is determined by Snell's law of diffraction :

$$\frac{1}{c_\alpha}\cos\Omega_\alpha = \frac{1}{c_\beta}\cos\Omega_\beta \tag{1.2}$$

where Ω_α is the angle between the incident wave vector and the diffracting edge. This cone has been observed by Rahmat-Samii [24] in a hotel room, see Fig. 1.3. A ray of light is incident on the corner of a table and generates a cone of diffracted rays, whose intersection with the door is a circle.

GTD is also a ray tracing method, meaning that at a given observation point $\mathbf{x}$, the total field $\mathbf{u}^{tot}$ is the sum of the fields carried by each ray passing through $\mathbf{x}$:

$$\mathbf{u}^{tot}(\mathbf{x}) = \mathbf{u}^{(GE)}(\mathbf{x}) + \sum_\beta \mathbf{u}_\beta^{diff}(\mathbf{x}) \tag{1.3}$$

where $\mathbf{u}^{(GE)}$ is the GE displacement field, composed of the incident, reflected and refracted fields and $\mathbf{u}_\beta^{diff}$ is the diffracted field of type $\beta = L, TH, TV$. In this chapter, the bold font is used to denote vectors. The diffracted field's amplitude decreases as the distance r from the point of impact $\mathbf{x}_\beta^\alpha$ of the incident wave on the diffracting edge grows (see Fig. 1.2). As for the GE field, the diffracted

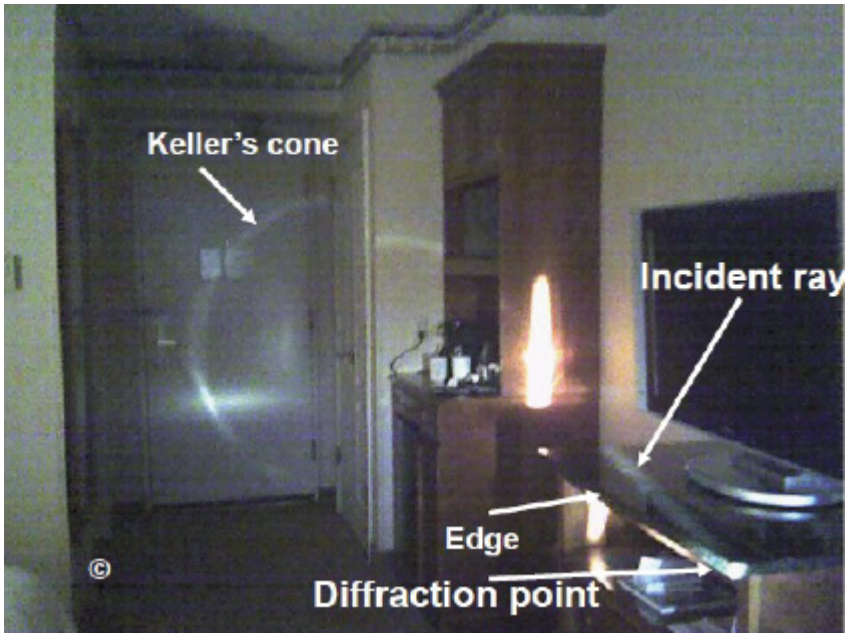

Figure 1.3 – Observation of Keller's cone of diffraction

field is proportional to the field incident on the edge. This proportionality is characterized by a multiplicative coefficient called the diffraction coefficient, which depends on the propagation medium, on the geometry of the diffracting object and on the direction of observation. This is summarized for an incident plane wave by the following equation :

$$\mathbf{u}_{\beta}^{diff}(\mathbf{x}) = u_{\alpha}(x_{\beta}^{\alpha}) D_{\beta}^{\alpha} \frac{e^{ik_{\beta}r}}{\sqrt{k_{\beta} r \sin \Omega_{\beta}}} \mathbf{e}_{\beta}(\mathbf{x}) \tag{1.4}$$

where u_{α} is the scalar value of the incident field, D_{β}^{α} is the diffraction coefficient, k_{β} is the diffracted wave's wave number and $\mathbf{e}_{\beta}(M)$ is the unit polarization vector of the diffracted wave at point $\mathbf{x}$.

This principle is called the locality principle, because it stipulates that the value of the field at any given point is fully determined by the field in the close vicinity of the point from which the ray carrying the observed field emanates. Computation of diffracted fields can therefore be reduced to a number of canonical problems, such as diffraction by a tip or a half plane. In the present thesis, the canonical problem of interest is diffraction by a wedge.

GTD is a high-frequency model which accounts for edge-diffracted waves. However, the resulting field is discontinuous at shadow boundaries and the

diffraction coefficient possesses poles in the directions of geometrical reflection and transmission, rendering the diffracted field divergent in these directions. The resulting field is therefore not physical. Some uniform corrections have been proposed to solve this problem, resulting in continuous fields. They are presented in the following.

1.2 Uniform corrections

1.2.1 Kirchhoff Approximation (KA)

The Kirchhoff Approximation (KA), also called Physical Optics (PO) was first developed in optics by Baker and Copson [17] before being extended to acoustic and electromagnetic waves [25, 26] and being adapted by Chapman to elastic waves [27], where it is essentially used for NDT applications [18, 19].

The Kirchoff Approximation is a high frequency approximation for which the scattering surface is assumed to behave locally like a plane. This means that for each point of the surface, the plane tangent to the surface at that point is determined and the displacement field on the illuminated side is computed using GE. The other side of the plane is shadowed and the total displacement field vanishes. The jump in the displacement between both sides of this plane is called Crack Opening Displacement (COD) and noted $[\mathbf{u}(\mathbf{x})]$. It leads to an integral formulation of the scattered field, called the Rayleigh-Sommerfeld integral [27] :

$$u_p(\mathbf{x}) = \int_{S^+} [u_i(\mathbf{x}')] G_{ij}^{(p)}(\mathbf{x},\mathbf{x}') n_j(\mathbf{x}')\, d^2\mathbf{x}' \tag{1.5}$$

where u_p is the p-th coordinate of the displacement scattered field, S^+ is the lit side of the scattering surface, n is the outward normal to S^+ and $G_{ij}^{(p)}(\mathbf{x},\mathbf{x}')$ is the (ij) component of Green's stress tensor $G^{(p)}(\mathbf{x},\mathbf{x}')$, which is the stress produced at $\mathbf{x}$ by a unit traction acting along the p-axis at point $\mathbf{x}'$ on S^+ and its expression is given in [27]. In this integral, Green's tensor is used to propagate the local solution $[\mathbf{u}(\mathbf{x}')]$ to the whole propagation domain.

The KA scattered field models diffraction and reflection and is continuous in the whole space. Comparisons between KA, GTD and the exact solution have been made for a strip-like crack illuminated by a transversal wave [27, 22]. The results of [27] are reproduced in Fig. 1.4. KA gives good results for observation directions close to the geometrical reflections, as can be expected since the model is based on the GE field. However, further away from these regions, it is inaccurate, as opposed to the GTD which models diffraction correctly.

The GTD solution, which models diffraction well, is non-uniform in the sense

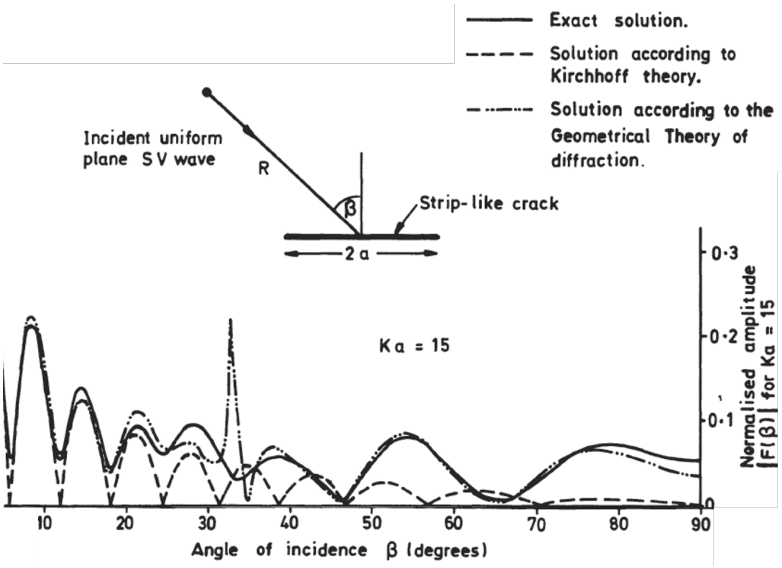

Figure 1.4 – (Reproduced from [27]) Scattering of a transversal (also called shear) plane wave in steel by a smooth strip-like crack of width $2a$. The far-field of the backscattered TV (noted SV here) waves according to Kirchhoff theory and GTD, compared with the exact solution, for $Ka = 15$ ($K = k_T$ = transverse wavenumber).

that it diverges at shadow boundaries. The KA on the other hand, is uniform but doesn't model diffraction correctly. Furthermore, it requires meshing of the scattering surface. To overcome inaccuracies of the GTD and KA models, an other model has been developed, called the Physical Theory of Diffraction (PTD).

1.2.2 Physical Theory of Diffraction (PTD)

The Physical Theory of Diffraction (PTD) was first developed for acoustic and electromagnetic waves by Ufimtsev [20] and was extended to elastodynamics in the case of a half-plane by Zernov et al. [21]. It is also applied to ultrasonic scattering near critical angles [22, 3]. An ultrasonic NDT system has been developed by Darmon et al. [22] for simulating the response of cracks. The idea is to combine GTD and KA models to overcome their shortcomings. This is done by adding a corrective term to the KA diffracted field which is the difference between the GTD and the KA diffracted fields :

$$\mathbf{u}^{tot(PTD)} = \mathbf{u}_{\alpha}(\mathbf{x}) + \mathbf{u}^{sc(PTD)}(\mathbf{x}) \tag{1.6}$$

where $\mathbf{u}_\alpha$ is the incident field and

$$\mathbf{u}^{sc(PTD)}(\mathbf{x}) = \sum_\beta \left[\mathbf{u}_\beta^{\alpha(KA)}(\mathbf{x}) + u_\alpha(\mathbf{x}_\beta^\alpha)\left(D_\beta^{\alpha(GTD)}(\mathbf{x}) - D_\beta^{\alpha(KA)}(\mathbf{x})\right)\frac{e^{ik_\beta S_\beta}}{\sqrt{k_\beta r \sin\Omega_\beta}}\right] \tag{1.7}$$

where $\mathbf{u}_\beta^{\alpha(KA)}$ is obtained by (1.5), $D_\beta^{\alpha(GTD)}$ is the GTD diffraction coefficient and $D_\beta^{\alpha(KA)}$ is the KA diffraction coefficient obtained by an asymptotic evaluation of (1.5) for $k_\beta r >> 1$ (see appendix A), which corresponds to the contribution of the scattering edges to the Rayleigh-Sommerfeld integral. In the far-field, the KA diffraction coefficient diverges at specular directions, compensating the divergence of the GTD diffraction coefficient. The diffracted field then disappears, leaving only the Kirchhoff evaluation, which is accurate in directions of geometrical reflection.

Far from the incident and specular directions, we have :

$$\mathbf{u}_\beta^{\alpha(KA)}(\mathbf{x}) \approx \mathbf{u}_\beta^{diff(KA)}(\mathbf{x}) \approx u_\alpha(\mathbf{x}_\beta^\alpha) D_\beta^{\alpha(KA)}(\mathbf{x}) \frac{e^{ik_\beta S_\beta}}{\sqrt{k_\beta r \sin\Omega_\beta}} \tag{1.8}$$

Substituting this into (1.7), we find that in these regions, the KA contribution vanishes and only the GTD field remains, which models diffraction accurately.

The Physical Theory of Diffraction (PTD) has been developed in the NDT software platform CIVA and the PTD, KA and GTD models have been compared to each-other and to a finite elements model for the response of cracks [22]. It provides a good description of the scattered field in the directions of specular reflection, as well as far from the shadow boundaries, where the main contribution is diffraction from the edge. However, it requires meshing of the scattering surface for the KA model as well as meshing of the flaw contour for the GTD model, which can render it computationally expensive for large scatterers. Another uniform model has been developed, which does not required meshing of the scattering surface, called the Uniform Asymptotic Theory (UAT).

1.2.3 Uniform Asymptotic Theory (UAT)

The Uniform Asymptotic Theory (UAT) was first developed for two-dimensional acoustics and electromagnetics by Lewis and Boersma [28] and was extended to three-dimensional problems by Ahluwalia [29] and to a curved wedge by Lee and Deschamps [30] before being applied to elastodynamics by Achenbach et al. [16]. It is a correction of the GTD model where the GE field is modified to

compensate the divergence in the GTD field and smooth the discontinuity in the GE field. The total field (1.3) becomes :

$$\mathbf{u}^{tot(UAT)}(\mathbf{x}) = \left[\overline{F}(\xi_\alpha) - \hat{\overline{F}}(\xi_\alpha)\right]\mathbf{u}_\alpha(\mathbf{x}) + \sum_\beta \left[\overline{F}(\xi_\beta) - \hat{\overline{F}}(\xi_\beta)\right]\mathbf{u}_\beta^{ref}(\mathbf{x}) + \mathbf{u}_\beta^{diff(GTD)}(\mathbf{x}) \tag{1.9}$$

where $\overline{F}$ is the Fresnel function, defined by

$$\overline{F}(X) = \frac{1}{\sqrt{i\pi}} \int_X^{+\infty} e^{it^2}\, dt \tag{1.10}$$

and

$$\hat{\overline{F}}(X) = e^{i\frac{\pi}{4}} \frac{e^{iX^2}}{2X\sqrt{\pi}} \tag{1.11}$$

$\mathbf{u}_\beta^{ref}$ is the reflected field of type β, $\mathbf{u}_\beta^{diff(GTD)}$ is the GTD diffracted field of type β and ξ_α and ξ_β are detour parameters defined in [30]. They evaluate the proximity of the observation point to the shadow boundary of the incident wave for ξ_α and of the reflected wave for ξ_β. The presence of the Fresnel function $\overline{F}$ smooths the discontinuity in the GE field while the function $\hat{\overline{F}}$ compensates the divergence of the GTD diffracted field. Therefore, the total UAT field is spatially uniform. Note that in (1.9) the incident and reflected fields are defined in the the whole space. This means in particular that they must be artificially extended to their shadow zones. This is achieved by constructing the fictitious rays in the shadow zones [31, 32], see Fig. 1.5.

UAT is a spatially uniform method which models diffraction accurately. However, it requires tracing of fictitious rays and is therefore difficult to implement for complex geometries. To overcome this difficulty, a uniform model which is simpler to implement, the Uniform Theory of Diffraction (UTD) has been developed.

1.2.4 Uniform Theory of Diffraction (UTD)

The Uniform Theory of Diffraction (UTD) was initially developed for acoustic and electromagnetic waves by Kouyoumjian and Pathak [33, 34] and was extended to elastodynamics by Kamta-Djakou during her PhD thesis [23, 1]. This method consists of correcting the GTD diffraction coefficient in the vicinity of shadow boundaries using a transition function F. For the problem of diffraction

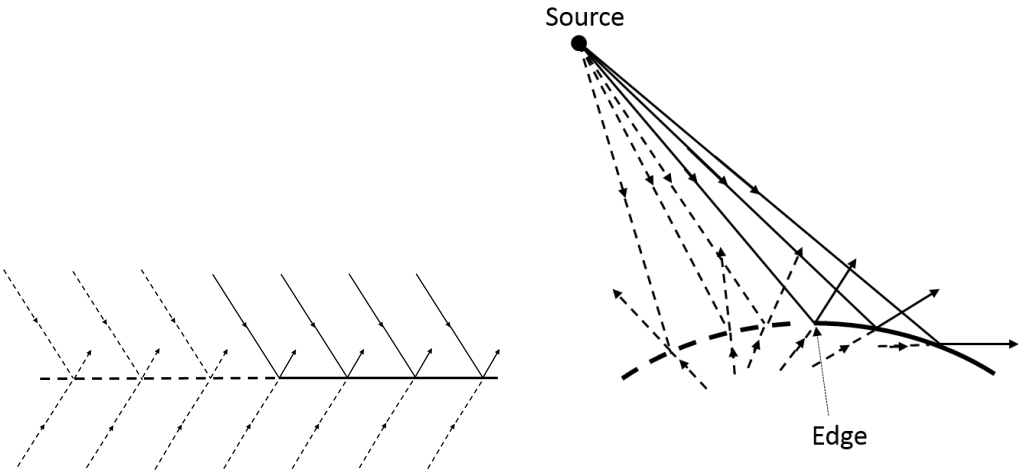

(a) Fictitious rays constructed in the case of a straight scatterer

(b) Fictitious rays constructed in the case of a curved scatterer

Figure 1.5 – (Reproduced from [31, 32]) Extension of the reflected field to its shadow zone using fictitious rays. Dashed thick lines are extensions of the scatterers beyond the crack edge and dashed thin lines are incident and fictitious reflected rays on these extensions.

by a wedge of angle φ, this is expressed by Kamta-Djakou [1] as :

$$D_\beta^{\alpha(UTD)}(\zeta,\theta) = (-1)^{M_\beta+1} D_\beta^{\alpha(GTD)}(\theta)\left[\sum_{j=1}^{M_\beta} F(\zeta a_\beta^j)\prod_{\substack{k=1\\k\neq j}}^{M_\beta}\frac{s_\beta^k}{(s_\beta^j - s_\beta^k)}\right] \tag{1.12}$$

where θ is the direction of observation, $(\lambda_\beta^j), 1 \leq j \leq M_\beta$ are the poles of the diffraction coefficient mentioned in section 1.1.2 (methods of computation of these poles will be given in the following chapters) and

$$a_\beta^j = -i(s_\beta^j)^2 = 2\cos^2\left(\frac{\lambda_\beta^j - \theta}{2}\right) \tag{1.13}$$

ζ is a far-field parameter which can be defined as

$$\zeta = k_\beta r \sin\Omega_\beta. \tag{1.14}$$

Finally, F is a transition function defined as the complex conjugate of the Kouyoumjian function [33]

$$F(X) = -2i\sqrt{i\pi X}e^{-iX}\overline{F}\left(\sqrt{X}\right), \quad -\frac{\pi}{2} < \text{argX} < \frac{3\pi}{2}, \tag{1.15}$$

$\overline{F}$ is the Fresnel function defined by (1.10).

Far from the shadow boundaries, $\zeta a_\beta^j >> 1$ and

$$F(\zeta a_\beta^j) \to 1 \text{ and } (-1)^{M_\beta+1}\left[\sum_{j=1}^{M_\beta}\prod_{\substack{k=1\\k\neq j}}^{M_\beta}\frac{s_\beta^k}{(s_\beta^j - s_\beta^k)}\right] = 1 \tag{1.16}$$

In this case, the UTD solution for the diffracted field is the same as the GTD diffracted field. Close to the shadow boundaries, Kamta-Djakou [1] has shown that the transition functions makes the diffracted field discontinuous when crossing shadow boundaries and that these irregularities compensate exactly those of the GE field, so that the total field computed using (1.3) is uniform.

The Uniform Theory of Diffraction (UTD) has been validated numerically in far-field configurations in [1]. It models the diffracted field well and provides a spatially uniform solution while being simple to implement.

The PTD, UAT and UTD methods presented are all uniform *corrections* of the GTD field. This means that they all rely on a preexisting GTD solution, which must therefore be accurate. In the following, the two main existing GTD approaches to the problem of diffraction of an elastic wave by a stress-free wedge are presented.

1.3 Principal GTD elastic wedge diffraction models

As seen in the previous section, an accurate uniform scattering model requires a trust-worthy initial GTD solution in order to be developed. The aim of this thesis will therefore be to develop a generic and trust-worthy wedge diffraction GTD model. To our knowledge, there is no fully analytical resolution of the problem of elastic wedge diffraction available in scientific literature, and the preferred approach is semi-analytical. We begin this work by a review of the two main existing 2D elastic wedge-diffraction models. These two models have been presented and compared by Gautesen and Fradkin [12], who also discuss their numerical validation. Experimental validation of these codes has been done by Chapman et al. [35].

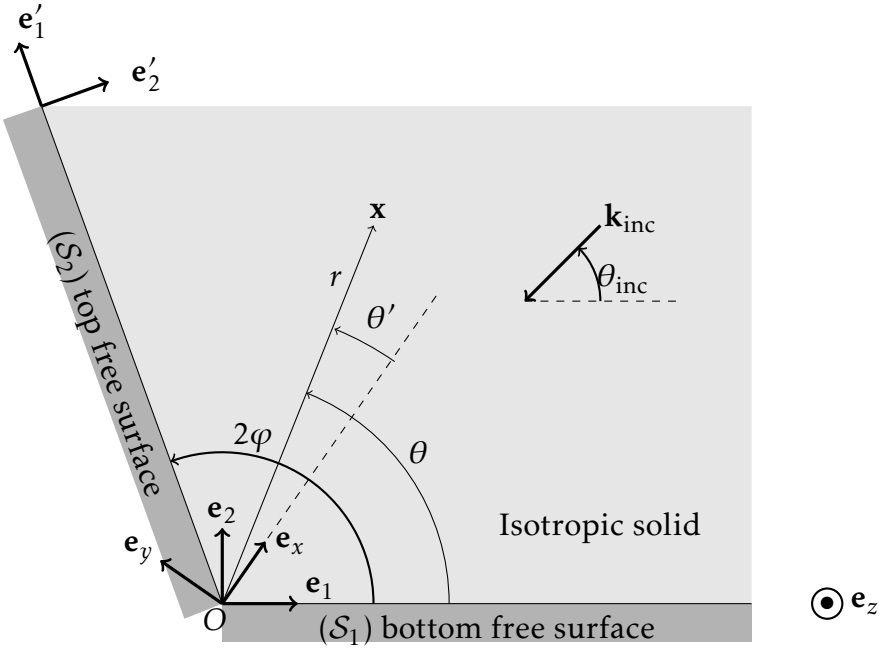

Figure 1.6 – Stress-free wedge of angle 2φ illuminated by a plane wave of wave vector $\mathbf{k}^{\text{inc}}$. The dotted line is the wedge bisector.

1.3.1 Problem statement

The geometry of the problem is visible in Fig. 1.6. A stress-free wedge of angle $2\varphi < \pi$ and infinite in the direction of its edge is illuminated by a a plane wave which forms an angle θ_{inc} with the bottom face of the wedge. The problem is two-dimensional in the sense that the incident wave vector is in the plane normal to wedge edge. In all the following, the harmonic time-dependency factor $e^{-i\omega t}$ (where ω is the circular frequency and t is time) will be omitted. $(0;\mathbf{e}_{x_1},\mathbf{e}_{y_1},\mathbf{e}_z)$ is the orthonormal basis of a Cartesian coordinate system where the z-axis coincides with the wedge edge and the x_1 axis coincides with the bottom face of the wedge. The polar coordinates associated to this system are $\mathbf{x} = (r,\theta)$. In this coordinate system, the incident wave vector is :

$$\mathbf{k}^{inc} = -(\cos\theta_{inc}, \sin\theta_{inc})_{(\mathbf{e}_{x_1},\mathbf{e}_{y_1})} \tag{1.17}$$

$(0;\mathbf{e}_x,\mathbf{e}_y,\mathbf{e}_z)$ is the orthonormal basis of a Cartesian coordinate system where the x-axis coincides with the wedge bisector and the polar coordinates associated to this system are $\mathbf{x} = (r,\theta')$.

In both of the following approaches, the symmetry of the problem with respect to the wedge bisector is used and the problem is split in two : a symmetric

problem (regarding the polarization of the incident wave) and an antisymmetric problem. This is done by introducing a wave vector symmetric to $\mathbf{k}^{inc}$ with respect to the bisector :

$$\mathbf{k}_{sym} = (-\cos\theta'_{inc}, \sin\theta'_{inc})_{(\mathbf{e}_x,\mathbf{e}_y)} \tag{1.18}$$

In the case of an incident L wave, the symmetric problem is constructed by considering that the incident wave for this problem is the sum of two plane waves of which the wave vectors are $\mathbf{k}^{inc}$ and $\mathbf{k}_{sym}$, see Fig. 1.7a. In this case, the polarization vectors $\mathbf{p}^{inc} = \mathbf{k}^{inc}$ and $\mathbf{p}_{sym} = \mathbf{k}_{sym}$ are symmetric. The antisymmetric problem is constructed by setting the incident wave to be the sum of two plane waves of which the wave vectors are $\mathbf{k}^{inc}$ and $-\mathbf{k}_{sym}$, see Fig. 1.7b. In this case the polarization vectors $\mathbf{p}^{inc}$ and $-\mathbf{p}_{sym}$ are antisymmetric.

In the case of an incident T wave, the polarization vector is normal to the wave vector. Therefore, symmetric problem is constructed by setting $\mathbf{k}^{inc}$ and $-\mathbf{k}_{sym}$ as the incident wave vectors, see Fig. 1.7b and the antisymmetric problem is constructed by setting $\mathbf{k}^{inc}$ and $\mathbf{k}_{sym}$ as the incident wave vectors, see Fig. 1.7a.

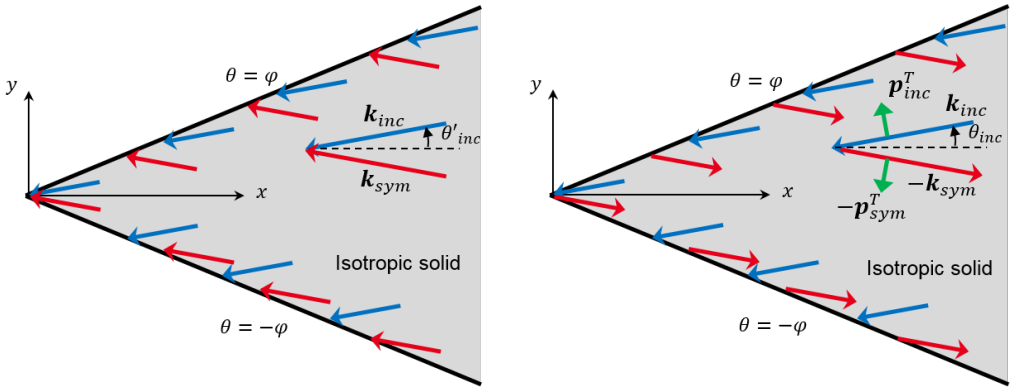

(a) Symmetric problem for an incident longitudinal wave or antisymmetric problem for an incident transversal wave

(b) Antisymmetric problem for an incident longitudinal wave or symmetric problem for an incident transversal wave

Figure 1.7 – (Reproduced from [1]) Symmetric and antisymmetric problems. Blue and red vectors are the wave vectors and green vectors are the polarization vectors of the transversal waves.

Both of the semi-analytic resolutions that will be described in the following deal with the symmetric and antisymmetric problems separately, in order to reduce the numerical part of the resolution by half. The first approach presented is called the Sommerfeld Integral (SI) method. The main steps of the resolution

are presented but the technical details are not given here and can be found in [1].

1.3.2 The Sommerfeld Integral (SI) Method

The Sommerfeld Integral (SI) method was first proposed by Budaev [36, 37, 38] and Budaev and Bogy [39, 40, 41] have proposed the corresponding numerical scheme. The theory was completed and clarified by Kamotski et al. [42].

In this approach, the elastodynamic potentials ψ_L and ψ_T are the unknowns. They are related to the displacement field by :

$$\mathbf{u} = \nabla\psi_L + \nabla \times (\psi_T \mathbf{e}_z) \tag{1.19}$$

where ∇ is the gradient operator and $\nabla\times$ is the curl operator. These potentials satisfy the Helmoltz equations in the angular domain [16] :

$$\Delta\psi_L + k_L^2\psi_L = 0 \text{ and } \Delta\psi_T + k_T^2\psi_T = 0 \text{ for } |\theta'| < \varphi \tag{1.20}$$

In addition, the wedge faces are stress-free, meaning :

$$\sigma_{r\theta'} = 0 \text{ and } \sigma_{\theta'\theta'} = 0 \text{ for } |\theta'| = \varphi \tag{1.21}$$

Sommerfeld [43] has given an exact expression of these potentials in the form of an integral. This integral satisfies (1.20) as well as the radiation conditions at infinity [44] :

$$\psi_*(k_* r, \theta') = \int_{\gamma_+ + \gamma_-} e^{-ik_* r\cos\lambda} \Psi_*(\theta' + \lambda)\, d\lambda \tag{1.22}$$

where $* = L, T, \lambda$ is a complex angle, Ψ_* are unknown amplitudes and contours γ_+ and γ_- are represented on Fig. 1.8.

Following the decomposition of the problem, the unknown amplitudes can be decomposed into symmetric and antisymmetric amplitudes. The superscript " + " refers to the symmetric problem and the superscript " − " refers to the antisymmetric one. We then have :

$$\Psi_*(\lambda) = \Psi_*^+(\lambda) + \Psi_*^-(\lambda) \tag{1.23}$$

where

$$\Psi_L^\pm(\lambda) = \frac{1}{2}[\Psi_L(\lambda) \pm \Psi_L(-\lambda)] \tag{1.24a}$$

$$\Psi_T^\pm(\lambda) = \frac{1}{2}[\Psi_L(\lambda) \mp \Psi_L(-\lambda)] \tag{1.24b}$$

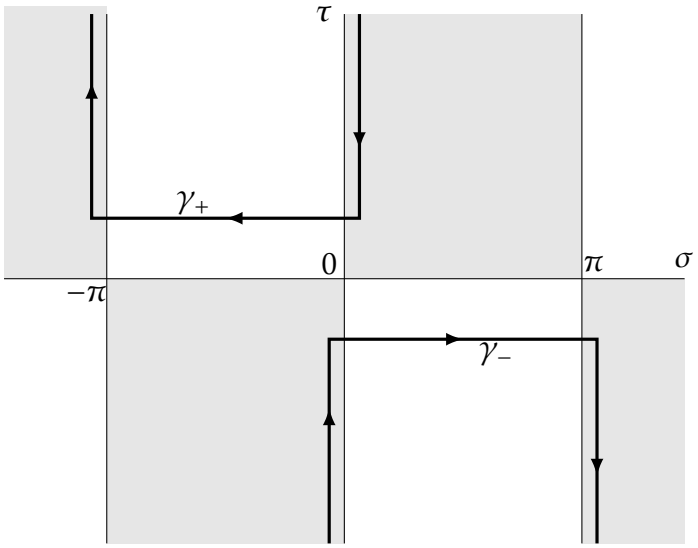

Figure 1.8 – Sommerfeld contours of integration γ_+ and γ_- in the complex plane $\lambda = \sigma + i\tau$.

The symmetric and antisymmetric potentials $\psi_*^\pm$ associated to these amplitudes using (1.22) are the solutions of the symmetric and antisymmetric problems. Kamotski et al. [42] have shown that subsituting (1.22) into (1.21) yields the following system of functional equations :

$$\begin{pmatrix} \Psi_L^\pm(g(\lambda)+\varphi) \\ \Psi_T^\pm(\lambda+\varphi) \end{pmatrix} = \pm \begin{pmatrix} r_L^L(\lambda) & r_L^T(\lambda) \\ r_T^L(\lambda) & r_T^T(\lambda) \end{pmatrix} \begin{pmatrix} \Psi_L^\pm(g(\lambda)-\varphi) \\ \Psi_T^\pm(\lambda-\varphi) \end{pmatrix} + \kappa^2 c_1^\pm \frac{\sqrt{\kappa^{-2}-\cos^2\lambda}}{\mathcal{R}(\lambda)} \begin{pmatrix} \cos 2\lambda - \tan\varphi \sin 2\lambda \\ \sin 2\lambda + \tan\varphi \dfrac{\sin\lambda\cos 2\lambda}{\sqrt{\kappa^{-2}-\cos^2\lambda}} \end{pmatrix} \tag{1.25}$$

where $\kappa = c_L/c_T$,

$$g(\lambda) = \arccos(\kappa\cos\lambda), \tag{1.26}$$

the potential reflection coefficients r_L^L, r_L^T, r_T^L and r_T^T for the traction-free elastic half-space are known explicitly and are given in [42], function $\mathcal{R}$ is called the Rayleigh function :

$$\mathcal{R}(\lambda) = \cos^2 2\lambda + 2\sqrt{\kappa^{-2}-\cos^2\lambda}\sin 2\lambda\cos\lambda \tag{1.27}$$

and finally $c_1^\pm$ are unknown constants.

Representation (1.22) gives the total elastodynamic potentials, including incident and reflected fields. It is well known that the poles of the Sommerfeld

amplitudes Ψ_* lead to the GE field. The Sommerfeld amplitudes $\Psi_*^{\pm}$ can therefore be decomposed into two parts : a "singular part" $\Psi_*^{\pm sing}$, containing these poles and a "regular part" $\Psi_*^{\pm reg}$

$$\Psi_*^{\pm} = \Psi_*^{\pm sing} + \Psi_*^{\pm reg} \tag{1.28}$$

where $\Psi_*^{\pm reg}$ is regular in the strip

$$\{\lambda \in \mathbb{C}, \pi/2 - \varphi \leq \mathrm{Re}\lambda \leq \pi/2 + \varphi\}. \tag{1.29}$$

The choice of this strip is explained by Budaev and Bogy [39]. In order to determine the unknown functions $\Psi_L^{\pm}$ and $\Psi_T^{\pm}$ in the whole complex plane, it is sufficient to determine them in any strip of width 2φ. System (1.25) then provides an analytic continuation of these functions to the rest of the complex plane. Resolution of (1.25) is simplified in the strip (1.29), notably because the function g defined by (1.26) maps the axis $\mathrm{Re}\lambda = \frac{\pi}{2}$ to itself. The "singular part" of the Sommerfeld amplitudes is given by

$$\Psi_*^{\pm sing}(\lambda) = \sum_j \frac{res^{\pm}(\pm\lambda_*^j)}{2} \cot\left(\frac{\lambda \mp \lambda_*^j}{2}\right), \tag{1.30}$$

$\pm\lambda_*^j$ are the poles of the Sommerfeld amplitudes $\Psi_*^{\pm sing}$ and $res^{\pm}(\pm\lambda_*^j)$ are the corresponding residues. These poles and residues are determined analytically thanks to a recursive pole propagation algorithm, which is explained in great detail by Kamta-Djakou in [1] and will not be reproduced here. Decomposition (1.28) is then substituted into (1.25) and the resulting system is solved numerically, thanks to the scheme proposed by Kamotski et al. [42], to obtain the regular functions $\Psi_*^{\pm reg}$ for wedge angles lower than π.

The diffracted elastodynamic potentials ψ_β^{GTD} can be expressed in terms of the Sommerfeld amplitudes by evaluating integral (1.22) asymptotically with the steepest descent method (see appendix A) :

$$\psi_\beta^{GTD}(k_\beta r, \theta') = i\sqrt{2i\pi}[\Psi_\beta(\theta' - \pi) - \Psi_\beta(\pi + \theta')]\frac{e^{ik_\beta r}}{\sqrt{k_\beta r}} \tag{1.31}$$

Using (1.19), the diffracted displacement field is given by :

$$\mathbf{u}^{diff(SI)}(r, \theta') = D_L^{SI}(\theta')\frac{e^{ik_L r}}{\sqrt{k_L r}}\mathbf{e}_{r'} + D_T^{SI}(\theta')\frac{e^{ik_T r}}{\sqrt{k_T r}}\mathbf{e}_{\theta'} \tag{1.32}$$

where

$$D_\beta^{SI}(\theta') = -k_\beta\sqrt{2i\pi}[\Psi_\beta(\theta'-\pi) - \Psi_\beta(\pi+\theta')] \tag{1.33}$$

To summarize, following the steps of Kamotski et al. [42], the GTD diffraction coefficient of a stress-free wedge of angle $2\varphi < \pi$ can be computed. First, Sommerfeld's integral formulation of the elastodynamic potentials (1.22) is used to determine two systems of functional equations (1.25) of which the symmetric and antisymmetric Sommerfeld amplitudes are solution. These systems are then solved by determining the poles and residues of the Sommerfeld amplitudes analytically and computing the remaining regular function numerically. Finally, the GTD diffraction coefficient is deduced from an asymptotic evaluation of the Sommerfeld integral.

An other semi-analytic resolution technique is called the Laplace Transform (LT) method and is presented in the following. Once again, the main steps of the resolution will be presented but the technical details are not given.

1.3.3 The Laplace Transform (LT) Method

The Laplace Transform (LT) method was first developed by Gautesen in the case of an incident Rayleigh wave [45, 46, 47, 48, 49] and in the case of an incident longitudinal wave on a right-angled wedge [50]. It has been extended to the case of an L or T elastic wave incident on a wedge of angle $2\varphi < \pi$ by Gautesen and Fradkin [12].

In this approach, the unknown quantity is the elastodynamic displacement $\mathbf{u} = (u_1, u_2)_{(\mathbf{e}_1,\mathbf{e}_2)}$. Gautesen [45] has expressed the components of the displacement field in the entire space (not just inside the wedge) as a single-layer potential (meaning it is defined by a convolution with Green's stress tensor), analogously to Lax's electromagnetic extinction theorem [51] :

$$\begin{aligned} H(2\varphi-\theta)u_p(\mathbf{x}) = u_p^{inc}(\mathbf{x}) - \sum_{i=1}^{2}\int_0^{+\infty}\Big[G_{i2}^{(p)}(x_1-l,x')u_i(l,0) \\ + \sum_{j=1}^{2}\sum_{m=1}^{2} G_{jm}^{(p)}(x_1 - l\cos 2\varphi, x' - l\sin 2\varphi)e_j'^{(i)}e_m'^{(2)}u^{(i)}(l)\Big]dl \end{aligned} \tag{1.34}$$

where the integration variable l travels along the wedge faces, H is the Heaviside function ($H(x) = 1$ for $x > 0$ and 0 elsewhere) $(0;\mathbf{e}_1',\mathbf{e}_2',\mathbf{e}_z)$ is an orthonormal basis, shown on Fig. 1.6 where the x'-axis coincides with the top free surface and where $\mathbf{e}_2'$ is directed towards the inside of the wedge, $G^{(p)}$ is Green's stress tensor,

defined in section 1.2.1 and

$$u^{(i)}(l) = \mathbf{u}(l\cos 2\varphi, l\sin 2\varphi).\mathbf{e}'_i \tag{1.35}$$

where $u^{(1)}$ and $u^{(2)}$ are respectively the tangetial and normal displacements at points $(l\cos 2\varphi, l\sin 2\varphi)_{(\mathbf{e}_1,\mathbf{e}_2)}$. Equation (1.34) is simplified by working in the region $x' < 0$ where, in the case $2\varphi < \pi$, the left-hand side of (1.34) vanishes. The equation then contains four unknowns $(u_1, u_2)(l, 0)$ and $(u^{(1)}, u^{(2)})(l)$. In order to reduce the number of unknowns by half, the problem is once again symmetrized as described in subsection 1.3.1. As in the previous section, the " + " sign describes the symmetric problem and the " − " sign describes the antisymmetric problem. We then have :

$$u^{(i)\pm}(l) = \pm u_i^{\pm}(l, 0), \qquad i = 1, 2, \qquad l > 0 \tag{1.36}$$

Equation (1.3.1) is then reduced to :

$$u_p^{inc\pm}(\mathbf{x}) = \sum_{i=1}^{2} \int_0^{+\infty} \Big[G_{i2}^{(p)}(x_1 - l, x') u_i^{\pm}(l, 0) \pm \sum_{j=1}^{2} \sum_{m=1}^{2} G_{jm}^{(p)}(x_1 - l\cos 2\varphi, x' - l\sin 2\varphi) e_j'^{(i)} e_m'^{(2)} u_i^{\pm}(l, 0) \Big] dl \tag{1.37}$$

The Laplace transform of the displacement field is defined by :

$$\hat{u}_i(\xi) = k_T \int_0^{+\infty} u_i^{\pm}(l, 0) e^{ik_T l\xi}\, dl \tag{1.38}$$

In the Laplace domain, for the sake of simplicity, the superscript ± is omitted but implied. In order to separate the contributions of the longitudinal and transversal waves, the curl and divergence operators of equation (1.37) are successively taken. The Laplace transform, defined by (1.38), is then applied to the resulting system, yielding

$$A(\xi) \begin{pmatrix} \hat{u}_1(\xi) \\ \hat{u}_2(\xi) \end{pmatrix} = \begin{pmatrix} f_T(\xi) - \hat{U}_T s(\xi) \\ f_L(\xi) - \hat{U}_L(\xi) \end{pmatrix} \tag{1.39}$$

where $U_T = \nabla \times \mathbf{u}^{\pm}$ and $U_L = \nabla.\mathbf{u}^{\pm}$ and

$$\hat{U}_T(\xi) = \pm[-a(T_T)\hat{u}_1(T_T) + \overline{b}_T(\xi)\hat{u}_2(T_T)] \tag{1.40a}$$

$$\hat{U}_L(\xi) = \pm[\overline{b}_L(\xi)\hat{u}_1(T_L) + a(T_L)\hat{u}_2(T_L)] \tag{1.40b}$$

and

$$A(\xi) = \begin{pmatrix} a(\xi) & -b_T(\xi) \\ b_L(\xi) & a(\xi) \end{pmatrix} \tag{1.41}$$

In equations (1.40) and (1.41), we have, for $* = L, T$:

$$a(\xi) = \kappa_T - 2\xi^2 \tag{1.42a}$$

$$b_*(\xi) = 2\xi\gamma_*(\xi) \tag{1.42b}$$

$$\overline{b}_*(\xi) = 2T_*\eta_* \tag{1.42c}$$

where $\kappa_* = c_L/c_*$ and

$$\gamma_*(\xi) = \sqrt{\kappa_*^2 - \xi^2} \tag{1.43a}$$

$$T_*(\xi) = \xi\cos 2\varphi + \gamma_*(\xi)\sin 2\varphi \tag{1.43b}$$

$$\eta_*(\xi) = \xi\sin 2\varphi - \gamma_*(\xi)\cos 2\varphi \tag{1.43c}$$

and finally

$$f_*(\xi) = \begin{cases} \mp 2\pi\kappa_T^2[\sin\theta_{inc}\,\delta(\xi - \kappa_*\cos\theta_{inc})\sin(2\varphi - \theta_{inc})\delta(\xi - \kappa_*\cos(2\varphi - \theta_{inc}))] & \text{if } * = \alpha \\ 0 & \text{else} \end{cases} \tag{1.44}$$

where α is the type of the incident wave. Functions f_* contain information about the incident wave and its symmetric with respect to the wedge bisector. Indeed, the Dirac delta function can be written as the sum of two distributions [12] :

$$2\pi\delta(\xi - \xi_0) = i\left[\frac{1}{\xi - \xi_0 + i0} - \frac{1}{\xi - \xi_0 - i0}\right] \tag{1.45}$$

The Dirac delta functions in (1.44) therefore contain the initial poles of the symmetric and antisymmetric problems. The incident pole $\kappa_\alpha\cos\theta_{inc}$ and its symmetric $\kappa_\alpha\cos(2\varphi - \theta_{inc})$ can therefore be propagated using an iterative scheme. Note that equations (1.39) to (1.44) actually describe two systems of functional equations : one for the symmetric problem and one for the antisymmetric problem.

As for the SI method, the solution $\hat{\mathbf{u}}$ can be decomposed into two parts : a singular part $\hat{\mathbf{u}}^{sing}$ containing the poles of $\hat{\mathbf{u}}$, which represent the GE field and a regular part $\hat{\mathbf{u}}^{reg}$:

$$\hat{\mathbf{u}} = \hat{\mathbf{u}}^{sing} + \hat{\mathbf{u}}^{reg} \tag{1.46}$$

where $\hat{\mathbf{u}}^{reg}$ is regular in the whole complex plane except for the branch

$$\{\xi \in \mathbb{C},\ \ \mathrm{Im}\xi = 0,\ \ \mathrm{Re}\xi < -1\}, \tag{1.47}$$

which is the branch cut of γ_L defined in (1.43a), and, for $i = 1, 2$,

$$\hat{u}_i^{sing} = \sum_j \frac{res(\xi_i^j)}{\xi - \xi_i^j} \tag{1.48}$$

where ξ_i^j are the poles of $\hat{u}_i$ and $res(\xi_i^j)$ are the corresponding residues. These poles and residues are determined analytically thanks to a recursive pole propagation algorithm, which is detailed in [1] and will not be reproduced here. Decomposition (1.46) is then substituted into (1.39) and the resulting system is solved numerically using the scheme proposed by Gautesen and Fradkin [12]. Using a far-field high frequency approximation of the extinction theorem (1.34), Gautesen and Fradkin show that the diffracted field is given by :

$$H(2\varphi - \theta)\mathbf{u}^{diff(LT)}(r,\theta) = D_L^{LT}(\theta)\frac{e^{ik_L r}}{\sqrt{k_L r}}\mathbf{e}_r + D_T^{LT}(\theta)\frac{e^{ik_T r}}{\sqrt{k_T r}}\mathbf{e}_\theta \tag{1.49}$$

where the diffraction coefficients of the symmetric and antisymmetric problems are :

$$\begin{aligned}\sqrt{8\pi i}\kappa_T^2 D_L^{LT(\pm)} = {} & 2\pi\kappa_T^2 D_L^{LT(inc)\pm} + \sin(2\theta)\hat{u}_1(-\cos\theta) + (\kappa_T^2 - 2\cos^2\theta)\hat{u}_2(-\cos\theta) \\ & \mp [\sin(4\varphi - 2\theta)\hat{u}_1(-\cos(2\varphi - \theta)) + (\kappa_T^2 - 2\cos^2(2\varphi - \theta))\hat{u}_2(-\cos(2\varphi - \theta))]\end{aligned} \tag{1.50a}$$

$$\begin{aligned}\sqrt{8\pi i}D_T^{LT(\pm)} = {} & 2\pi D_T^{LT(inc)\pm} + \kappa_T[\cos(2\theta)\hat{u}_1(-\kappa_T\cos\theta) + \sin(2\theta)\hat{u}_2(-\kappa_T\cos\theta)] \\ & \pm [\cos(4\varphi - 2\theta)\hat{u}_1(-\kappa_T\cos(2\varphi - \theta)) + \sin(4\varphi - 2\theta)\hat{u}_2(-\kappa_T\cos(2\varphi - \theta))]\end{aligned} \tag{1.50b}$$

where

$$D_\beta^{LT(inc)\pm} = \begin{cases} \delta(\theta - \pi - \theta_{inc}) \pm \delta(\theta - \pi - 2\varphi + \theta_{inc}) & \text{if} \quad \alpha = \beta \\ 0 & \text{else} \end{cases} \tag{1.51}$$

These expressions are analogous to the expressions of the diffraction coefficients (3.44) and (3.45) determined with the spectral functions method in section 3.2.3, where the solution is given with respect to two unknown functions, corresponding to each wedge face.

To conclude this section, a second method for computing the GTD diffraction

coefficient of a stress-free wedge of angle $2\varphi < \pi$ has been presented, following the steps of Gautesen and Fradkin [12]. First, the extinction theorem is used to determine an integral formulation of the elastodynamic displacement field in the entire domain. Using this formulation, two functional systems of equations are derived (one for the symmetric problem and one for the antisymmetric problem) of which the components of the Laplace transform of the displacement field are the solution. These two systems are solved separately by determining the poles and residues of the unknowns and computing the remaining regular functions numerically. Finally the GTD diffraction coefficient is deduced using high frequency asymptotics.

The two semi-analytical models that have been presented here have been validated numerically [12] and experimentally [35]. They have been developed for stress-free wedges of angle $2\varphi < \pi$. Though they could probably be extended to wedges of angle higher than π, this has, to our knowledge, not been done yet in the general case of an L or T incident wave. Furthermore, these methods are valid for 2D configurations (when the incident wave vector is in the plane normal to the wedge edge). A third method, called the Spectral Functions (SF) method has been developed by Croisille and Lebeau [52] in the case of an acoustic wave incident on an immersed solid wedge of angle lower than π and has been used by Kamotski and Lebeau [53] to prove existence and uniqueness of the solution to the problem of diffraction of an elastic wave by a wedge of arbitrary angle (lower or higher than π). However, the corresponding resolution scheme is not given in [53]. In this thesis, this method will be extended to the 2D cases of an acoustic wave or an elastic wave diffracted by a stress-free wedge of arbitrary angle and to the 3D case of an elastic wave diffracted by a stress-free wedge of arbitrary angle.

Conclusion

In this first chapter, a brief summary of existing high frequency scattering models is given. The first model is the Geometrical Elastodynamics (GE) model, which is faster than numerical models (such as finite elements or finite differences) but only computes the incident and reflected field and does not account for diffraction, leading to discontinuities of the predicted total field at shadow boundaries. To correct this and account for diffraction by edges, the Geometrical Theory of Diffraction (GTD) has been developed but breaks down at shadow boundaries. Both of these models are non-uniform in the sense that the resulting scattered field is not spatially continuous and therefore is not physical.

In order to produce a physically relevant scattered field, some uniform high-frequency models have been proposed. The Kirchhoff Approximation (KA) is

spatially uniform but doesn't model diffraction accurately. In order to overcome the limitations of the GTD and KA, they are combined in an other uniform model, called the Physical Theory of Diffraction (PTD). It is spatially uniform and computes the diffracted wave accurately. However, it can be computationally expensive. A less costly uniform method is the Uniform Asymptotic Theory (UAT). Like PTD, it is a uniform model and is accurate for both the GE contribution to the scattered field and the edge-diffracted contribution to the scattered field. However, UAT requires tracing of fictitious rays, which makes it difficult to implement for complex geometries. Finally, the Uniform Theory of Diffraction (UTD) is a spatially uniform model which has been validated numerically for a half plane scatterer, is computationally cheap and is simple to implement.

Apart from the Kirchhoff approximation, all of these uniform models are corrections of the GTD model. In order to correctly compute the edge diffracted field from a wedge, a generic and trustworthy GTD solution is then necessary. For the canonical problem of elastic wave diffraction by a stress-free wedge, the two main existing GTD solutions are the Sommerfeld Integral (SI) method and the Laplace Transform (LT) method. For the moment, these methods have only been developed in 2D and for wedge angles lower than π. The objective of this thesis is to develop a semi-analytical resolution scheme, based on a third method called the Spectral Functions (SF) method, and to extend it to the case of a 3D incidence.

CHAPTER 2

The spectral functions method for acoustic wave diffraction by a stress-free wedge : theory and validation

Outline of the current chapter

Introduction

In the first chapter of this manuscript, a review of the main high-frequency scattering models and the importance of having a reliable GTD wedge diffraction

coefficient was explained. In this chapter, we begin by studying the simpler case of acoustic wave diffraction.

The mathematical theory of wedge diffraction was first introduced by Sommerfeld [43], who gave an analytical expression of the exact solution of the diffraction problem of a scalar plane wave as a contour integral [44]. Macdonald [54] has expressed the scalar solution as a series, using the variables separation technique. Sommerfeld [43] gave an analytical formula of the Geometrical Theory of Diffraction (GTD) diffraction coefficient for an arbitrary-angled wedge (with Neumann or Dirichlet boundary conditions) illuminated by a scalar plane wave. This wedge GTD coefficient can be used for scalar wave diffraction both in electromagnetics [33] and in acoustics [31, 55].

For a long time, methods of computation have been studied without proof of solvability for the wedge diffraction problem. Castro and Kapanadze [56] have proven existence and uniqueness of the solution for acoustic and electromagnetic plane waves using a detailed Fredholm analysis. Kamotski and Lebeau [53] have proven existence and uniqueness of the solution to the elastic plane wave diffraction by a soft wedge (Dirichlet boundary) problem using the Spectral Functions method in which the diffracted wave is modeled thanks to these spectral functions. Their demonstration is valid for all wedge angles but they do not propose any method of computation of the solution. The Spectral Functions method was at first developed by Croisille and Lebeau [52] who proposed a numerical algorithm in order to compute these functions for elastic wedges of angle lower than π immersed in a fluid. In this chapter, wedges of any angle (even larger than π) are taken into account, and the outside medium is void. There is only one wave type to be considered and Dirichlet or Neumann boundary conditions are supposed, as opposed to the case studied by Croisille and Lebeau [52] where three propagation modes coupled by the boundary conditions are considered, but only for wedge angles lower than π.

In the field of seismic diffraction, other approaches have been developed. The problem of acoustic diffraction in a system of wedge-shaped regions was studied by Klem-Musatov [57]. Using the Malyuzhinetz transform, this problem is reduced to a system of functional equations. However, this system is too complex to be solved in general cases. A successive approximations method is proposed in the particular case of a wedge-shaped separation between two media having the same acoustic wave velocity or in the case where the medium containing the incident wave is a wedge of angle lower than π. In the very general case of acoustic wave propagation in a homogeneous or inhomogeneous medium delimited by an arbitrary-shaped boundary, a mathematical model has been rigorously presented by Aizenberg and Ayzenberg [58], providing the analytical feasible fundamental solution for this problem. The notion of feasible

fundamental solution is a generalization of Green's function for an unbounded medium. Ayzenberg [59] shows how this general mathematical model can be numerically applied to the case of wedge diffraction. This method is applied in the case of a spherical source and it appears that parallel computation is necessary to obtain a short computation time, whereas the spectral functions method is applied here in the case of plane-wave diffraction and a simple architecture is sufficient to obtain results for a short computation time.

The aim of this chapter is to develop and implement the methodology of Croisille and Lebeau [52] in the two-dimensional (i.e. the incident wave vector lies in the plane normal to the edge) case of an acoustic wave diffracted by a soft wedge immersed in a fluid (Dirichlet boundary condition) and propose a numerical validation of the method for angles both smaller and larger than π. The expansion to all wedge angles is obtained using Kamotski and Lebeau's [53] idea of defining a new angular variable, $\tilde{\varphi}$, defined in equation (2.48), thanks to which the complete resolution and the computation of the solution are proposed and developed here for all wedge angles with a single method. Numerical validation will be achieved by comparing the GTD approximation of the diffraction coefficient obtained using the spectral functions method, with the analytical expression given in [31, 55] of the GTD approximation of the exact solution.

The outline of the chapter is the following: section 2.1. presents the problem and the diffraction coefficients are expressed in terms of the spectral functions. The resolution of the problem is discussed in section 2.2. All this is then summarized in section 2.3. Finally, numerical results are given in section 2.4. and compared to the analytical Sommerfeld solution.

2.1 Problem statement

Let us consider a stress-free wedge of angle φ immersed in a fluid Ω_f constituted of the junction of two faces $\mathcal{S}_1$ and $\mathcal{S}_2$ (see Fig. 2.1). The inward unit vectors normal to each of these faces are noted n_1 and n_2 respectively. The Cartesian coordinate system $(O;\mathbf{e}_{x_1},\mathbf{e}_{y_1})$ is linked to the face $\mathcal{S}_1$ of the wedge and $(O;\mathbf{e}_{x_2},\mathbf{e}_{y_2})$ is linked to the face $\mathcal{S}_2$. These Cartesian coordinate systems have the same origin located on the wedge edge which coincides with the z-axis. Let $\mathbf{x} = (x_1,y_1)_{(\mathbf{e}_{x_1},\mathbf{e}_{y_1})} = (x_2,y_2)_{(\mathbf{e}_{x_2},\mathbf{e}_{y_2})}$ be a position vector $\mathbf{x} = (r,\theta)$ in a local basis of polar coordinates associated to the Cartesian coordinates (x_1,y_1). The time convention used in this chapter and in all the following chapters is $\exp(i\omega t)$.

The wedge is thus irradiated by a velocity potential plane wave in the form

$$g^{\text{inc}}(\mathbf{x},t) = A\, e^{i(\omega t - \mathbf{k}^{\text{inc}}\cdot\mathbf{x})} \tag{2.1}$$

where A is the amplitude of the incident velocity potential, ω is the circular frequency, t is time and

$$\mathbf{k}^{\text{inc}} = k_0(-\cos\theta_{\text{inc}}, -\sin\theta_{\text{inc}})_{(\mathbf{e}_{x_1},\mathbf{e}_{y_1})} \tag{2.2}$$

is the wave vector of the incident wave with $k_0 = \omega/c_0$ being the wave number and c_0 is the sound velocity in the fluid. The velocity potential in the fluid g satisfies the motion equation in the fluid medium Ω_f surrounding the wedge

$$\frac{\partial^2 g}{\partial t^2} - c_0^2 \triangle g = 0 \tag{2.3}$$

and the boundary condition on the wedges faces

$$Bg\,|_{\mathcal{S}_j} = 0, \quad j = 1,2, \tag{2.4}$$

where the expression of operator B is given by (2.5a) for Dirichlet boundary conditions and by (2.5b) for Neumann boundary conditions :

$$Bg = g \quad \text{for Dirichlet boundary conditions (soft wedge)} \tag{2.5a}$$

$$Bg = \frac{\partial g}{\partial n} \quad \text{for Neumann boundary conditions (rigid wedge)} \tag{2.5b}$$

This common notation makes it possible to treat both cases simultaneously in the following developments.

The dimensionless form of the problem is obtained by defining the function h by

$$g(\mathbf{x},t) = 2A\, e^{i\omega t}\, h(k_0\mathbf{x}). \tag{2.6}$$

The dimensionless function h is the sum of the incident dimensionless wave h_{inc} and of the scattered dimensionless wave v

$$h = h_{inc} + v \tag{2.7}$$

In this decomposition, the scattered wave v is the sum of two fields : the Geometric-Elastodynamic (GE) field, which is the sum of the possibly multiple specular reflections of the incident wave and of fictitious fields compensating the incident wave in shadow zones, and the diffracted field. A detailed description of the GE field, in the case of a half-plane scatterer, is given by Kamta-Djakou et

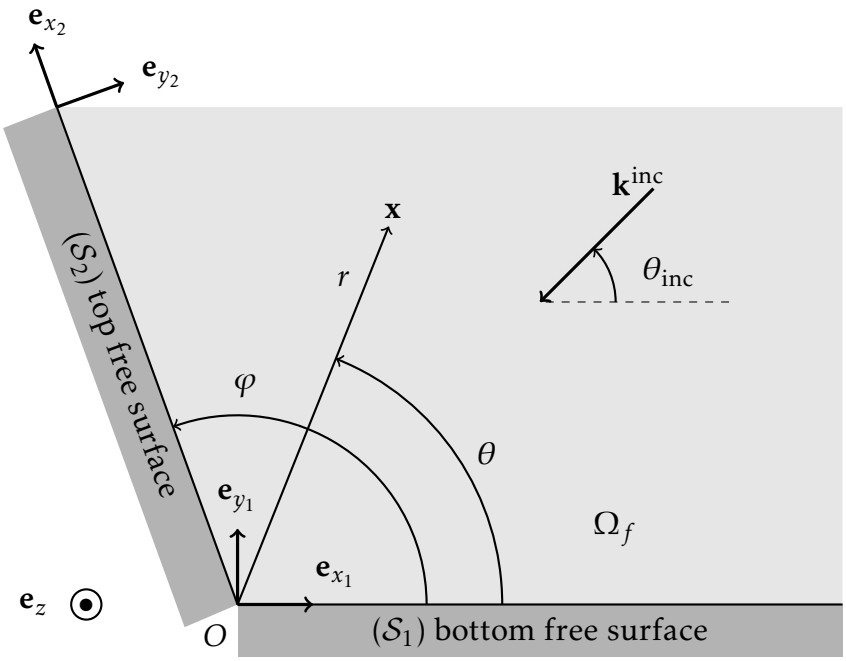

Figure 2.1 – Stress-free wedge of angle φ illuminated by a plane wave of wave vector $\mathbf{k}^{\text{inc}}$.

al. [23].

The system (2.3)-(2.4) is equivalent to the following system of equations for the dimensionless problem, obtained by inserting Fourier transform (2.6) and decomposition (2.7) into equations (2.3) and (2.4)

$$\begin{cases} (\triangle + 1)v = 0 & \text{in } \Omega_f, \\ Bv = -Bh_{inc} & \text{on } \mathcal{S}_j, \quad j = 1, 2 \end{cases} . \tag{2.8}$$

In order to obtain a solution to this problem which is physically relevant, the limiting absorption principle is used. It consists in substituting the wave number k_0 by a complex one $k_0 e^{-i\epsilon}$ with $\epsilon > 0$. This means that absorption occurs in the medium and thus the scattered waves attenuate with the distance. The system (2.8) then becomes :

$$(S_\epsilon^*) \quad \begin{cases} (\triangle + e^{-2i\epsilon})v^\epsilon = 0 & \text{in } \Omega_f, \\ Bv^\epsilon = -Bh_{\text{inc}}^\epsilon & \text{on } \mathcal{S}_j, \quad j = 1, 2 \end{cases} \tag{2.9}$$

The physically relevant solution to (2.8), called the outgoing solution, can now be defined. It is the one obtained when taking $\epsilon \to 0$ in (2.9). This limit is

noted v^0. Its integral representation is found hereafter.

2.1.1 Outgoing solution: integral representation

First, a special class of distributions is defined.

Def. 2.1.1. *The distribution $f \in \mathcal{A}$ if :*

- $f \in \mathcal{S}'(\mathbb{R})$ *(f is a tempered distribution)*
- $supp(f) \subset [0, +\infty[$
- $\exists C_0 > 0$ *such that*
$$\sup_{-\pi<\theta<0} \int_{\rho>C_0} |\hat{f}(\rho e^{i\theta})|^2 \, d\rho < \infty$$
where $\hat{f}$ is the Fourier transform of f defined by $\hat{f}(\xi) = \int_{\mathbb{R}} f(x) e^{-ix\xi} \, dx$.
- $\hat{f}(\xi)$ *is holomorphic near $\xi = 1$*

The outgoing solution to (2.8) can now be defined properly.

Def. 2.1.2. *An outgoing solution of the equation (2.8) is a solution v of the form*

$$v = v_1|_{\Omega_f} + v_2|_{\Omega_f} \tag{2.10}$$

where, for $j = 1, 2$:

$$v_j = -\lim_{\epsilon \to 0} \left(\Delta + e^{-2i\epsilon}\right)^{-1} \left[\alpha_j \otimes \delta_{\mathcal{S}_j}\right] \tag{2.11}$$

$\alpha_j \in \mathcal{A}$ are unknown and $\delta_{\mathcal{S}_1}$ and $\delta_{\mathcal{S}_2}$ are the Dirac delta functions on the faces $\mathcal{S}_1$ and $\mathcal{S}_2$ of the wedge respectively (these functions verify $\delta_{\mathcal{S}_j}(x, y) = 1$ on $\mathcal{S}_j$, and $\delta_{\mathcal{S}_j}(x, y) = 0$ elsewhere).

The following theorem is proven by Croisille and Lebeau in [52] :

Theorem 2.1.1. *The equation (2.8) admits a unique outgoing solution.*

The aim of this chapter is to extend and detail the computation of this outgoing solution for the stress-free wedge immersed in a fluid using the spectral functions method.

The double Fourier transform of a tempered distribution and its inverse are defined by :

$$\hat{f}(\xi, \eta) = \int \int_{\mathbb{R}^2} f(x, y) e^{-i(x\xi + y\eta)} \, \mathrm{d}x \mathrm{d}y \tag{2.12a}$$

$$f(x,y) = \frac{1}{4\pi^2} \int\int_{\mathbb{R}^2} \hat{f}(\xi,\eta) e^{i(x\xi+y\eta)} \mathrm{d}\xi \mathrm{d}\eta \tag{2.12b}$$

The double Fourier transform of (2.11) using (2.12a) gives

$$\hat{v_j^\epsilon} = \left[\xi^2 + \eta^2 - e^{-2i\epsilon}\right]^{-1} \hat{\alpha_j}. \tag{2.13}$$

The dimensionless velocity potential v_j^ϵ is then found by applying the inverse Fourier transform in ξ and η to (2.13).

$$v_j^\epsilon = \frac{1}{4\pi^2} \int_{-\infty}^{+\infty} \left(\int_{-\infty}^{+\infty} \frac{e^{iy_j\eta}}{\xi^2 + \eta^2 - e^{-2i\epsilon}} \mathrm{d}\eta \right) \hat{\alpha_j}(\xi)\, e^{ix_j\xi} \mathrm{d}\xi. \tag{2.14}$$

For $\epsilon \neq 0$, the inner integrand poles are given by

$$\eta = \pm\sqrt{e^{-2i\epsilon} - \xi^2} = \pm\zeta_0^\epsilon \tag{2.15}$$

and are never crossed by integration along the real axis. The inner integral on η in (2.14) can be computed using the residue theorem which leads to the following result

$$v_j^\epsilon(x_j,y_j) = \frac{i}{4\pi} \int_{-\infty}^{+\infty} \frac{e^{i|y_j|\zeta_0^\epsilon(\xi)} e^{ix_j\xi}}{\zeta_0^\epsilon(\xi)} \hat{\alpha_j}(\xi) \mathrm{d}\xi. \tag{2.16}$$

This integral is well defined if $\mathrm{Im}(\zeta_0^\epsilon) > 0$, so that the exponential in the integral decreases with the distance y_j and the absorption principle is respected. Function $\zeta_0^\epsilon(\xi)$ then satisfies for ξ real

$$\zeta_0^\epsilon(\xi) = i\sqrt{\xi^2 - e^{-i\epsilon}} \quad \text{if} \quad |\xi| \geq 1, \tag{2.17a}$$

$$\zeta_0^\epsilon(\xi) = -\sqrt{e^{-i\epsilon} - \xi^2} \quad \text{if} \quad |\xi| \leq 1. \tag{2.17b}$$

The branch points of the function $\zeta_0^\epsilon(\xi)$ are $\pm e^{-i\epsilon}$ and are also poles of the integrand in (2.16). For $\epsilon > 0$, integral (2.16) is well defined because these complex singular points are never crossed by the integration contour (the real axis). The integration contour of (2.16), is deformed into the contour Γ_0 illustrated on Fig. 2.2 so that these singular points $\pm e^{-i\epsilon}$ are not crossed by the new contour Γ_0 when $\epsilon \to 0$ (for which the physical outgoing solution of (2.9) is obtained). The curved arrows on Fig. 2.2 are described later in section 2.2.2.2.

Thus, even for $\epsilon = 0$, the integral

$$v_j^0(x_j, y_j) = \frac{i}{4\pi} \int_{\Gamma_0} \frac{e^{i|y_j|\zeta_0^0(\xi)} e^{ix_j\xi}}{\zeta_0^0(\xi)} \hat{\alpha}_j(\xi)\, \mathrm{d}\xi \tag{2.18}$$

converges. Using (2.10), our initial solution is then

$$v(\mathbf{x}) = v_1^0(x_1, y_1) + v_2^0(x_2, y_2) \tag{2.19}$$

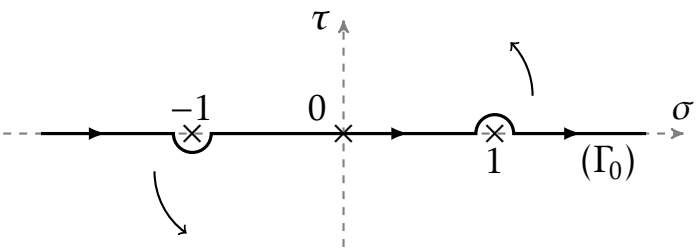

Figure 2.2 – Integration contour Γ_0 in the complex plane $\xi = \sigma + i\tau$. The curved arrows show the deformation of Γ_0 into the imaginary axis.

In the next section, an asymptotic evaluation of integral (2.18) is conducted in order to obtain a far-field approximation of the diffracted wave. The GTD diffraction coefficient is defined and its expression (2.28) is given with respect to the spectral functions $\hat{\alpha}_1(\xi)$ and $\hat{\alpha}_2(\xi)$.

2.1.2 Far-field asymptotics

Variable change $\xi = \cos\beta$, $\mathrm{d}\xi = -\sin\beta\, \mathrm{d}\beta$ allows us to transform (2.18) for $j = 1$ in

$$v_1^0(r\cos\theta, r\sin\theta) = \frac{i}{4\pi} \int_{C_0} e^{ir(\cos\beta\cos\theta - |\sin\theta|\sin\beta)} \hat{\alpha}_1(\cos\beta)\, \mathrm{d}\beta, \tag{2.20}$$

where C_0 is depicted on Fig. 2.3.

Let us introduce the variable $\bar{\theta}$ defined as

$$\bar{\theta} = \begin{cases} \theta & \text{if } \theta < \pi \\ 2\pi - \theta & \text{if } \theta \geq \pi \end{cases}. \tag{2.21}$$

Finally, using (2.21) in (2.20), we have

$$v_1^0(r\cos\theta, r\sin\theta) = \frac{i}{4\pi} \int_{C_0} e^{ir\cos(\beta+\bar{\theta})} \hat{\alpha}_1(\cos\beta)\, \mathrm{d}\beta. \tag{2.22}$$

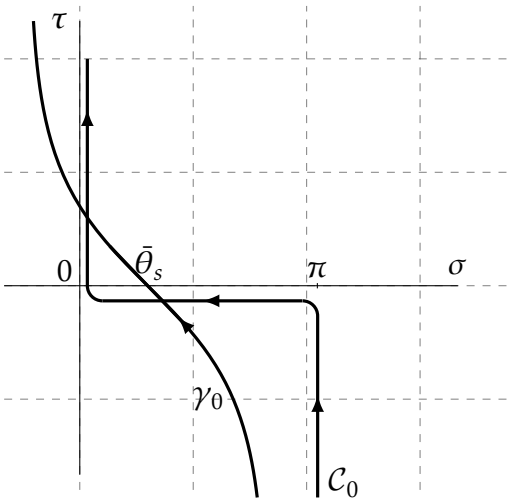

Figure 2.3 – Integration path $\mathcal{C}_0$ and the steepest descent path γ_0 in the complex plane $\beta = \sigma + i\tau$. $\bar{\theta}_s$ is the phase stationary point.

The same process is applied to (2.18) for $j = 2$ and leads to

$$v_2^0(r\cos(\varphi-\theta), r\sin(\varphi-\theta)) = \frac{i}{4\pi}\int_{C_0} e^{ir\cos(\beta+\overline{\varphi-\theta})}\hat{\alpha}_2(\cos\beta)\,\mathrm{d}\beta \tag{2.23}$$

with $\overline{\varphi-\theta}$ defined in the same way as (2.21). The saddle points of the phase functions in equations (2.22) and (2.23) are respectively $\beta = \bar{\theta}_s = \pi - \bar{\theta}$ and $\beta = \bar{\theta}_s = \pi - \overline{\varphi-\theta}$. These saddle points are always in the interval $[0,\pi]$. Poles of the spectral functions $\hat{\alpha}_1$ and $\hat{\alpha}_2$ may be crossed during the deformation of contour C_0 into the steepest descent path γ_0 (see Fig. 2.3). These poles and their corresponding residues are determined in section 2.2.2.1. They contribute to the integrals (2.18) and lead to the geometrical field, noted $v^{(GE)}$. Their contribution can be computed using the residue theorem. The resulting integral after the contour deformation is approximated using the steepest descent method (see appendix A). The contribution of the saddle points $\bar{\theta}_s$ are respectively:

$$v_1^{0(\mathrm{diff})}(x_1,y_1) = \frac{e^{-i\frac{\pi}{4}}}{2\sqrt{2\pi}}\frac{e^{-ir}}{\sqrt{r}}\hat{\alpha}_1(-\cos\theta) \tag{2.24}$$

and

$$v_2^{0(\mathrm{diff})}(x_2,y_2) = \frac{e^{-i\frac{\pi}{4}}}{2\sqrt{2\pi}}\frac{e^{-ir}}{\sqrt{r}}\hat{\alpha}_2(-\cos(\varphi-\theta)). \tag{2.25}$$

Finally in the far-field approximation, $r \gg 1$, using (2.19) and (2.24) - (2.25), the total field is

$$v^{\text{tot}} = v^{(\text{GE})} + v^{\text{diff}} \tag{2.26}$$

where v^{diff} is the field diffracted by the wedge edge

$$v^{diff} = \frac{e^{-i\frac{\pi}{4}}}{2\sqrt{2\pi}} \frac{e^{-ir}}{\sqrt{r}} [\hat{\alpha}_1(-\cos\theta) + \hat{\alpha}_2(-\cos(\varphi - \theta))]. \tag{2.27}$$

Using (2.6) and (2.27), the GTD diffraction coefficient is defined as

$$D^{GTD} = \frac{e^{-i\frac{\pi}{4}}}{2\sqrt{2\pi}} [\hat{\alpha}_1(-\cos\theta) + \hat{\alpha}_2(-\cos(\varphi - \theta))] \tag{2.28}$$

where $\hat{\alpha}_1$ and $\hat{\alpha}_2$ are unknown spectral functions.

One of the aims of this chapter is to compute the spectral functions $\hat{\alpha}_1(\xi)$ and $\hat{\alpha}_2(\xi)$ in order to find the GTD diffraction coefficient (2.28). The accuracy of the spectral functions method is then evaluated by comparing results of (2.28) with analytic expressions (2.109) in the case of Dirichlet boundaries and (2.112) in the case of Neumann boundaries. Section 2.2 is devoted to the computation of the spectral functions $\hat{\alpha}_1$ and $\hat{\alpha}_2$.

2.2 Spectral functions computation

To compute the spectral functions, the functional equations satisfied by these spectral functions $\hat{\alpha}_1$ and $\hat{\alpha}_2$ first have to be determined.

2.2.1 Functional equations of spectral functions

The velocity potential in the boundary conditions of the system (2.9) is substituted by its expression (2.19). It then leads to the following system of equations for the boundary conditions on each wedge face:

$$\begin{cases} Bv_1^0(x_1, 0) + Bv_2^0(x_2\cos\varphi, x_2\sin\varphi) = -Bv_{\text{inc}}^0 \,|_{S_1} \\ Bv_1^0(x_1\cos\varphi, x_1\sin\varphi) + Bv_2^0(x_2, 0) = -Bv_{\text{inc}}^0 \,|_{S_2} \end{cases} . \tag{2.29}$$

The Fourier transform is applied to the potential velocity expression on the face of each wedge

$$\mathcal{F}(x_j \mapsto v_j^0(x_j,0))(\xi) = \frac{i}{4\pi}\int_{\Gamma_0}\frac{\hat{\alpha_j}(\lambda)}{\zeta_0^0(\lambda)}\left(\int_0^\infty e^{-ix_j(\xi-\lambda)}dx_j\right)\mathrm{d}\lambda, \tag{2.30}$$
$$= \frac{1}{4\pi}\int_{\Gamma_0}\frac{\hat{\alpha_j}(\lambda)}{\zeta_0^0(\lambda)(\xi-\lambda)}\mathrm{d}\lambda$$

and

$$\mathcal{F}\left(x_j \mapsto v_j^0\left(x_j\cos\varphi, x_j\sin\varphi\right)\right)(\xi) = \frac{i}{4\pi}\int_{\Gamma_0}\frac{\hat{\alpha_j}(\lambda)}{\zeta_0^0(\lambda)}\left(\int_0^\infty e^{-ix_j\left(\xi-\lambda\cos\varphi-|\sin\varphi|\zeta_0^0(\lambda)\right)}dx_j\right)\mathrm{d}\lambda, \tag{2.31}$$
$$= \frac{1}{4\pi}\int_{\Gamma_0}\frac{\hat{\alpha_j}(\lambda)}{\zeta_0^0(\lambda)\left[\xi-\lambda\cos\varphi-|\sin\varphi|\zeta_0^0(\lambda)\right]}\mathrm{d}\lambda.$$

The potential velocity's normal derivative on the face of each wedge is computed using (2.18), and by noting that for each face $n_j = y_j$ (see Fig. 2.1) :

$$\frac{\partial v_j^0}{\partial n_j}(x_j,y_j) = -\frac{1}{4\pi}\int_{\Gamma_0} te^{i\xi x_j}e^{i|y_j|\zeta_0^0(\xi)}\hat{\alpha_j}(\xi)\,d\xi, \tag{2.32}$$

where $t = \mathrm{sgn}\,\mathrm{y_j}$. In order to go from one Cartesian coordinate system to another, the following change in variables is given for $j = 1, 2$ (see Fig. 2.1) :

$$\begin{cases} x_{3-j} = x_j\cos\varphi + y_j\sin\varphi \\ y_{3-j} = x_j\sin\varphi - y_j\cos\varphi \end{cases} \tag{2.33}$$

This yields :

$$\frac{\partial v_j^0}{\partial n_{3-j}} = \frac{\partial v_j^0}{\partial y_{3-j}} = \sin\varphi\frac{\partial v_j^0}{\partial x_j} - \cos\varphi\frac{\partial v_j^0}{\partial y_j} \tag{2.34}$$
$$= -\frac{1}{4\pi}\int_{\Gamma_0}\frac{(\xi\sin\varphi - t\cos\varphi\zeta_0^0(\xi))}{\zeta_0^0(\xi)}e^{i(\xi x_j+|y_j|\zeta_0^0(\xi))}\hat{\alpha_j}(\xi)\,d\xi \tag{2.35}$$

The Fourier transform can now also be applied to the potential velocity's normal derivative on the each face of the wedge

$$\begin{aligned}\mathcal{F}(x_j \mapsto \frac{\partial v_j^0}{\partial n_j}(x_j,0))(\xi) &= -\frac{1}{4\pi}\int_{\Gamma_0}\hat{\alpha_j}(\lambda)\left(\int_0^\infty e^{-ix_j(\xi-\lambda)}dx_j\right)d\lambda \\ &= \frac{i}{4\pi}\int_{\Gamma_0}\frac{\hat{\alpha_j}}{\xi-\lambda}\,d\lambda \end{aligned} \tag{2.36}$$

and

$$\begin{aligned}&\mathcal{F}\left(x_j \mapsto \frac{\partial v_j^0}{\partial n_{3-j}}(x_j\cos\varphi, x_j\sin\varphi)\right)(\xi) \\ &= -\frac{1}{4\pi}\int_{\Gamma_0}\frac{(\lambda\sin\varphi - t\cos\varphi\zeta_0^0(\lambda))}{\zeta_0^0(\lambda)}\hat{\alpha_j}(\lambda)\left(\int_0^\infty e^{-ix_j\left(\xi-\lambda\cos\varphi-|\sin\varphi|\zeta_0^0(\lambda)\right)}dx_j\right)d\lambda, \\ &= \frac{i}{4\pi}\int_{\Gamma_0}\frac{[\lambda\sin\varphi - t\cos\varphi\zeta_0^0(\lambda)]\,\hat{\alpha_j}(\lambda)}{\zeta_0^0(\lambda)\left[\xi-\lambda\cos\varphi-|\sin\varphi|\zeta_0^0(\lambda)\right]}\,d\lambda, \end{aligned} \tag{2.37}$$

here $t = \operatorname{sgn}\sin\varphi$.

The dimensionless incident wave on the faces $\mathcal{S}_1$ and $\mathcal{S}_2$ of the wedge which is involved at the right side of (2.29) is respectively:

$$v_{\text{inc}}^0(x_1,y_1) = \frac{1}{2}e^{i(x_1\cos\theta_{inc}+y_1\sin\theta_{inc})}, \tag{2.38a}$$

$$v_{\text{inc}}^0(x_2,y_2) = \frac{1}{2}e^{i(x_2\cos(\varphi-\theta_{inc})+y_2\sin(\varphi-\theta_{inc}))} \tag{2.38b}$$

Therefore, applying the Fourier transform to (2.29) leads to the following functional system of equations:

$$\begin{cases} DM(\hat{\alpha}_1)(\xi) + TM(\hat{\alpha}_2)(\xi) = \dfrac{W_1}{\xi - Z_1} \\ TM(\hat{\alpha}_1)(\xi) + DM(\hat{\alpha}_2)(\xi) = \dfrac{W_2}{\xi - Z_2} \end{cases} \tag{2.39}$$

where $Z_1 = \cos\theta_{\text{inc}}$, $Z_2 = \cos(\varphi-\theta_{\text{inc}})$, $W_1 = W_2 = 1$ in the case of Dirichlet boundary conditions and $W_1 = \sin\theta_{inc}$, $\quad W_2 = \sin(\varphi-\theta_{inc})$ in the case of Neumann boundary conditions. DM is an integral operator defined as

$$DM(\hat{\alpha}_1)(\xi) = \int_{\Gamma_0} DM(\xi,\lambda)\,\hat{\alpha}_1(\lambda)\,d\lambda = \frac{1}{2i\pi}\int_{\Gamma_0}\frac{dm(\lambda)}{\xi-\lambda}\hat{\alpha}_1(\lambda)\,d\lambda \tag{2.40}$$

where

$$dm(\lambda) = \frac{1}{\zeta_0^0(\lambda)} \tag{2.41}$$

in the case of Dirichlet boundary conditions and

$$dm(\lambda) = 1 \tag{2.42}$$

in the case of Neumann boundary conditions.

TM is an integral operator defined as

$$TM(\hat{\alpha}_1)(\xi) = \int_{\Gamma_0} TM(\xi,\lambda)\,\hat{\alpha}_1(\lambda)\,\mathrm{d}\lambda = \frac{1}{2i\pi}\int_{\Gamma_0} \frac{tm(\lambda)}{\xi - \lambda\cos\varphi - |\sin\varphi|\zeta_0^0(\lambda)}\hat{\alpha}_1(\lambda)\,\mathrm{d}\lambda \tag{2.43}$$

where

$$tm(\lambda) = \frac{1}{\zeta_0^0(\lambda)} \tag{2.44}$$

in the case of Dirichlet boundary conditions and

$$tm(\lambda) = \frac{\lambda\sin\varphi - t\cos\varphi\zeta_0^0(\lambda)}{\zeta_0^0(\lambda)} \tag{2.45}$$

in the case of Neumann boundary conditions. Note that the function TM can be expressed as

$$TM(\xi,\lambda) = \frac{1}{2i\pi}\frac{tm(\lambda)}{\xi - T_0(\lambda)}, \tag{2.46}$$

where, applying the variable change $\lambda = \cos\theta$

$$T_0(\lambda = \cos\theta) = \lambda\cos\tilde{\varphi} + \sin\tilde{\varphi}\,\zeta_0^0(\lambda) = \cos(\theta + \tilde{\varphi}) \tag{2.47}$$

with

$$\tilde{\varphi} = \begin{cases} \varphi & \text{if} \quad 0 < \varphi < \pi \\ 2\pi - \varphi & \text{if} \quad \pi < \varphi < 2\pi \end{cases} \tag{2.48}$$

Function T_0 is therefore called the translation operator, since it translates the complex angle θ to $\theta + \tilde{\varphi}$. By using this angular variable $\tilde{\varphi}$, defined differently for wedge angles lower and higher than π, the description of the spectral functions method can be written the same way for wedge angles φ lower and higher than π, even if the final results (the diffraction coefficients) are different for wedge angles $\pi < \varphi < 2\pi$ and $2\pi - \varphi$. Indeed, the variable φ appears in all the resolution (for example, it appears in the expression of pole Z_2), whereas the variable $\tilde{\varphi}$

appears only in the definition of the function T_0 in (2.47) and of the domain Ω_0 in which T_0 operates, defined as

$$\Omega_0 = \{\xi \in \mathbb{C},\ \xi = \cos\theta,\ 0 < \mathrm{Re}\,\theta < \pi - \tilde{\varphi}\}. \tag{2.49}$$

Domain Ω_0 is delineated by the hyperbola

$$\partial\Omega_0^+ = \{\xi \in \mathbb{C}, \quad \xi = \cos\theta, \quad \mathrm{Re}\theta = \pi - \tilde{\varphi}\}. \tag{2.50}$$

Domain Ω_0 and its upper boundary $\partial\Omega_0^+$ are illustrated on Fig. 2.4. Domain Ω_0 is the grey area in Fig. 2.4.

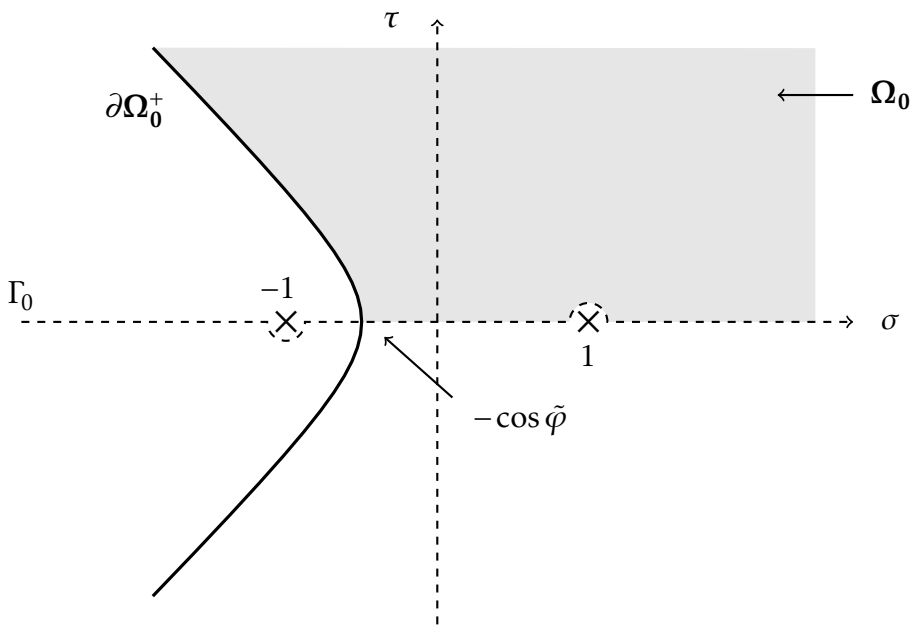

Figure 2.4 – Domain Ω_0 (the grey area) and its upper boundary $\partial\Omega_0^+$ in the complex plane $\xi = \sigma + i\tau$. The lower boundary of Ω_0 is the semi-axis $[-\cos\tilde{\varphi}, +\infty[$.

Having found the system of functional equations, it is now resolved following the methodology of Croisille and Lebeau [52].

2.2.2 System resolution

The resolution of the system of functional equations (2.39) is necessary in order to find the values of the spectral functions $\hat{\alpha}_1$ and $\hat{\alpha}_2$. With these values, the diffraction coefficients can be computed using equation (2.28).

It is shown in [52] that the actions of DM and TM integral operators onto a singular function are constituted of a "singular term" and of a "regular term".

For a singular function

$$\phi(\xi) = \frac{1}{\xi - z}, \quad z \in \mathbb{C}\backslash]-\infty, -1] \text{ with } \operatorname{Im} z \geqslant 0, \tag{2.51}$$

contour Γ_0 is deformed into contour Γ_1 in integral operator DM defined by (2.40) (thus crossing the whole upper half of the complex plane, as illustrated in Fig. 2.5), and into contour $\partial\Omega_0^+$ in integral operator TM defined by (2.43) (thus crossing sub-domains Ω_0 and $Im\xi < 0, \xi \notin \Omega_0$ as illustrated in Fig. 2.4). Using the residue theorem, the result can be decomposed as

$$DM(\phi)(\xi) = \int_{\Gamma_0} DM(\xi, \lambda) \cdot \frac{1}{\lambda - z} d\lambda = \frac{dm(z)}{\xi - z} + D_p(\xi, z) \tag{2.52a}$$

$$TM(\phi)(\xi) = \int_{\Gamma_0} TM(\xi, \lambda) \cdot \frac{1}{\lambda - z} d\lambda = \frac{tm(z)}{\xi - T_0(z)} 1_{\Omega_0}(z) + T_p(\xi, z), \tag{2.52b}$$

where the function T_0 is defined in (2.47) and where

$$1_{\Omega_0}(z) = \begin{cases} 1 & \text{if } z \in \Omega_0, \\ 0 & \text{else} \end{cases} \tag{2.53}$$

and integrals D_p and T_p are the regular terms, expressed as

$$D_p(\xi, z) = \frac{1}{2\pi i} \int_{\Gamma_1} \frac{dm(\lambda)}{\xi - \lambda} \cdot \frac{1}{\lambda - z} d\lambda, \tag{2.54a}$$

$$T_p(\xi, z) = \frac{1}{2\pi i} \int_{\partial\Omega_0^+} \frac{tm(\lambda)}{\xi - T_0(\lambda)} \cdot \frac{1}{\lambda - z} d\lambda. \tag{2.54b}$$

Croisille and Lebeau [52] proved that $D_p(z, \cdot)$ and $T_p(z, \cdot)$ belong to a special class of functions $\mathcal{H}$ defined hereafter

Def. 2.2.1. *H^+ is the space of functions f which are analytical in $\{z \in \mathbb{C},\ Imz < 0\}$ and verify :*

$$\sup_{c>0} \int_{-\infty}^{+\infty} |f(x - ic)|^2 \, dx < +\infty \tag{2.55}$$

Def. 2.2.2. *$\mathcal{H}$ is the space of the functions f analytical in $\mathbb{C}\backslash]-\infty, -1]$ such that $\forall \epsilon \in]0, \pi[, f(e^{i\epsilon} \cdot) \in H^+$.*

In the sequel, using the decomposition of the DM and TM operators for a function of the form of (2.51), it will be shown that the unknown spectral functions $\hat{\alpha}_1$ and $\hat{\alpha}_2$ in the system (2.39) have a singular part. The first step for the resolution of the system (2.39) is then to determine this singular part.

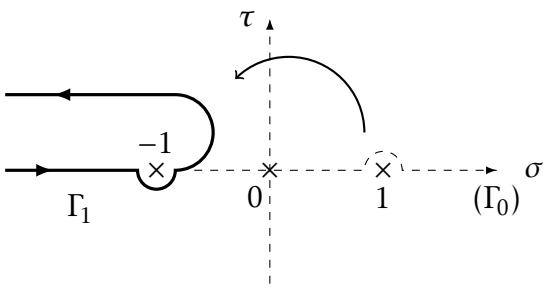

Figure 2.5 – Contour Γ_1. The curved arrow shows the deformation of Γ_0 (dashed line) into Γ_1.

2.2.2.1 Singular part

It is well known that poles of the spectral functions lead to the reflections of the incident field on the wedge faces (these reflections can be multiple), and to the fictitious fields that compensate the incident wave in the shadow zones. The sum of these reflections with the fictitious compensating fields constitute the aforementioned GE field. The singular part of the spectral functions contains these poles. The goal of this subsection is to calculate the poles and the corresponding residues and then to determine the expression of the singular part of the spectral functions, by employing a recursive algorithm.

Knowing the incident field on the wedge faces, which corresponds to the right-hand side of system (2.39), the spectral function $\hat{\alpha}_j$ can be written as

$$\hat{\alpha}_j(\xi) = \frac{V_j}{\xi - Z_j} + X'_j(\xi), \quad j = 1,2 \tag{2.56}$$

where Z_1, Z_2 are the initial poles, given in (2.39) with unknown residues V_1 and V_2 and the functions X'_j are unknown, $j = 1,2$. Replacing (2.56) in (2.52a), it is found that

$$DM(\hat{\alpha}_j)(\xi) = \frac{dm(Z_j)\cdot V_j}{\xi - Z_j} + D_p(\xi, Z_j)\cdot V_j + DM(X'_j)(\xi). \tag{2.57}$$

Substituting (2.57) in (2.39) yields, for $j = 1,2$:

$$D_p(\xi, Z_j).V_j + DM(X'_j)(\xi) + TM(\hat{\alpha}_{3-j})(\xi) = \frac{W_j - dm(Z_j).V_j}{\xi - Z_j} \tag{2.58}$$

In the above equation, the term $D_p(\xi, Z_j)$ is regular and Z_j is not a pole of $DM(X'_j)$ or $TM(\hat{\alpha}_{3-j})$ (in decomposition (2.56) it is assumed that all the information

regarding the initial pole is contained in the term $\frac{V_j}{\xi - Z_j}$). Therefore, the right-hand side of (2.58) can not admit Z_j as a pole. This implies that $V_j = dm^{-1}(Z_j).W_j$, so that the right hand side of the system (2.39) is suppressed by the first term in the right hand side of (2.57). A new version of the system can be written on a single line with new unknown functions X'_j, $j = 1, 2$:

$$DM(X'_j)(\xi) + TM(X'_{3-j})(\xi) = -TM\left(\frac{V_{3-j}}{\xi - Z_{3-j}}\right)(\xi) - D_p(V_j, Z_j)(\xi) \qquad j = 1, 2 \tag{2.59}$$

Applying (2.52b) yields

$$TM\left(\frac{V_j}{\xi - Z_j}\right)(\xi) = \frac{tm(Z_j) \cdot V_j}{\xi - T_0(Z_j)} 1_{\Omega_0}(Z_j) + T_p(\xi, Z_j) \cdot V_j \qquad j = 1, 2 \tag{2.60}$$

Thus, X'_j has a pole at $\xi = Z_j^{(1)} = T_0(Z_{3-j})$ if $Z_{3-j} \in \Omega_0$. The wave incident on face $\mathcal{S}_{3-j}$ is reflected. This reflected wave is incident on face $\mathcal{S}_j$, generating a new pole $Z_j^{(1)} = T_0(Z_{3-j})$. The unknown function X'_j in (2.56) is then decomposed as

$$X'_j(\xi) = \frac{V_j^{(1)}}{\xi - Z_j^{(1)}} + X''_j(\xi), \quad j = 1, 2 \tag{2.61}$$

where the function X''_j is unknown. Once again, the residues $V_j^{(1)}$ of these generated poles $Z_j^{(1)}$ are determined by the fact that they should cancel the singular term in $DM(X'_j)(\xi)$, found using formula (2.52a), compensating the singular term in the TM operator in (2.60).

This pole propagation process is applied recursively in order to determine all the poles of the spectral functions $\hat{\alpha}_j$. Croisille and Lebeau [52] have shown that the number of generated poles is finite and the recursive process stops when the generated poles are no longer in the domain Ω_0 defined in (2.49). All the generated poles then belong to Ω_0. Physically, this means that any incident ray leaves the wedge after a finite number of reflections.

At the end of this process, the spectral functions have the following decomposition

$$\hat{\alpha}_j = Y_j + X_j, \tag{2.62}$$

where Y_j is the singular part, X_j is the regular part and $j = 1, 2$ is the face index.

The singular part is expressed as

$$Y_j(\xi) = \sum_i \frac{V_j^{(i)}}{\xi - Z_j^{(i)}}, \tag{2.63}$$

where $i \in \mathbb{N}$, $Z_j^{(0)} = Z_j$ is the initial pole on each face of the wedge, $V_j^{(0)} = V_j$ is the corresponding initial residue on each face of the wedge, both linked to the incident field as expressed in (2.39),

$$Z_j^{(i+1)} = T_0(Z_{3-j}^{(i)}) \quad j = 1, 2 \tag{2.64}$$

are the different generated poles with their respective residues

$$V_j^{(i+1)} = -dm^{-1}(T_0(Z_{3-j}^{(i)}))\, tm(Z_{3-j}^{(i)}))\, V_{3-j}^{(i)}\, 1_{\Omega_0}(Z_{3-j}^{(i)}), \quad j = 1, 2. \tag{2.65}$$

Figure 2.6 represents the generated poles in the complex plane for two different cases : figure 2.6a for a wedge of angle $\varphi = 80^o$ with an incident angle of $\theta_{inc} = 55^o$ and figure 2.6b for $\varphi = 20^o$ and $\theta_{inc} = 15^o$. As the wedge angle decreases, the number of poles increases, some poles being very close to one another, rendering the method less accurate for very small wedge angles.

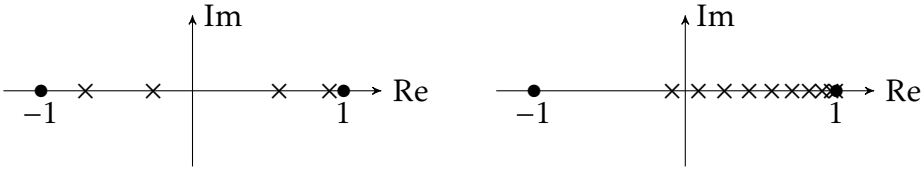

(a) $\varphi = 80^o$, $\theta_{inc} = 55^o$ (b) $\varphi = 20^o$, $\theta_{inc} = 15^o$

Figure 2.6 – Poles generated by the recursive algorithm plotted in the complex plane

The second step of the system resolution is the determination of the regular part X_j of the spectral function $\hat{\alpha}_j$, see Eq. (2.62). The regular part is determined by using the Galerkin collocation method. Section 2.2.2.2 gives the principal steps of this resolution method.

2.2.2.2 Regular part

After the determination of the singular part of the solution using the pole propagation process explained in section 2.2.2.1, the remaining system 2.39 is

by construction

$$\begin{cases} DM(X_1)(\xi) + TM(X_2)(\xi) = -\sum_k \left(D_p(\xi, Z_1^{(k)}) \cdot V_1^{(k)} + T_p(\xi, Z_2^{(k)}) \cdot V_2^{(k)} \right) \\ TM(X_1)(\xi) + DM(X_2)(\xi) = -\sum_k \left(T_p(\xi, Z_1^{(k)}) \cdot V_1^{(k)} + D_p(\xi, Z_2^{(k)}) \cdot V_2^{(k)} \right) \end{cases} \tag{2.66}$$

where X_j, $j = 1, 2$ are the regular parts of the spectral functions (2.62), D_p and T_p functions are defined in (2.54) and $Z_j^{(k)}$ are the poles of spectral function $\hat{\alpha}_j$ and their respective residues are $V_j^{(k)}$. According to Croisille and Lebeau [52], D_p and T_p are holomorphic on $\mathbb{C}\backslash]-\infty, -1]$ and therefore functions X_1 and X_2 are also holomorphic on this domain.

The functions $X_j(\xi)$, being holomorphic on $\mathbb{C}\backslash]-\infty, -1]$, can be approached in the vectorial subspace generated by functions φ_k, $1 \leq k \leq N$:

$$X_j(\xi) \approx \sum_{k=1}^{N} \tilde{X}_j^k \, \varphi_k(\xi), \quad \tilde{X}_j^k \in \mathbb{C}. \tag{2.67}$$

The coordinates $\tilde{X}_j^k$ are unknown. The system (2.66) then becomes, for $j = 1, 2$

$$\sum_{k=1}^{N} \left[\tilde{X}_j^k \int_{\Gamma_0} DM(\xi, \lambda) \varphi_k(\lambda) \, \mathrm{d}\lambda + \tilde{X}_{3-j}^k \int_{\Gamma_0} TM(\xi, \lambda) \varphi_k(\lambda) \, \mathrm{d}\lambda \right] = u_j(\xi), \tag{2.68}$$

where

$$u_j(\xi) = -\sum_k \left(D_p(\xi, Z_j^k) \cdot V_j^k + T_p(\xi, Z_{3-j}^k) \cdot V_{3-j}^k \right) \qquad j = 1, 2 \tag{2.69}$$

In the following, the integration contour Γ_0 pictured on Fig. 2.2 is deformed into the imaginary axis. If $f(\lambda)$ is a holomorphic function on $\mathbb{C}\backslash]-\infty, -1]$, the function $\tilde{f}(y) = f(iy)$ is introduced so that $\tilde{f}$ is holomorphic on $\mathbb{C} \setminus i[1, \infty[$. The variable change $\lambda = iy$ gives a new basis

$$e_{a_k}(y) = i\tilde{\varphi}_k(y) \tag{2.70}$$

The variable changes $\lambda = iy$ and $\xi = ix$ in (2.68) lead to the following system ($j = 1, 2$)

$$\sum_{k=1}^{N} \left[\tilde{X}_j^k \int_{-\infty}^{\infty} \widetilde{DM}(x, iy) \, e_{a_k}(y) \mathrm{d}y + \tilde{X}_{3-j}^k \int_{-\infty}^{\infty} \widetilde{TM}(x, iy) \, e_{a_k}(y) \mathrm{d}y \right] = \tilde{u}_j(x) \tag{2.71}$$

where $\widetilde{DM}(x,iy) = DM(ix,iy)$ and $\widetilde{TM}(x,iy) = TM(ix,iy)$. Following [52], we introduce another subspace of finite dimension in $L^2(\mathbb{R})$ which is generated by vectors e_{b_k} with

$$e_{b_k}(y) = \frac{d_k}{y - ib_k}, \quad \mathrm{Re(b_k)} \in [1,\infty[\quad \text{and} \quad \mathrm{Im(b_k)} = 0^-. \tag{2.72}$$

Points b_k are called collocation points. The system (2.71) is projected in this subspace using the following relation, for an arbitrary regular function f (recall that $\tilde{f}(iy) = f(iy)$) :

$$\langle \tilde{f} | e_{b_k} \rangle_{L^2(\mathbb{R})} = (-2i\pi)\, d_k\, f(b_k) \tag{2.73}$$

Using (2.73), the projection of the system (2.71) onto the subspace generated by $(e_{b_k}), 1 \le k \le N$ leads to the following new system (for $j = 1, 2$)

$$\begin{cases} \sum_{k=1}^{N} \left[\tilde{X}_j^k \int_{-\infty}^{\infty} DM(b_1,iy) e_{a_k}(y)\,\mathrm{d}y + \tilde{X}_{3-j}^k \int_{-\infty}^{\infty} TM(b_1,iy) e_{a_k}(y)\,\mathrm{d}y \right] = u_j(b_1) \\ \qquad\qquad \vdots \\ \sum_{k=1}^{N} \left[\tilde{X}_j^k \int_{-\infty}^{\infty} DM(b_N,iy) e_{a_k}(y)\,\mathrm{d}y + \tilde{X}_{3-j}^k \int_{-\infty}^{\infty} TM(b_N,iy) e_{a_k}(y)\,\mathrm{d}y \right] = u_j(b_N) \end{cases} \tag{2.74}$$

where

$$e_{a_k}(y) = \frac{d_k}{y - ia_k} = i\tilde{\varphi}_k(y), \quad \text{with} \quad d_k = \sqrt{\frac{a_k}{\pi}} \quad \text{and} \quad a_k \in [1,\infty[, \tag{2.75}$$

which leads to the choice of the initial basis of approximation :

$$\varphi_k(\xi) = \frac{d_k}{\xi + a_k}, \quad a_k \in [1,\infty[, \quad d_k = \sqrt{\frac{a_k}{\pi}}. \tag{2.76}$$

The approximation of the solution $X_j(\xi)$ in this subspace of finite dimension is called a Galerkin approximation. The points $(a_k)_{1\le k\le N}$ are chosen in $[1,\infty[$ so that the approximation (2.67) leads to a function which is holomorphic in $\mathbb{C}\backslash]-\infty,-1]$ and the parameters d_k are chosen using (2.73) in order to verify $\|e_{a_k}\|^2 = 1$.

The obtained system (2.74) is a linear system of equations and can be put in a matrix format:

$$\begin{pmatrix} \mathbb{D} & \mathbb{T} \\ \mathbb{T} & \mathbb{D} \end{pmatrix} \begin{pmatrix} \mathbb{X}_1 \\ \mathbb{X}_2 \end{pmatrix} = \begin{pmatrix} \mathbb{U}_1 \\ \mathbb{U}_2 \end{pmatrix} \tag{2.77}$$

where

$$\mathbb{X}_j = \begin{pmatrix} \tilde{X}_j^1 \\ \vdots \\ \tilde{X}_j^N \end{pmatrix},\ \tilde{X}_j^k \in \mathbb{C}; \qquad \mathbb{U}_j = \begin{pmatrix} u_j(b_1) \\ \vdots \\ u_j(b_N) \end{pmatrix},\ u_j(b_k) \in \mathbb{C} \tag{2.78}$$

and

$$\mathbb{D}_{lk} = \int_{-\infty}^{\infty} DM(b_l, iy) e_{a_k}(y)\,\mathrm{d}y \tag{2.79}$$

$$\mathbb{T}_{lk} = \int_{-\infty}^{\infty} TM(b_l, iy) e_{a_k}(y)\,\mathrm{d}y \tag{2.80}$$

are the matrix elements of $\mathbb{D}$ and $\mathbb{T}$ respectively. System (2.77) can be rewritten as

$$\begin{cases} (\mathbb{D}+\mathbb{T})(\mathbb{X}_1+\mathbb{X}_2) = \mathbb{U}_1+\mathbb{U}_2 \\ (\mathbb{D}-\mathbb{T})(\mathbb{X}_1-\mathbb{X}_2) = \mathbb{U}_1-\mathbb{U}_2 \end{cases}. \tag{2.81}$$

To approximate the regular part of the spectral functions (2.67), its coordinates $\tilde{X}_j^k$ in the Galerkin basis φ_k, $1 \le k \le N$, defined in (2.76) must be determined. These coordinates are the solutions of the linear system of equations (2.77) or (2.81). To resolve such a system, the matrices $\mathbb{D}$ and $\mathbb{T}$ and the right hand side $\mathbb{U}_{1,2}$ must be computed.

Matrix calculation The first step is to determine $\mathbb{D}$ and $\mathbb{T}$ matrices. Expliciting $DM(\cdot,\cdot)$ and e_{a_k} in definition (2.79), using their expressions given in (2.40) and (2.75) respectively, elements $\mathbb{D}_{lk}$ can be expressed as

$$(-2i\pi)\mathbb{D}_{lk} = -id_k\mathcal{D}(a_k, b_l) \tag{2.82}$$

with the function $\mathcal{D}(a,b)$ defined for $a > 1$ and $b > 1$ as

$$\mathcal{D}(a,b) = \int_{-\infty}^{+\infty} \frac{dm(iy)}{y+ib}\frac{1}{y-ia}dy \tag{2.83}$$

This integral's value can be determined analytically. The details of the computation being a bit heavy, they are given in appendix C.7.1.

Expliciting $TM(\cdot,\cdot)$ and e_{a_k} in definition (2.80), using their expressions given in (2.43) and (2.75) respectively, elements $\mathbb{T}_{lk}$ can be expressed as

$$(-2i\pi)\mathbb{T}_{lk} = -d_k\mathcal{T}(a_k, b_l) \tag{2.84}$$

where the function $\mathcal{T}(a,b)$ is defined for $a>1$ and $b>1$ as

$$\mathcal{T}(a,b)=\int_{-\infty}^{+\infty}\frac{tm(iy)}{b-iy\cos 2\varphi+|\sin 2\varphi|\sqrt{1+y^2}}\frac{1}{y-ia}dy. \tag{2.85}$$

This integral's value can be determined analytically. The details of the computation being a bit heavy, they are given in appendix D.9.1.

The matrices $\mathbb{D}$ and $\mathbb{T}$ are completely determined using (2.82) and (2.84) respectively. Their analytical properties are also known. In order to resolve the linear system of equations (2.77) or (2.81), their right hand side constituted of $\mathbb{U}_1$ and $\mathbb{U}_2$ must also be computed.

Determination of the right hand side of the system of equations Using (2.69), the right hand side of the system (2.74) which is evaluated at the collocation points b_l, given in (2.72), $l\in\{1,2,\dots,N\}$, is

$$u_j(b_l)=-\sum_k\left(D_p(b_l,Z_j^{(k)})\cdot V_j^{(k)}+T_p(b_l,Z_{3-j}^{(k)})\cdot V_{3-j}^{(k)}\right)\qquad j=1,2 \tag{2.86}$$

where D_p and T_p functions are defined in (2.52) and $Z_j^{(k)}$, $V_j^{(k)}$ are defined in (2.64-2.65), $k\in\mathbb{N}^*$.

Taking the definition of the D_p function in (2.52a), and deforming the contour Γ_0 pictured on Fig. 2.2 into the imaginary axis by applying the variable change $\lambda=iy$, we get

$$D_p(b_l,z)=\frac{1}{2\pi}\mathcal{D}(-z,b_l)-\frac{dm(z)}{b_l-z}. \tag{2.87}$$

where dm is defined by (2.41) in the case of Dirichlet boundary condtions and by (2.42) in the case of Neumann boundary conditions.

Similarly, using the definition of the T_p function given in (2.52b), and by deforming the integrand contour Γ_0 pictured on Fig. 2.2 into the imaginary axis by applying the variable change $\lambda=iy$ we have

$$T_p(b_l,z)=\frac{1}{2i\pi}\mathcal{T}(-z,b_l)-\frac{dm(z)}{b_l-T_0(z)}\mathbf{1}(z\in\Omega_0). \tag{2.88}$$

Expressions (2.87) of D_p and (2.88) of T_p functions are incorporated in the right hand side of the system (2.86) with $z=Z_j^k$ for each $u_j(b_l)$, $j=1,2$. In this new expression, with the pole propagation process explained in section 2.2.2.1, singular terms of D_p and T_p functions cancel each other. The remaining term in

the right hand side of the system (2.86) is therefore, for $j = 1, 2; \quad l \in \{1, 2, \ldots, N\}$

$$(2\pi i)\, u_j(b_l) = -\sum_k \left(i\mathcal{D}(-Z_j^{(k)}, b_l) \cdot V_j^{(k)} + \mathcal{T}(-Z_{3-j}^{(k)}, b_l) \cdot V_{3-j}^{(k)} \right) + \frac{2\pi i}{b_l - Z_j^{(0)}} \tag{2.89}$$

Once all matrix terms have been calculated, system (2.77) is resolved numerically using the numeric library Eigen for C++. With the resolution of this linear system of equations, the coordinates $\tilde{X}_j^k$ of the regular term X_j of the spectral functions are known and therefore the regular term X_j is approximated using (2.67). The spectral functions $\hat{\alpha}_j$ are then completely determined using (2.62), (2.63) and (2.67).

2.2.3 Propagation of the solution

The regular part approximation described previously is not accurate in the entire complex plane. There exists a procedure, called "propagation of the solution", which allows to propagate the accuracy of the regular part $X_j(\xi)$ of the spectral functions from $\xi \notin \Omega_0^-$, $\mathrm{Im}(\xi) < 0$, near the Galerkin collocation points $a_k, 1 \leq k \leq N \in [1, +\infty[$ (domain Ω_0^- is defined hereafter in (2.90)) where the numerical approximation (2.67) is valid, to the domain Ω_0^- where it is not. The sub-space Ω_0^- is defined by

$$\Omega_0^- = \{\xi \in \mathbb{C},\ \mathrm{Im}(\xi) < 0,\ \xi = \cos(\theta),\ \tilde{\varphi} < \mathrm{Re}(\theta) < \pi\} \tag{2.90}$$

and is represented in Fig. 2.7. The procedure consists in deriving new recursive equations by deforming the contour Γ_0 in the integrals of the right-hand side of (2.66) into a new contour Γ_2 and taking into account the poles crossed in the process.

To begin, the contour Γ_0 in the DM integral operator is deformed into contour Γ_2, visible Fig. 2.8. The half-space $\{\lambda, \mathrm{Im}\ \lambda < 0\}$ is then crossed during this contour deformation as shown by the curved arrow on Fig. 2.8.

During this contour deformation, only the poles of the DM function (2.40) which are

$$\lambda = \xi, \quad \text{with } \mathrm{Im}(\xi) < 0 \tag{2.91}$$

are crossed and therefore, applying the residue theorem, we have for $\xi \in \mathbb{C}$, $\mathrm{Im}(\xi) < 0$, $j = 1, 2$,

$$DM(X_j)(\xi) = \int_{\Gamma_0} DM(\xi, \lambda) X_j(\lambda)\, d\lambda = \int_{\Gamma_2} DM(\xi, \lambda) X_j(\lambda)\, d\lambda + dm(\xi) X_j(\xi). \tag{2.92}$$

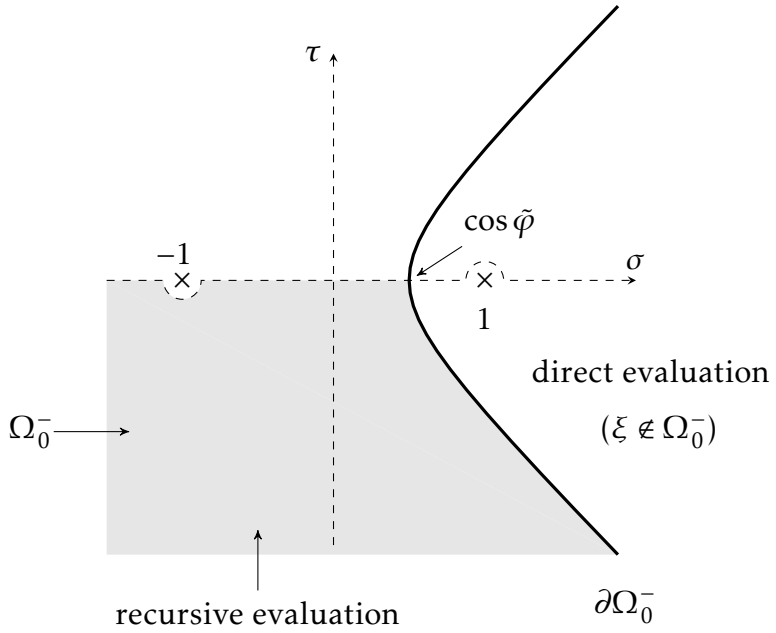

Figure 2.7 – Domain Ω_0^- and its lower boundary $\partial\Omega_0^-$ in the complex plane $\xi = \sigma + i\tau$. Ω_0^- is delimited by $\partial\Omega_0^-$ andthe semi-axis $]-\infty, \cos\widetilde{2\varphi}]$.

The poles of the TM function (2.43) are

$$\lambda = T_0^{-1}(\xi) = \xi\cos\tilde{\varphi} - \sin\tilde{\varphi}\,\zeta_0(\xi) = \cos(\theta - \tilde{\varphi}) \quad \text{if} \quad \xi = \cos\theta \tag{2.93}$$

T_0^{-1} operates in domain Ω_0^- onto $\mathbb{C}$, so that the cosine function in (2.93) is always well defined. Therefore, these poles are crossed during this contour deformation if and only if $\xi \in \Omega_0^-$ (see dotted area on Fig. 2.7). The domain Ω_0^- is delineated by the hyperbola

$$\partial\Omega_0^- = \{\xi \in \mathbb{C},\ \mathrm{Im}(\xi) < 0, \xi = \cos\theta, \mathrm{Re}\,\theta = \tilde{\varphi}\}. \tag{2.94}$$

Domain Ω_0^- and contour $\partial\Omega_0^-$ are illustrated on Fig. 2.7.

Applying the residue theorem to the TM integral operator then gives for $\xi \in \mathbb{C}$, $\mathrm{Im}(\xi) < 0$, $j = 1, 2$,

$$\int_{\Gamma_0} TM(\xi,\zeta)X_j(\zeta)\,d\zeta = \int_{\Gamma_2} TM(\xi,\zeta)X_j(\zeta)\,d\zeta + M_0(\xi).X_j(T_0^{-1}(\xi)), \tag{2.95}$$

where the transfer operator M_0 is defined as :

$$M_0(\xi = \cos\theta) = -\frac{\sin(\theta - \tilde{\varphi})}{\sin\theta} tm(T_0^{-1}(\xi)) 1_{\Omega_0^-}(\xi) \tag{2.96}$$

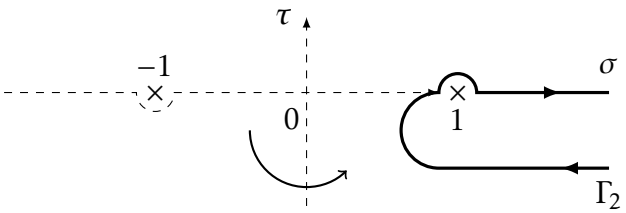

Figure 2.8 – Contour Γ_2. The curved arrow shows the deformation of Γ_0 into Γ_2.

Using (2.92) and (2.95) in the system of functional equations (2.66), a new equivalent system is obtained for $\xi \in \mathbb{C}$, $\mathrm{Im}(\xi) < 0$:

$$\begin{cases} X_1(\xi) = g_1(\xi) - dm^{-1}(\xi) M_0(\xi) X_2(T_0^{-1}(\xi)) \\ \\ X_2(\xi) = g_2(\xi) - dm^{-1}(\xi) M_0(\xi) X_1(T_0^{-1}(\xi)) \end{cases} \tag{2.97}$$

where

$$g_j(\xi) = dm(\xi)^{-1} \left[u_j(\xi) - \int_{\Gamma_2} DM(\xi, \lambda) X_j(\lambda) \, \mathrm{d}\lambda - \int_{\Gamma_2} TM(\xi, \lambda) X_{3-j}(\lambda) \, \mathrm{d}\lambda \right] \tag{2.98}$$

Formula (2.97) is called the recursive formula because it uses the value of the regular function X_2 at point $T_0^{-1}(\xi)$, where the numerical approximation for the regular part may be valid, to compute the value of X_1 at the point ξ where the approximation is not valid (and vice-versa). If the translation from ξ to $T_0^{-1}(\xi)$ is not sufficient to reach the domain $\mathbb{C}\backslash\Omega_0^-$ where the approximation is valid, then the use of the formula is repeated as many times as necessary (computing $X_2(T_0^{-1}(\xi))$ using the value of $X_1(T_0^{-2}(\xi))$, etc.), until domain $\mathbb{C}\backslash\Omega_0^-$ is reached. This recursive evaluation can be summed up in one concise formula, using a newly defined operator $\mathcal{G}_j^{(k)}$, $k \in \mathbb{N}$:

$$\mathcal{G}_j(\xi^{(k)}) = \begin{cases} g_j(\xi^{(k)}) \text{ if } k \text{ is even} \\ g_{3-j}(\xi^{(k)}) \text{ if } k \text{ is odd} \end{cases} \tag{2.99}$$

Using this definition, the recursive evaluation of the regular parts of the spectral

functions if given for $j = 1, 2$:

$$X_j(\xi) = \sum_k R^{(k)} \mathcal{G}_j^{(k)}(\xi^{(k)}), \tag{2.100}$$

where $k \in \mathbb{N}$, $\xi^{(0)} = \xi$ is the initial point at which function X_j is evaluated and $R^{(0)} = 1$. The computation points $\xi^{(k)}$ and the coefficients $R^{(k)}$ are determined recursively :

$$\xi^{(k+1)} = T_0^{-1}(\xi^{(k)}) \quad \text{if} \quad \xi^{(\mathrm{k})} \in \Omega_0^- \tag{2.101}$$

are the generated evaluation points with the corresponding coefficients

$$R^{(k+1)} = -R^{(k)}.dm^{-1}(\xi^{(k)}).M_0(\xi^{(k)}) \tag{2.102}$$

The term $1_{\Omega_0^-}$ appears in the expression (2.96) of the transfer operator M_0, ensuring that the process stops when the generated evaluation points are no longer in Ω_0^-.

In practice, formulation (2.100) is implemented to evaluate the regular part of the system numerically. In order to do so, the points $\xi^{(k)}$ and the corresponding coefficients $R^{(k)}$ are determined recursively, using an algorithm similar to the one used to determine the poles and residues of the spectral functions. To calculate g_j functions, we need to compute

$$\int_{\Gamma_2} DM(\xi, \lambda) X_j(\lambda) \mathrm{d}\lambda \approx \sum_k \tilde{X}_j^k \int_{\Gamma_2} DM(\xi, \lambda) \varphi_k(\lambda) \mathrm{d}\lambda \tag{2.103}$$

and

$$\int_{\Gamma_2} TM(\xi, \lambda) X_j(\lambda) \mathrm{d}\lambda \approx \sum_k \tilde{X}_j^k \int_{\Gamma_2} TM(\xi, \lambda) \varphi_k(\lambda) \mathrm{d}\lambda \tag{2.104}$$

If $\mathrm{Im}(\xi) < 0$, substituting the explicit expression of φ_k, given by (2.76), into (2.103) and using the residue theorem combined with the variable change $\lambda = iy$ yields the definition of a new operator $\mathcal{ND}$:

$$\int_{\Gamma_2} DM(\xi, \lambda) \frac{1}{\lambda + a} \, \mathrm{d}\lambda = \frac{1}{2\pi} \mathcal{D}(a, \xi) - \frac{dm(\xi)}{\xi + a} = \mathcal{ND}(a, \xi). \tag{2.105}$$

For the TM contributions, the poles $\lambda = T_0^{-1}(\xi)$ are taken into account if and only if $\xi \in \Omega_0^-$. Thus, for $\xi \in \Omega_0^-$, $\mathrm{Im}(\xi) < 0$, the residue theorem combined with

the variable change $\lambda = iy$ yields the definition of a new operator $\mathcal{NT}$:

$$\int_{\Gamma_2} TM(\xi,\lambda)\frac{1}{\lambda+a}\,\mathrm{d}\lambda = \frac{1}{2i\pi}\mathcal{T}(a,\xi) - \frac{dm(\xi)}{T_0^-(\xi)+a} = \mathcal{NT}(a,\xi) \tag{2.106}$$

Formula (2.67) finally leads to, for $\xi \in \Omega_0^-$ and $j = 1,2$,

$$dm(\xi)\,g_j(\xi) - u_j(\xi) = -\left(\sum_k \tilde{X}_j^k\, d_k\, N\mathcal{D}(a_k,\xi) + \sum_k \tilde{X}_{3-j}^k\, d_k\, N\mathcal{T}(a_k,\xi)\right) \tag{2.107}$$

This concludes the description of the semi-analytical evaluation of the spectral functions. For the sake of clarity, a summary of the method is presented in the following section.

2.3 Summary of the spectral functions method

The Spectral Functions (SF) method can be summarized in the following manner : first, following Croisille and Lebeau [52], the solution of the acoustic scattering problem is expressed as a complex integral (2.18), using a version of the limiting absorption principle which guarantees the physical correctness of the solution (see section 2.1.1). This integral expression is given with respect to two unknown functions (one for each wedge face) called the spectral functions. The integral formulation is then used in section 2.1.2 to determine a far-field approximation of the wedge's edge diffracted field, which is fully determined by the value of a coefficient called the diffraction coefficient (2.28), which is also expressed with respect to the spectral functions. The rest of the method is therefore devoted to the semi-analytic computation of these spectral functions. To this aim, a system of functional equations solved by the spectral function is determined in section 2.2.1 using the Fourier transform of the wedge scattering problem's boundary conditions. This system is used to decompose the spectral functions as the sum of two parts: a singular part y_j, determined analytically thanks to a recursive algorithm in section 2.2.2.1, and a regular part X_j approximated numerically using a Galerkin collocation method in section 2.2.2.2. Finally, in section 2.2.3, a recursive method called the "propagation of the solution" is used to improve the accuracy of the evaluation of the regular part in the entire complex plane. Some numerical results are presented in the sequel.

2.4 Numerical results

In this section, a far-field ($k_0 r >> 1$) asymptotic evaluation of the diffraction coefficient is computed using the stationary phase method (see section 2.1.2):

$$D^{GTD}(\theta) = \frac{e^{-i\frac{\pi}{4}}}{\sqrt{2\pi}}[\hat{\alpha}_1(-\cos\theta) + \hat{\alpha}_2(-\cos(\varphi-\theta))] \tag{2.108}$$

(where $\hat{\alpha}_1$ and $\hat{\alpha}_2$ are the spectral functions). This asymptotic evaluation is compared to the analytic expression of the diffraction coefficient of the scattering of a plane wave with a wedge at interfaces fluid/void as expressed by Sommerfeld [43]. Keller [14] gives an analytical expression of the GTD approximation of the coefficient in the case of the diffraction of a scalar plane wave by a wedge with Dirichlet boundary conditions which can be used in the case of a stress-free (soft) wedge immersed in a fluid :

$$\begin{aligned} D^{(\mathrm{Dir})}(\theta) = \frac{e^{-i\frac{\pi}{4}}}{2\mathcal{N}\sqrt{2\pi}} \Bigg[& \cot\left(\frac{\pi + (\theta+\theta_{\mathrm{inc}})}{2\mathcal{N}}\right) + \cot\left(\frac{\pi - (\theta+\theta_{\mathrm{inc}})}{2\mathcal{N}}\right) \\ & - \cot\left(\frac{\pi + (\theta-\theta_{\mathrm{inc}})}{2\mathcal{N}}\right) - \cot\left(\frac{\pi - (\theta-\theta_{\mathrm{inc}})}{2\mathcal{N}}\right)\Bigg], \end{aligned} \tag{2.109}$$

with $\mathcal{N} = \varphi/\pi$.

To apply the recursive procedure described in 2.2.3, calculation points ξ must have a negative imaginary part. The calculation points considered are then

$$\xi_1 = -\cos\theta - i\,10^{-3} \quad \text{and} \quad \xi_2 = -\cos(\varphi-\theta) - i\,10^{-3}, \tag{2.110}$$

where θ is the observation angle in the wedge (see Fig. 2.1).

For the Galerkin basis defined in (2.75), the parameters a_k are chosen as an exponential law, so that they are distributed along the axis $[1,\infty[$. The parameters b_k are chosen close to the a_k collocation points but in the lower half of the complex plane :

$$\begin{aligned} a_k &= 1.1 + 0.05\left(10^{\frac{k-1}{4}} - 1\right), \quad 1 \le k \le 20 \\ b_k &= a_k - i0.1, \quad 1 \le k \le 20. \end{aligned} \tag{2.111}$$

The module of the diffraction coefficients computed using the spectral functions and the Sommerfeld integral method for various wedge angles and various incidence angles are plotted in terms of the observation angle θ, $0 \le \theta \le \varphi$ and presented on Fig. 2.9 (commented in the following).

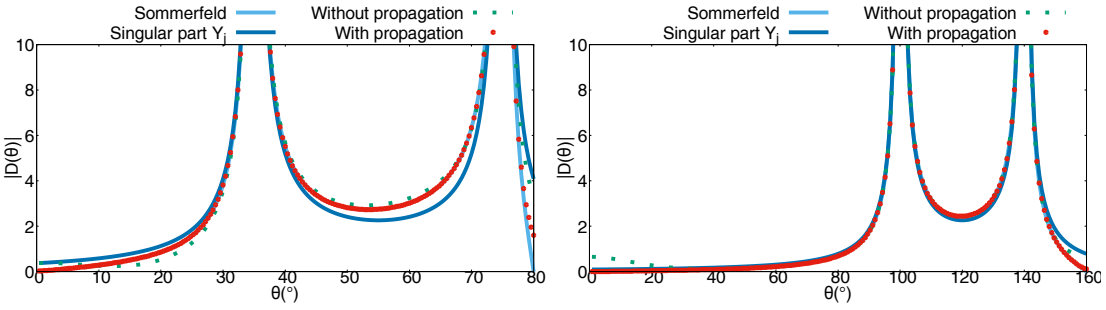

(a) $\varphi = 80^o$, $\theta_{\text{inc}} = 55^o$ (b) $\varphi = 160^o$, $\theta_{\text{inc}} = 40^o$

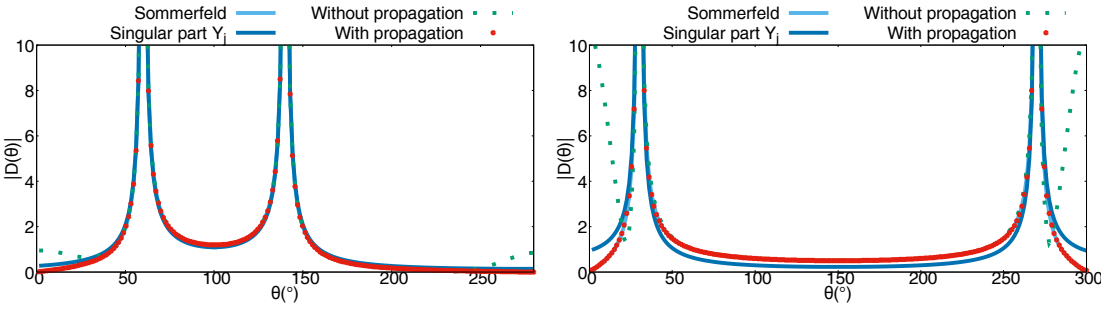

(c) $\varphi = 280^o$, $\theta_{\text{inc}} = 240^o$ (d) $\varphi = 300^o$, $\theta_{\text{inc}} = 150^o$

Figure 2.9 – Diffraction coefficient computed with the spectral functions and with the Sommerfeld method, in the case of Dirichlet boundary conditions.

In the case of Neumann boundary conditions, a far-field evaluation of the diffraction, given by (2.28) is compared to the analytic expression of the diffraction coefficient given by Sommerfeld [43]. The GTD approximation of this coefficient is also given by Keller [14] :

$$D^{(\text{Neu})}(\theta) = \frac{e^{-i\frac{\pi}{4}}}{2\mathcal{N}\sqrt{2\pi}}\left[\cot\left(\frac{\pi+(\theta+\theta_{\text{inc}})}{2\mathcal{N}}\right)+\cot\left(\frac{\pi-(\theta+\theta_{\text{inc}})}{2\mathcal{N}}\right)\right.$$
$$\left.+\cot\left(\frac{\pi+(\theta-\theta_{\text{inc}})}{2\mathcal{N}}\right)+\cot\left(\frac{\pi-(\theta-\theta_{\text{inc}})}{2\mathcal{N}}\right)\right] \tag{2.112}$$

The results are presented on Fig 2.10.

In each of these figures, the continuous light blue line represents the modules of the diffraction coefficients obtained using the Sommerfeld integral method, the continuous dark blue line represents those obtained using the Spectral function singular part Y_j alone, the short-dashed green line represents those obtained using the Spectral functions method without propagation of the solution and the red circles represent those obtained using the spectral functions method with

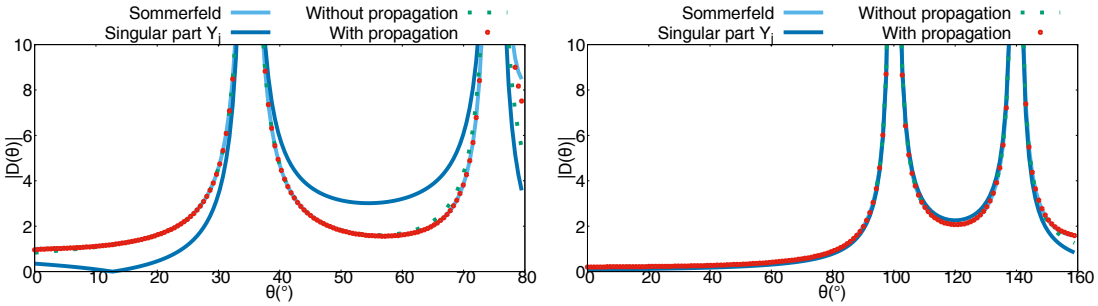

(a) $\varphi = 80^o$, $\theta_{\text{inc}} = 55^o$ (b) $\varphi = 160^o$, $\theta_{\text{inc}} = 40^o$

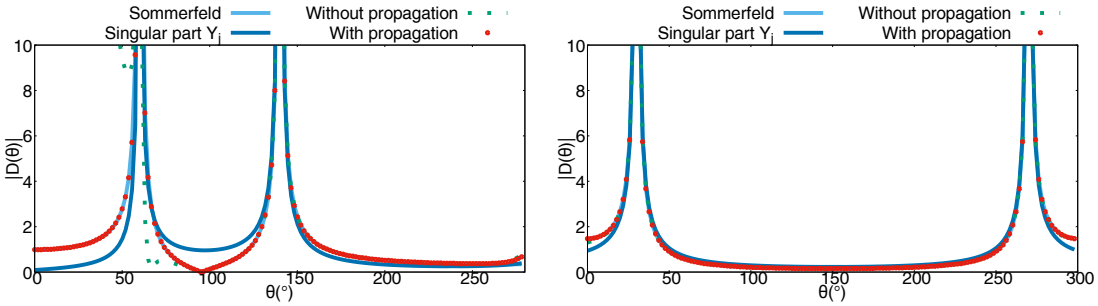

(c) $\varphi = 280^o$, $\theta_{\text{inc}} = 240^o$ (d) $\varphi = 300^o$, $\theta_{\text{inc}} = 150^o$

Figure 2.10 – Diffraction coefficient computed with the spectral functions and with the Sommerfeld method, in the case of Neumann boundary conditions.

propagation of the solution described in paragraph 2.2.3.

On Figs. 2.9a, 2.9b, 2.10a and 2.10b the wedge angles are lower than π and on figs. 2.9d, 2.9c, 2.10d and 2.10c the wedge angles are greater than π. In all cases, it appears clearly that both the regular part of the solution and the recursive method are necessary to obtain optimal results. When both of these are included, diffraction coefficients obtained with Spectral functions are close to those of the Sommerfeld method. In addition, the run time to evaluate the diffraction coefficients in 250 different observation points, in each of the presented configurations, using an Intel(R) Xeon(R) CPU E3-1240 v3 is under 0.1 seconds for both methods.

Conclusion

The spectral functions method is developed here to model diffraction of an acoustic wave by stress-free soft or hard wedges. The main steps of the method have been summarized in section 2.3. The diffraction coefficient obtained using the

spectral functions method has been compared to the analytic one obtained from the asymptotic evaluation of the Sommerfeld integral. The numerical results obtained thanks to the spectral functions method are very close to those given by the analytical solution and the result is obtained at a very low computational cost. This proves the applicability and feasibility of the spectral functions method, as well as its efficiency and its precision. It may therefore be extended to more complex wedge diffraction cases such as 2D and 3D elastic wave diffraction, as will be shown in the following chapters.

CHAPTER 3

2D elastic plane-wave diffraction by a stress-free wedge of arbitrary angle

Outline of the current chapter

Introduction

In the previous chapter, the spectral functions method was developed in the case of an acoustic wave incident on a wedge with Dirichlet or Neumann boundaries. In the case of a plane elastic wave, it seems that the solution cannot be computed analytically. Therefore, semi-analytical resolutions and far-field ($kr >> 1$, k being the wave number and r being the distance of observation) asymptotics have become common approaches. In this regard, the Geometrical Theory of Diffraction (GTD) was first introduced in electromagnetics by Keller [14] and applied to elastodynamics by Achenbach et al. in 2D (when the incident wave vector is in the plane normal to the edge) and in 3D [16, 15]. The total asymptotic fields obtained with this method are spatially non-uniform in the sense that they diverge at shadow boundaries of the Geometrical Elastodynamics (GE) field. To solve this problem, some uniform corrections of the GTD have been developed. The Physical Theory of Diffraction (PTD) has been developed in electromagnetics by Ufimtsev [20] and extended to elastic waves [21, 60] but it is computationally expensive for large scatterers. Another uniform correction is the Uniform Asymptotic Theory (UAT) developed in elastodynamics by Achenbach et al. [16]. This method has been tested by Fradkin and Stacey [61], using a finite difference algorithm. It requires an artificial extension of the scattering surface and the construction of fictitious rays [31]. For these reasons, a more commonly used uniform correction of the GTD method is the Uniform Theory of Diffraction (UTD). It was developed in electromagnetics by Kouyoumjian and Pathak [33] using the Pauli-Clemmow [62] asymptotic approximation of integrals. Kamta Djakou et al. [23] have extended it to elastodynamics with application to the scattering from a half-plane. This method is computationally efficient but still requires a trustworthy diffraction model in order to be applied. For the scalar case of 2D wedge diffraction of a shear horizontally polarized incident wave, a comparison of asymptotic (GTD and uniform) and exact solutions has been carried out in elastodynamics by Aristizabal et al. [63].

The problem of acoustic diffraction in a system of wedge-shaped regions was studied by Klem-Musatov [57], but this system is too complex to be solved in general cases. For the very general problem of acoustic wave propagation in a homogeneous or inhomogeneous medium delimited by an arbitrary-shaped boundary, a mathematical model has been rigorously presented by Aizenberg and Ayzenberg [58]. Ayzenberg [59] shows how this model can be numerically applied to the case of wedge diffraction. However, it appears that parallel programming is necessary to obtain a short computation time.

Another method, in which the free-space Green's tensor is used to express the Fourier transform of the displacement on the edges, was first developed by Gautesen for the case of a longitudinal wave diffracted by an elastic quarter-

space [50] and extended to the case of a scattered Rayleigh wave for wedge angles in the range $[63^o, 180^o]$ for wedge angles lower than π [49, 45] and to $[189^o, 327^o]$ for wedge angles higher than π [46]. This method has also been applied to horizontally polarized shear waves scattered by a wedge-shaped interface between two different elastic materials [64]. The problem of elastic wave diffraction by a wedge has also been tackled by Budaev [65, 66, 36] and reduced to a singular integral equation. However, no clear numerical scheme of resolution has been proposed. Budaev and Bogy [39] have applied this method to the case of an incident Rayleigh wave and have proposed a corresponding numerical resolution. However, the theoretical development was incomplete and has been clarified by Kamotski et al. [42]. Budaev and Bogy's method, called the Sommerfeld Integral (SI) method, and Gautesen's method, called the Laplace Transform (LT) method have both been extended by Gautesen and Fradkin [12] to the case of an elastic wave diffracted by a stress-free wedge of angle lower than π. They offer a comparison of the two methods and an experimental validation is given by Chapman et al. [35].

Another boundary integral approach was developed by Croisille and Lebeau [52] in the case of an acoustic plane wave scattered by an immersed elastic wedge. This is called the spectral functions method and was described both theoretically and numerically for the case of an immersed wedge of angle lower than π [52]. The spectral functions method was also used by Kamotski and Lebeau [53] to prove existence and uniqueness of the solution to the 2D problem of a plane elastic wave diffracted by a stress free wedge of arbitrary angle. However, no numerical scheme of resolution was given. The aim of this chapter is to propose and implement the numerical aspects of the spectral functions method in the 2D case of a stress-free elastic wedge of any angle. The results are validated by comparison to Gautesen's LT code [12] for wedge angles lower than π and to the spectral finite elements code of Imperiale et al. developed for the commercial software CIVA [67] for wedge angles higher than π.

The structure of the chapter is the following. The problem at hand is stated in section 3.1. Section 3.2 presents an integral formulation of the solution in terms of two unknown functions called the spectral functions. This formulation is then used to compute a far-field approximation of the displacement field, following the steps of Kamotski and Lebeau [53], using an unknown coefficient called the diffraction coefficient, expressed in terms of the spectral functions. In section 3.3, the semi-analytical computation of these spectral functions is presented in detail. The first part of this computation consists in determining the poles and residues of these functions thanks to an algorithm adapted from Croisille and Lebeau [52] for the stress-free elastic wedge of any angle. The second step is to approximate the remaining regular part of the spectral functions, and the newly

developed necessary computations are detailed here. The third and final step is called the "propagation of the solution". It is based on a system of recursive equations determined by Croisille and Lebeau [52], which has been modified in order to be applicable to our case, and the computations necessary to a numerical evaluation of these equations are given here. Finally, some numerical results and validation of diffraction coefficients are given in section 3.4 and experimental validation is presented in 3.5.

3.1 Problem statement

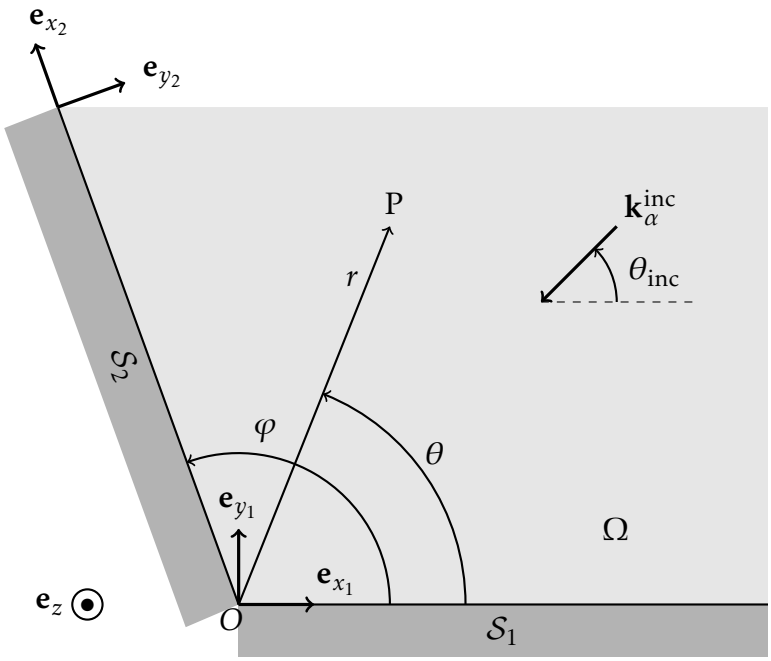

Figure 3.1 – Plane wave incident on a stress-free wedge of angle φ

Let us consider the diffraction problem of a plane longitudinal elastic wave $\mathbf{u}^{inc}$ incident on a wedge delimited by the stress-free infinite plane faces $\mathcal{S}_1$ and $\mathcal{S}_2$. The inside of the wedge is a homogeneous isotropic medium occupying the space Ω defined by :

$$\Omega = \{(r\cos\theta, r\sin\theta) \backslash \theta \in]0, \varphi[\} \tag{3.1}$$

And the incident plane wave is of the form

$$\mathbf{u}^{inc}(\mathbf{x}, t) = \mathbf{A}_\alpha e^{i(\mathbf{k}_\alpha^{inc}\cdot\mathbf{x} - \omega t)} \tag{3.2}$$

$\alpha = L, T$ is the type of the incident plane wave (longitudinal or transversal), $\mathbf{A}_\alpha$ is the amplitude vector and $\mathbf{k}_\alpha^{inc}$ is the incident wave vector. The Cartesian coordinate system $(O;\mathbf{e}_{x_1},\mathbf{e}_{y_1})$ is linked to the face $\mathcal{S}_1$ of the wedge and $(O;\mathbf{e}_{x_2},\mathbf{e}_{y_2})$ is linked to the face $\mathcal{S}_2$, as shown in Fig. 3.1. These coordinate systems have the same origin located on the wedge edge which coincides with the z-axis. Let $\mathbf{x} = (x_1', y_1')_{(\mathbf{e}_{x_1},\mathbf{e}_{y_1})} = (x_2', y_2')_{(\mathbf{e}_{x_2},\mathbf{e}_{y_2})}$ be a position vector $\mathbf{x} = (r,\theta)$ in a local basis of polar coordinates associated to the coordinates (x_1', y_1'). In the following, except when specified otherwise, all vectors are expressed in the coordinate system $(O;\mathbf{e}_{x_1},\mathbf{e}_{y_1})$. The incident wave vector is given by

$$\mathbf{k}_\alpha^{inc} = \frac{\omega}{c_\alpha}\begin{pmatrix}\cos\theta_{inc}\\ \sin\theta_{inc}\end{pmatrix} \tag{3.3}$$

$c_L = \sqrt{(\underline{\lambda}+2\underline{\mu})/\rho}$ is the velocity of the longitudinal waves, $c_T = \sqrt{\underline{\mu}/\rho}$ is the velocity of the transversal ones and $\underline{\lambda}, \underline{\mu}$ are the Lamé coefficients. The amplitude vector may be colinear (in the case of a longitudinal wave) or normal (in the case of a transversal wave) to the incident wave vector. It will then be directed by $\hat{\mathbf{i}}_\mathbf{L}$ or $\hat{\mathbf{i}}_\mathbf{T}$ respectively :

$$\hat{\mathbf{i}}_\mathbf{L} = \begin{pmatrix}\cos\theta_{inc}\\ \sin\theta_{inc}\end{pmatrix} \quad \hat{\mathbf{i}}_\mathbf{T} = \begin{pmatrix}-\sin\theta_{inc}\\ \cos\theta_{inc}\end{pmatrix} \tag{3.4}$$

In all the following, bold characters are reserved for matrices in order to simplify notations and the time-harmonic factor $e^{-i\omega t}$ is omitted.

The unknown displacement field u is a solution of the linear elasticity equations for a homogeneous isotropic medium and verifies stress-free boundary conditions on the wedge faces. Let us suppose that the total displacement field is the sum of an incident and a scattered field :

$$u = u_0 + u^{inc} \tag{3.5}$$

The dimensionless problem is obtained thanks to the following change in variables :

$$x = \frac{\omega}{c_L}x', \quad y = \frac{\omega}{c_L}y' \tag{3.6a}$$

$$u_0(x', y') = v(x, y) \tag{3.6b}$$

The problem that we wish to solve is the following :

$$(\mathcal{P}^\alpha) \qquad \begin{cases} (E+1)v = 0 & (\Omega)\\ Bv = -B\mathrm{v}_\alpha^{\mathrm{inc}} & (\mathcal{S})\end{cases} \tag{3.7}$$

where E and B are respectively the elasticity and normal stress operators:

$$Ev = \mu\Delta v + (\lambda + \mu)\nabla\nabla v \tag{3.8}$$
$$Bv = (\lambda\nabla v.\mathbb{I}_2 + 2\mu\varepsilon(v)).n \tag{3.9}$$

$\mathbb{I}_2$ is the two-dimensional identity matrix and n is the inward normal to the faces of the wedge ($n = e_{y_j}$ on $\mathcal{S}_j$). The dimensionless Lamé coefficients are given by

$$\lambda = \frac{\lambda}{\rho c_L^2}, \quad \mu = \frac{\mu}{\rho c_L^2} \tag{3.10}$$

The deformations tensor is given by

$$\varepsilon(v) = \frac{1}{2}\begin{pmatrix} 2\dfrac{\partial v_1}{\partial x} & \dfrac{\partial v_1}{\partial y} + \dfrac{\partial v_2}{\partial x} \\ \dfrac{\partial v_1}{\partial y} + \dfrac{\partial v_2}{\partial x} & 2\dfrac{\partial v_2}{\partial y} \end{pmatrix} \tag{3.11}$$

where (v_1, v_2) are the components of vector v and the dimensionless incident waves are

$$\mathrm{v}_{\mathrm{L}}^{\mathrm{inc}}(\mathrm{r},\theta) = \begin{pmatrix} \cos\theta_{inc} \\ \sin\theta_{inc} \end{pmatrix} \mathrm{e}^{\mathrm{ir}\nu_{\mathrm{L}}\cos(\theta-\theta_{\mathrm{inc}})} \qquad \mathrm{v}_{\mathrm{T}}^{\mathrm{inc}}(\mathrm{r},\theta) = \begin{pmatrix} -\sin\theta_{inc} \\ \cos\theta_{inc} \end{pmatrix} \mathrm{e}^{\mathrm{ir}\nu_{\mathrm{T}}\cos(\theta-\theta_{\mathrm{inc}})} \tag{3.12}$$

Finally, let us define the following ratios :

$$\nu_L = 1 \qquad \nu_T = \frac{c_L}{c_T} \qquad \nu_R = \frac{c_L}{c_R}, \tag{3.13}$$

where c_R is the Rayleigh wave velocity.

3.2 Integral Formulation of the solution

The first step in solving problem $(\mathcal{P}^\alpha)$ is to formulate the solution as an integral, following the formalism of Kamotski and Lebeau [53]. In order to do so, a new class of functions is defined, as well as the outgoing solution of the problem. The main ideas of their development are reproduced here.

3.2.1 Limiting absorption principle

The limiting absorption principle is applied to $(\mathcal{P}^\alpha)$, meaning that it is considered as a special case ($\varepsilon = 0$ i.e. no medium absorption) of the problem

$$(\mathcal{P}_\varepsilon^\alpha) \qquad \begin{cases} (E + e^{-2i\varepsilon})v^\varepsilon = 0 & (\Omega) \\ Bv^\varepsilon = -B\mathrm{v}_\alpha^{\mathrm{inc}} & (\mathcal{S}) \end{cases} \tag{3.14}$$

Kamotski and Lebeau [53] have shown that this problem admits a unique solution, which is the sum of two contributions, corresponding to each of the faces of the wedge

$$v^\varepsilon = v_1^\varepsilon + v_2^\varepsilon, \tag{3.15}$$

where functions v_j^ε are defined in all of $\mathbb{R}^2$ by

$$v_j^\varepsilon = -(E + e^{-2i\varepsilon})^{-1}\left[\begin{pmatrix}\alpha_j \\ \beta_j\end{pmatrix} \otimes \delta_{\mathcal{S}_j}\right], \tag{3.16}$$

where $\delta_{\mathcal{S}_j}$ is the Dirac distribution associated to face $\mathcal{S}_j$. It is defined by its action on an arbitrary test function $f \in C_0^\infty(\mathbb{R}^2)$:

$$\langle \delta_{\mathcal{S}_j}, f \rangle = \int_0^\infty f((x_j, 0)\, dx_j \tag{3.17}$$

The distributions α_j and β_j are unknown and are supposed to belong to the special class $\mathcal{A}$ given by definition 2.1.1. The notation $\hat{f}$ refers to the Fourier transform of the function f:

$$\hat{f}(\xi) = \int_{\mathbb{R}} e^{-ix\xi} f(x)\, dx \tag{3.18}$$

and $\mathcal{S}'(\mathbb{R})$ is the space of tempered distributions on $\mathbb{R}$. Using this definition, Kamotski and Lebeau [53] then obtain the following: Existence and uniqueness of the outgoing solution was demonstrated by Kamotski and Lebeau [53] and is not the object of this paper. Our goal is to propose a detailed method of numerical computation of this solution.

The limiting absorption principle presented above leads to a rigorous definition of the solution to the problem $(\mathcal{P}^\alpha)$. It is also useful in order to derive an integral formulation of this solution.

3.2.2 Integral formulation

In order to compute the integral formulation of the solution, the two-sided Fourier transform of a tempered distribution and its inverse are defined in the same manner as in the previous chapter :

$$\hat{f}(\xi,\eta) = \int\int_{\mathbb{R}^2} f(x,y)e^{-i(x\xi+y\eta)}\,\mathrm{d}x\mathrm{d}y \tag{3.19a}$$

$$f(x,y) = \frac{1}{4\pi^2}\int\int_{\mathbb{R}^2} \hat{f}(\xi,\eta)e^{i(x\xi+y\eta)}\mathrm{d}\xi\,\mathrm{d}\eta \tag{3.19b}$$

The first step is to take the two-sided Fourier transform of equation (3.16). This is permitted since all the encountered distributions are tempered distributions (as discussed in the previous subsection).

$$\hat{v}_j^\epsilon(\xi,\eta) = (\mathbf{M} - e^{-2i\varepsilon}\mathbb{I}_2)^{-1}\Sigma_j(\xi), \tag{3.20}$$

where Σ_j, $j = 1,2$ are two unknown functions called the spectral functions such that

$$\Sigma_j(\xi) = \begin{pmatrix}\hat{\alpha}_j(\xi)\\ \hat{\beta}_j(\xi)\end{pmatrix}, \tag{3.21}$$

and the matrix

$$\mathbf{M} = \begin{pmatrix}(\lambda+\mu)\xi^2 + \mu(\xi^2+\eta^2) & (\lambda+\mu)\xi\eta\\ (\lambda+\mu)\xi\eta & (\lambda+\mu)\eta^2 + \mu(\xi^2+\eta^2)\end{pmatrix} \tag{3.22}$$

is the two-sided Fourier transform of the elasticity operator E defined by (3.8). By using the fact that $\lambda + 2\mu = 1$ and $\mu = 1/\nu_T^2$, parameters λ and μ can be replaced by their expression with respect to ν_T^2 and by substituting (3.22) into (3.20), functions $\hat{v}_j^\epsilon$ can be expressed as:

$$\hat{v}_j^\varepsilon(\xi,\eta) = \begin{pmatrix}a(\xi,\eta) & b(\xi,\eta)\\ b(\xi,\eta) & a(\eta,\xi)\end{pmatrix}\Sigma_j(\xi), \tag{3.23}$$

where

$$a(\xi,\eta) = \frac{\xi^2 + \nu_T^2\eta^2 - \nu_T^2 e^{-2i\varepsilon}}{(\xi^2+\eta^2-e^{-2i\varepsilon})(\xi^2+\eta^2-\nu_T^2e^{-2i\varepsilon})} \tag{3.24a}$$

$$b(\xi,\eta) = \frac{(1-\nu_T^2)\xi\eta}{(\xi^2+\eta^2-e^{-2i\varepsilon})(\xi^2+\eta^2-\nu_T^2e^{-2i\varepsilon})} \tag{3.24b}$$

The two-sided Fourier transform of v_j^ε can now be reversed

$$v_j^\varepsilon(x_j,y_j)=\frac{1}{4\pi^2}\int_{-\infty}^{+\infty}e^{ix_j\xi}\int_{-\infty}^{+\infty}e^{iy_j\eta}\begin{pmatrix}a(\xi,\eta) & b(\xi,\eta)\\ b(\xi,\eta) & a(\eta,\xi)\end{pmatrix}d\eta\,\Sigma_j(\xi)\,d\xi \tag{3.25}$$

The inner integral is computed using Gauss' residue theorem. The poles of the integrand are $\eta=\pm\zeta_*^\varepsilon(\xi), *=L,T$, with

$$\zeta_*^\varepsilon(\xi)=\sqrt{e^{-2i\varepsilon}\nu_*^2-\xi^2} \tag{3.26}$$

thus yielding:

$$v_j^\varepsilon(x_j,y_j)=\frac{i}{4\pi}e^{2i\varepsilon}\int_{-\infty}^{+\infty}e^{ix_j\xi}\sum_{*=L,T}e^{i|y_j|\zeta_*^\varepsilon(\xi)}M_*^\varepsilon(\xi,\operatorname{sgn}y_j)\Sigma_j(\xi)\,d\xi, \tag{3.27}$$

where, noting $t=\operatorname{sgn}y_j$

$$\mathbf{M_L^\varepsilon}(\xi,t)=\begin{pmatrix}\frac{\xi^2}{\zeta_L^\varepsilon(\xi)} & t\xi\\ t\xi & \zeta_L^\varepsilon(\xi)\end{pmatrix}\quad\text{and}\quad\mathbf{M_T^\varepsilon}(\xi,t)=\begin{pmatrix}\zeta_T^\varepsilon(\xi) & -t\xi\\ -t\xi & \frac{\xi^2}{\zeta_T^\varepsilon(\xi)}\end{pmatrix} \tag{3.28}$$

According to Croisille and Lebeau [52], after slightly deforming the integration contour from $\mathbb{R}$ to Γ_0 represented in Fig. 3.2 integral (3.27) converges when $\varepsilon\to 0$:

$$v_j(x_j,y_j)=\frac{i}{4\pi}\int_{\Gamma_0}e^{ix_j\xi}\sum_{*=L,T}e^{i|y_j|\zeta_*(\xi)}\mathbf{M}_*(\xi,\operatorname{sgn}y_j)\Sigma_j(\xi)\,d\xi \tag{3.29}$$

In order to simplify notations, the exponent $\varepsilon=0$ has been omitted. The function ζ_* defined by taking $\varepsilon=0$ in (3.26) has multiple branch cuts. In order to satisfy the radiation condition at infinity

$$\lim_{|y_j|\to+\infty}\|v_j^\varepsilon(x_j,y_j)\|=0, \tag{3.30}$$

we chose $\operatorname{Im}\zeta_*(\xi)>0$:

$$\zeta_*(\xi)=\begin{cases}i\sqrt{\xi^2-\nu_*^2} & \text{for } |\xi|\geq\nu_*\\ -\sqrt{\nu_*^2-\xi^2} & \text{for } |\xi|\leq\nu_*\end{cases} \tag{3.31}$$

The integral formulation (3.29) is an expression of the solution in terms of an unknown function Σ_j called the spectral function. In the next section, by computing a far-field asymptotic approximation of this integral, we define a

function of the observation angle θ (see Fig. 3.1) called the diffraction coefficient and express this coefficient in terms of Σ_1 and Σ_2.

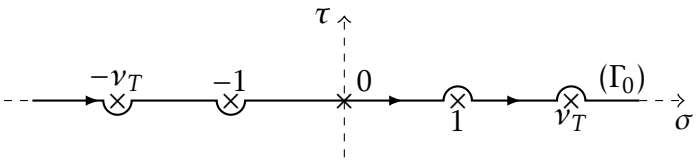

Figure 3.2 – Integration contour Γ_0 in the complex plane $\xi = \sigma + i\tau$.

3.2.3 Far-field asymptotics

Let $P = (x', y') = (r\cos\theta, r\sin\theta)$ be an observation point, represented in Fig. 3.1. According to equation (3.6), the diffracted field at P is given by:

$$u_0(x', y') = v(\frac{\omega}{c_L} r\cos\theta, \frac{\omega}{c_L} r\sin\theta) \tag{3.32}$$

Let $R = \frac{\omega r}{c_L}$ denote the far-field parameter. Our goal is to determine an asymptotic evaluation of the diffracted field when $R \to +\infty$. To do so, we begin by applying the following change of variables in integral (3.29) :

$$\begin{aligned} \xi &= \nu_* \cos\lambda \\ d\xi &= -\nu_* \sin\lambda \, d\lambda, \end{aligned} \tag{3.33}$$

yielding, in polar coordinates

$$v_1(r\cos\theta, r\sin\theta) = \frac{i}{4\pi} \int_{C_0} \sum_{*=L,T} \nu_*^2 e^{i\nu_* r\cos(\lambda+\bar{\theta})} \mathbf{P}_*(\lambda, t) \Sigma_1(\nu_* \cos\lambda) \, d\lambda, \tag{3.34}$$

where $t = \operatorname{sgn}\sin\theta$, $\bar{\theta}$ is defined by equation (2.21), contour C_0 is represented in Fig. 3.3 and

$$\mathbf{P_L}(\lambda, t) = \begin{pmatrix} \cos^2\lambda & -t\cos\lambda\sin\lambda \\ -t\cos\beta\sin\lambda & \sin^2\lambda \end{pmatrix} \tag{3.35}$$

$$\mathbf{P_T}(\lambda) = \mathbb{I}_2 - \mathbf{P_L}(\lambda) \tag{3.36}$$

Note that $\mathbf{P}_*(\lambda, -1) = \mathbf{P}_*(-\lambda, 1)$. In the following, we will use the notation $\mathbf{P}_*(\lambda) = \mathbf{P}_*(\lambda, 1)$.

An asymptotic evaluation of (3.34) is determined using the steepest descent method. This consists of deforming integration contour C_0 into $\gamma_{\bar{\theta}}$ represented

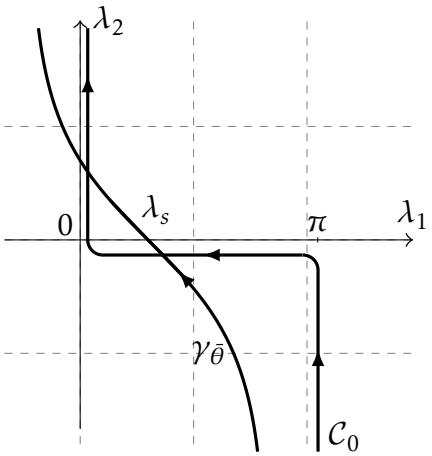

Figure 3.3 – Integration contours C_0 and $\gamma_{\bar{\theta}}$ in the complex plane $\lambda = \lambda_1 + i\lambda_2$. λ_s is the stationary phase point.

in Fig. 3.3. The approximation is then the sum of two contributions:

$$v_1 = v_1^{sing} + v_1^{diff}, \tag{3.37}$$

where v_1^{sing} is the contribution of all the singularities of the spectral function Σ_1 crossed by the contour deformation and v_1^{diff} is the contribution of the phase function's saddle point $\lambda_s = \pi - \bar{\theta}$, corresponding to the field diffracted by the wedge edge. We will see that the singularities crossed are either simple poles (corresponding to the reflected waves on the wedge faces or to the Rayleigh surface waves) or branch points (corresponding to head waves). In this paper, we are only concerned with the determination of the edge-diffracted field, which corresponds to the contribution of the saddle-point and is given by:

$$v_1^{diff}(r\cos\theta, r\sin\theta) = \frac{e^{-i\pi/4}}{2\sqrt{2\pi}} \sum_{*=L,T} \nu_*^2 \frac{e^{-i\nu_* r}}{\sqrt{\nu_* r}} \mathbf{P}_*(\pi - \theta)\Sigma_1(-\nu_* \cos\theta) \tag{3.38}$$

Note that asymptotic evaluation (3.38) is only valid when the saddle point λ_s does not coincide with a singular point (pole or branch point) of the spectral function Σ_1. The poles of the spectral functions will be determined analytically in section 3.3.2. The branch points of functions v_j, $j = 1, 2$ are located at $\xi = \pm\nu_L$ and $\xi = \pm\nu_T$. Applying (3.33), this means that :

$$\nu_* \cos\lambda_s = -\nu_* \cos\theta = \pm\nu_L = \pm 1 \tag{3.39a}$$

$$\text{or} \quad \nu_* \cos\lambda_s = -\nu_* \cos\theta = \pm\nu_T \tag{3.39b}$$

For $* = L$, (3.39a) yields $\theta = 0$ or $\theta = \pi$, meaning that the direction of observation is grazing along the wedge's horizontal face $\mathcal{S}_1$. (3.39b) does not have a real solution for $* = L$. For $* = T$, (3.39a) yields $\theta = \theta_c = \text{acos}(1/\nu_T)$ or $\theta = \pi - \theta_c$, θ_c is called the critical angle, and (3.39b) yields $\theta = 0$ or $\theta = \pi$. Borovikov [68] gives some clues as to how to treat the case where the stationary phase point coincides with another singularity of the integrand but no high-frequency asymptotics prove satisfactory in some situations of practical interest [69] and are neither available when the critical transition zones overlap penumbras, that is when all three critical points (stationary, critical and pole) coalesce [70]. In this chapter, it is assumed that λ_s does not coalesce with a singularity of the integrand.

Similar considerations yield:

$$v_2^{diff}(x_2, y_2) = \frac{e^{-i\pi/4}}{2\sqrt{2\pi}} \sum_{*=L,T} \nu_*^2 \frac{e^{-i\nu_* r}}{\sqrt{\nu_* r}} \mathbf{P}_*(\pi - (\varphi - \theta)) \Sigma_2(-\nu_* \cos(\varphi - \theta)) \tag{3.40}$$

The branch points are now located at $\bar{\theta} = \varphi$, $\bar{\theta} = \pi - \varphi$, $\bar{\theta} = \varphi - \theta_c$ and $\bar{\theta} = \pi - (\varphi - \theta_c)$. The total diffracted field is the sum of the saddle-point contributions from each face

$$v^{diff} = v_1^{diff} + v_2^{diff} \tag{3.41}$$

This can be identified with the total diffracted field written in terms of longitudinal and transversal contributions,

$$v^{diff} = v_L^{diff} \hat{i}_L + v_T^{diff} \hat{i}_T, \tag{3.42}$$

with $\hat{i}_*$ defined by (3.4), leading to the following definition of the diffraction coefficient D_β^α :

$$v_\beta^{diff}(r\cos\theta, r\sin\theta) = D_\beta^\alpha(\theta) \frac{e^{-i\nu_\beta r}}{\sqrt{\nu_\beta r}} \mathrm{v}_{\text{inc}}^\alpha(\mathrm{r}\cos\theta, \mathrm{r}\sin\theta), \tag{3.43}$$

where $\beta = L, T$ is the type of the diffracted wave. The diffracted field is thus represented by a cylindrical wave, proportional to the incident wave and weighted by the diffraction coefficient. By substituting (3.38)-(3.40) into (3.41) and (3.43) into (3.42) and identifying the results, we finally obtain the expression of the diffraction coefficients in terms of the components $(\hat{\alpha}_j, \hat{\beta}_j)$, $j = 1, 2$ of the spectral

functions Σ_j, $j = 1, 2$, see (3.21)

$$D_L^\alpha(\theta) = \frac{e^{-i\pi/4}}{2\sqrt{2\pi}}\Big(\hat{\alpha}_1(-\cos\theta)\cos\theta + \hat{\beta}_1(-\cos\theta)\sin\theta + \hat{\alpha}_2(-\cos(\varphi-\theta))\cos(\varphi-\theta) + \hat{\beta}_2(-\cos(\varphi-\theta))\sin(\varphi-\theta)\Big) \tag{3.44}$$

$$D_T^\alpha(\theta) = \nu_T^2\frac{e^{-i\pi/4}}{2\sqrt{2\pi}}\Big(-\hat{\alpha}_1(-\nu_T\cos\theta)\sin\theta + \hat{\beta}_1(-\nu_T\cos\theta)\cos\theta + \hat{\alpha}_2(-\nu_T\cos(\varphi-\theta))\sin(\varphi-\theta) - \hat{\beta}_2(-\nu_T\cos(\varphi-\theta))\cos(\varphi-\theta)\Big) \tag{3.45}$$

In order to determine the field diffracted by a wedge illuminated by an incident plane wave, it is sufficient to compute the diffraction coefficient. This coefficient has been expressed in terms of two unknown functions called the spectral functions. The semi-analytical computation of these functions is presented in the following section

3.3 Semi-analytical evaluation of the spectral functions

The first step in computing the spectral functions is to determine a system of functional equations of which they are a solution. We will then show that these functions can be decomposed into two parts : a singular function, computed analytically, and a regular function, approached numerically.

3.3.1 Functional equations

In the previous section, the diffracted wave has been expressed in terms of two unknown functions called the spectral functions. In this subsection, a system of functional equations satisfied by these functions is determined.

The system of functional equations is determined using the boundary conditions on the faces of the wedge (3.7). These can be expressed separately for each face of the wedge, using decomposition (3.15):

$$\begin{cases} B\Big(v_1(x_1,0) + v_2(x_2\cos\varphi, x_2\sin\varphi)\Big) = -B\mathrm{v}_\alpha^{\mathrm{inc}}|_{\mathcal{S}_1} \\ B\Big(v_2(x_2,0) + v_1(x_1\cos\varphi, x_1\sin\varphi)\Big) = -B\mathrm{v}_\alpha^{\mathrm{inc}}|_{\mathcal{S}_2} \end{cases} \tag{3.46}$$

Let us note (v_j^1, v_j^2), $j = 1, 2$ the coordinates of vector v_j in the Cartesian coordinate

system (x_j, y_j), represented in Fig. 3.1. By expliciting the normal stress operator (3.9) in each of these systems, system (3.46) can be expressed as

$$\begin{cases} B_1(v_1) + B_2(v_2) = -B\mathbf{v}_*^{\text{inc}}|_{\mathcal{S}_1} \\ B_1(v_2) + B_2(v_1) = -B\mathbf{v}_*^{\text{inc}}|_{\mathcal{S}_2} \end{cases}, \tag{3.47}$$

where two new operators are defined:

$$B_1(v_1) = \begin{pmatrix} \mu\left(\frac{\partial v_1^1}{\partial y_1} + \frac{\partial v_1^2}{\partial x_1}\right) \\ \\ \frac{\partial v_1^2}{\partial y_1} + \lambda \frac{\partial v_1^1}{\partial x_1} \end{pmatrix} \tag{3.48}$$

$$B_2(v_2) = \begin{pmatrix} \mu\sin(2\varphi)\left(\frac{\partial v_2^1}{\partial x_2} - \frac{\partial v_2^2}{\partial y_2}\right) - \mu\cos(2\varphi)\left(\frac{\partial v_2^1}{\partial y_2} + \frac{\partial v_2^2}{\partial x_2}\right) \\ \\ (\lambda + 2\mu\sin^2\varphi)\frac{\partial v_2^1}{\partial x_2} + (\lambda + 2\mu\cos^2\varphi)\frac{\partial v_2^2}{\partial y_2} - \mu\sin(2\varphi)\left(\frac{\partial v_2^1}{\partial y_2} + \frac{\partial v_2^2}{\partial x_2}\right) \end{pmatrix} \tag{3.49}$$

The functional equations satisfied by the spectral functions are obtained by taking the Fourier transform of this system.

The partial derivatives of v_1 with respect to x_1 and y_1 are evaluated in $y_1 = 0, x_1 \geq 0$ using (3.29) before being substituted into (3.48). Finally, by using the following formula

$$\int_0^{+\infty} e^{-ix(\xi-\zeta)}\, dx = \frac{1}{i(\xi-\zeta)}, \quad \text{Im}\xi < 0, \quad \text{Im}\zeta > 0,$$

the Fourier transform of operator B_1 is obtained :

$$\begin{aligned} \int_0^{+\infty} e^{-ix\xi} B_1(v_1)(x)\, dx &= \frac{1}{2}\mathbf{DM}(\Sigma_1)(\xi) \\ &= \frac{1}{2}\int_{\Gamma_0} \mathbf{DM}(\xi,\zeta)\Sigma_1(\zeta)\, d\zeta \end{aligned}, \tag{3.50}$$

with

$$\mathbf{DM}(\xi,\zeta) = \frac{1}{2i\pi}\frac{1}{\xi-\zeta}\mathbf{dm}(\zeta) = \frac{1}{2i\pi}\frac{1}{\xi-\zeta}\begin{pmatrix} -1 & A(\zeta) \\ B(\zeta) & -1 \end{pmatrix} \tag{3.51}$$

and

$$A(\zeta) = \frac{z}{\zeta_T(z)}(1 - 2\mu Q(\zeta)) \tag{3.52a}$$

$$B(\zeta) = -\frac{\zeta}{\zeta_L(\zeta)}(1 - 2\mu Q(\zeta)) \tag{3.52b}$$

$$Q(\zeta) = \zeta_L(\zeta)\zeta_T(\zeta) + \zeta^2, \tag{3.52c}$$

where $\zeta_*, * = L, T$ is given by (3.31).

The Fourier transform of operator B_2 is obtained through a similar process. The partial derivatives of v_2 are evaluated in $x_2 = x\cos\varphi, y_2 = x\sin\varphi, x \geq 0$ and then substituted into (3.49) before applying the Fourier transform, , defined by (3.18), to the results. Finally, by using the following formula

$$\int_0^{+\infty} e^{-ix(\xi-(\zeta\cos\varphi+\zeta_*(\xi)\sin\tilde{\varphi}))}\,dx = \frac{1}{i(\xi-(\zeta\cos\varphi+\zeta_*(\xi)|\sin\varphi|)}, \quad \mathrm{Im}\xi < 0, \quad \mathrm{Im}\zeta > 0 \tag{3.53}$$

and by noting

$$D_*(\xi,\zeta) = \frac{1}{\xi-(\zeta\cos\varphi+\zeta_*(\zeta)\sin\tilde{\varphi})} \tag{3.54}$$

the Fourier transform of B_2 is obtained :

$$\int_0^{+\infty} e^{-ix\xi} B_2(v_2)(x)\,dx = \frac{1}{2}\mathbf{TM}(\Sigma_2)(\xi) = \frac{1}{2}\int_{\Gamma_0} \mathbf{TM}(\xi,\zeta)\Sigma_2(\zeta)\,d\zeta, \tag{3.55}$$

where

$$\mathbf{TM}(\xi,\zeta) = \frac{1}{2\pi i}\sum_{*=L,T} D_*(\xi,\zeta)\mathbf{tm}_*(\zeta, \mathrm{sgn}\ \sin\varphi) \tag{3.56}$$

and, having $t = \mathrm{sgn}\ \sin\varphi$,

$$\begin{cases} \mathbf{tm}_L(\zeta,t) = \left(\frac{\zeta}{\zeta_L(\zeta)}f_L;\, t f_L\right) \\ f_L = \begin{pmatrix} \mu[\cos(2\varphi)(2t\zeta\zeta_L) - \sin(2\varphi)(\zeta^2-\zeta_L^2)] \\ -\lambda + 2\mu[\sin(2\varphi)(t\zeta\zeta_L) - \zeta^2\sin^2\varphi - \zeta_L^2\cos^2\varphi] \end{pmatrix} \end{cases} \tag{3.57}$$

$$\begin{cases} \mathbf{tm}_T(\zeta,t) = \left(-t f_T;\, \frac{\zeta}{\zeta_T(\zeta)}f_T\right) \\ f_T = \mu\begin{pmatrix} \cos(2\varphi)(\zeta^2-\zeta_T^2) + \sin(2\varphi)(2t\zeta\zeta_T) \\ \sin(2\varphi)(\zeta^2-\zeta_T^2) - \cos(2\varphi)(2t\zeta\zeta_T) \end{pmatrix}. \end{cases} \tag{3.58}$$

The Fourier transform of the normal stress operator on each face of the wedge is given by a sum of these two operators. The right-hand side of the system of functional equations is obtained by computing the Fourier transform of $-Bv_\alpha^{inc}|_{\mathcal{S}_j}$, $j = 1, 2$ where B is defined by (3.9) and the incident field is given by (3.12):

$$\begin{cases} \mathbf{DM}(\Sigma_1) + \mathbf{TM}(\Sigma_2) = \dfrac{W_1^\alpha}{\xi - \nu_\alpha\cos\theta_{inc}} \\ \mathbf{TM}(\Sigma_1) + \mathbf{DM}(\Sigma_2) = \dfrac{W_2^\alpha}{\xi - \nu_\alpha\cos(\varphi-\theta_{inc})} \end{cases}, \tag{3.59}$$

where

$$W_1^L = -2\begin{pmatrix} \mu \sin 2\theta_{inc} \\ 1 - 2\mu\cos^2\theta_{inc} \end{pmatrix} \quad W_2^L = -2\begin{pmatrix} \mu \sin 2(\varphi - \theta_{inc}) \\ 1 - 2\mu\cos^2(\varphi - \theta_{inc}) \end{pmatrix}$$
$$W_1^T = -2\nu_T\begin{pmatrix} \mu\cos 2\theta_{inc} \\ \mu\sin 2\theta_{inc} \end{pmatrix} \qquad W_2^T = 2\nu_T\begin{pmatrix} \mu\cos 2(\varphi - \theta_{inc}) \\ \mu\sin 2(\varphi - \theta_{inc}) \end{pmatrix} \tag{3.60}$$

Using this system of functional equations, it is possible to decompose the spectral functions into two parts : a singular function and a regular function. The first step is to extract the poles of the spectral functions.

3.3.2 Singular part

The poles and corresponding residues of the spectral functions, which lead to the reflections of the incident field on the wedge faces (these reflections can be multiple and can also lead to mode conversion) and to the fictitious fields that compensate the incident wave in the shadow zones, are computed analytically by a recursive procedure. In order to apply this procedure, it is necessary to define the following translation operator ($* = L, T$):

$$T_*(\xi = \nu_* \cos\theta) = \xi\cos\tilde{\varphi} + \zeta_*(\xi)\sin\tilde{\varphi} = \nu_*\cos(\theta + \tilde{\varphi}), \tag{3.61}$$

where $\tilde{\varphi}$ is defined in the previous chapter by (2.48). This function is a translation operator in the sense that it translates the angle θ to $\theta + \tilde{\varphi}$. The cosine function is well defined for θ, $0 \leq \mathrm{Re}\theta \leq \pi$. In order for the cosine in the translation operator to also be well defined, it is necessary to impose

$$\xi \in \Omega_*^+ = \{\xi = \nu_*\cos\theta,\ 0 \leq \mathrm{Re}\theta < \pi - \tilde{\varphi},\ \mathrm{Im}\xi \geq 0\}, \tag{3.62}$$

where Ω_*^+ is represented in Fig. 3.4.

In order to extract the poles of the spectral functions, it is necessary to determine the action of operators **DM** and **TM** on a simple pole. In order to do so, contour Γ_0 in (3.50) is deformed into contour Γ_1 (see Fig. 3.5) and Cauchy's residue theorem is applied, yielding, for $V \in \mathbb{C}^2$, $z \in \mathbb{C}\backslash]-\infty, -1]$, $z \notin \{\nu_L, \nu_T\}$, $\mathrm{Im}z \geq 0$, $\xi \in \Omega_*^+$, $\mathrm{Im}\xi < 0$

$$\int_{\Gamma_0} \mathbf{DM}(\xi, \zeta).\frac{V}{\zeta - z}\, d\zeta = \frac{\mathbf{dm}(z).V}{\xi - z} + D_p(z, \xi), \tag{3.63}$$

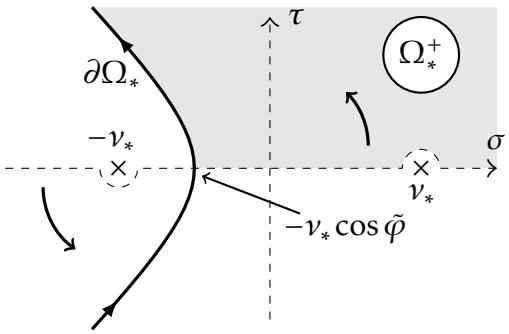

Figure 3.4 – Domain Ω_*^+ and contour $\partial\Omega_*$ in the complex plane $\xi = \sigma + i\tau$. The curved arrows indicate the contour deformation from Γ_0 to $\partial\Omega_*$

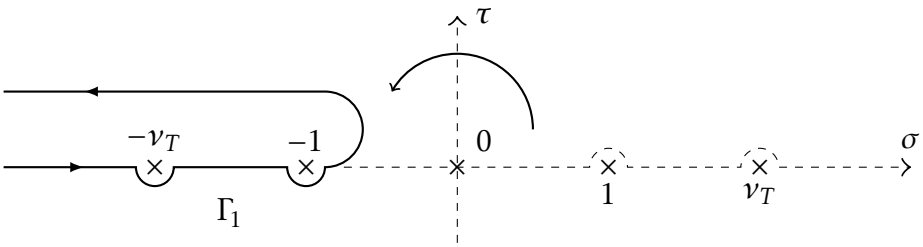

Figure 3.5 – Contour Γ_1 in the complex plane $\xi = \sigma + i\tau$. The curved arrow indicates the contour deformation from Γ_0 to Γ_1

where

$$D_p(z,\xi) = \int_{\Gamma_1} \frac{\mathbf{DM}(\xi,\zeta)}{\zeta - z}.V\,d\zeta \tag{3.64}$$

Similarly, we deform contour Γ_0 in (3.55) into contour $\partial\Omega_*$, represented Fig. 3.4 and apply once again Cauchy's residue theorem:

$$\int_{\Gamma_0} \mathbf{TM}(\xi,\zeta).\frac{1}{\zeta - z}\,d\zeta = \sum_{*=L,T} \frac{\mathbf{tm}_*(z).V}{\xi - T_*(z)}\mathbf{1}_{\Omega_*}(z) + T_p(z,\xi) \tag{3.65}$$

where $\mathbf{1}_{\Omega_*}(z) = 1$ if $z \in \Omega_*^+$ and 0 elsewhere and

$$T_p(z,\xi) = \frac{1}{2i\pi} \sum_{*=L,T} \int_{\partial\Omega_*} D_*(\xi,\zeta).\frac{\mathbf{tm}_*(\zeta)}{\zeta - z}.V\,d\zeta \tag{3.66}$$

Croisille and Lebeau [52] proved that $D_p(z,\cdot)$ and $T_p(z,\cdot)$ belong to a special class of functions $\mathcal{H}^2$ defined in the previous chapter by Def. 2.2.2.

Let us now extract all the poles and corresponding residues from the spectral

functions, using system (3.59). We begin by defining X_j' by :

$$\Sigma_j(\xi) = \frac{V_j^{(0)}}{\xi - Z_j^{(0)}} + X_j'(\xi), \;\; j = 1, 2, \tag{3.67}$$

where $V_j^{(0)}$ is unknown and $Z_1^{(0)} = \nu_\alpha \cos\theta_{inc}$ and $Z_2^{(0)} = \nu_\alpha \cos(\varphi - \theta_{inc})$. Substituting (3.67) into (3.59) and applying formula (3.63) yields :

$$\begin{cases} \mathbf{DM}(X_1') + \mathbf{TM}(X_2') + \mathbf{TM}(\frac{V_2^{(0)}}{\xi - Z_2^{(0)}}) = \frac{W_1^\alpha}{\xi - Z_1^{(1)}} - \frac{\mathbf{dm}(Z_1^{(0)}).V_1^{(0)}}{\xi - Z_1^{(0)}} - D_p(Z_1^{(0)}, \xi).V_1^{(1)} \\ \mathbf{TM}(X_1') + \mathbf{DM}(X_2') + \mathbf{TM}(\frac{V_1^{(0)}}{\xi - Z_1^{(0)}}) = \frac{W_2^\alpha}{\xi - Z_2^{(0)}} - \frac{\mathbf{dm}(Z_2^{(0)}).V_2^{(0)}}{\xi - Z_2^{(0)}} - D_p(Z_2^{(0)}, \xi).V_2^{(0)} \end{cases} \tag{3.68}$$

In the above equations, the terms $D_p(Z_j^{(0)}, \xi)$ are regular and $Z_j^{(0)}$ is not a pole of $DM(X_j')$ or $TM(\Sigma_{3-j})$ (in decomposition (3.67) it is assumed that all the information regarding the initial pole is contained in the term $\frac{V_j}{\xi - Z_j^{(0)}}$). Therefore, the right-hand side of this system does not admit $Z_j^{(0)}$ as a pole. This implies that the singular terms in the right-hand side of the system must compensate each other, yielding :

$$V_j^{(0)} = \mathbf{dm}^{-1}(Z_j^{(0)}).W_j^\alpha \tag{3.69}$$

We have $\det(\mathbf{dm}(z)) \neq 0$ as long as $z \neq \nu_R$. In the following, we will suppose that this is the case. Physically, this means that the incident wave is not a Rayleigh wave and neither are any of the waves reflected by the wedge faces. Furthermore, we suppose that the hypothesis $z \notin \{\nu_L, \nu_T\}$ that has been made in (3.63) and (3.65) remains true for all the poles. This means that neither the incident, nor any of the reflected waves is an incoming grazing one. Kamotski [70] proves existence and uniqueness of the solution in the case where this is not true.

Applying (3.65), two new poles appear :

$$Z_{j,L}^{(1)} = T_L(Z_j^{(0)}) \;\text{ et }\; Z_{j,T}^{(1)} = T_T(Z_j^{(0)}) \tag{3.70}$$

This leads to the definition of X_j'':

$$X_j' = X_j'' + \frac{V_{j,L}^{(1)}}{\xi - Z_{j,L}^{(1)}} + \frac{V_{j,T}^{(1)}}{\xi - Z_{j,T}^{(1)}}, \tag{3.71}$$

where $V_{j,L}^{(1)}$ and $V_{j,T}^{(1)}$ are unknown vectors. Once again, we substitute this into the system and apply (3.63). Residues $V_{j,*}^{(1)}$ are determined by the fact that they should compensate the other singular terms on the right-hand side of the system:

$$V_{j,*}^{(1)} = -\mathbf{dm}^{-1}(T_*(Z_{3-j}^{(0)})).\mathbf{tm}_*(Z_{3-j}^{(0)}).V_{3-j}^{(0)}\mathbf{1}_{\Omega_*}(Z_{3-j}^{(0)}) \tag{3.72}$$

These steps are repeated recursively as long as the poles $Z_{j,L}^{(k)} \in \Omega_L^+$ and $Z_{j,T}^{(k)} \in \Omega_T^+$. When this is the case, (3.65) can be applied, creating new poles in the right-hand side of the system. These new poles are then extracted from the spectral functions using (3.63), and so on. In the end, we have, for $\operatorname{Im}\xi < 0$:

$$\Sigma_j(\xi) = Y_j(\xi) + X_j(\xi) \tag{3.73}$$

$$Y_j(\xi) = \sum_k \sum_{*=L,T} \frac{V_{j,*}^{(k)}}{\xi - Z_{j,*}^{(k)}}, \tag{3.74}$$

where

$$\begin{array}{ll} Z_1^{(0)} = \nu_\alpha \cos\theta_{inc}, & Z_2^{(0)} = \nu_\alpha \cos(\varphi - \theta_{inc}) \\ Z_{j,L}^{(k+1)} = T_L(Z_{3-j,*}^{(k)}) & Z_{j,T}^{(k+1)} = T_T(Z_{3-j,*}^{(k)}) \end{array} \tag{3.75}$$

and

$$\begin{array}{c} V_j^{(0)} = \mathbf{dm}^{-1}(Z_j^{(0)}).W_j^\alpha \\ V_{j,L}^{(k+1)} = -\mathbf{dm}^{-1}(Z_{j,L}^{(k+1)}).\mathbf{tm}_L(Z_{3-j,*}^{(k)}).V_{3-j,*}^{(k)}.\mathbf{1}_{\Omega_L}(Z_{3-j,*}^{(k)}) \\ V_{j,T}^{(k+1)} = -\mathbf{dm}^{-1}(Z_{j,T}^{(k+1)}).\mathbf{tm}_T(Z_{3-j,*}^{(k)}).V_{3-j,*}^{(k)}.\mathbf{1}_{\Omega_T}(Z_{3-j,*}^{(k)}) \end{array} \tag{3.76}$$

The recursive procedure stops when the poles $Z_{j,*}^{(k)}$ exit $\Omega_L^+ \cup \Omega_T^+$ (*i.e.* when the translation operators T_L and T_T can no longer be applied to them). Croisille and Lebeau [52] have shown that this defines a finite number of poles. Physically, this means that an incident ray exits the wedge after a finite number of reflections and mode conversions. We have thus extracted all the poles from the spectral functions and have computed them analytically, along with their corresponding residues.

3.3.3 Regular part

The singular parts Y_j of the spectral functions having been determined, two new functions X_1 and X_2 are defined by (3.73). In the following, a numerical approximation method for X_j is proposed. In order to do so, a system of functional

equations solved by X_1, X_2 is derived by subtracting vector

$$\begin{pmatrix} \mathbf{DM}(Y_1) + \mathbf{TM}(Y_2) \\ \mathbf{TM}(Y_1) + \mathbf{DM}(Y_2) \end{pmatrix}, \tag{3.77}$$

where Y_1 and Y_2 are given by equations (3.74) to (3.76), from both sides of (3.59) :

$$\begin{cases} \mathbf{DM}(X_1)(\xi) + \mathbf{TM}(X_2)(\xi) = u_1(\xi) \\ \mathbf{TM}(X_1)(\xi) + \mathbf{DM}(X_2)(\xi) = u_2(\xi) \end{cases}, \tag{3.78}$$

with, for $j = 1, 2$

$$u_j(\xi) = -\sum_k \sum_{*=L,T} \left[D_p(Z^{(k)}_{j,*}, \xi).V^{(k)}_{j,*} + T_p(Z^{(k)}_{3-j,*}, \xi).V^{(k)}_{3-j,*} \right] \tag{3.79}$$

Croisille and Lebeau [52] have shown that this system has a unique solution (X_1, X_2) in $\mathcal{H}^2$ (defined in Def.2.2.2). In the sequel, a numerical approximation of the regular parts X_j will be computed using a Galerkin collocation method.

The functional space $\mathcal{H}$ is approached by a finite-dimension space generated by the basis functions φ_k. In this space, functions X_j are approximated by

$$X_j(\xi) \approx \sum_{k=1}^{N} \tilde{X}^k_j \varphi_k(\xi),\ \tilde{X}^k_j \in \mathbb{C}^2\ , j = 1, 2 \tag{3.80}$$

where coefficients $\tilde{X}^k_j \in \mathbb{C}^2$ are unknown.

Substituting this approximation into (3.78) and applying variable change $\zeta = iy$ to this system before evaluating it at points $\xi = b_1, ..., b_N$ leads to the following linear system of equations :

$$\begin{cases} \sum_{k=1}^{N} \tilde{X}^k_1 \int_{-\infty}^{+\infty} \mathbf{DM}(b_1, iy) e_{a_k}(y)\, dy + \tilde{X}^k_2 \int_{-\infty}^{+\infty} \mathbf{TM}(b_1, iy) e_{a_k}(y)\, dy = u_1(b_1) \\ \vdots \\ \sum_{k=1}^{N} \tilde{X}^k_1 \int_{-\infty}^{+\infty} \mathbf{TM}(b_N, iy) e_{a_k}(y)\, dy + \tilde{X}^k_2 \int_{-\infty}^{+\infty} \mathbf{DM}(b_N, iy) e_{a_k}(y)\, dy = u_2(b_N) \end{cases}, \tag{3.81}$$

where, following 2.2.2.2, we have :

$$e_{a_k}(y) = \sqrt{\frac{a_k}{\pi}} \frac{1}{y - ia_k},\ (a_k)_{1 \le k \le N} \in ([1, +\infty[)^N \tag{3.82}$$

The basis functions φ_k are deduced using (2.70) :

$$\varphi_k(\xi) = \sqrt{\frac{a_k}{\pi}}\frac{1}{\xi + a_k},\ 1 \le k \le N \tag{3.83}$$

This system can be expressed in terms of matrices

$$\begin{pmatrix} \mathbb{D} & \mathbb{T} \\ \mathbb{T} & \mathbb{D} \end{pmatrix}\begin{pmatrix} \mathbb{X}_1 \\ \mathbb{X}_2 \end{pmatrix} = \begin{pmatrix} \mathbb{U}_1 \\ \mathbb{U}_2 \end{pmatrix} \Longleftrightarrow \begin{cases} (\mathbb{D}+\mathbb{T})(\mathbb{X}_1+\mathbb{X}_2) = \mathbb{U}_1+\mathbb{U}_2 \\ (\mathbb{D}-\mathbb{T})(\mathbb{X}_1-\mathbb{X}_2) = \mathbb{U}_1-\mathbb{U}_2 \end{cases} \tag{3.84}$$

where, for $1 \le l,k \le N$:

$$\begin{aligned} \mathbb{D}_{lk} = \int_{-\infty}^{+\infty} \mathbf{DM}(b_l, iy) e_{a_k}(y)\, dy &= \frac{1}{2i\pi}\int_{-\infty}^{+\infty} \frac{\mathbf{dm}}{b_l - iy}\sqrt{\frac{a_k}{\pi}}\frac{1}{y - ia_k}\, dy \\ &= -\frac{\sqrt{a_k}}{2\pi\sqrt{\pi}}\begin{pmatrix} \mathcal{D}_1(a_k,b_l) & \mathcal{D}_2(a_k,b_l) \\ \mathcal{D}_3(a_k,b_l) & \mathcal{D}_1(a_k,b_l) \end{pmatrix} = \frac{\sqrt{a_k}}{2\pi\sqrt{\pi}}\mathbb{D}(a_k,b_l) \end{aligned} \tag{3.85}$$

The explicit expressions of operators $\mathcal{D}_i, 1 \le i \le 3$ and their values are computed in appendix C. The other coefficients of the system are, for $1 \le l,k \le N$

$$\begin{aligned} \mathbb{T}_{lk} = \int_{-\infty}^{+\infty} \mathbf{TM}(b_l, iy) e_{a_k}(y)\, dy &= \frac{1}{2i\pi}\int_{-\infty}^{+\infty} \sum_{*=L,T} \frac{\mathbf{tm}_*(iy, \operatorname{sgn}\sin\varphi)}{b_l - T_*(iy)}\sqrt{\frac{a_k}{\pi}}\frac{1}{y - ia_k}\, dy \\ = \frac{1}{2i\pi}\sqrt{\frac{a_k}{\pi}}\sum_{*=L,T}\int_{-\infty}^{+\infty} &\frac{\mathbf{tm}_*(iy,\epsilon)}{[b_l - (iy\cos\varphi + \zeta_*(iy)|\sin\varphi|)](y - ia_k)}\, dy, \end{aligned} \tag{3.86}$$

where $\epsilon = \operatorname{sgn}(\sin\varphi)$. Let us define

$$\mathbb{T}_{lk} = \frac{\mu}{2i\pi}\sqrt{\frac{a_k}{\pi}}\begin{pmatrix} \mathcal{T}_1^L(a_k,b_l) + \mathcal{T}_1^T(a_k,b_l) & \mathcal{T}_2^L(a_k,b_l) + \mathcal{T}_2^T(a_k,b_l) \\ \mathcal{T}_3^L(a_k,b_l) + \mathcal{T}_3^T(a_k,b_l) & \mathcal{T}_4^L(a_k,b_l) + \mathcal{T}_4^T(a_k,b_l) \end{pmatrix} = \frac{1}{2i\pi}\sqrt{\frac{a_k}{\pi}}\mathbb{T}(a_k,b_l) \tag{3.87}$$

The explicit expressions of operators $\mathcal{T}_i^*, 1 \le i \le 4, * = L,T$ and their values are computed in appendix D.

Finally, for $j = 1,2$:

$$\mathbb{X}_j = \begin{pmatrix} \tilde{X}_j^1 \\ \vdots \\ \tilde{X}_j^1 \end{pmatrix},\ \tilde{X}_j^k \in \mathbb{C}^2; \qquad \mathbb{U}_j = \begin{pmatrix} u_j(b_1) \\ \vdots \\ u_j(b_N) \end{pmatrix},\ u_j(b_k) \in \mathbb{C}^2 \tag{3.88}$$

where $u_j(\xi)$ is given by (3.79). Applying variable change $\zeta = iy$ to the definition of D_p given by (3.63) and substituting (3.85) in the result gives

$$D_p(z,\xi) = \frac{1}{2\pi}\mathbb{D}(-z,\xi) - \frac{\mathbf{dm}(z)}{\xi - z} \tag{3.89}$$

Similarly, applying variable change $\zeta = iy$ to (3.65) and substituting (3.87) in the result yields

$$T_p(z,\xi) = \frac{1}{2i\pi}\mathbb{T}(-z,\xi) - \sum_{*=L,T} \frac{\mathbf{tm}_*(z,\epsilon)}{b - T_*(z)}\mathbf{1}_{\Omega_*}(z) \tag{3.90}$$

Equations (3.89) and (3.90) are substituted into (3.79). By construction, the singular terms cancel each other and the remaining terms are :

$$u_j(\xi) = -\frac{1}{2i\pi}\sum_k \sum_{*=L,T} \left(i\mathbb{D}(-Z^{(k)}_{j,*},\xi).V^{(k)}_{j,*} + \mathbb{T}(-Z^{(k)}_{3-j,*},\xi).V^{(k)}_{3-j,*} \right) + \frac{W^{\alpha}_j}{\xi - Z^{(0)}_j} \tag{3.91}$$

Using these results, the linear system (3.84) can be implemented and solved numerically thanks to the C++ library Eigen, and an evaluation of the regular part of the spectral functions is obtained. However, for values of ξ lying in certain parts of the complex plane, this evaluation is not sufficiently accurate. The technique used to solve this problem is called the propagation of the solution.

3.3.4 Propagation of the solution

The method described hereafter is used to "propagate" the accuracy of the solution to (3.78) to the whole complex plane. This is done by determining a new system of recursive equations solved by X_1, X_2 in which the regular part X_j is expressed using the value of X_1, X_2 in a domain where the numerical approximation is valid.

By deforming Γ_0 into Γ_2, represented in Fig. 3.6, the half-plane Im $\xi < 0$ is entirely crossed. Note that the branch points $\pm\nu_*, * = L, T$ are not crossed during this deformation, indicated by the curved arrow in Fig. 3.6. The contribution of poles $\zeta = \xi$, Im$\xi < 0$, is given by Cauchy's integral formula :

$$\int_{\Gamma_0} \mathbf{DM}(\xi,\zeta)X_j(\zeta)\,d\zeta = \int_{\Gamma_2} \mathbf{DM}(\xi,\zeta)X_j(\zeta)\,d\zeta + \mathbf{dm}(\xi).X_j(\xi) \tag{3.92}$$

It is now necessary to define the inverse transformation operator $T_*^{-1} : \Omega_*^- \rightarrow$

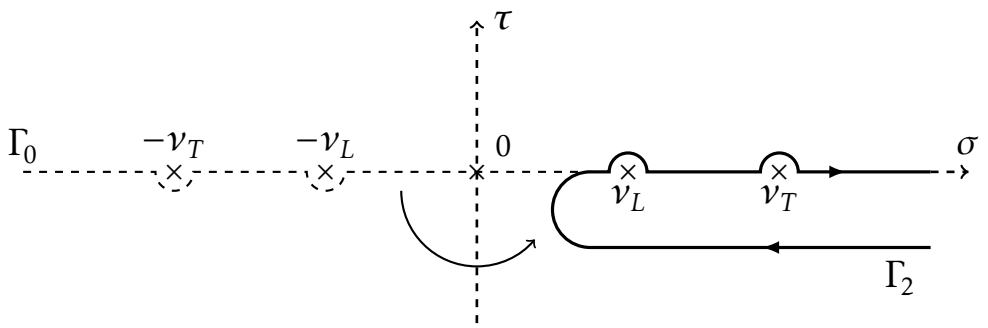

Figure 3.6 – Integration contour Γ_2 in the complex place $\xi = \sigma + i\tau$. The curved arrow indicates the contour deformation from Γ_0 to Γ_2.

$\mathbb{C}, * = L, T$:

$$T_*^{-1}(\xi = \nu_* \cos\theta) = \xi \cos\tilde{\varphi} - \zeta_*(\xi) \sin\tilde{\varphi} = \nu_* \cos(\theta - \tilde{\varphi}). \tag{3.93}$$

This function is a translation operator in the sense that it translates the angle θ to $\theta - \tilde{\varphi}$. The cosine function is well defined for θ, $0 \leq \mathrm{Re}\theta \leq \pi$. In order for the cosine in the translation operator to also be well defined, it is necessary to impose

$$\xi \in \Omega_*^- = \{\xi = \nu_* \cos\theta,\ \tilde{\varphi} \leq \mathrm{Re}\theta \leq \pi,\ \mathrm{Im}\xi < 0\}, \tag{3.94}$$

where Ω_*^- is represented in Fig. 3.7. By deforming contour Γ_0 into contour $\partial\Omega_*^-$ (also represented in Fig. 3.7), domain Ω_*^- is crossed. Note that the branch points $\pm\nu_*, * = L, T$ are not crossed during this deformation. The poles of the integrand are located at $\zeta = T_*^{-1}(\xi)$ and, since the contour deformation spans subspace Ω_*^-, these poles are crossed by the deformation if and only if they are located in this subspace. Their contribution is taken into account using Cauchy's integral formula :

$$\int_{\Gamma_0} \mathbf{TM}(\xi, \zeta) X_j(\zeta)\, d\zeta = \sum_{*=L,T} \int_{\partial\Omega_*^-} \frac{\mathbf{tm}_*(\zeta)}{\xi - T_*(\zeta)} . X_j(\zeta)\, d\zeta + \mathbf{M}_*(\xi) . X_j(T_*^{-1}(\xi)) \mathbf{1}_{\Omega_*^-}(\xi), \tag{3.95}$$

where $\mathbf{1}_{\Omega_*^-}(\xi) = 1$ when $\xi \in \Omega_*^-$ and 0 elsewhere and

$$\mathbf{M}_*(\xi = \nu_* \cos\theta) = -\frac{\sin(\theta - \tilde{\varphi})}{\sin\theta} \mathbf{tm}_*(T_*^{-1}(\xi)) \tag{3.96}$$

The recursive system of functional equations solved by the regular part is

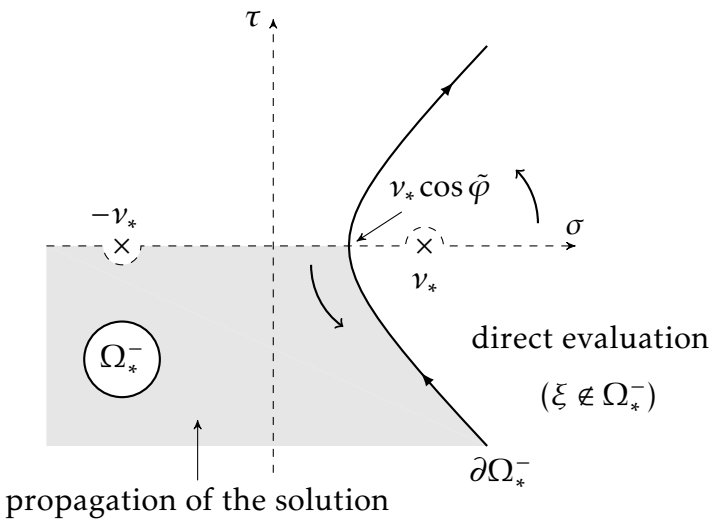

Figure 3.7 – Domain Ω_*^- and contour $\partial\Omega_*^-$ in the complex plane $\xi = \sigma + i\tau$. The curved arrows indicate contour deformation from Γ_0 to $\partial\Omega_*^-$.

obtained by substituting (3.92) and (3.95) into (3.78):

$$\begin{cases} X_1(\xi) = g_1(\xi) - \mathbf{dm}^{-1}(\xi).\sum\limits_{*=L,T} \mathbf{M}_*(\xi).X_2(T_*^{-1}(\xi))\mathbf{1}_{\Omega_*^-}(\xi) \\ X_2(\xi) = g_2(\xi) - \mathbf{dm}^{-1}(\xi).\sum\limits_{*=L,T} \mathbf{M}_*(\xi).X_1(T_*^{-1}(\xi))\mathbf{1}_{\Omega_*^-}(\xi) \end{cases}, \tag{3.97}$$

where , for $j = 1, 2$

$$g_j(\xi) = \mathbf{dm}^{-1}(\xi)\left(u_j(\xi) - \int_{\Gamma_2} \mathbf{DM}(\xi,\zeta)X_j(\zeta)\,d\zeta - \int_{\partial\Omega_*^-} \mathbf{TM}(\xi,\zeta)X_{3-j}(\zeta)\,d\zeta\right) \tag{3.98}$$

This new recursive system is used to evaluate the spectral functions in the domain $W = \{\mathrm{Im}(\xi) < 0, \xi \notin \partial\Omega_*^-\}$. To do so, functions g_j must be evaluated numerically.

Each of the integrals appearing in the definition of g_j are evaluated separately using the approximation of the regular part (3.80) for the computation of terms $X_j(\zeta)$ and $X_{3-j}(\zeta)$.

Substituting (3.85) into (3.92) yields :

$$\int_{\Gamma_2} \mathbf{DM}(\xi,\zeta)\varphi_k(\zeta)\,d\zeta = \int_{\Gamma_0} \mathbf{DM}(\xi,\zeta)\varphi_k(\zeta)\,d\zeta - \mathbf{dm}(\xi).\varphi_k(\xi) = \frac{1}{2\pi}\sqrt{\frac{a_k}{\pi}}\mathbb{D}(a_k,\xi) - \mathbf{dm}(\xi).\varphi_k(\xi) \tag{3.99}$$

and substituting (3.87) into (3.95) yields:

$$\begin{aligned}\int_{\partial\Omega_*^-} \mathbf{TM}(\xi,\zeta)\varphi_k(\zeta)\,d\zeta &= \int_{\Gamma_0} \mathbf{TM}(\xi,\zeta)\varphi_k(\zeta)\,d\zeta - \sum_{*=L,T} \mathbf{M}_*(\xi).\varphi_k(T_*^{-1}(\xi)) \\ &= \frac{1}{2i\pi}\sqrt{\frac{a_k}{\pi}}\mathbb{T}(a_k,\xi) - \sum_{*=L,T} \mathbf{M}_*(\xi).\varphi_k(T_*^{-1}(\xi))\mathbf{1}_{\Omega_*^-}(\xi)\end{aligned} \tag{3.100}$$

Finally, (3.99) and (3.100) can be injected into (3.98) :

$$\mathbf{dm}(\xi).g_j(\xi) = u_j(\xi) - \sum_{k=1}^{N}\sqrt{\frac{a_k}{\pi}}\left(\mathbb{NID}(a_k,\xi).\tilde{X}_j^k + \mathbb{NT}(a_k,\xi).\tilde{X}_{3-j}^k\right), \tag{3.101}$$

where

$$\mathbb{NID}(a,b) = \frac{1}{2\pi}\mathbb{D}(a,b) - \frac{\mathbf{dm}(b)}{a+b} \tag{3.102}$$

and

$$\mathbb{NT}(a,b) = \frac{1}{2i\pi}\mathbb{T}(a,b) - \sum_{*=L,T}\frac{\mathbf{M}_*(b)}{T_*^{-1}(b)+a}. \tag{3.103}$$

In system (3.97), the value of the regular part of the spectral function in domain Ω_*^-, visible Fig. 3.7, is expressed using its value in the domain $\xi \notin \Omega_*^-$, where the numerical approximation (3.80) is valid. To do so, functions g_j, $j = 1,2$ are evaluated using (3.101). The accuracy of the numerical evaluation in domain $\xi \notin \Omega_*^-$ is therefore propagated to domain Ω_*^-.

This concludes the semi-analytical computation of the spectral functions. Once the spectral functions are determined, the diffraction coefficients are computed every $0,2^o$, using equations (3.44)-(3.45). Numerical comparisons with other codes are presented in the following.

3.4 Numerical validation

The longitudinal and transversal diffraction coefficients are computed using (3.44) and (3.45). The spectral functions are evaluated in $\xi = \nu_* \cos\theta - i10^{-8}$ (a small negative imaginary part is added to ensure that the recursive equations (3.97) are valid). This is achieved by, first, computing the poles and residues of the spectral functions analytically using the recursive algorithm described in subsection 3.3.2. Then, the regular parts of the spectral functions are approached numerically by solving (3.78) thanks to the Galerkin collocation method de-

scribed in subsection 3.3.3, where the Galerkin parameters are set to:

$$a_k = 1.0001 + 0.05e^{k\frac{\log 10}{4}} - 1, \qquad b_k = a_k - 0.1i, \qquad 1 \leq k \leq 20 \tag{3.104}$$

Finally, the solution is rendered accurate in the entire complex domain by applying the recursive procedure called the propagation of the solution described in subsection 3.3.4.

Following these steps, the diffraction coefficients have been computed every 0.2^o for a steel wedge in which $c_L = 5700m.s^{-1}, c_T = 3100m.s^{-1}$. The results are presented hereafter.

3.4.1 For $\varphi < \pi$

For wedge angles $\varphi < \pi$, the Laplace Transform (LT) code of Gautesen and Fradkin [12], based on the method briefly recalled in 1.3.3 has been used to validate the results of the Spectral Functions (SF) method.

Fig. 3.8 shows the absolute value of the diffraction coefficients with respect to the observation angle obtained for a wedge of angle $\varphi = 80^o$ illuminated by a wave incident with an angle $\theta_{inc} = 55^o$. The green line represents the diffraction coefficients obtained using only the singular parts Y_j of the spectral functions. The dark blue line is the diffraction coefficient obtained using the LT code and the red circles represent the result obtained using the SF code. In Fig. 3.8a, the pole at $\theta = 35^o$ corresponds to the L wave incident on $\mathcal{S}_1$ and doubly reflected (by $\mathcal{S}_1$ first then by $\mathcal{S}_2$). The pole at $\theta = 75^o$ correspond to L wave incident on $\mathcal{S}_2$ and double reflected (by $\mathcal{S}_2$ first then by $\mathcal{S}_1$). In Fig. 3.8b, the incident L wave on each face of the wedge generates two poles, due to the mode conversion occurring at each reflection. For example, the pole at $\theta = 54^o$ corresponds to an L wave incident on $\mathcal{S}_1$, reflected with mode conversion into a T wave which is in turn reflected by $\mathcal{S}_2$. In Figs. 3.8b and 3.8d, the spikes at $\theta = 23^o$ correspond to head haves propagating along face $\mathcal{S}_2$ and the spikes at $\theta = 57^o$ correspond to head waves propagating along face $\mathcal{S}_1$. In all four figures, the blue and red plots are perfectly overlapping. The singular part alone, however, is not sufficient to compute accurate coefficients.

Fig. 3.9 shows the absolute value of the diffraction coefficients with respect to the observation angle obtained for a wedge of angle $\varphi = 160^o$ illuminated by a wave incident with an angle $\theta_{inc} = 40^o$. The light blue line represents the diffraction coefficients obtained without applying the "propagation of the solution" technique for the SF code. The dark blue line is the diffraction coefficient obtained using the LT code and the red circles represent the result obtained using the SF code, including the "propagation of the solution" technique. In Fig. 3.9a, the pole at $\theta = 140^o$ corresponds to the L wave reflected by $\mathcal{S}_1$ and the

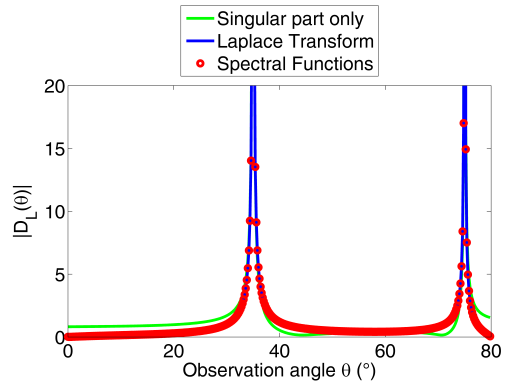

(a) Diffracted and incident L waves

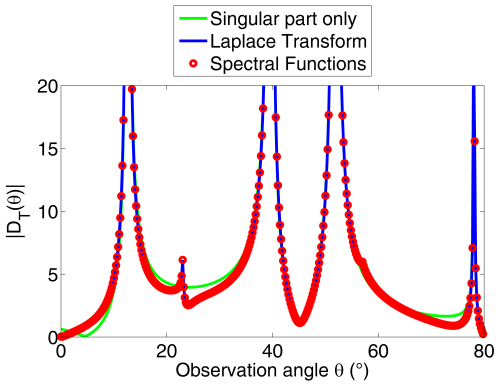

(b) Diffracted T wave and incident L wave

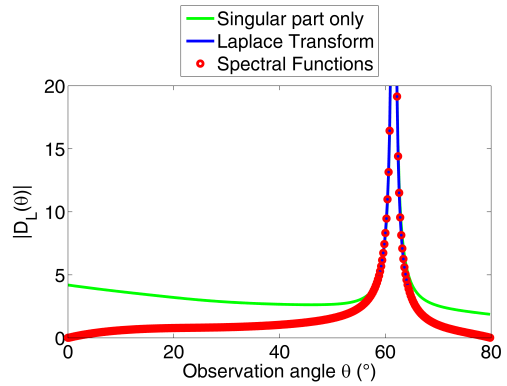

(c) Diffracted L wave and incident T wave

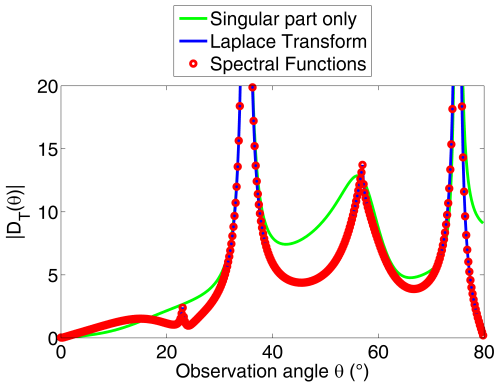

(d) Diffracted and incident T waves

Figure 3.8 – Diffraction coefficients for $\varphi = 80^o, \theta_{inc} = 55^o$

pole at $\theta = 100^o$ corresponds to the L wave reflected by $\mathcal{S}_2$. In all four figures, the dark blue and the red plots are perfectly overlapping. Furthermore, the "propagation of the solution" technique is necessary in order to avoid coefficients which diverge near the wedge faces.

For all of the tested configurations (different wedge and incidence angles), the results are conclusive. The results using the spectral functions method are extremely close to those obtained using the LT code, which has been validated both numerically and experimentally [12, 35]. This constitutes a satisfying validation for wedge angles $\varphi \leq \pi$. Some additional numerical comparisons have been made in the next section for the case of a wedge of angle $\varphi > \pi$.

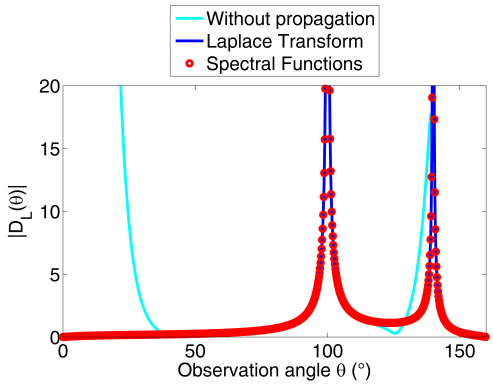

(a) Diffracted and incident L waves

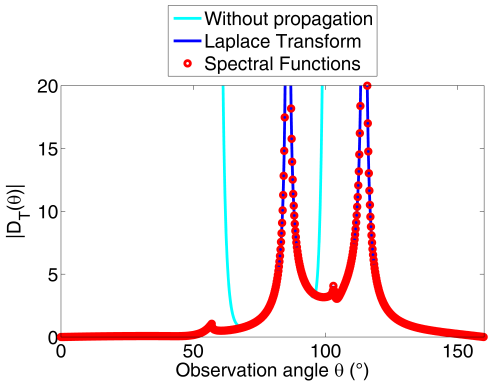

(b) Diffracted T wave and incident L wave

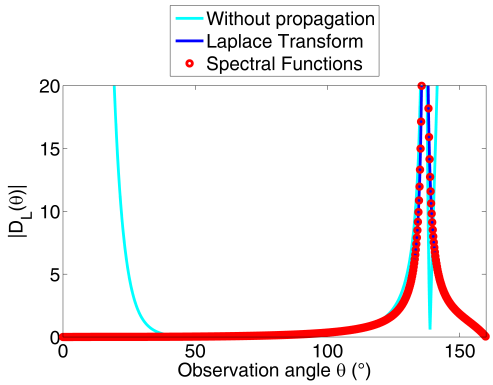

(c) Diffracted L wave and incident T wave

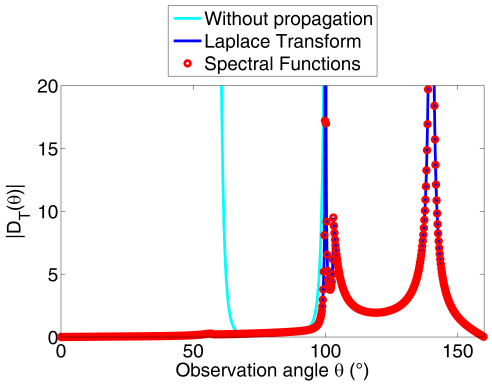

(d) Diffracted and incident T waves

Figure 3.9 – Diffraction coefficients for $\varphi = 160^o, \theta_{inc} = 40^o$

3.4.2 For $\varphi > \pi$

For wedge angles $\varphi \geq \pi$, the existing LT code can not be used. Therefore, the spectral finite elements code of Imperiale et al. developed for the commercial software CIVA [67] has been used as a reference solution for numerical validation purposes. The scattered wave fronts have been computed using this Finite Elements (FE) method and the diffraction coefficients are extracted from these. The frequency of the incident wave is set to $f = 1,0$MHz. The FE computation box is visible on the snapshots in Fig. 3.10. The mesh size is $h = 0,0432$mm and the simulation time step is set to verify the Courant-Friedrichs-Lewy (CFL) stability condition ($\delta t = 1,40963\mu s$). The boundaries of the FE computation box which correspond to the wedge edges are set to be stress-free boundaries and the other boundaries of the domain are Perfectly Matched Layers (PML), which are absorbing boundaries used to mimic an infinite propagation domain.

The FE code computes the reflected and diffracted wave field in the time-domain. The incident wave is a pulse with a plane wavefront and the value of the diffracted wave field is extracted along the cylindrical diffracted wavefront as detailed in the following. To do so, a snapshot is taken at a time where the diffracted wavefronts are located inside the FE box but the furthest possible from the edge, in order for the far-field approximation to be applicable, whilst minimizing interferences that may occur from non-physical waves reflected from the borders of the FE computation domain. These snapshots are presented in Fig. 3.10 for two different propagation times.

Fig. 3.10a shows the snapshot used in the case of an L wave incident with an angle $\theta_{inc} = 135^o$. The cylindrical wavefronts of the L (dLW) and T (dTW) waves diffracted from the wedge edge are visible, as well as the reflected L (rLW) and T (rTW) waves on each face of the wedge. Finally, Rayleigh waves (RW) propagating along each face of the wedge interfere with the diffracted T wave at the vicinity of the wedge faces for the chosen propagation time. Similarly, fig. 3.10b shows the snapshot simulated in the case of a T wave incident with an angle $\theta_{inc} = 135^o$. Once again, the cylindrical wavefronts of the L (dLW) and T (dTW) waves diffracted from the wedge edge are visible. In this case, there is no mode conversion and only reflected T waves (rTW) appear. Rayleigh waves (RW) which interfere with the diffracted T wave are also visible in this case and head waves (HW) are emanated from each face at the medium's longitudinal critical angle (for a steel/void interface, this angle is $\theta_c \approx 57^o$ inside steel). Some models have recently been proposed to mimic some head waves for half-plane scatterers [60, 3] or for a wedge [71].

In order to extract diffraction coefficients from the FE wave field, formula (3.43) is used. The diffraction coefficient's absolute value is deduced from the FE

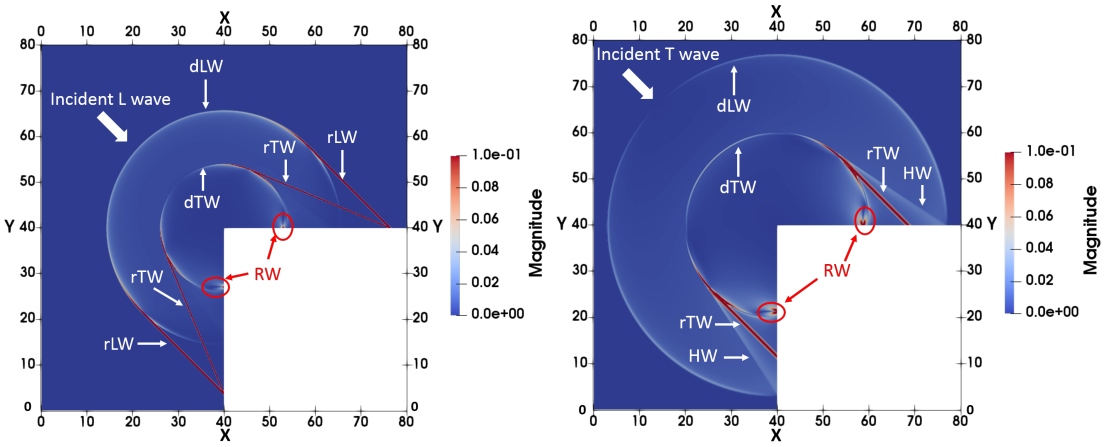

(a) Incident L wave, $t = 5ms$. (b) Incident T wave, $t = 6,5ms$.

Figure 3.10 – Finite elements snapshots. Distances are given in millimeters.

wave field by :

$$|D_\beta^\alpha(\theta)| = \frac{\|v_\beta^{diff}(r\cos\theta, r\sin\theta)\|}{\|v_{inc}^\alpha(r\cos\theta, r\sin\theta)\|}\sqrt{\nu_\beta r} \tag{3.105}$$

For each of these snapshots, the distance r from the edge to the wavefront of the considered (L or T) edge diffracted wave is computed using the wave velocity and the chosen propagation time, and the norm of the field $\|v_\beta^{diff}\|$ is extracted on the point of the FE mesh which is closest to the wavefront for each observation angle θ. The diffraction coefficient is finally computed using formula (3.105). The results are shown in Fig. 3.11.

Fig. 3.11 shows the absolute value of the diffraction coefficients, obtained for a wedge of angle $\varphi = 270^o$ illuminated by a wave incident with an angle $\theta_{inc} = 135^o$, plotted with respect to the observation angle. The blue line is the diffraction coefficient extracted from the finite elements wave front and the dashed red line is the result obtained from the SF code.

Overall, both lines overlap quite well, though some differences are observed. The most obvious difference between the plots is that the FE diffraction coefficient always remains finite, whereas the SF diffraction coefficient possesses poles (except for Fig. 3.11b where there are no reflected L waves). This is due to the fact that the SF diffraction coefficient is a GTD-like coefficient obtained from a far-field asymptotic evaluation (3.43) and it diverges at shadow boundaries [14, 23]. The FE code notably computes the reflected waves as well as the diffracted waves in angular regions surrounding the reflected poles ; consequently, reflected waves give a contribution to the FE diffraction coefficient.

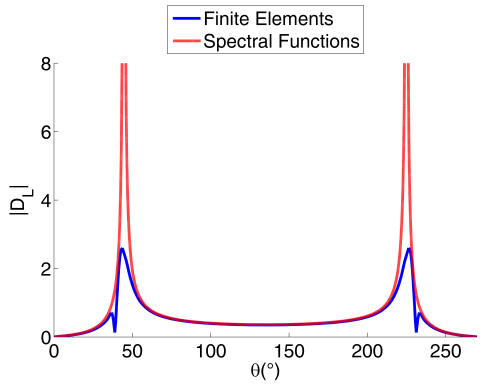

(a) Diffracted and incident L waves. $r = 25,6$mm.

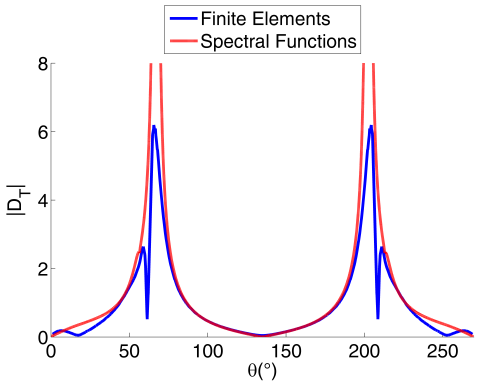

(b) Diffracted T wave and incident L wave. $r = 13,9$mm.

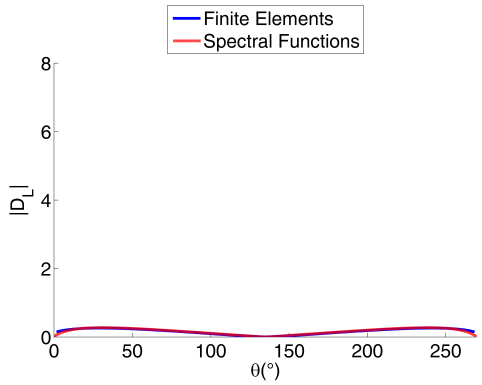

(c) Diffracted L wave and incident T wave. $r = 36,5$mm.

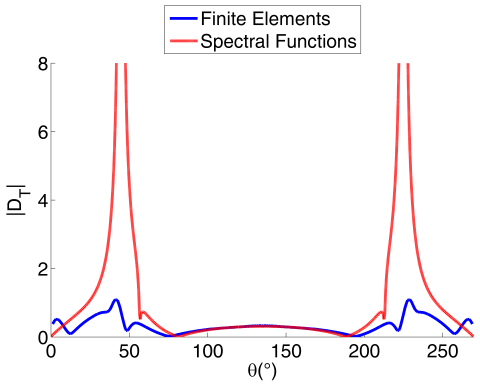

(d) Diffracted and incident T waves. $r = 19,8$mm.

Figure 3.11 – Diffraction coefficients for $\varphi = 270^o, \theta_{inc} = 135^o$

The contribution of these reflected plane waves to the FE diffraction coefficient, computed using (3.105), grows with the distance r, since it contains the factor $\sqrt{\nu_\beta r}$ and the reflected plane waves have theoretically constant amplitudes. Interference between these plane reflected waves and the cylindrical diffracted waves explain the spikes that can be observed in the FE diffraction coefficients, near the poles of the GTD diffraction coefficients in Figs. 3.11a, 3.11b and 3.11d. Some uniform methods have been proposed to handle the divergence of GTD diffraction coefficients and build a spatially uniform total field and some of them have been applied to elastodynamic half-plane scattering [23, 21, 60].

On Figs. 3.11b and 3.11d for diffracted T waves, the FE diffraction coefficient seems to have a slightly different behavior near the wedge edges than the SF diffraction coefficients. Since this discrepancy is only visible in the T diffraction coefficient, it seems unlikely that it is due to the branch points at angles $\theta = 0$ and $\theta = \varphi$ mentioned in section 3.2.3, as these branch points would affect both L and T diffracted waves. The observed discrepancy is more probably due to interference of the diffracted T wavefront with the Rayleigh waves observed on Figs. 3.10a and 3.10b, which modifies the observed FE amplitude along the diffracted T wavefront. In addition, on these figures, the very slight spikes at $\theta = 57^o$ and $\theta = 213^o$ in the SF diffraction coefficient correspond to head waves and associated branch points when $\theta = \theta_c$ and $\theta = \varphi - \theta_c$. Regarding the diffraction coefficients calculated from the FE simulation, since the value of the diffracted wave field is extracted along the cylindrical diffracted wavefront, the head waves are accounted in the FE diffraction coefficient when they interfere with both diffracted and reflected waves (location at the intersection of the HW, rTW and dTW in the FE snapshot).

Away from shadow boundaries (where the non-uniform SF code diverges) and domain borders i.e. in regions where diffracted waves do not interfere with other waves and where the SF asymptotic evaluation is theoretically valid, the FE and SF codes give very similar results.

3.5 Experimental validation

The LT code used to validate the SF method for wedge angles lower than π has been validated experimentally by Chapman et al. [35]. Their experimental set-up is thoroughly described in [35] and will only be summarized here. The results of their experimental measurements will be used to validate the SF code experimentally.

Two isotropic ferritic steel ($c_L = 5900\,m.s^{-1}$, $c_T = 3230\,m.s^{-1}$) cylindrical sectors of radius 150mm, thickness 100mm wedges and of angles $\varphi = 80^o$ and $\varphi = 100^o$ are inspected in pulse-echo configuration, meaning that the emitting

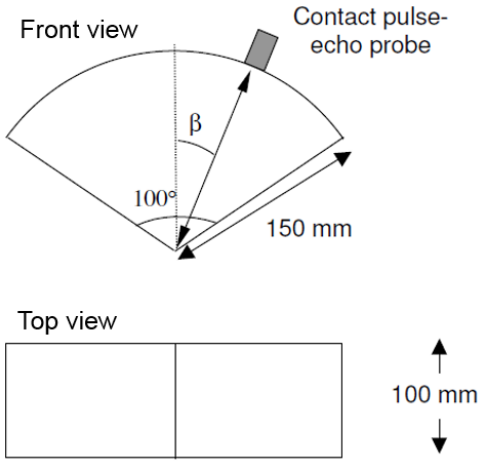

Figure 3.12 – (Reproduced from [35]) Front and Top view of the wedge inspected in pulse-echo configuration.

transducer is also the receiving transducer. In terms of the diffraction coefficient, this means that the observation angle is equal to the incidence angle.

The inspections have been done at frequencies 2MHz and 5MHz to check that the diffraction coefficients do not depend on the frequency. The experimental set-up is shown in Fig. 3.12. Since the diffraction coefficients measured at both frequencies are identical, only the results obtained at 2MHz are presented here. Figs. 3.13 and 3.14 present the comparison between the backscattering coefficients computed using the LT code, the coefficients computed using the SF code and the values measured experimentally presented in [35].

Figs. 3.13a-3.13b and Figs 3.13c-3.13d show the absolute values of the L and T backscattering diffraction coefficients respectively, for wedges of angle $\varphi = 80^o$ and 100^o. Figs. 3.14a-3.14b and Figs 3.14c-3.14d show the angular phases of the L and T backscattering diffraction coefficients respectively, for wedges of angle $\varphi = 80^o$ and 100^o. In each of these figures, the full blue line represents the results obtained using the LT diffraction coefficients, the dashed red line represents the results obtained using the SF diffraction coefficients and the black diamonds represent the results measured experimentally.

In each of the tested configurations, the results are conclusive. In ultrasonic NDT, the margin of measurements incertitude is of 2dB in pulse-echo configuration. The difference between the experimental measurements and the numerical results is below the 2dB threshold (the maximum difference being of 1.96dB), except in directions of specular reflection where the GTD model fails. Outside these directions, there is a very good agreement between the experimental measurements of the absolute values of the diffraction coefficients and the numerical

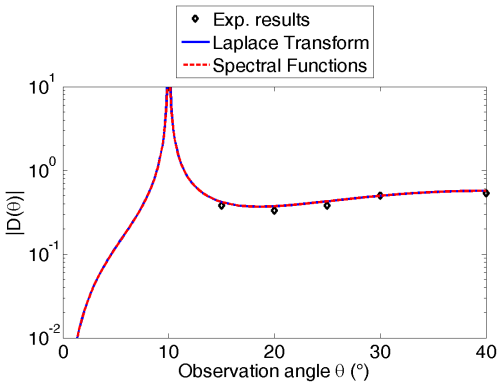

(a) Incident and diffracted L wave, $\varphi = 80^o$.

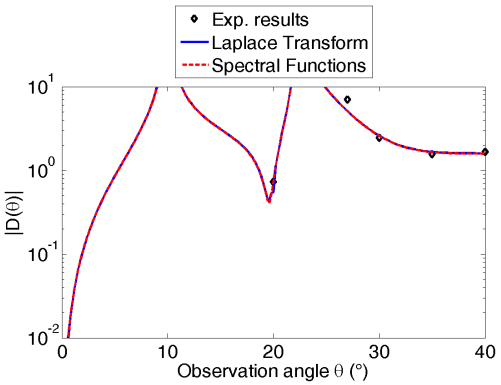

(b) Incident and diffracted T wave, $\varphi = 80^o$.

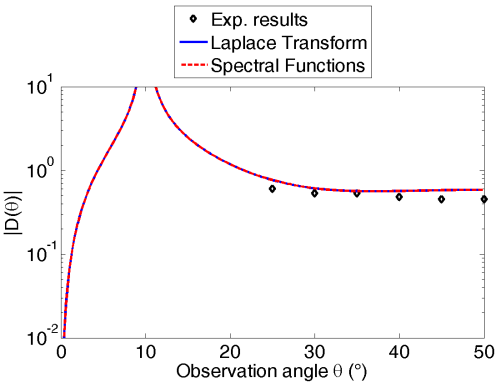

(c) Incident and diffracted L wave, $\varphi = 100^o$.

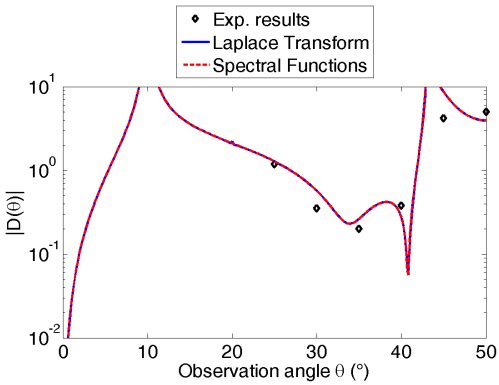

(d) Incident and diffracted T wave, $\varphi = 100^o$.

Figure 3.13 – Absolute value of the backscattering diffraction coefficients for wedges $\varphi = 80^o$ and 100^o.

results. The angular phases of the diffraction coefficients computed numerically almost allways coincide with the experimental measurements, except for those taken between two shadow boundaries (see for example Fig. 3.14b, at angle $\theta = 20^o$), where the diffraction coefficient varies abruptly, creating a high level of uncertainty. This is not surprising, as the phase of GTD coefficients is discontinuous at shadow boundaries, as explained in 1.1.2. A slight discrepancy between the phases of the two codes can also be noted in Fig. 3.14b, at grazing observation angles.

This provides an experimental validation for the SF code.

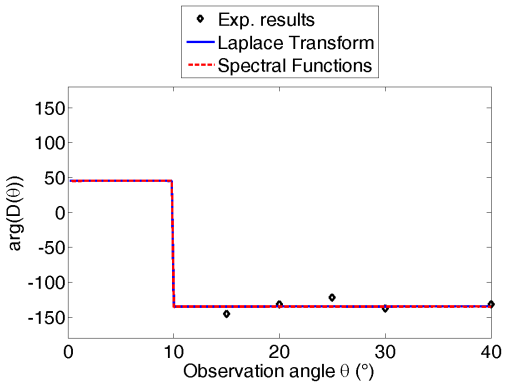

(a) Incident and diffracted L wave, $\varphi = 80^o$.

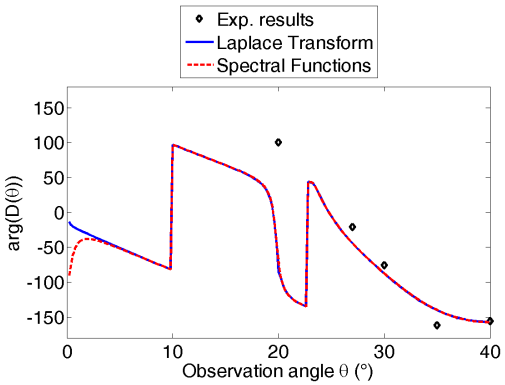

(b) Incident and diffracted T wave, $\varphi = 80^o$.

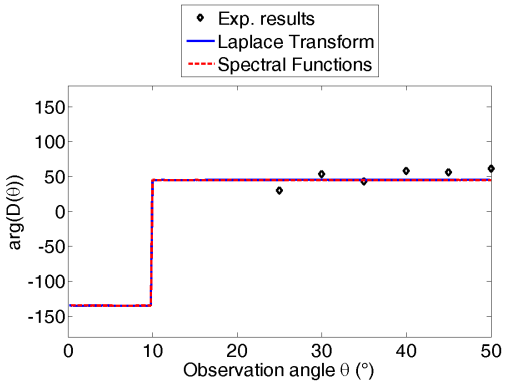

(c) Incident and diffracted L wave, $\varphi = 100^o$.

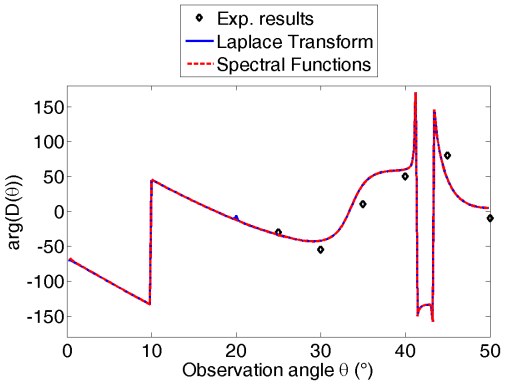

(d) Incident and diffracted T wave, $\varphi = 100^o$.

Figure 3.14 – Angular phase of the backscattering diffraction coefficients (in degrees) for wedges $\varphi = 80^o$ and $\varphi = 100^o$.

Conclusion

The spectral functions method for modeling the diffraction of an elastic wave by a stress-free wedge is presented here. It extends the region of validity of previously existing semi-analytical methods for high-frequency computation to all wedge angles. The numerical aspects of the computation are fully detailed and the diffraction coefficient obtained using this method has been compared to the one obtained using the Laplace Transform (LT) code in the case of a wedge angle lower than π, and to a spectral finite elements code in the case of a wedge angle higher than π. When compared to the Laplace Transform (LT) semi-analytical computation method for wedge angles lower than π, the spectral functions code gives excellent results. For wedge angles higher than π, a finite

elements code is used for validation and the spectral functions method gives very good results in the domain of validity of the far-field asymptotic model. Finally, the results of the code are compared to experimental measurements, and the results are also good.

CHAPTER 4

3D elastic wave diffraction by a stress-free wedge of arbitrary angle

Outline of the current chapter

Introduction

In the previous chapters of this manuscript, the spectral functions method has been presented in the case of an acoustic wave incident on an infinite wedge with Dirichlet or Neumann boundaries and in the case of an elastic wave incident on a stress-free wedge. Both of these problems have been treated in the case of 2D incidences, meaning that the incident ray is in the plane normal to the wedge edge. In this chapter, we will extend the spectral functions method to the case of 3D incidences. This extension will be done for elastic waves incident on stress-free wedges and it will be shown that the 3D code developed for the elastic case can be applied to the limit case of an acoustic wave incident on a wedge with Dirichlet boundary conditions, as well as to the 2D elastic problem.

The problem of 3D wedge diffraction has been studied over the past century in acoustics, electromagnetics and in to a lesser degree in elastodynamics. The problem was introduced notably by Sommerfeld [43], who gave an exact expression of the solution to the scattering problem of a scalar plane wave by a wedge with Dirichlet or Neumann boundaries in the form of a contour integral. This integral can be used to obtain an analytical expression of the Geometrical Theory of Diffraction (GTD) diffraction coefficient both in electromagnetics and in acoustics [31, 55]. Independently, Macdonald [54] has expressed the solution to the same problem as an infinite series. Proof that the Sommerfeld and the Macdonald approaches are equivalent was developed by Carslaw [72].

In the case of an incident acoustic wave, Rawlins [73] determined an expression of the solution as a real integral for a spherical acoustic wave diffracted by a wedge with Dirichlet or Neumann boundaries when the aperture angle is an integer multiple of $\frac{\pi}{n}$, where n is also an integer. In the case of an electromagnetic wave, Rojas [74] derived a uniform asymptotic solution for a plane wave incident on an impedant wedge when the wedge angle is a multiple of $\frac{\pi}{2}$. By generalizing the Malyuzhinets technique [44], Bernard [75] reduced the 3D problem of a plane electromagnetic wave diffracted by an impedant wedge of arbitrary angle to a scalar functional equation with only one unknown and provides examples of numerical resolution of this equation in the case where the relative impedance of the wedge faces is 1 and in the case of a half or full plane with arbitrary impedance. Finally, an application of the Wiener-Hopf technique to the case of electromagnetic plane wave diffraction by impenetrable wedges of arbitrary angles was developed by Daniele in 2D [76] and extended to 3D cases by Daniele and Lombardi [77].

In elastodynamics, a GTD solution to the 3D problem of plane wave diffraction by a stress-free half plane was developed by Achenbach and Gautesen [16, 15, 78] and Gautesen [48, 49] proposed a semi-analytical scheme of resolution of the far-field scattering problem of a skew incident Rayleigh wave diffracted by a

quarter-space (i.e. a wedge of angle $\frac{\pi}{2}$ or $\frac{3\pi}{2}$). To our knowledge, no resolution scheme has been developed for a skew incident longitudinal or transversal plane elastic wave diffracted by an arbitrary-angled wedge. Therefore, it is the aim of this chapter.

In the first part of this chapter, the problem is presented. In the second part, an integral formulation of the solution is derived, depending on two unknown functions, called the spectral functions. The 3D diffraction coefficient is defined and expressed with respect to these spectral functions. In the third part, the semi-analytical evaluation of these functions is detailed. Finally, the corresponding code is tested numerically in the fourth part.

4.1 Problem statement

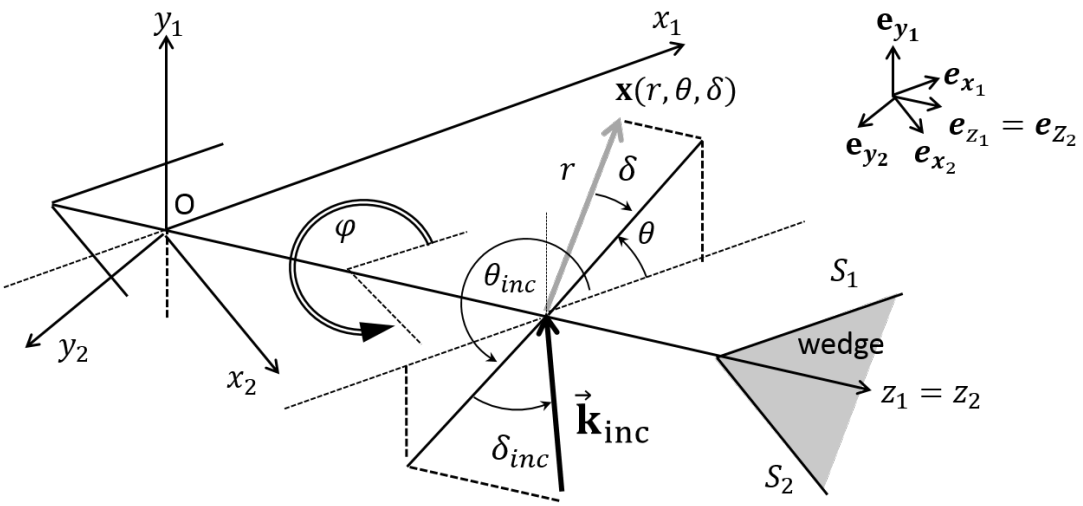

Figure 4.1 – Geometry of the problem

Let us consider the problem of an elastic wave diffracted by a stress-free infinite wedge delimited by faces $\mathcal{S}_1$ and $\mathcal{S}_2$. The geometry of the problem is shown on Fig. 4.1. Vector $\mathbf{x} = (r, \theta, \delta)$ is an observation point in the propagation domain indexed by its spherical coordinates and the domain Ω is the inside of the wedge, defined by :

$$\Omega = \{(r\cos\theta\cos\delta, r\sin\theta\cos\delta, r\sin\delta) \setminus \theta \in]0, \varphi[, \delta \in]-\frac{\pi}{2}, \frac{\pi}{2}[\} \tag{4.1}$$

The incident wave is a plane wave of the form

$$\mathbf{u}^{inc}(\mathbf{x},t) = \mathbf{A}_\alpha e^{i(\mathbf{k}_\alpha^{inc}\cdot\mathbf{x}-\omega t)} \tag{4.2}$$

where $\mathbf{A}_\alpha$ is the amplitude vector of the incident wave and $\mathbf{k}_\alpha^{inc}$ is the incident wave vector. The type of the incident wave is denoted α (α =L for a longitudinal wave, TH for transverse horizontal and TV for transverse vertical). $(O;\mathbf{e}_{x_1},\mathbf{e}_{y_1},\mathbf{e}_{z_1})$ is a Cartesian coordinate system associated to face $\mathcal{S}_1$ and $(O;\mathbf{e}_{x_2},\mathbf{e}_{y_2},\mathbf{e}_{z_2})$ is a Cartesian coordinate system associated to face $\mathcal{S}_2$. In all the following, vectors are expressed in the coordinate system $\mathbf{x} = (x_1', y_1', z_1')_{(\mathbf{e}_{x_1},\mathbf{e}_{y_1},\mathbf{e}_{z_1})}$, unless explicitly mentioned otherwise. In this system, the incident wave vector is given by :

$$\mathbf{k}_\alpha^{inc} = \frac{\omega}{c_\alpha}\begin{pmatrix}\cos\theta_{inc}\cos\delta_{inc}\\ \sin\theta_{inc}\cos\delta_{inc}\\ \sin\delta_{inc}\end{pmatrix} \tag{4.3}$$

As always, c_L is the velocity of longitudinal waves and c_T is the velocity of transverse waves.

The amplitude vector can be directed by three different two-by-two orthogonal vectors, depending on the incident wave's polarization. These unit polarization vectors are noted $\hat{i}_*$, where $* = L, TH, TV$ and are given by Achenbach [16] :

$$\hat{i}_L = \begin{pmatrix}\cos\theta_{inc}\cos\delta_{inc}\\ \sin\theta_{inc}\cos\delta_{inc}\\ \pm\sin\delta_{inc}\end{pmatrix}\hat{i}_{TV} = \begin{pmatrix}\mp\cos\theta_{inc}\sin\delta_{inc}\\ \mp\sin\theta_{inc}\sin\delta_{inc}\\ \cos\delta_{inc}\end{pmatrix}\hat{i}_{TH} = \begin{pmatrix}-\sin\theta_{inc}\\ \cos\theta_{inc}\\ 0\end{pmatrix} \tag{4.4}$$

where the top sign gives the polarization of an incident wave and the bottom sign gives the polarization of a diffracted wave.

For a homogeneous, isotropic material, the linear elasticity equation solved by the displacement field $\mathbf{u}$ is

$$\underline{\mu}\Delta\mathbf{u} + (\underline{\lambda}+\underline{\mu})\nabla\nabla\mathbf{u} = \rho\frac{\partial^2\mathbf{u}}{\partial t^2} \tag{4.5}$$

On each of the wedge faces, the displacement field verifies the zero-stress boundary conditions, expressed as :

$$(\underline{\lambda}\nabla\mathbf{u}.\mathbb{I}_\mathbf{3} + 2\underline{\mu}\varepsilon(\mathbf{u})).\mathbf{n} = 0 \tag{4.6}$$

where $\mathbb{I}_\mathbf{3}$ is the identity matrix of the third order, n is the inward facing normal to the wedge face ($n = \mathbf{y}_1$ on $\mathcal{S}_1$ and $n = \mathbf{y}_2$ on $\mathcal{S}_2$) and $\underline{\lambda}, \underline{\mu}$ are the Lamé coefficients

of the considered elastic medium. The expression of the deformations tensor is :

$$\varepsilon(\mathbf{u}) = \frac{1}{2}\begin{pmatrix} 2\dfrac{\partial u_1}{\partial x_1'} & \dfrac{\partial u_1}{\partial y_1'} + \dfrac{\partial u_2}{\partial x_1'} & \dfrac{\partial u_1}{\partial z_1'} + \dfrac{\partial u_3}{\partial x_1'} \\ \dfrac{\partial u_1}{\partial y_1'} + \dfrac{\partial u_2}{\partial x_1'} & 2\dfrac{\partial u_2}{\partial y_1'} & \dfrac{\partial u_2}{\partial z_1'} + \dfrac{\partial u_3}{\partial y_1'} \\ \dfrac{\partial u_1}{\partial z_1'} + \dfrac{\partial u_3}{\partial x_1'} & \dfrac{\partial u_2}{\partial z_1'} + \dfrac{\partial u_3}{\partial y_1'} & 2\dfrac{\partial u_3}{\partial z_1'} \end{pmatrix} \tag{4.7}$$

Kamotski and Lebeau [53] have proven existence and uniqueness of the solution to this problem in the 2D the case. We will suppose that their demonstration is still valid in the 3D case.

From hereon after, bold characters will be reserved to matrices in order to simplify notations. The solutions being time harmonic, the factor $e^{-i\omega t}$ will be implied but omitted everywhere. Furthermore, since there is no obstacle to propagation in the z direction, $e^{i\frac{\omega}{c_\alpha}\sin\delta_{inc}z_1'}$ is also a common factor to all the terms which appear in the solution.

The total field is written as the sum of an incident field u^{inc} and a scattered field u_0

$$u = u_0 + u^{inc} \tag{4.8}$$

The dimensionless problem is obtained by applying the following variable change :

$$x = \frac{\omega}{c_L}x', \quad y = \frac{\omega}{c_L}y', \quad z = \frac{\omega}{c_L}z' \tag{4.9a}$$

$$u_0(x', y', z') = v(x, y)e^{i\nu_\beta \sin\delta_\beta z} \tag{4.9b}$$

where δ_β is the angle of Snell's cone of diffraction (determined by Snell's law of diffraction, given by (4.10)), the dimensionless Lamé parameters λ, μ are given in the previous chapter by (3.10) and parameters ν_L and ν_T are also defined in the previous chapter, by (3.13). Since $e^{i\nu_\alpha \sin\delta_{inc}z}$ is a common factor to all the terms of the solution, we can deduce Snell's law of diffraction :

$$\nu_\alpha \sin\delta_{inc} = -\nu_\beta \sin\delta_\beta \tag{4.10}$$

where β denotes the type of the diffracted wave. To simplify notations, the following parameter τ is defined by :

$$\tau = \nu_\alpha \sin\delta_{inc} \tag{4.11}$$

Note that we therefore always have $\tau \in [-\nu_\alpha, \nu_\alpha]$. u_0's z-dependency is entirely contained in the factor $e^{i\tau z}$ which will be implied but omitted in all the following.

Substituting (4.8) and (4.9) into (4.5) and (4.6) and using (4.7) yields the dimensionless problem

$$(\mathcal{P}^*) \qquad \begin{cases} (E+1)v = 0 & (\Omega) \\ Bv = -Bv_\alpha^{inc} & (\mathcal{S}) \end{cases} \tag{4.12}$$

where (v_1, v_2, v_3) are the components of vector v :

$$Ev = \mu(\Delta v - \tau^2 v) + (\lambda+\mu)\begin{pmatrix} \frac{\partial^2 v_1}{\partial x^2} + \frac{\partial^2 v_2}{\partial x \partial y} + i\tau\frac{\partial v_3}{\partial x} \\ \frac{\partial^2 v_1}{\partial x \partial y} + \frac{\partial^2 v_2}{\partial y^2} + i\tau\frac{\partial v_3}{\partial y} \\ i\tau\left(\frac{\partial v_1}{\partial x} + \frac{\partial v_2}{\partial y}\right) - \tau^2 v_3 \end{pmatrix} \tag{4.13}$$

and

$$Bv = \begin{pmatrix} \mu\left(\frac{\partial v_x}{\partial y} + \frac{\partial v_y}{\partial x}\right) \\ \frac{\partial v_y}{\partial y} + \lambda\left(\frac{\partial v_x}{\partial x} + i\tau v_z\right) \\ \mu\left(\frac{\partial v_z}{\partial y} + i\tau v_y\right) \end{pmatrix} \tag{4.14}$$

where E and B are respectively the dimensionless linear elasticity operator and normal stress operator and λ, μ are the dimensionless Lamé parameters, defined by (3.10). The dimensionless incident field is given by

$$\begin{aligned} \mathrm{v}_{\mathrm{L}}^{\mathrm{inc}}(\mathrm{r},\theta) &= \begin{pmatrix} \cos\theta_{inc}\cos\delta_{inc} \\ \sin\theta_{inc}\cos\delta_{inc} \\ \sin\delta_{inc} \end{pmatrix} \mathrm{e}^{\mathrm{i}\mathrm{r}\nu_{\mathrm{L}}\cos(\theta-\theta_{\mathrm{inc}})\cos\delta_{\mathrm{inc}}} \\ \mathrm{v}_{\mathrm{TH}}^{\mathrm{inc}}(\mathrm{r},\theta) &= \begin{pmatrix} -\sin\theta_{inc} \\ \cos\theta_{inc} \\ 0 \end{pmatrix} \mathrm{e}^{\mathrm{i}\mathrm{r}\nu_{\mathrm{T}}\cos(\theta-\theta_{\mathrm{inc}})\cos\delta_{\mathrm{inc}}} \\ \mathrm{v}_{\mathrm{TV}}^{\mathrm{inc}}(\mathrm{r},\theta) &= \begin{pmatrix} -\cos\theta_{inc}\sin\delta_{inc} \\ -\sin\theta_{inc}\sin\delta_{inc} \\ \cos\delta_{inc} \end{pmatrix} \mathrm{e}^{\mathrm{i}\mathrm{r}\nu_{\mathrm{T}}\cos(\theta-\theta_{\mathrm{inc}})\cos\delta_{\mathrm{inc}}} \end{aligned} \tag{4.15}$$

The first equation of system (4.12) is the dimensionless version of the linear elasticity equation and the second equation is the dimensionless version of the stress-free boundary conditions.

4.2 Integral formulation of the solution

As in the previous chapters, the first step in solving problem $(\mathcal{P}^\alpha)$ is to formulate the solution as an integral.

4.2.1 Limiting absorption principle

The limiting absorption principle is applied to $(\mathcal{P}^\alpha)$. This means that it is considered as a special case ($\varepsilon = 0$) of the problem

$$(\mathcal{P}_\varepsilon^*) \qquad \begin{cases} (E + e^{-2i\epsilon})v^\varepsilon = 0 & (\Omega) \\ Bv^\varepsilon = -Bv_*^{inc} & (\mathcal{S}) \end{cases} \tag{4.16}$$

Following Kamotski and Lebeau [53], we will once again suppose that the solution can be expressed as the sum of two contributions, corresponding to each of the wedge faces :

$$v^\varepsilon = v_1^\varepsilon + v_2^\varepsilon \tag{4.17}$$

where functions v_j^ε are now defined on all of $\mathbb{R}^3$ by

$$v_j^\varepsilon = -(E + e^{-2i\varepsilon})^{-1} \left[\begin{pmatrix} \alpha_j \\ \beta_j \\ \gamma_j \end{pmatrix} \otimes \delta_{\mathcal{S}_j} \right] \tag{4.18}$$

Distributions $\alpha_j, \beta_j, \gamma_j$ are unknown and belong to the special class $\mathcal{A}$ defined in chapter 2 of this thesis, Def. 2.1.1. We can now define the outgoing solution of $(\mathcal{P}^\alpha)$ analogously to the 2D case :

Def. 4.2.1. *v is called an outgoing solution of equation (4.12) if v is a solution of the form*

$$v = v_1|_\Omega + v_2|_\Omega \tag{4.19}$$

where, for $j = 1, 2$:

$$v_j = -\lim_{\varepsilon \to 0} (E + e^{-2i\varepsilon})^{-1} \left[\begin{pmatrix} \alpha_j \\ \beta_j \\ \gamma_j \end{pmatrix} \otimes \delta_{\mathcal{S}_j} \right] \tag{4.20}$$

where $\alpha_j, \beta_j, \gamma_j \in \mathcal{A}$ and where $\delta_{\mathcal{S}_1}$ and $\delta_{\mathcal{S}_2}$ are the Dirac distributions associated to the wedge faces $\mathcal{S}_1$ and $\mathcal{S}_2$ respectively.

The following theorem was proved by Kamotski and Lebeau [53] in the 2D case. We will suppose that their proof can be adapted to the 3D case and that the theorem is still true.

Theorem 4.2.1. *Equation* (4.12) *admits a unique outgoing solution.*

Now that the outgoing solution has been defined, we will derive an integral formulation of this solution.

4.2.2 Integral formulation

The two-sided Fourier transform and its inverse transform are defined in chapter 2 of this manuscript by (2.12). The first step in determining an integral formulation of the solution is to apply the two-sided Fourier transform to (4.18). This is possible because all the distributions that appear in this equation are tempered distributions and they therefore admit a Fourier transform. We then have :

$$\hat{v}_j^{\varepsilon}(\xi,\eta) = (\mathbf{M} - e^{-2i\varepsilon}\mathbb{I}_{\mathbf{3}})^{-1}\Sigma_j(\xi) \tag{4.21}$$

where $\Sigma_j, j = 1,2$ are the unknown spectral functions, defined by :

$$\Sigma_j(\xi,) = \begin{pmatrix} \hat{\alpha_j}(\xi) \\ \hat{\beta_j}(\xi) \\ \hat{\gamma_j}(\xi) \end{pmatrix} \tag{4.22}$$

and where $\mathbf{M}$ is the two-sided Fourier transform of operator E. Its expression is :

$$\mathbf{M}(\xi,\eta) = \begin{pmatrix} \xi^2+\mu(\eta^2+\tau^2) & (\lambda+\mu)\xi\eta & (\lambda+\mu)\xi\tau \\ (\lambda+\mu)\xi\eta & \eta^2+\mu(\xi^2+\tau^2) & (\lambda+\mu)\eta\tau \\ (\lambda+\mu)\xi\tau & (\lambda+\mu)\eta\tau & \tau^2+\mu(\xi^2+\eta^2) \end{pmatrix} \tag{4.23}$$

Substituting λ by $1-2\mu$ and μ by $1/\nu_T^2$, (4.23) yields

$$(\mathbf{M} - e^{-2i\varepsilon}\mathbb{I}_3)^{-1} = \frac{\begin{pmatrix} \xi^2+\nu_T^2(\eta^2+\tau^2-e^{-2i\varepsilon}) & (1-\nu_T^2)\xi\eta & (1-\nu_T^2)\xi\tau \\ (1-\nu_T^2)\xi\eta & \eta^2+\nu_T^2(\xi^2+\tau^2-e^{-2i\varepsilon}) & (1-\nu_T^2)\tau\eta \\ (1-\nu_T^2)\xi\tau & (1-\nu_T^2)\tau\eta & \tau^2+\nu_T^2(\eta^2+\xi^2-e^{-2i\varepsilon}) \end{pmatrix}}{(\xi^2+\eta^2+\tau^2-e^{-2i\varepsilon})(\xi^2+\eta^2+\tau^2-\nu_T^2e^{-2i\varepsilon})} \tag{4.24}$$

Finally, the integral formulation of v_j is obtained by inverting the two-sided Fourier transform applied in (4.21) :

$$v_j^{\varepsilon}(x_j,y_j) = \frac{1}{4\pi^2}\int_{\mathbb{R}^2} e^{ix_j\xi}\left(\int_{-\infty}^{+\infty} e^{iy_j\eta}(\mathbf{M} - e^{-2i\varepsilon}\mathbb{I}_{\mathbf{3}})^{-1}\,d\eta\right)\Sigma_j(\xi)\,d\xi \tag{4.25}$$

The poles of $(\mathbf{M} - e^{-2i\varepsilon}\mathbb{I}_3)^{-1}$ (which are the poles of the integrand of the inner integral on η in (4.25)) are located at $\eta = \pm\zeta_*^\varepsilon(\xi)$, where $* = L, T$ and

$$\zeta_*^\epsilon(\xi) = \sqrt{e^{-2i\varepsilon}\nu_*^2 - (\xi^2 + \tau^2)} \tag{4.26}$$

Let us define $\tilde{\nu}_*, * = L, T$ by

$$\tilde{\nu}_*^\varepsilon = \sqrt{e^{-2i\varepsilon}\nu_*^2 - \tau^2} \tag{4.27}$$

If the incident wave is longitudinal, then, according to (4.11), $\tau = \sin\delta_{inc}$ and

$$\tilde{\nu}_L^0 = \sqrt{1 - \sin^2\delta_{inc}} = \cos\delta_{inc} \quad \in \mathbb{R} \tag{4.28a}$$

$$\tilde{\nu}_T^0 = \sqrt{\nu_T^2 - \sin^2\delta_{inc}} \quad \in \mathbb{R}, \tag{4.28b}$$

since $\nu_L = 1$ and $\nu_T = \frac{c_L}{c_T} > 1$. However, if the incident wave is transverse, then $\tau = \nu_T \sin\delta_{inc}$ and we have

$$\tilde{\nu}_T^0 = \sqrt{\nu_T^2 - \nu_T^2\sin^2\delta_{inc}} = \nu_T\cos\delta_{inc} \quad \in \mathbb{R}, \tag{4.29}$$

and for $\tilde{\nu}_L^0$, two cases may occur :

- if $|\sin\delta_{inc}| \leq \dfrac{\nu_L}{\nu_T}$, then $\tilde{\nu}_L^0 = \sqrt{\nu_L - \nu_T^2\sin^2\delta_{inc}} \quad \in \mathbb{R}$ (4.30)
- if $|\sin\delta_{inc}| > \dfrac{\nu_L}{\nu_T}$, then $\tilde{\nu}_L^0 = \sqrt{1 - \nu_T^2\sin^2\delta_{inc}} = i\sqrt{\nu_T^2\sin^2\delta_{inc} - 1} \quad \in i\mathbb{R}$ (4.31)

As we will see, in the case described by (4.30), the computations made in the 3D case are analogous to those described in the previous chapter. On the other hand, in the case described by (4.31), the presence of an imaginary branch point modifies and complicates all the occurring complex integral contour deformations. In any case,

$$\zeta_*^\varepsilon(\xi) = \sqrt{\tilde{\nu}_*^{\varepsilon^2} - \xi^2} \tag{4.32}$$

The inner integral of (4.25) is computed using Cauchy's residue theorem :

$$v_j^\varepsilon(x_j,y_j) = \frac{i}{4\pi} e^{2i\varepsilon} \int_{\mathbb{R}} e^{ix_j\xi} \sum_{*=L,T} e^{i|y_j|\zeta_*^\varepsilon(\xi)} \mathbf{M}_*^\varepsilon(\xi, \operatorname{sgn} y_j)\Sigma_j(\xi)\, d\xi \tag{4.33}$$

where $t = \operatorname{sgn}(y_j)$ and $\mathbf{M}_*^\varepsilon(\xi,t), * = L,T$ are defined by

$$\mathbf{M}_\mathbf{L}^\varepsilon(\xi,t) = \begin{pmatrix} \frac{\xi^2}{\zeta_L^\varepsilon} & t\xi & \frac{\xi\tau}{\zeta_L^\varepsilon} \\ t\xi & \zeta_L^\varepsilon & t\tau \\ \frac{\xi\tau}{\zeta_L^\varepsilon} & t\tau & \frac{\tau^2}{\zeta_L^\varepsilon} \end{pmatrix} \tag{4.34a}$$

$$\mathbf{M}_\mathbf{T}^\varepsilon(\xi,t) = \begin{pmatrix} \zeta_T^\varepsilon + \frac{\tau^2}{\zeta_T^\varepsilon} & -t\xi & -\frac{\xi\tau}{\zeta_T^\varepsilon} \\ -t\xi & \frac{\xi^2+\tau^2}{\zeta_T^\varepsilon} & -t\tau \\ -\frac{\xi\tau}{\zeta_T^\varepsilon} & -t\tau & \zeta_T^\varepsilon + \frac{\xi^2}{\zeta_T^\varepsilon} \end{pmatrix} \tag{4.34b}$$

These matrices can be computed in two different manners, providing a way to test this result. The first way to compute these matrices is by direct computation of the residues of matrix $(\mathbf{M} - e^{-2i\varepsilon}\mathbb{I}_\mathbf{3})^{-1}$ when applying the Cauchy theorem to compute the inner integral of (4.25) to obtain (4.33), where matrix $\mathbf{M}$ is given by (4.23), at poles $\pm\zeta_*^\varepsilon(\xi), * = L,T$. The second option for computing these matrices starts by computing the eigen vectors and eigen values of $\mathbf{M}$. The three eigen vectors of $\mathbf{M}$ and the corresponding eigen values are :

$$\mathbf{M}\begin{pmatrix} \xi \\ \eta \\ \tau \end{pmatrix} = (\xi^2+\eta^2+\tau^2)\begin{pmatrix} \xi \\ \eta \\ \tau \end{pmatrix} \tag{4.35a}$$

$$\mathbf{M}\begin{pmatrix} -\eta \\ \xi \\ 0 \end{pmatrix} = \frac{\xi^2+\eta^2+\tau^2}{\nu_T^2}\begin{pmatrix} -\eta \\ \xi \\ 0 \end{pmatrix} \tag{4.35b}$$

$$\mathbf{M}\begin{pmatrix} -\xi\tau \\ \eta\tau \\ \xi^2+\eta^2 \end{pmatrix} = \frac{\xi^2+\eta^2+\tau^2}{\nu_T^2}\begin{pmatrix} -\xi\tau \\ \eta\tau \\ \xi^2+\eta^2 \end{pmatrix} \tag{4.35c}$$

These three vectors are linearly independent and constitute a vector basis of $\mathbb{C}^3$. This means that any vector of $\mathbb{C}^3$ can be expressed as a linear combination of

these three vectors. Notably :

$$\Sigma_j = \begin{pmatrix} \hat{\alpha}_j \\ \hat{\beta}_j \\ \hat{\gamma}_j \end{pmatrix} = \frac{\xi\hat{\alpha}_j + \eta\hat{\beta}_j + \tau\hat{\gamma}_j}{\xi^2+\eta^2+\tau^2}\begin{pmatrix} \xi \\ \eta \\ \tau \end{pmatrix} + \frac{\xi\hat{\beta}_j - \eta\hat{\alpha}_j}{\xi^2+\eta^2}\begin{pmatrix} -\eta \\ \xi \\ 0 \end{pmatrix} + \frac{(\xi^2+\eta^2)\hat{\gamma}_j - \tau(\xi\hat{\alpha}_j + \eta\hat{\beta}_j)}{(\xi^2+\eta^2)(\xi^2+\eta^2+\tau^2)}\begin{pmatrix} -\xi\tau \\ \eta\tau \\ \xi^2+\eta^2 \end{pmatrix} \tag{4.36}$$

This allows us to write the term $(\mathbf{M} - e^{-2i\varepsilon}\mathbb{I}_3)^{-1}\Sigma_j$ as the sum of three contributions :

$$\begin{aligned}(\mathbf{M} - e^{-2i\epsilon}\mathbb{I}_3)^{-1}\Sigma_j = {} & \frac{\xi\hat{\alpha}_j + \eta\hat{\beta}_j + \tau\hat{\gamma}_j}{\xi^2+\eta^2+\tau^2}[(\xi^2+\eta^2+\tau^2) - e^{-2i\varepsilon}]^{-1}\begin{pmatrix} \xi \\ \eta \\ \tau \end{pmatrix} \\ & + \frac{\xi\hat{\beta}_j - \eta\hat{\alpha}_j}{\xi^2+\eta^2}[\frac{\xi^2+\eta^2+\tau^2}{\nu_T^2} - e^{-2i\varepsilon}]^{-1}\begin{pmatrix} -\eta \\ \xi \\ 0 \end{pmatrix} \\ & + \frac{(\xi^2+\eta^2)\hat{\gamma}_j - \tau(\xi\hat{\alpha}_j + \eta\hat{\beta}_j)}{(\xi^2+\eta^2)(\xi^2+\eta^2+\tau^2)}[\frac{\xi^2+\eta^2+\tau^2}{\nu_T^2} - e^{-2i\varepsilon}]^{-1}\begin{pmatrix} -\xi\tau \\ \eta\tau \\ \xi^2+\eta^2 \end{pmatrix}\end{aligned} \tag{4.37}$$

Expression (4.37) therefore simplifies the evaluation of the residues of the integral on η in (4.25) at poles $\pm\zeta_*^\varepsilon(\xi)$. This second computation method thus yields

$$v_j^\varepsilon(x_j, y_j) = \frac{i}{4\pi}e^{2i\varepsilon}\int_{\mathbb{R}} e^{ix_j\xi}\sum_{*=L,TH,TV} e^{i|y_j|\zeta_*^\varepsilon(\xi)}\mathbf{M}_*^\varepsilon(\xi, \operatorname{sgn} y_j)\Sigma_j(\xi)\,d\xi \tag{4.38}$$

where $\mathbf{M}_\mathbf{L}^\varepsilon(\xi, t)$, is given by (4.34a) and

$$\mathbf{M}_\mathbf{TV}^\varepsilon(\xi, t) = \begin{pmatrix} \frac{\xi^2\tau^2}{\zeta_T^\varepsilon(\xi^2+\zeta^2)} & \frac{t\xi\tau^2}{\xi^2+\zeta_T^{\varepsilon 2}} & \frac{-\xi\tau}{\zeta_T^\varepsilon} \\ \frac{t\xi\tau^2}{\xi^2+\zeta_T^{\varepsilon 2}} & \frac{\zeta_T^\varepsilon\tau^2}{\xi^2+\zeta_T^{\varepsilon 2}} & -t\tau \\ \frac{-\xi\tau}{\zeta_T^\varepsilon} & -t\tau & \frac{\xi^2+\zeta_T^{\varepsilon 2}}{\zeta_T^\varepsilon} \end{pmatrix} \tag{4.39a}$$

$$\mathbf{M}_\mathbf{TH}^\varepsilon(\xi, t) = \left(1 + \frac{\tau^2}{\xi^2+\zeta_T^{\varepsilon 2}}\right)\begin{pmatrix} \zeta_T^\varepsilon & -t\xi & 0 \\ -t\xi & \frac{\xi^2}{\zeta_T^\varepsilon} & 0 \\ 0 & 0 & 0 \end{pmatrix} \tag{4.39b}$$

Note that $\mathbf{M}_\mathbf{T}^\varepsilon = \mathbf{M}_\mathbf{TH}^\varepsilon + \mathbf{M}_\mathbf{TV}^\varepsilon$. Expressions (4.33) and (4.38) are equivalent.

Integral (4.33) or (4.38) is well defined for $\operatorname{Im}\zeta_*^\varepsilon > 0$, so that the exponential in the integral decreases with the distance y_j. The branch cut for the square root

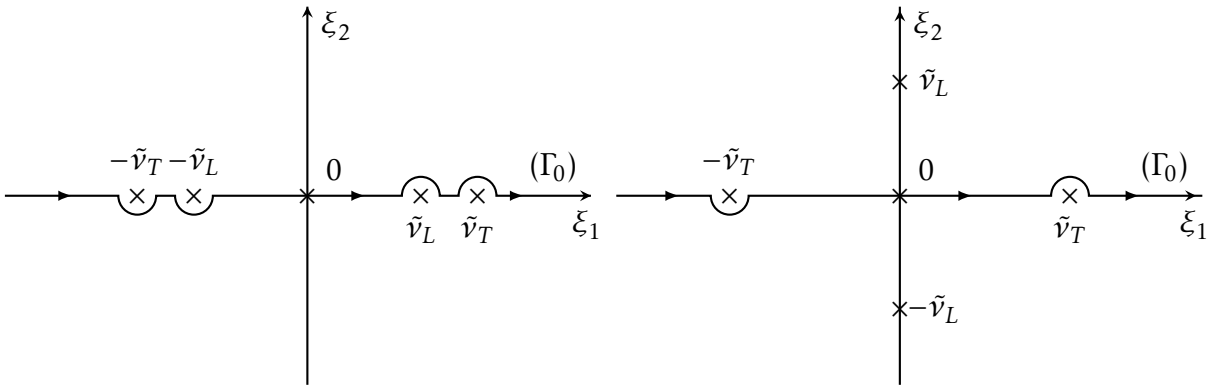

(a) Contour Γ_0 in the case where $\tilde{\nu}_L \in \mathbb{R}$ (b) Contour Γ_0 in the case where $\tilde{\nu}_L \in i\mathbb{R}$

Figure 4.2 – Contour Γ_0 in the complex plane $\xi = \xi_1 + i\xi_2$

in the definition of ζ_*^ε (4.32) is therefore defined by:

$$\zeta_*^\varepsilon = \begin{cases} i\sqrt{\xi^2 - \tilde{\nu}_*^{\epsilon 2}} & \text{if} \quad |\xi| \geq |\tilde{\nu}_*^\epsilon| \\ -\sqrt{\tilde{\nu}_*^{\epsilon 2} - \xi^2} & \text{if} \quad |\xi| < |\tilde{\nu}_*^\epsilon| \end{cases} \tag{4.40}$$

For values of $\varepsilon \in]0, \pi[$, the integration contour never crosses the branch points of ζ_*^ε, which are located at $\pm\tilde{\nu}_*^\varepsilon$ ($\tilde{\nu}_*^\varepsilon$ is given by (4.27)), outside of the real axis.

According to Croisille et Lebeau [52], convergence in the 2D case is verified for $\varepsilon \to 0$. We will suppose that this is still the case in 3D. The integration contour $\mathbb{R}$ is deformed into contour Γ_0, visible on Fig. 4.2a in the case where $\tilde{\nu}_L^0 \in \mathbb{R}$, described in (4.30) and on Fig. 4.2b in the other case, described in (4.31). Physically, if we define a critical angle for diffraction δ_c by $\sin\delta_c = \frac{v_L}{v_T}$, then the case described in (4.30) corresponds to the case where the incident skew angle (the angle between the incident wave vector and the plane normal to the wedge edge) is lower than the critical angle. On the contrary, the case described by (4.31) corresponds to the case where the incident skew angle is higher than this critical angle and, according to Snell's law of diffraction (4.10), there is no diffracted longitudinal wave. In both cases, the branch points of the integrand are avoided.

In all the following, superscript $\varepsilon = 0$ will be omitted in order to alleviate notations. Finally:

$$v_j(x_j, y_j) = \frac{i}{4\pi} \int_{\Gamma_0} e^{ix_j\xi} \sum_{*=L,T} e^{i|y_j|\zeta_*(\xi)} \mathbf{M}_*(\xi, \operatorname{sgn} y_j) \Sigma_j(\xi)\, d\xi \tag{4.41}$$

Integral formulation (4.41) is an expression of the solution in terms of the

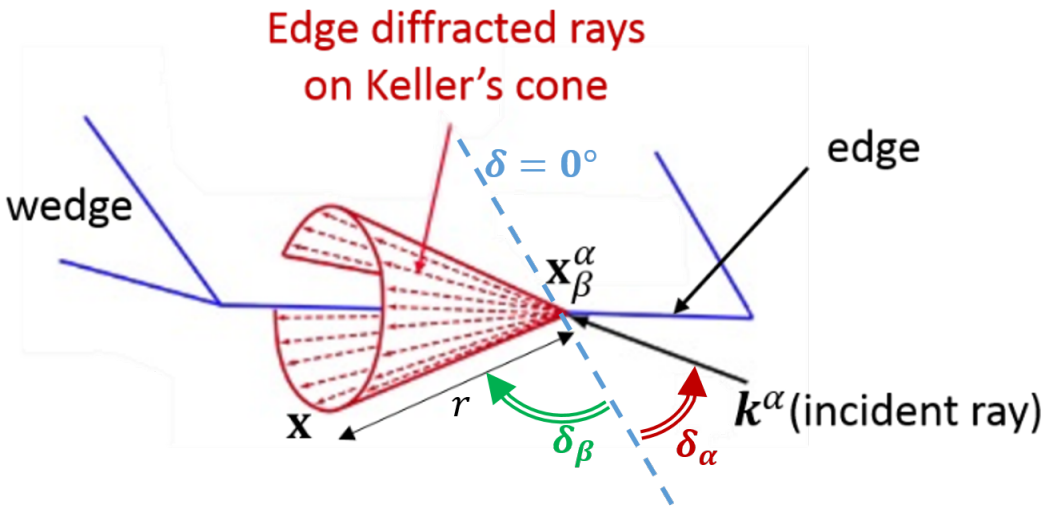

Figure 4.3 – Keller's cone of diffraction

unknown spectral function Σ_j. In the next section, a far-field approximation of this integral is derived and the diffraction coefficient is defined.

4.2.3 Far field approximation

$x = (x_1', y_1', z_1') = (r\cos\theta\cos\delta_\beta, r\sin\theta\cos\delta_\beta, -r\sin\delta_\beta)$ is an observation point, indexed by its spherical coordinates, visible on Fig. 4.1. In order for the diffracted field to be observable at this point, x is located on one of Keller's cones of diffraction, visible on Fig. 4.3. The observation skew angle δ_β is set by Snell's law of diffraction (4.10).

According to (4.9), the scattered field at point P is :

$$u_0(x_1', y_1', z_1') = v(\frac{\omega}{c_L} r\cos\theta\cos\delta_\beta, \frac{\omega}{c_L} r\sin\theta\cos\delta_\beta) e^{-ik_\beta \sin\delta_\beta z_1'} \tag{4.42}$$

The far field parameter is $R = \frac{\omega r}{c_L}$. The aim is to determine the asymptotic behavior of $v(R\cos\theta\cos\delta_\beta, R\sin\theta\cos\delta_\beta)$ when $R \to +\infty$. The first step is to apply the following change of variables in integral v_1, given by (4.33) :

$$\begin{aligned} \xi &= \tilde{\nu}_* \cos\lambda \\ d\xi &= -\tilde{\nu}_* \sin\lambda \, d\lambda \end{aligned} \tag{4.43}$$

yielding, when $\tilde{\nu}_L \in \mathbb{R}$

$$v_1(r,\theta,\delta_\beta) = \frac{i}{4\pi}\int_{C_0}\sum_{*=L,T}\tilde{\nu}_*^2 e^{i\tilde{\nu}_* R\cos\delta_\beta\cos(\lambda+\bar{\theta})}\mathbf{P}_*(\lambda,t)\Sigma_1(\tilde{\nu}_*\cos\lambda)\,d\lambda \tag{4.44}$$

where $\bar{\theta}$ has been defined in the second chapter of this manuscript by (2.21) and

$$\mathbf{P_L}(\lambda,t) = \begin{pmatrix} \cos^2\lambda & -t\cos\lambda\sin\lambda & \frac{\tau}{\tilde{\nu}_L}\cos\lambda \\ -t\cos\lambda\sin\lambda & \sin^2\lambda & -t\frac{\tau}{\tilde{\nu}_L}\sin\lambda \\ \frac{\tau}{\tilde{\nu}_L}\cos\lambda & -t\frac{\tau}{\tilde{\nu}_L}\sin\lambda & \frac{\tau^2}{\tilde{\nu}_L^2} \end{pmatrix} \tag{4.45}$$

and

$$\mathbf{P_T}(\lambda,t) = \begin{pmatrix} \sin^2\lambda + \frac{\tau^2}{\tilde{\nu}_T^2} & t\cos\lambda\sin\lambda & -\frac{\tau}{\tilde{\nu}_T}\cos\lambda \\ t\cos\lambda\sin\lambda & \cos^2\lambda + \frac{\tau^2}{\tilde{\nu}_T^2} & t\frac{\tau}{\tilde{\nu}_T}\sin\lambda \\ -\frac{\tau}{\tilde{\nu}_T}\cos\lambda & t\frac{\tau}{\tilde{\nu}_T}\sin\lambda & 1 \end{pmatrix} \tag{4.46}$$

$t = \operatorname{sgn}\sin\theta$ and contour C_0 is visible on Fig. 4.4. Note that contour C_0 does not fit exactly on the $\frac{\pi}{2}$-spaced grid in represented in the complex plane. This corresponds to adding an infinitely small imaginary part to the axis Γ_0 represented in Fig. 4.2, in order to avoid the branch points $\xi = \pm\tilde{\nu}_*$ located at $\lambda = 0$ and $\lambda = \pi$, where λ is given by (4.43).

In the case defined by (4.31), let us define η_L in the following manner :

$$\tilde{\nu}_L = i\eta_L, \quad \eta_L \in \mathbb{R} \tag{4.47}$$

Variable change (4.43) then yields :

$$\begin{aligned} \xi &= \tilde{\nu}_L\cos\lambda = i\eta_L\cos(\lambda_1 + i\lambda_2) \\ &= \eta_L(\sin\lambda_1\sinh\lambda_2 + i\cos\lambda_1\cosh\lambda_2) \end{aligned} \tag{4.48}$$

The integration contour on ξ, Γ_0, follows the real axis, except near the branch point $\pm\nu_*$. The new contour integration contour C_0^L on λ (determined by variable change (4.48)), thus verifies :

$$\operatorname{Im}(\xi) = 0 \iff \cos\lambda_1 = 0 \iff \lambda_1 = \pm\frac{\pi}{2} \tag{4.49}$$

When ξ travels along Γ_0, going from $-\infty$ to $+\infty$, then, according to (4.48) and (4.49), λ_2 goes from $-\infty$ to $+\infty$ or vice-versa, depending on the sign of λ_1. For

example, if $\lambda_1 = -\frac{\pi}{2}$, then

$$\xi \to -\infty \iff \sin\lambda_1 \sinh\lambda_2 + i\cos\lambda_1 \cosh\lambda_2 = -\sinh\lambda_2 \to -\infty \iff \lambda_2 \to +\infty \tag{4.50}$$

The final step to determining contour C_0^L is therefore to determine the sign of λ_1. Suppose that $\lambda_1 = -\frac{\pi}{2}$, then applying variable change (4.43) in integral formulation (4.33) produces an evanescent term :

$$\begin{aligned} v_1(r,\theta,\delta_\beta) = &-\frac{i}{4\pi}\int_{C_0^L} \eta_L^2 e^{-\eta_L R\cos\delta\cos(\lambda+\bar{\theta})}\mathbf{P_L}(\lambda,t)\Sigma_1(i\eta_L\cos\lambda)\,d\lambda \\ &+\frac{i}{4\pi}\int_{C_0} \tilde{\nu}_T^2 e^{i\tilde{\nu}_T R\cos\delta\cos(\lambda+\bar{\theta}))}\mathbf{P_T}(\lambda,t)\Sigma_1(\tilde{\nu}_T\cos\lambda)\,d\lambda \end{aligned} \tag{4.51}$$

where contour C_0^L is visible on Fig. 4.4. The exponential term in the first integral of (4.51) is $e^{-\eta_L R\cos\delta\cos(\lambda+\bar{\theta})}$. In order to determine the behavior of this term when $R \to +\infty$, the sign of the other terms in the exponential must be determined. Knowing $\eta_L > 0$ and $\cos\delta > 0$, it remains to determine the sign of $\cos(\lambda+\bar{\theta})$. For $\lambda \in C_0^L$, we have :

$$\lambda = -\frac{\pi}{2} + i\lambda_2 \tag{4.52}$$

This yields

$$\cos(\lambda+\bar{\theta}) = \cos(\bar{\theta}-\frac{\pi}{2})\cosh\lambda_2 - i\sin(\bar{\theta}-\frac{\pi}{2})\sinh\lambda_2 \tag{4.53}$$

Having $\bar{\theta} \in [0,\pi]$, we have $\cos(\bar{\theta}-\frac{\pi}{2}) = \sin\bar{\theta} \geq 0$ and

$$|e^{-\eta_L R\cos\delta\cos(\lambda+\bar{\theta})}| = e^{-\eta_L R\cos\delta\sin\bar{\theta}\cosh\lambda_2} \tag{4.54}$$

The amplitude of the integrand in the first integral of (4.51) decreases exponentially as the distance from the edge grows. On the contrary, if $\lambda_1 = \frac{\pi}{2}$, then we would have :

$$\cos(\lambda+\bar{\theta}) = \cos(\bar{\theta}+\frac{\pi}{2})\cosh\lambda_2 - i\sin(\bar{\theta}+\frac{\pi}{2})\sinh\lambda_2 \tag{4.55}$$

and

$$|e^{-\eta_L R\cos\delta\cos(\lambda+\bar{\theta})}| = e^{\eta_L R\cos\delta\sin\bar{\theta}\cosh\lambda_2} \tag{4.56}$$

The amplitude of the integrand in the first integral of (4.51) would then increase exponentially as the distance from the edge grows, which is physically impossible.

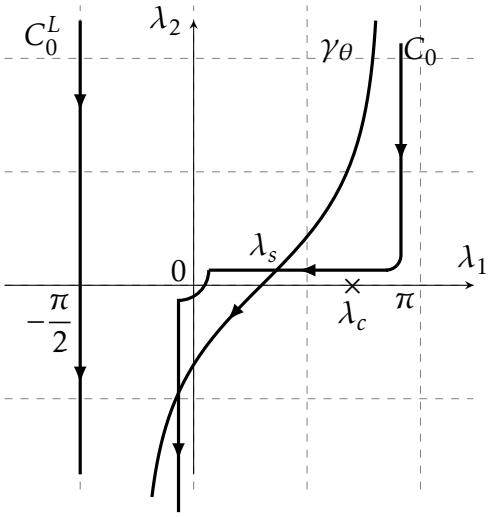

Figure 4.4 – Contours C_0, C_0^L and γ_θ in the complex plane $\lambda = \lambda_1 + i\lambda_2$. The stationary phase points are noted λ_s.

Therefore, C_0^L, visible on Fig. 4.4, is defined by

$$C_0^L = -\frac{\pi}{2} - i\mathbb{R} \tag{4.57}$$

The far-field evaluation of the integral is obtained by applying the steepest descent method, presented in appendix A, to (4.44). To do so, contour C_0 is deformed into contour γ_θ, also visible in Fig. 4.4. In the case $\tilde{v}_L \in \mathbb{R}$, this leads to

$$v_1 = v_1^{sing} + v_1^{diff} \tag{4.58}$$

where v_1^{sing} is the contribution of all the singularities of the spectral functions crossed during the deformation from C_0 to γ_θ, corresponding to the reflected waves (for the poles of the spectral functions) and head waves (for the branch points λ_c of the function v_1), and v_1^{diff} is the contribution of the stationary phase point $\lambda_s = \pi - \overline{\theta}$, corresponding to the edge-diffracted wave and computed using (A.4). In the following, it is assumed that the saddle point λ_s does not coalesce with a branch point. The branch points of functions v_j, $j = 1, 2$ are located at $\xi = \pm\tilde{v}_L$ and $\xi = \pm\tilde{v}_T$. Applying (4.43), this means that :

$$\tilde{v}_* \cos\lambda_s = -\tilde{v}_* \cos\theta = \pm\tilde{v}_L \tag{4.59a}$$

$$\text{or} \quad \tilde{v}_* \cos\lambda_s = -\tilde{v}_* \cos\theta = \pm\tilde{v}_T \tag{4.59b}$$

For $* = L$, (4.59a) yields $\theta = 0$ or $\theta = \pi$, meaning that the direction of observation is grazing along the wedge's horizontal face $\mathcal{S}_1$. (4.59b) does not have a real solution for $* = L$. For $* = T$, (4.59a) yields $\theta = \theta_c = \text{acos}(\tilde{v}_\text{L}/\tilde{v}_\text{T})$ or $\theta = \pi - \theta_c$, θ_c is called the critical angle for reflection, and (4.59b) yields $\theta = 0$ or $\theta = \pi$. Borovikov [68] gives some clues as to how to treat the case where the stationary phase point coincides with another singularity of the integrand but no high-frequency asymptotics prove satisfactory in some situations of practical interest [69] and are neither available when the critical transition zones overlap penumbras, that is when all three critical points (stationary, critical and pole) coalesce [70]. In the present work, only the contribution of the edge-diffracted waves will be computed. In order to simplify notations, we will note $\mathbf{P}_*(\lambda, 1) = \mathbf{P}_*(\lambda)$, using the fact that $t = \pm 1$ and $\mathbf{P}_*(\lambda, -1) = \mathbf{P}_*(-\lambda)$). The contribution of diffracted waves is

$$v_1^{diff}(r, \theta, \delta_\beta) = \frac{e^{-i\pi/4}}{2\sqrt{2\pi}} \sum_{*=L,T} \tilde{v}_*^2 \frac{e^{-i\tilde{v}_* R\cos\delta_\beta}}{\sqrt{\tilde{v}_* R\cos\delta_\beta}} \mathbf{P}_*(\pi - \theta)\Sigma_1(-\tilde{v}_*\cos\theta) \tag{4.60}$$

Analogously,

$$v_2^{diff}(r, \varphi - \theta, \delta_\beta) = \frac{e^{-i\pi/4}}{2\sqrt{2\pi}} \sum_{*=L,T} \tilde{v}_*^2 \frac{e^{-i\tilde{v}_* R\cos\delta_\beta}}{\sqrt{\tilde{v}_* R\cos\delta_\beta}} \mathbf{P}_*(\pi - (\varphi - \theta))\Sigma_1(-\tilde{v}_*\cos(\varphi - \theta)) \tag{4.61}$$

In the case where $\tilde{v}_L = i\eta_L \in i\mathbb{R}$, the far-field evaluation is obtained by applying the steepest descent method, presented in appendix A, to (4.51). Contour C_0 is deformed into contour γ_θ and contour C_0^L is deformed into contour γ_θ^L. This leads to

$$v_1 = v_1^{sing} + v_1^{diff} + v_1^{evan} \tag{4.62}$$

where v_1^{sing} is the contribution of all the singularities of the spectral functions crossed during the deformation from C_0 to γ_θ corresponding to the reflected waves (for the poles of v_1) and head waves (for the branch points λ_c of the spectral functions, which are determined in the same manner as for the case $\tilde{v}_L \in \mathbb{R}$ detailed above, except that now (4.59a) does not have a real solution for $*$=T), v_1^{diff} is the contribution of the stationary phase point to the integral on C_0, corresponding to the diffracted wave, and v_1^{evan} is the contribution of the integral on C_0^L, which decays exponentially as the far-field parameter R grows, making it an evanescent longitudinal wave. Only the contribution of the transversal diffracted waves will be computed here. Contribution v_1^{diff} is computed using

(A.4) :

$$v_1^{diff}(r,\theta,\delta_\beta) = \frac{e^{-i\pi/4}}{2\sqrt{2\pi}}\tilde{\nu}_T^2 \frac{e^{-i\tilde{\nu}_T R\cos\delta_\beta}}{\sqrt{\tilde{\nu}_T R\cos\delta_\beta}}\mathbf{P_T}(\pi-\theta)\Sigma_1(-\tilde{\nu}_T\cos\theta) \tag{4.63}$$

Analogously,

$$v_2^{diff}(r,\varphi-\theta,\delta_\beta) = \frac{e^{-i\pi/4}}{2\sqrt{2\pi}}\tilde{\nu}_T^2 \frac{e^{-i\tilde{\nu}_T R\cos\delta_\beta}}{\sqrt{\tilde{\nu}_T R\cos\delta_\beta}}\mathbf{P_T}(\pi-(\varphi-\theta))\Sigma_2(-\tilde{\nu}_T\cos(\varphi-\theta)) \tag{4.64}$$

In any case, the total diffracted field is

$$v^{diff} = v_1^{diff} + v_2^{diff} \tag{4.65}$$

Let us now isolate L, TH and TV diffracted waves in order to compute the corresponding diffraction coefficients, defined by

$$v_\beta^{diff}(r,\theta,\delta_\beta) = D_\beta^\alpha(\theta)\frac{e^{-i\tilde{\nu}_\beta R\cos\delta_\beta}}{\sqrt{\tilde{\nu}_\beta R\cos\delta_\beta}}v^{inc}(r\cos\theta, r\sin\theta)\hat{i}_\beta \tag{4.66}$$

Using the expressions of the unit vectors given by (4.4), the β diffracted wave is given by $v^{diff}\cdot\hat{i}_\beta$. This yields :

$$D_\beta^\alpha(\theta) = \frac{e^{-i\pi/4}}{2\sqrt{2\pi}}\sum_{j=1,2}\tilde{\nu}_\beta^{2\,t}\Sigma_j(-\tilde{\nu}_\beta\cos\theta_j)\cdot\left(\mathbf{P}_\beta(\pi-\theta_j).\hat{i}_\beta\right) \tag{4.67}$$

where $\theta_1 = \theta$ and $\theta_2 = \varphi - \theta$.

In order to determine the field diffracted by a wedge illuminated by an incident plane wave, it is sufficient to compute the diffraction coefficient. This coefficient has been expressed in terms of two unknown functions called the spectral functions. The semi-analytical computation of these functions is presented in the following section

4.3 Semi-analytical evaluation of the spectral functions

The first step in computing the spectral functions is to determine a system of functional equations of which they are a solution. We will then show that these functions can be decomposed into two parts : a singular function, computed

analytically, and a regular function, approached numerically.

4.3.1 Functional equations

In the previous section, the diffracted wave has been expressed in terms of two unknown functions called the spectral functions. In this subsection, a system of functional equations satisfied by these functions is determined.

The first step in determining a system of functional equations verified by the spectral functions, is to substitute decomposition (4.17) into the boundary conditions :

$$\begin{cases} B\Big(v_1(x_1,0)+v_2(x_2\cos\varphi,x_2\sin\varphi)\Big) = -B\mathrm{v}_\alpha^{\mathrm{inc}}|_{\mathcal{S}_1} \\ B\Big(v_2(x_2,0)+v_1(x_1\cos\varphi,x_1\sin\varphi)\Big) = -B\mathrm{v}_\alpha^{\mathrm{inc}}|_{\mathcal{S}_2} \end{cases} \tag{4.68}$$

Let us note (v_j^1, v_j^2, v_j^3) the coordinates of v_j in the Cartesian coordinate system (x_j, y_j, z_j), where (x_1, y_1, z_1) is the coordinate system associated with face $\mathcal{S}_1$ and (x_2, y_2, z_2) is the coordinate system associated with face $\mathcal{S}_2$. These two coordinate systems are linked by (for $j = 1, 2$):

$$\begin{cases} x_j = \cos\varphi.x_{3-j} + \sin\varphi.y_{3-j} \\ y_j = \sin\varphi.x_{3-j} - \cos\varphi.y_{3-j} \\ z_j = z_{3-j} \end{cases} \tag{4.69}$$

Applying (4.69) to each line of (4.68) yields:

$$\begin{cases} B_1(v_1) + B_2(v_2) = -Bv_\alpha^{inc}|_{\mathcal{S}_1} \\ B_1(v_2) + B_2(v_1) = -Bv_\alpha^{inc}|_{\mathcal{S}_2} \end{cases} \tag{4.70}$$

where

$$B_1(v) = \begin{pmatrix} \mu\Big(\frac{\partial v_1}{\partial y_1} + \frac{\partial v_2}{\partial x_1}\Big) \\ \frac{\partial v_2}{\partial y_1} + \lambda\Big(\frac{\partial v_1}{\partial x_1} + \frac{\partial v_3}{\partial z_1}\Big) \\ \mu\Big(\frac{\partial v_2}{\partial z_1} + \frac{\partial v_3}{\partial y_1}\Big) \end{pmatrix} \tag{4.71}$$

and

$$B_2(v) = \begin{pmatrix} \mu\sin(2\varphi)\Big(\frac{\partial v_1}{\partial x_2} - \frac{\partial v_2}{\partial y_2}\Big) - \mu\cos(2\varphi)\Big(\frac{\partial v_1}{\partial y_2} + \frac{\partial v_2}{\partial x_2}\Big) \\ (\lambda + 2\mu\sin^2\varphi)\frac{\partial v_1}{\partial x_2} + (\lambda + 2\mu\cos^2\varphi)\frac{\partial v_2}{\partial y_2} - \mu\sin(2\varphi)\Big(\frac{\partial v_1}{\partial y_2} + \frac{\partial v_2}{\partial x_2}\Big) + \lambda\frac{\partial v_3}{\partial z_2} \\ \mu\sin\varphi\Big(\frac{\partial v_3}{\partial x_2} + \frac{\partial v_1}{\partial z_2}\Big) - \mu\cos\varphi\Big(\frac{\partial v_2}{\partial z_2} + \frac{\partial v_3}{\partial y_2}\Big) \end{pmatrix} \tag{4.72}$$

Operator B_1 is obtained by projecting $B(v_1)$ onto $\mathcal{S}_1$. This is immediate because v_1 is defined on $\mathcal{S}_1$ and its components (v_1^1, v_1^2, v_1^3) are expressed in the associated

Cartesian coordinate system (x_1, y_1, z_1). Operator B_2 is obtained by projecting $B(v_2)$ onto $\mathcal{S}_1$. This is done by projecting its components (v_2^1, v_2^2, v_2^3) onto $\mathcal{S}_1$ and by expressing (x_1, y_1, z_1) as functions of (x_2, y_2, z_2), as v_2 is only defined on $\mathcal{S}_2$. This is done using (4.69). The second equation of system (4.70) is obtained in a similar manner, where the roles of v_1 and v_2 are reversed.

The functional equations system solved by the spectral functions is obtained by substituting the integral formulation (4.41) of v_1 and v_2 into (4.70), evaluating the first equation at $x_1 \geq 0, y_1 = 0$ and the second at $x_2 \geq 0, y_2 = 0$ and applying the Fourier transform, defined by (3.18) to the result. This yields :

$$\begin{aligned} \int_0^{+\infty} e^{-ix\xi} B_1(v_1)(x)\, dx &= \frac{1}{2}\mathbf{DM}(\Sigma_1)(\xi) \\ &= \frac{1}{2}\int_{\Gamma_0} \mathbf{DM}(\xi,\zeta)\Sigma_1(\zeta)\, d\zeta \end{aligned} \tag{4.73}$$

where

$$\begin{aligned} \mathbf{DM}(\xi,\zeta) &= \frac{1}{2i\pi}\frac{1}{\xi-\zeta}\mathbf{dm}(\zeta) \\ &= \frac{1}{2i\pi}\frac{1}{\xi-\zeta}\begin{pmatrix} -1 & \frac{\zeta}{\zeta_T}(1-2\mu Q(\zeta)) & 0 \\ -\frac{\zeta}{\zeta_L}(1-2\mu Q(\zeta)) & -1 & -\frac{\tau}{\zeta_L}(1-2\mu Q(\zeta)) \\ 0 & \frac{\tau}{\zeta_T}(1-2\mu Q(\zeta)) & -1 \end{pmatrix}, \end{aligned} \tag{4.74}$$

$\zeta_*, * = L, T$ are defined by taking $\varepsilon = 0$ in (4.32) and

$$Q(\zeta) = \zeta_L\zeta_T + \zeta^2 + \tau^2 \tag{4.75}$$

The evaluation of $B_2(v_2)$ at $x_1 \geq 0, y_1 = 0$ is the evaluation of $B_2(v_2)$ at $x_2 = x\cos\varphi, y_2 = x\sin\varphi, x \geq 0$. The Fourier transform of the second term is therefore

$$\begin{aligned} \int_0^{+\infty} e^{-ix\xi} B_2(v_2)(x)\, dx &= \frac{1}{2}\mathbf{TM}(\Sigma_2)(\xi) \\ &= \frac{1}{2}\int_{\Gamma_0} \mathbf{TM}(\xi,\zeta)\Sigma_2(\zeta)\, d\zeta \end{aligned} \tag{4.76}$$

where

$$\mathbf{TM}(\xi,\zeta) = \frac{1}{2i\pi}\sum_{*=L,TH,TV} D_*(\xi,\zeta)\mathbf{tm}_*(\zeta, \operatorname{sgn}\sin\varphi), \tag{4.77}$$

$$D_*(\xi,\zeta) = \frac{1}{\xi - (\zeta\cos\varphi + \zeta_*(\zeta)|\sin\varphi|)} \tag{4.78}$$

We note ϵ =sgn sin φ, and the following matrices of rank 1 are defined :

$$\begin{cases} \mathbf{tm}_L(\zeta) = \left[\frac{\zeta}{\zeta_L} f_L\,;\, \epsilon f_L\,;\, \frac{\tau}{\zeta_L} f_L\right] \\ f_L = \begin{pmatrix} \mu[\cos(2\varphi)(2\epsilon\zeta\zeta_L) - \sin(2\varphi)(\zeta^2 - \zeta_L^2)] \\ -\lambda + 2\mu[\sin(2\varphi)(\epsilon\zeta\zeta_L) - \zeta^2\sin^2\varphi - \zeta_L^2\cos^2\varphi] \\ -2\mu\tau[\zeta\sin\varphi - \epsilon\zeta_L\cos\varphi] \end{pmatrix}, \end{cases} \tag{4.79}$$

$$\begin{cases} \mathbf{tm}_{TH}(\zeta) = [-t f_{TH}\,;\, \frac{\zeta}{\zeta_T} f_{TH}\,;\, 0] \\ f_{TH} = \mu\left(1 + \frac{\tau^2}{\zeta^2+\zeta_T^2}\right)\begin{pmatrix} \sin(2\varphi)(2\epsilon\zeta\zeta_T) + \cos(2\varphi)(\zeta^2 - \zeta_T^2) \\ \sin(2\varphi)(\zeta^2 - \zeta_T^2) - \cos(2\varphi)(2\epsilon\zeta\zeta_T) \\ \tau[\epsilon\zeta_T\sin\varphi + \zeta\cos\varphi] \end{pmatrix} \end{cases} \tag{4.80}$$

and

$$\begin{cases} \mathbf{tm}_{TV}(\zeta) = [\frac{\zeta\tau}{\zeta_T(\zeta^2+\zeta_T^2)} f_{TV}\,;\, \frac{\epsilon\tau}{\zeta^2+\zeta_T^2} f_{TV}\,;\, -\frac{1}{\zeta_T} f_{TV}] \\ f_{TV} = \mu\begin{pmatrix} \tau\cos(2\varphi)(2\epsilon\zeta\zeta_T) - \tau\sin(2\varphi)(\zeta^2 - \zeta_T^2) \\ 2\tau[\sin(2\varphi)(\epsilon\zeta\zeta_T) - \zeta^2\sin^2\varphi - \zeta_T^2\cos^2\varphi] \\ \left(\tau^2 - \zeta^2 + \zeta_T^2\right)[\epsilon\zeta_T\cos\varphi - \zeta\sin\varphi] \end{pmatrix} \end{cases} \tag{4.81}$$

In the following, let us note for simplification:

$$\mathbf{tm}_T = \mathbf{tm}_{TH} + \mathbf{tm}_{TV} \tag{4.82}$$

It has been checked that setting $\tau = 0$ in the explicit expressions of **DM** and **TM** operators leads to the same expressions as those found in the previous chapter, concerning the 2D case.

Finally, the Fourier transform of the boundary conditions on the wedge faces is obtained by summing (4.73) and (4.76). The right-hand side of the system is obtained by taking the Fourier transform of $-Bv_\alpha^{inc}|_{\mathcal{S}_j}$, $j = 1, 2$, where B is defined by (4.14) and the incident field is given by (4.15). The final system of functional equations solved by the spectral functions is

$$\begin{cases} \mathbf{DM}(\Sigma_1) + \mathbf{TM}(\Sigma_2) = \dfrac{W_1^\alpha}{\xi - \nu_\alpha\cos\theta_{inc}\cos\delta_{inc}} \\ \mathbf{TM}(\Sigma_1) + \mathbf{DM}(\Sigma_2) = \dfrac{W_2^\alpha}{\xi - \nu_\alpha\cos(\varphi - \theta_{inc})\cos\delta_{inc}} \end{cases} \tag{4.83}$$

where

$$W_1^L = -2\begin{pmatrix} \mu\cos^2\delta_{inc}\sin(2\theta_{inc}) \\ 1-2\mu(\cos^2\theta_{inc}\cos^2\delta_{inc}+\sin^2\delta_{inc}) \\ \mu\sin(2\delta_{inc})\sin(\theta_{inc}) \end{pmatrix}$$

$$W_2^L = -2\begin{pmatrix} \mu\cos^2\delta_{inc}\sin(2\varphi-2\theta_{inc}) \\ 1-2\mu(\cos^2(\varphi-\theta_{inc})\cos^2\delta_{inc}+\sin^2\delta_{inc}) \\ \mu\sin(2\delta_{inc})\sin(\varphi-\theta_{inc}) \end{pmatrix}$$

$$W_1^{TV} = 2\nu_T\mu\begin{pmatrix} \frac{1}{2}\sin(2\theta_{inc})\sin(2\delta_{inc}) \\ \sin(2\delta_{inc})\sin^2\theta_{inc} \\ -\sin\theta_{inc}\cos(2\delta_{inc}) \end{pmatrix} \quad W_2^{TV} = 2\nu_T\mu\begin{pmatrix} \frac{1}{2}\sin(2\varphi-2\theta_{inc})\sin(2\delta_{inc}) \\ \sin(2\delta_{inc})\sin^2(\varphi-\theta_{inc}) \\ -\sin(\varphi-\theta_{inc})\cos(2\delta_{inc}) \end{pmatrix} \tag{4.84}$$

$$W_1^{TH} = -2\nu_T\mu\begin{pmatrix} \cos\delta_{inc}\cos(2\theta_{inc}) \\ \sin(2\theta_{inc})\cos\delta_{inc} \\ \cos\theta_{inc}\sin\delta_{inc} \end{pmatrix} \quad W_2^{TH} = 2\nu_T\mu\begin{pmatrix} \cos\delta_{inc}\cos(2\varphi-2\theta_{inc}) \\ \sin(2\varphi-2\theta_{inc})\cos\delta_{inc} \\ \cos(\varphi-\theta_{inc})\sin\delta_{inc} \end{pmatrix}$$

Thanks to these functional equations, the spectral functions can be decomposed into two parts : a singular function and a regular function. The evaluation of each of these parts is described in the following.

4.3.2 Singular part

The first step in evaluating the spectral functions is to determine their poles and corresponding residues. As in the previous chapters, this is done by a recursive procedure, using the following translation function which appears in (4.78) (for $* = L, T$) :

$$T_*(\xi = \tilde{\nu}_*\cos\theta) = \xi\cos\varphi + \zeta_*(\xi)\sin\tilde{\varphi} = \tilde{\nu}_*\cos(\theta+\tilde{\varphi}) \tag{4.85}$$

where $\tilde{\varphi}$ is defined in the second chapter of this manuscript, by (2.48). This translation operator is defined on subspace Ω_*^+, represented on Fig. 4.5 :

$$\xi \in \Omega_*^+ = \{\xi = \tilde{\nu}_*\cos\theta,\ 0 \le \mathrm{Re}\theta < \pi - \tilde{\varphi}\} \tag{4.86}$$

In order to determine the action of operator **DM** on a simple pole z, $\mathrm{Im}z \ge 0$ (as it has been done in previous chapters in equations (2.52a) and (3.63)) contour Γ_0 in (4.73) is deformed into contour Γ_1. Contour Γ_1 is visible in Fig. 4.6 for the case $\tilde{\nu}_L \in \mathbb{R}$ and Cauchy's residue theorem can then be applied for $\mathrm{Im}z \ge 0$, $\mathrm{Im}\xi < 0$ with $z \in \mathbb{C}\backslash(]-\infty, -\tilde{\nu}_L] \cup \{\pm\tilde{\nu}_L, \pm\tilde{\nu}_T\})$.

In the case $\tilde{\nu}_L \in i\mathbb{R}$, contour Γ_1 is visible in Fig. 4.7. Fig. 4.7a shows an intermediate step in the contour deformation from Γ_0 to Γ_1. The arrow shows the

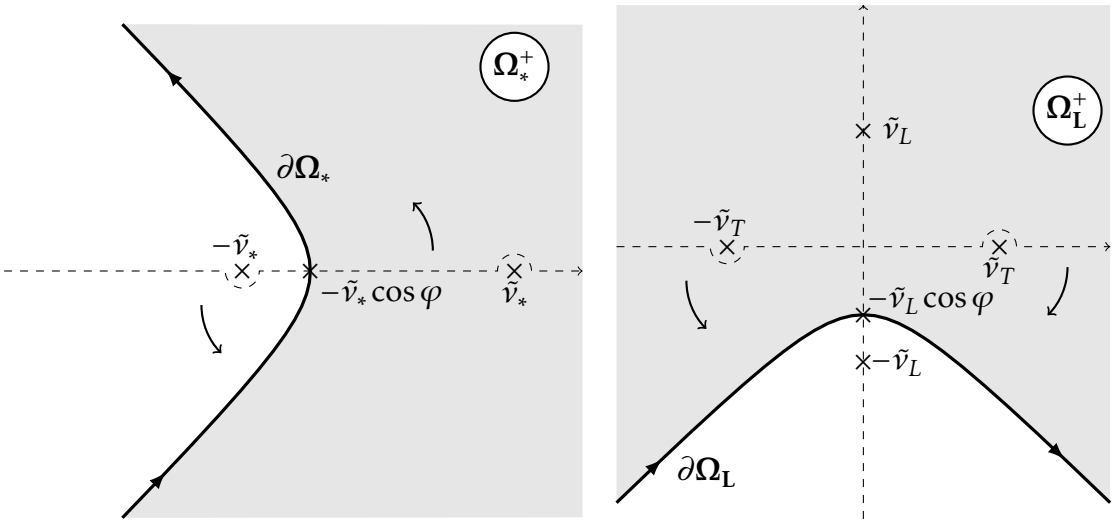

(a) Contour $\partial\Omega_*$ and domain Ω_*^+ in the case $\tilde{\nu}_L \in \mathbb{R}$. The curved arrows show deformation of contour Γ_0 onto $\partial\Omega_*$.

(b) Contour $\partial\Omega_L$ and domain Ω_L^+ in the case $\tilde{\nu}_L \in i\mathbb{R}$. The curved arrows show deformation of contour Γ_0 onto $\partial\Omega_L$.

Figure 4.5 – Domains Ω_* and contours $\partial\Omega_*$ in cases $\tilde{\nu}_L \in \mathbb{R}$ and $\tilde{\nu}_L \in i\mathbb{R}$.

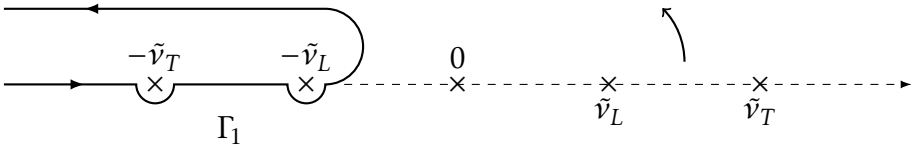

Figure 4.6 – Contour Γ_1 in the case $\tilde{\nu}_L \in \mathbb{R}$. The arrow shows the deformation of contour Γ_0 into Γ_1.

direction of deformation of the quarter-cycle which links the two parts of Γ_1 (one which circumvents $[-\infty, -\tilde{\nu}_T[$ and one which circumvents $]\tilde{\nu}_L, +i\infty]$) in Fig. 4.7a. The radius of this quarter-cycle tends to infinity during the deformation, resulting in the final contour, which is the reunion of contours Γ_1^a and Γ_1^b, represented in Fig. 4.7b. Cauchy's residue theorem can then be applied for $z \geq 0$, $\mathrm{Im}\xi < 0$ and $z \in \mathbb{C}\backslash(]-\infty, -\tilde{\nu}_T] \cup [\tilde{\nu}_L, +i\infty[\cup \{\pm\tilde{\nu}_L, \pm\tilde{\nu}_T\})$. In both cases ($\tilde{\nu}_L \in \mathbb{R}$ and $\tilde{\nu}_L \in i\mathbb{R}$), application of the residue theorem yields :

$$\int_{\Gamma_0} \mathbf{DM}(\xi,\zeta).\frac{1}{\zeta - z}\, d\zeta = \frac{\mathbf{dm}(z)}{\xi - z} + \mathbf{D_p}(z,\xi), \tag{4.87}$$

where

$$\mathbf{D_p}(z,\xi) = \int_{\Gamma_1} \frac{\mathbf{DM}(\xi,\zeta)}{\zeta - z}\, d\zeta \tag{4.88}$$

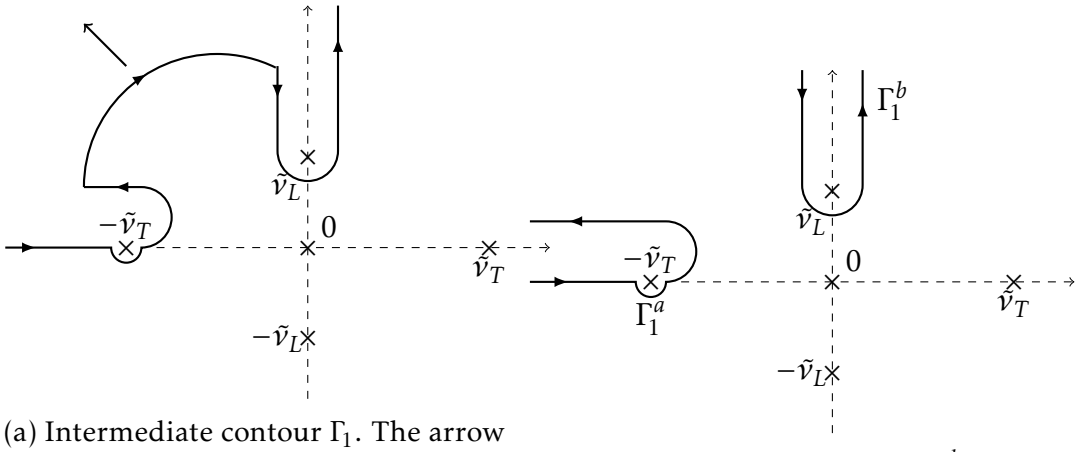

(a) Intermediate contour Γ_1. The arrow shows the direction of the deformation.

(b) Final contour $\Gamma_1 = \Gamma_1^a \cup \Gamma_1^b$

Figure 4.7 – Deformation of contour Γ_0 onto contour $\Gamma_1 = \Gamma_1^a \cup \Gamma_1^b$ in the case $\tilde{\nu}_L \in i\mathbb{R}$.

Similarly, in order to determine the action of operator **TM** on a simple pole z, $\mathrm{Im} z \geq 0$, contour Γ_0 in (4.76) is deformed into contour $\partial\Omega_L$ for the L terms and $\partial\Omega_T$ for the T terms, both of which are visible in Fig. 4.5a for the case $\tilde{\nu}_L \in \mathbb{R}$. Cauchy's residue theorem is applied in that case, yielding, for $\mathrm{Im} z \geq 0$, $\mathrm{Im}\xi < 0$ with $z \in \mathbb{C}\backslash(]-\infty, -\tilde{\nu}_L] \cup \{\pm\tilde{\nu}_L, \pm\tilde{\nu}_T\})$:

$$\int_{\Gamma_0} \mathbf{TM}(\xi,\zeta).\frac{1}{\zeta - z}\, d\zeta = \sum_{*=L,T} \frac{\mathbf{tm}_*(z)}{\xi - T_*(z)} \mathbf{1}_{\Omega_*}(z) + \mathbf{T_p}(z,\xi) \tag{4.89}$$

where $\mathbf{1}_{\Omega_*}(z) = 1$ if $z \in \Omega_*$ and $\mathbf{1}_{\Omega_*}(z) = 0$ elsewhere and

$$\mathbf{T_p}(z,\xi) = \frac{1}{2i\pi} \sum_{*=L,T} \int_{\partial\Omega_*} D_*(\xi,\zeta).\frac{\mathbf{tm}_*(\zeta)}{\zeta - z}\, d\zeta \tag{4.90}$$

In the case where $\tilde{\nu}_L \in i\mathbb{R}$, $\partial\Omega_L$ is visible in Fig. 4.5b. During the deformation of contour Γ_0 into contour $\partial\Omega_L$, the pole z, $\mathrm{Im} z \geq 0$, is not crossed by the contour deformation which only spans a part of the lower half of the complex plane. Therefore, the pole z does not contribute to the integral. However, a pole that may be crossed during this contour deformation (if such a pole exists) is $\zeta_0 \in \Omega_L^+$ such that $T_L(\zeta_0) = \xi$ and $\mathrm{Im}\zeta_0 < 0$. We will now determine in which cases such a pole ζ_0 may appear. This will be done by supposing that ζ_0 exists and deriving some necessary conditions for the existence of ζ_0 to be possible.

Let us therefore suppose that there exists $\theta_0 = \theta_0' + i\theta_0'' \in \mathbb{C}$ such that $\zeta_0 =$

$\tilde{v}_L \cos\theta_0$ and $\xi = T_L(\zeta_0) = \tilde{v}_L \cos(\theta_0 + \tilde{\varphi})$ with $\tilde{v}_L = i\eta_L \in i\mathbb{R}$, we then have :

$$\mathrm{Im}\zeta_0 = \eta_L \cos\theta_0' \cosh\theta_0'' \tag{4.91}$$

Pole ζ_0 is crossed by the deformation of contour Γ_0 into $\partial\Omega_L^+$ (visible on Fig. 4.5b) if and only if $\mathrm{Im}\zeta_0 < 0$ and $\zeta_0 \in \Omega_L^+$, with Ω_L^+ defined by (4.86). These conditions lead to the following condition on θ_0' :

$$\frac{\pi}{2} < \theta_0' < \pi - \tilde{\varphi} \tag{4.92}$$

Condition (4.92) makes sense if and only if

$$\frac{\pi}{2} < \pi - \tilde{\varphi} \Leftrightarrow \tilde{\varphi} < \frac{\pi}{2} \tag{4.93}$$

From hereon after, we will suppose that this is not the case (this restriction is only made when $\tilde{v}_L \in i\mathbb{R}$) and that there is therefore no pole ζ_0 such that $T_L(\zeta_0) = \xi$. In practice, this is not too restrictive (it corresponds to wedge angles $\varphi < \frac{\pi}{2}$ or $\varphi > \frac{3\pi}{2}$) since, as explained in 2.2.2.1, the spectral functions method is less accurate for small values of $\tilde{\varphi}$. Therefore, when $\tilde{v}_L \in i\mathbb{R}$, Cauchy's residue theorem yields, for $\mathrm{Im}z \geq 0$, $\mathrm{Im}\xi < 0$ with $z \in \mathbb{C}\backslash(]-\infty, -\tilde{v}_L] \cup [\tilde{v}_L, +i\infty[\cup \{\pm\tilde{v}_L, \pm\tilde{v}_T\})$:

$$\int_{\Gamma_0} \mathbf{TM}(\xi,\zeta).\frac{1}{\zeta - z}\, d\zeta = \frac{\mathbf{tm}_T(z)}{\xi - T_T(z)} \mathbf{1}_{\Omega_T}(z) + \mathbf{T_p}(z,\xi) \tag{4.94}$$

with $\mathbf{T_p}$ defined by (4.90). The hypotheses $\mathrm{Im}z \geq 0$, $\mathrm{Im}\xi < 0$ is made in all three chapters of this manuscript. $\mathrm{Im}z <\geq 0$ corresponds to the location of the poles of the spectral functions in the complex plane, as will be shown in the following, and $\mathrm{Im}\xi < 0$ simplifies the reasoning as it assures us that z and ξ are in two different half-planes and it allows us later to apply the "propagation of the solution" technique, detailed in 4.3.4.

It is important to note that in all the aforementioned contour deformations, no branch points $\pm\tilde{v}_L$ or $\pm\tilde{v}_T$ of the integrands are crossed (in the deformation represented in Fig. 4.5b, points $\pm\tilde{v}_T$ are crossed but they are different from the branch points of the integrand which are $\pm\tilde{v}_L$). Therefore, it is assumed that Croisille and Lebeau's [52] proof that $\mathbf{D_p}(z,\cdot)$ and $\mathbf{T_p}(z,\cdot)$ belong to a special class of functions $\mathcal{H}^3$ can be adapted to the 3D case. It will therefore be assumed that in the case $\tilde{v}_L \in \mathbb{R}$, $\mathbf{D_p}(z,\cdot) \in \mathcal{H}^3$ and $\mathbf{T_p}(z,\cdot) \in \mathcal{H}^3$ and in the case $\tilde{v}_L \in i\mathbb{R}$, $\mathbf{D_p}(z,\cdot) \in \tilde{\mathcal{H}}^3$ and $\mathbf{T_p}(z,\cdot) \in \mathcal{H}^3$. $\mathcal{H}$ and $\tilde{\mathcal{H}}$ are defined hereafter

Def. 4.3.1. *$\mathcal{H}$ is the space of the functions f analytical in $\mathbb{C}\backslash]-\infty, -\tilde{v}_L]$ such that $\forall\epsilon \in]0,\pi[, f(e^{i\epsilon}\cdot) \in H^+$, where H^+ is defined in Def. 2.2.1.*

Def. 4.3.2. *$\tilde{\mathcal{H}}$ is the space of the functions f analytical in $\mathbb{C}\backslash(]-\infty,-\tilde{\nu}_T]\cup[\tilde{\nu}_L,+i\infty[)$ such that $\forall\epsilon\in]0,\pi[, f(e^{i\epsilon}\cdot)\in H^+$, where H^+ is defined in Def. 2.2.1.*

The recursive procedure used to extract all the poles and corresponding residues of the spectral functions is analogous to the one described in 3.3.2 and will not be repeated here. In the end, we have, for $\mathrm{Im}\xi<0$

$$\Sigma_j(\xi)=Y_j(\xi)+X_j(\xi) \tag{4.95}$$

where, when $\tilde{\nu}_L\in\mathbb{R}$:

$$Y_j(\xi)=\sum_k\sum_{*=L,T}\frac{V_{j,*}^{(k)}}{\xi-Z_{j,*}^{(k)}}, \tag{4.96}$$

with

$$\begin{array}{cc} Z_1^{(0)}=\nu_\alpha\cos\theta_{inc}\cos\delta_{inc}, & Z_2^{(0)}=\nu_\alpha\cos(\varphi-\theta_{inc})\cos\delta_{inc} \\ Z_{j,L}^{(k+1)}=T_L(Z_{3-j,*}^{(k)}) & Z_{j,T}^{(k+1)}=T_T(Z_{3-j,*}^{(k)}) \end{array} \tag{4.97}$$

and

$$\begin{array}{c} V_j^{(0)}=\mathbf{dm}^{-1}(Z_j^{(0)}).W_j^\alpha \\ V_{j,L}^{(k+1)}=-\mathbf{dm}^{-1}(Z_{j,*}^{(k+1)}).\mathbf{tm}_L(Z_{3-j,*}^{(k)}).V_{3-j,*}^{(k)}.\mathbf{1}_{\Omega_L}(Z_{3-j,*}^{(k)}) \\ V_{j,T}^{(k+1)}=-\mathbf{dm}^{-1}(Z_{j,*}^{(k+1)}).\mathbf{tm}_T(Z_{3-j,*}^{(k)}).V_{3-j,*}^{(k)}.\mathbf{1}_{\Omega_T}(Z_{3-j,*}^{(k)}) \end{array} \tag{4.98}$$

where W_j^α is given by (4.84). When $\tilde{\nu}_L\in i\mathbb{R}$,

$$Y_j(\xi)=\sum_k\frac{V_{j,T}^{(k)}}{\xi-Z_{j,T}^{(k)}}, \tag{4.99}$$

with

$$\begin{array}{c} Z_1^{(0)}=\nu_T\cos\theta_{inc}\cos\delta_{inc}, \\ Z_2^{(0)}=\nu_T\cos(\varphi-\theta_{inc})\cos\delta_{inc} \\ Z_{j,T}^{(k+1)}=T_T(Z_{3-j,T}^{(k)}) \end{array} \tag{4.100}$$

and

$$\begin{array}{c} V_j^{(0)}=\mathbf{dm}^{-1}(Z_j^{(0)}).W_j^\alpha \\ V_{j,T}^{(k+1)}=-\mathbf{dm}^{-1}(Z_{j,*}^{(k+1)}).\mathbf{tm}_T(Z_{3-j,*}^{(k)}).V_{3-j,*}^{(k)}.\mathbf{1}_{\Omega_T}(Z_{3-j,*}^{(k)}) \end{array} \tag{4.101}$$

The recursive procedure stops when no more poles can be found by deforming contour Γ_0 into $\partial\Omega_L$ or $\partial\Omega_T$. In the 2D case, Croisille and Lebeau [52] have shown that this defines a finite number of poles. The sequence of poles generated in the 3D case being similar to the ones generated in the 2D case (parameters ν_L and

ν_T in the 2D case are replaced by parameters $\tilde{\nu}_L$ and $\tilde{\nu}_T$), their demonstration is still valid here. We have thus extracted all the poles from the spectral functions and have computed them analytically, along with their corresponding residues.

4.3.3 Regular Part

The singular parts Y_j of the spectral functions having been determined, two new functions X_1 and X_2 are defined by (4.95). In the following, a numerical approximation method for X_j is proposed. In order to do so, a system of functional equations solved by X_1, X_2 is derived by subtracting vector

$$\begin{pmatrix} \mathbf{DM}(Y_1) + \mathbf{TM}(Y_2) \\ \mathbf{TM}(Y_1) + \mathbf{DM}(Y_2) \end{pmatrix}, \tag{4.102}$$

from both sides of (4.83), where Y_1 and Y_2 are given by equations (4.96) to (4.101) :

$$\begin{cases} \mathbf{DM}(X_1)(\xi) + \mathbf{TM}(X_2)(\xi) = u_1(\xi) \\ \mathbf{TM}(X_1)(\xi) + \mathbf{DM}(X_2)(\xi) = u_2(\xi) \end{cases}, \tag{4.103}$$

with, for $j = 1, 2$

$$u_j(\xi) = -\sum_k \sum_{*=L,T} \left[\mathbf{D_p}(Z^{(k)}_{j,*}, \xi).V^{(k)}_{j,*} + \mathbf{T_p}(Z^{(k)}_{3-j,*}, \xi).V^{(k)}_{3-j,*} \right] \tag{4.104}$$

It is assumed that Kamotski and Lebeau's [53] proof that this system (3.78) has a unique solution in $\mathcal{H}^2$ can be adapted to the 3D case, meaning that system (4.103) has a unique solution (X_1, X_2) in $\mathcal{H}^3$ if $\tilde{\nu}_L \in \mathbb{R}$ and in $\tilde{\mathcal{H}}^3$ if $\tilde{\nu}_L \in i\mathbb{R}$ where $\mathcal{H}$ is defined by Def. 4.3.1 and $\tilde{\mathcal{H}}$ is defined by Def. 4.3.2. Once again, a numerical approximation of the regular parts X_j will be computed using the Galerkin collocation method.

The functional space $\mathcal{H}$ is approached by the finite-dimension subspace generated by basis functions $(\varphi_k)_{1\leq k\leq 2N}$ defined by (2.76), with $(a_k)_{1\leq k\leq 2N} \in [\tilde{\nu}_L, +\infty[^N$. For a point $a_k \in [\tilde{\nu}_L, +\infty[$, the corresponding Galerkin function φ_k will have a pole at $-a_k \in]-\infty, -\tilde{\nu}_L]$. The basis $(\varphi_k)_{1\leq k\leq 2N}$ therefore generates a subspace of functions analytical in $\mathbb{C}\backslash]-\infty, -\tilde{\nu}_L]$.

The functional space $\tilde{\mathcal{H}}$ is approached by the finite-dimension subspace generated by basis functions $(\varphi_k)_{1\leq k\leq 2N}$ defined by (2.76), with $(a_k)_{1\leq k\leq N} \in [\tilde{\nu}_T, +\infty[^N$, $(a_k)_{N+1\leq k\leq 2N} \in]-i\infty, -\tilde{\nu}_L]^N$. For a point $a_k \in [\tilde{\nu}_T, +\infty[\cup]-i\infty, -\tilde{\nu}_L]$, the corresponding Galerkin function φ_k will have a pole at $-a_k \in]-\infty, -\tilde{\nu}_T] \cup [\tilde{\nu}_L, +i\infty[$. The basis $(\varphi_k)_{1\leq k\leq 2N}$ therefore generates a subspace of functions analytical in $\mathbb{C}\backslash (]-\infty, -\tilde{\nu}_T] \cup [\tilde{\nu}_L, +i\infty[)$.

In both cases, functions X_j are approximated in the adapted finite dimension subspace by :

$$X_j(\xi) \approx \sum_{k=1}^{N} \tilde{X}_j^k \varphi_k(\xi), \quad \tilde{X}_j^k \in \mathbb{C}^3 \tag{4.105}$$

Approximation (4.105) is substituted into (4.103) and the variable change $\zeta = iy$ is applied in the resulting system. This system is then evaluated at collocation points $\xi = b_1, ..., b_{2N}$, leading to a linear system of equations which can be written in matrix form :

$$\begin{pmatrix} \mathbb{D} & \mathbb{T} \\ \mathbb{T} & \mathbb{D} \end{pmatrix} \begin{pmatrix} \mathbb{X}_1 \\ \mathbb{X}_2 \end{pmatrix} = \begin{pmatrix} \mathbb{U}_1 \\ \mathbb{U}_2 \end{pmatrix} \Leftrightarrow \begin{cases} (\mathbb{D}+\mathbb{T})(\mathbb{X}_1+\mathbb{X}_2) = \mathbb{U}_1+\mathbb{U}_2 \\ (\mathbb{D}-\mathbb{T})(\mathbb{X}_1-\mathbb{X}_2) = \mathbb{U}_1-\mathbb{U}_2 \end{cases}, \tag{4.106}$$

where matrices $(6N \times 6N)$ are defined by 3×3 blocks:

$$\begin{aligned} \mathbb{D}_{lk} &= \int_{-\infty}^{+\infty} \mathbf{DM}(b_l, iy) e_{a_k}(y)\, dy = \frac{1}{2i\pi} \int_{-\infty}^{+\infty} \frac{\mathbf{dm}}{b_l - iy} \sqrt{\frac{a_k}{\pi}} \frac{1}{y - ia_k}\, dy \\ &= -\frac{\sqrt{a_k}}{2\pi\sqrt{\pi}} \begin{pmatrix} \mathcal{D}_1(a,b) & \mathcal{D}_2^T(a,b) & 0 \\ -\mathcal{D}_2^L(a,b) & \mathcal{D}_1(a,b) & -\mathcal{D}_3^L(a,b) \\ 0 & \mathcal{D}_3^T(a,b) & \mathcal{D}_1(a,b) \end{pmatrix} = \frac{\sqrt{a_k}}{2\pi\sqrt{\pi}} \mathbb{D}(a_k, b_l) \end{aligned} \tag{4.107}$$

where functions e_{a_k} are defined by (2.75) and the explicit expressions of coefficients of matrix $\mathbb{D}(a,b)$ and their values are computed in appendix C.7.3. The other matrices involved are, for $1 \le l, k \le 2N$

$$\begin{aligned} \mathbb{T}_{lk} &= \int_{-\infty}^{+\infty} \mathbf{TM}(b_l, iy) e_{a_k}(y)\, dy = \frac{1}{2i\pi} \int_{-\infty}^{+\infty} \sum_{*=L,T} \frac{\mathbf{tm}_*(iy, \operatorname{sgn}\sin\varphi)}{b_l - T_*(iy)} \sqrt{\frac{a_k}{\pi}} \frac{1}{y - ia_k}\, dy \\ &= \frac{1}{2i\pi} \sqrt{\frac{a_k}{\pi}} \sum_{*=L,T} \int_{-\infty}^{+\infty} \frac{\mathbf{tm}_*(iy, \epsilon)}{[b_l - (iy\cos\varphi + \zeta_*(iy)|\sin\varphi|)](y - ia_k)}\, dy, \end{aligned} \tag{4.108}$$

where $\epsilon = \operatorname{sgn}(\sin\varphi)$. Let us define

$$\mathbb{T}_{lk} = \frac{1}{2i\pi} \sqrt{\frac{a_k}{\pi}} \sum_{*=L,TH,TV} \begin{pmatrix} \mathcal{T}_1^*(a,b) & \mathcal{T}_2^*(a,b) & \mathcal{T}_3^*(a,b) \\ \mathcal{T}_4^*(a,b) & \mathcal{T}_5^*(a,b) & \mathcal{T}_6^*(a,b) \\ \mathcal{T}_7^*(a,b) & \mathcal{T}_8^*(a,b) & \mathcal{T}_9^*(a,b) \end{pmatrix} = \frac{1}{2i\pi} \sqrt{\frac{a_k}{\pi}} \mathbb{T}(a_k, b_l) \tag{4.109}$$

The explicit expressions of operators $\mathcal{T}_i^*, 1 \le i \le 9, * = L, TH, TV$ and their values

are computed in D.9.3. Finally:

$$\mathbb{X}_j = \begin{pmatrix} \tilde{X}_j^1 \\ \vdots \\ \tilde{X}_j^{2N} \end{pmatrix} \qquad \mathbb{U}_j = \begin{pmatrix} u_j(b_1) \\ \vdots \\ u_j(b_{2N}) \end{pmatrix} \tag{4.110}$$

where $u_j(\xi)$ is given by (4.104). The same considerations as those made in 3.3.3, equations (3.89) to (3.91), lead to an expression of u_j with respect to operators $\mathbb{D}(\cdot,\cdot)$ and $\mathbb{T}(\cdot,\cdot)$:

$$u_j(\xi) = -\frac{1}{2i\pi} \sum_k \sum_{*=L,T} \left(i\mathbb{D}(-Z_{j,*}^{(k)}, \xi).V_{j,*}^{(k)} + \mathbb{T}(-Z_{3-j,*}^{(k)}, \xi).V_{3-j,*}^{(k)} \right) + \frac{W_j^\alpha}{\xi - Z_j^{(0)}} \tag{4.111}$$

Using these results, the linear system (4.106) is implemented and solved numerically using the C++ library Eigen, and an evaluation of the regular part of the spectral functions is obtained. However, for values of ξ lying in certain parts of the complex plane, this evaluation is not sufficiently accurate. The technique used to solve this problem is called the propagation of the solution.

4.3.4 Propagation of the solution

The method called propagation of the solution is used to propagate the accuracy of the numerical approximation of the regular functions X_1 and X_2 from parts of the complex plane where they are evaluated accurately to parts of the complex plane where they are not. The validity domains in the complex plane will be detailed hereafter.

The first step of this procedure is to deform contour Γ_0 (visible in Fig. 4.2) in operator **DM** into contour Γ_2 in functional system (4.103). Contour Γ_2 is visible on Fig. 4.8 for the case $\tilde{v}_L \in \mathbb{R}$ and in Fig. 4.9 for the case $\tilde{v}_L \in i\mathbb{R}$. Fig.9 4.9a shows an intermediate step in the contour deformation from Γ_0 to Γ_2. The straight arrow shows the direction of deformation of the quarter-cycle linking the two parts of Γ_2 (the one which circumvents $[-\tilde{v}_L, -i\infty[$ and the one which circumvents $[\tilde{v}_T, +\infty[$) in fig. 4.9a. The radius of this quarter-cycle tends to infinity during the deformation, resulting in the final contour, which is the reunion of contours Γ_2^a and Γ_2^b, represented in Fig. 4.9b. During this deformation, the half-plane $\mathrm{Im}\xi < 0$ is crossed (with the exception of branch $[-\tilde{v}_L, -\infty[$ in the case $\tilde{v}_L \in i\mathbb{R}$). The contribution of pole ζ whose value is $\zeta = \xi$, $\mathrm{Im}\xi < 0$ crossed during this

contour deformation is given by Cauchy's residue formula :

$$\int_{\Gamma_0} \mathbf{DM}(\xi,\zeta)X_j(\zeta)\,d\zeta = \int_{\Gamma_2} \mathbf{DM}(\xi,\zeta)X_j(\zeta)\,d\zeta + \mathbf{dm}(\xi).X_j(\xi) \tag{4.112}$$

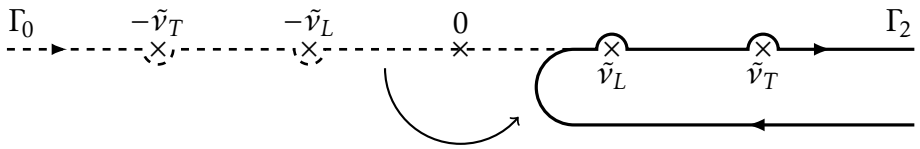

Figure 4.8 – Integration contour Γ_2 in the case $\tilde{\nu}_L \in \mathbb{R}$. The curved arrow indicates the contour deformation from Γ_0 to Γ_2.

The next step is to define the inverse translation operator $T_*^{-1} : \Omega_*^- \to \mathbb{C}, * = L, T$:

$$T_*^{-1}(\xi = \nu_* \cos\theta) = \xi\cos\tilde{\varphi} - \zeta_*(\xi)\sin\tilde{\varphi} = \nu_*\cos(\theta - \tilde{\varphi}). \tag{4.113}$$

$\cos\theta$ is well defined for $0 \leq \mathrm{Re}\theta \leq \pi$, therefore this operator is defined on subspace Ω_*^-, visible on Fig. 4.10 and defined as

$$\Omega_*^- = \{\xi \in \mathbb{C},\ \xi = \tilde{\nu}_* \cos\theta, \tilde{\varphi} \leq \mathrm{Re}(\theta) \leq \pi\} \tag{4.114}$$

Using these definitions, contour Γ_0 in operator **TM** is deformed into contour $\partial\Omega_*^-$, visible on Fig. 4.10. In the case where $\tilde{\nu}_L \in \mathbb{R}$, the contours are represented in Fig. 4.10a, and the deformation from Γ_0 to $\partial\Omega_*^-$ (represented by the arrows on the figure) only spans the bottom half of domain Ω_*^-. In the case where $\tilde{\nu}_L \in i\mathbb{R}$, the contour $\partial\Omega_L^-$ is represented in Fig. 4.10b, and the deformation from Γ_0 to $\partial\Omega_L^-$ (represented by the arrows on the figure) only spans the part of domain Ω_L^- which is contained in the upper half of the complex plane. In both cases, the poles ζ of the integrand are $\zeta = T_*^{-1}(\xi), \mathrm{Im}\xi < 0$. These poles are crossed if and only if $\xi \in \Omega_*^-$ and $\mathrm{Im}\xi < 0$, where domain Ω_*^- is represented in grey on Figs. 4.10a and 4.10b. Their contribution is determined thanks to Cauchy's residue theorem :

$$\int_{\Gamma_0} \mathbf{TM}(\xi,\zeta)X_j(\zeta)\,d\zeta = \sum_{*=L,T} \int_{\partial\Omega_*^-} \frac{\mathbf{tm}_*(\zeta)}{\xi - T_*(\zeta)}.X_j(\zeta)\,d\zeta + \mathbf{M}_*(\xi).X_j(T_*^{-1}(\xi))\mathbf{1}_{\Omega_*^-}(\xi), \tag{4.115}$$

where $\mathbf{1}_{\Omega_*^-}(\xi) = 1$ when $\xi \in \Omega_*^-$ and $\mathrm{Im}\xi < 0$ and $\mathbf{1}_{\Omega_*^-}(\xi) = 0$ elsewhere and

$$\mathbf{M}_*(\xi = \tilde{\nu}_* \cos\theta) = -\frac{\sin(\theta - \tilde{\varphi})}{\sin\theta}\mathbf{tm}_*(T_*^{-1}(\xi)) \tag{4.116}$$

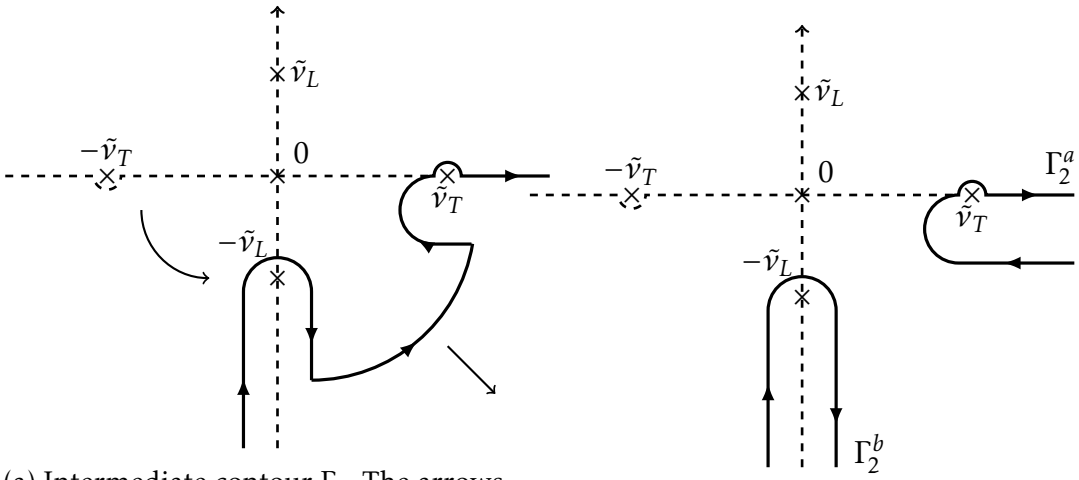

(a) Intermediate contour Γ_2. The arrows show the direction of the deformation.

(b) Final contour $\Gamma_2 = \Gamma_2^a \cup \Gamma_2^b$

Figure 4.9 – Deformation of contour Γ_0 onto contour $\Gamma_2 = \Gamma_2^a \cup \Gamma_2^b$ in the case $\tilde{\nu}_L \in i\mathbb{R}$.

The recursive system of functional equations solved by the regular part is obtained by substituting (4.112) and (4.115) into (4.103):

$$\begin{cases} X_1(\xi) = g_1(\xi) - \mathbf{dm}^{-1}(\xi).\sum\limits_{*=L,T} \mathbf{M}_*(\xi).X_2(T_*^{-1}(\xi))\mathbf{1}_{\Omega_*^-}(\xi) \\ X_2(\xi) = g_2(\xi) - \mathbf{dm}^{-1}(\xi).\sum\limits_{*=L,T} \mathbf{M}_*(\xi).X_1(T_*^{-1}(\xi))\mathbf{1}_{\Omega_*^-}(\xi) \end{cases}, \tag{4.117}$$

where , for $j = 1, 2$

$$g_j(\xi) = \mathbf{dm}^{-1}(\xi)\left(u_j(\xi) - \int_{\Gamma_2} \mathbf{DM}(\xi,\zeta)X_j(\zeta)\,d\zeta - \int_{\partial\Omega_*^-} \mathbf{TM}(\xi,\zeta)X_{3-j}(\zeta)\,d\zeta\right) \tag{4.118}$$

The same consideration as those made in 3.3.4 lead to an expression of functions g_j using operators $\mathbb{D}(\cdot,\cdot)$ and $\mathbb{T}(\cdot,\cdot)$:

$$\mathbf{dm}(\xi).g_j(\xi) = u_j(\xi) - \sum_{k=1}^{2N} \sqrt{\frac{a_k}{\pi}}\left(\mathbb{ND}(a_k,\xi).\tilde{X}_j^k + \mathbb{NT}(a_k,\xi).\tilde{X}_{3-j}^k\right), \tag{4.119}$$

where

$$\mathbb{ND}(a,b) = \frac{1}{2\pi}\mathbb{D}(a,b) - \frac{\mathbf{dm}(b)}{a+b} \tag{4.120}$$

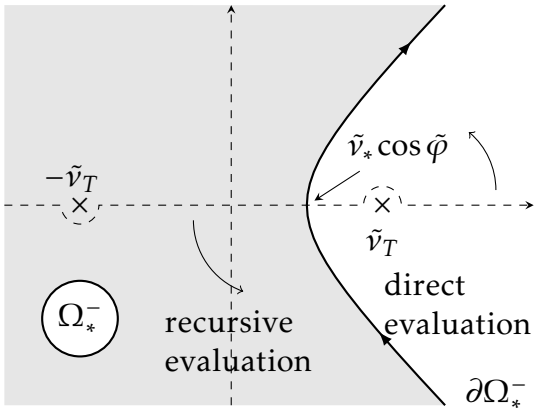

(a) Domain Ω_*^- and contour $\partial\Omega_*^-$ in the case $\tilde{\nu}_L \in \mathbb{R}$. The arrows show the deformation from contour Γ_0 to contour $\partial\Omega_*^-$.

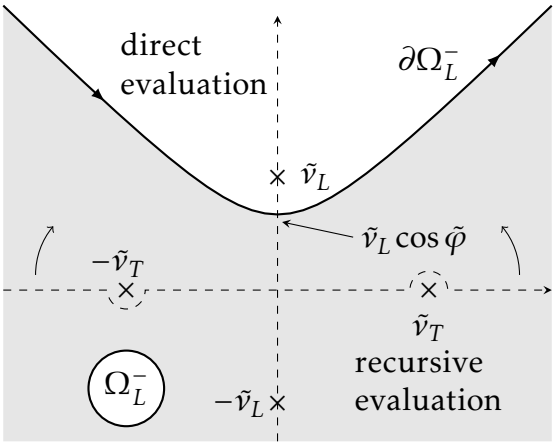

(b) Domain Ω_L^- and contour $\partial\Omega_L^-$ in the case $\tilde{\nu}_L \in i\mathbb{R}$. The arrows show the deformation from contour Γ_0 to contour $\partial\Omega_L^-$.

Figure 4.10 – Domains Ω_*^- and contours $\partial\Omega_*^-$ in cases $\tilde{\nu}_L \in \mathbb{R}$ and $\tilde{\nu}_L \in i\mathbb{R}$.

and

$$\mathbb{N}\mathbb{T}(a,b) = \frac{1}{2i\pi}\mathbb{T}(a,b) - \sum_{*=L,T} \frac{\mathbf{M}_*(b)}{T_*^{-1}(b)+a}. \tag{4.121}$$

In system (4.117), the value of the regular part of the spectral function in domain Ω_*^-, visible Fig. 4.10, is expressed using its value in the domain $\xi \notin \Omega_*^-$, where the numerical approximation (4.105) is valid. To do so, functions g_j, $j = 1,2$ are evaluated numerically using (4.119). The accuracy of the numerical evaluation in domain $\xi \notin \Omega_*^-$ is therefore propagated to domain Ω_*^-.

This concludes the semi-analytical computation of the spectral functions. The L, TH and TV diffraction coefficients can now be computed using (4.67). Numerical testing is presented in the following.

4.4 Numerical Tests

The spectral functions are evaluated numerically using the semi-analytical scheme described in the previous sections. This is achieved by, first, computing the poles and residues of the spectral functions analytically using the recursive algorithm described in subsection 4.3.2. Then, the regular parts of the spectral functions are approached numerically by solving (4.103) thanks to the Galerkin collocation method described in subsection 4.3.3. In the case where $\tilde{\nu}_L \in \mathbb{R}$, the

Galerkin parameters are set to:

$$a_k = 1.001 + 0.05e^{k\frac{\log 10}{4}} - 1, \qquad b_k = a_k - 0.1i, \qquad 1 \leq k \leq 20 \tag{4.122}$$

And in the case where $\tilde{\nu}_L \in i\mathbb{R}$, meaning for the case of an incident transversal wave with $|\delta_{inc}| > \delta_c$ (with $\delta_c \approx 33^o$ in steel), the Galerkin parameters are set to

$$\begin{aligned} a_k &= 1.001 + 0.05e^{k\frac{\log 10}{4}} - 1, & b_k &= a_k - 0.1i, & 1 \leq k \leq 10 \\ a_k &= -i[1.001 + 0.05e^{(k-10)\frac{\log 10}{4}} - 1], & b_k &= a_k + 0.1, & 11 \leq k \leq 20 \end{aligned} \tag{4.123}$$

Finally, the solution is rendered accurate in the entire complex domain by applying the recursive procedure called the propagation of the solution described in subsection 4.3.4.

Following these steps, the diffraction coefficients have been computed using (4.67) and tested numerically.

4.4.1 Comparison to the 2D code

The first test on the 3D code is to check that when $\delta_\alpha = 0$, the results obtained using the 3D code are the same as those obtained using the 2D code presented and validated numerically (see section 3.4) and experimentally (see section 3.5) in the previous chapter. This has been checked for the theoretical computations and must also be verified numerically.

The spectral functions are evaluated at $\xi = \tilde{\nu}_L \cos\theta - i10^{-6}$ (a small negative imaginary part is added to ensure that the recursive equations (4.117) are valid) every $0,5^o$ for $0 \leq \theta \leq \varphi$ and at $\delta_\alpha = 0^o$, using the 3D code. The L and TH diffraction coefficients are computed using (4.67), for an elastic wave propagating in a steel wedge ($c_L = 5700m.s^{-1}$, $c_T = 3200m.s^{-1}$). For the 3D problem, TH waves defined by (4.4) correspond to the T waves of the 2D problem. The results are compared to the diffraction coefficients, given by (3.44) and (3.45), obtained using the 2D elastic code presented in the previous chapter.

Figs. 4.11 and 4.12 show the absolute value of the diffraction coefficients obtained using the 2D and 3D SF codes for a wedge of angle $\varphi = 140^o$ illuminated by a wave incident with an angle $\theta_{inc} = 70^o$ and for a wedge of angle $\varphi = 250^o$ illuminated by a wave incident with an angle $\theta_{inc} = 65^o$.

In Figs. 4.11a-4.11c-4.12a-4.12c and Figs. 4.11b-4.11d-4.12b-4.12d, representing the L and T diffraction coefficients respectively, the thick blue line represents the results obtained using the 2D code and the dashed lines (red and green respectively) represent the results obtained using the 3D code.

In all of these figures, and in all other tested configurations, the 2D and 3D

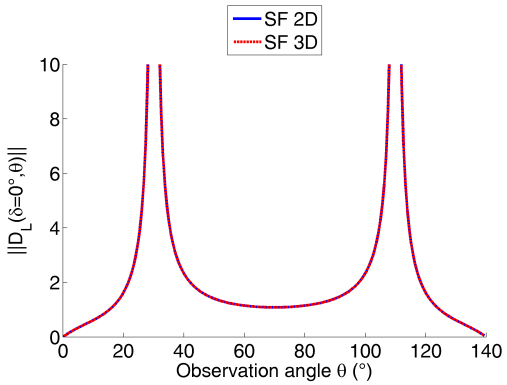

(a) Diffracted and incident L waves.

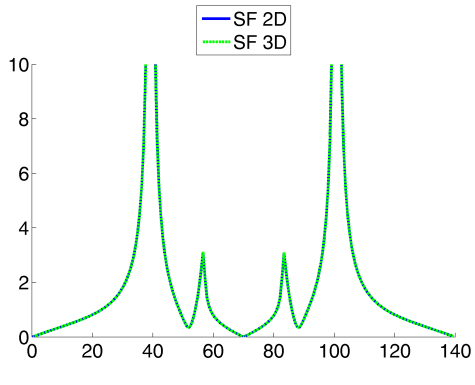

(b) Diffracted T wave and incident L wave.

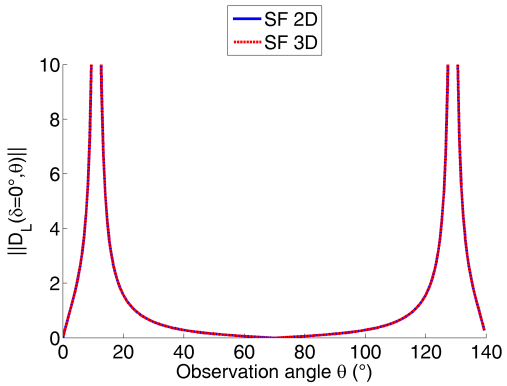

(c) Diffracted L wave and incident T wave.

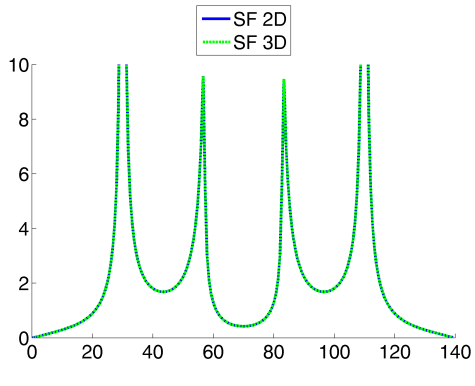

(d) Diffracted and incident T waves.

Figure 4.11 – Diffraction coefficients for $\varphi = 140^o, \theta_{inc} = 70^o$

plots are perfectly overlapping. When $\delta_\alpha = 0^o$, the 3D code yields exactly the same results as the 2D code, which is in accord with the theoretical computations. This validates the computation of the "2D terms" (meaning the terms that are not canceled by setting $\delta_\alpha = 0^o$) of the 3D code. The following numerical test, comparison of the 3D elastic code to Sommerfeld's analytical expression for an acoustic wave, validates a different set of terms (the ones that are purely 3D and longitudinal) computed by the spectral functions method.

4.4.2 Acoustic limit

In the second chapter of this manuscript, we have seen that Sommerfeld [43] provides an analytical expression for the GTD diffraction coefficient in the case of an acoustic wave incident on a wedge with Dirichlet or Neumann boundaries. This expression is still valid for 3D incidences, and the expression is provided

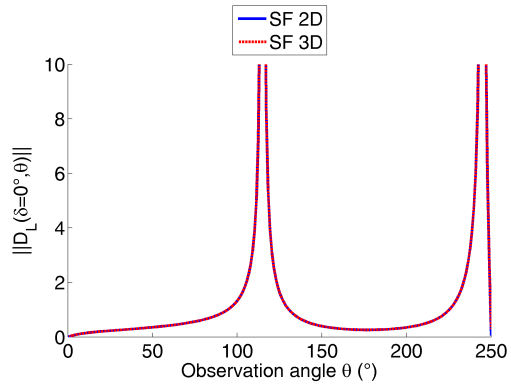

(a) Diffracted and incident L waves.

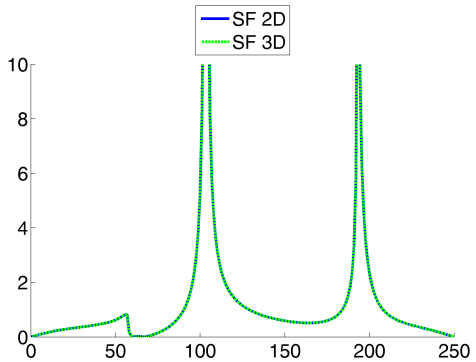

(b) Diffracted T wave and incident L wave.

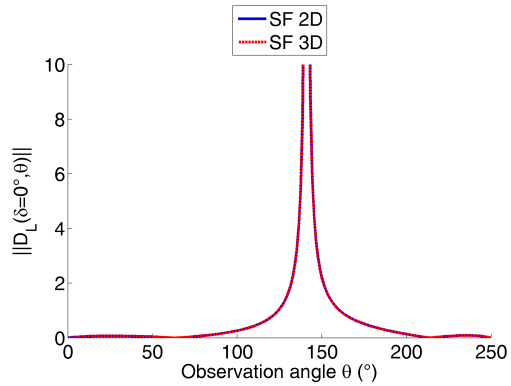

(c) Diffracted L wave and incident T wave.

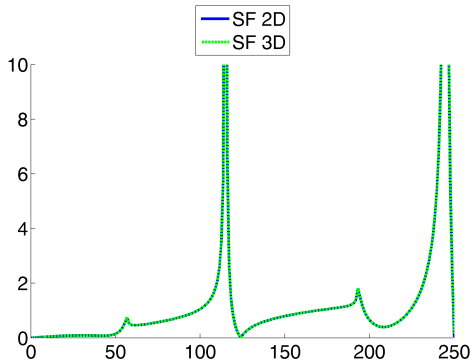

(d) Diffracted and incident T waves.

Figure 4.12 – Diffraction coefficients for $\varphi = 250^o, \theta_{inc} = 65^o$

by Keller [14]. In the case of a wedge with Dirichlet boundaries, we have :

$$v^{ac,diff}(r,\theta) = D^{Dir}(\theta)\frac{e^{-ik_0 r}}{\sqrt{k_0 r \cos\delta_\alpha}} \tag{4.124}$$

where $v^{ac,diff}$ is the acoustic diffracted field, k_0 is the acoustic wave number and D^{Dir}, is given by (2.109). For an acoustic wave, the diffraction coefficient does not depend on the incident skew angle δ_α. The dependency of the diffracted field with respect to this parameter is fully contained in the term $(k_0 r \cos\delta_\alpha)^{-1/2}$.

The case of an acoustic wave incident on a wedge with Dirichlet boundary conditions can be mimicked using the elastic code. By setting $c_L = 1$ and $c_T \to 0$ and considering incident L waves, the L diffraction coefficient should behave like the diffraction coefficient of an acoustic wave.

In the 3D elastic code, the wave velocities are set to $c_L = 1m.s^{-1}$ and $c_T = 10^{-7}m.s^{-1}$ and the incident wave is longitudinal. The spectral functions are evaluated at $\xi = \tilde{\nu}_L \cos\theta - i10^{-6}$ every $0,5^o$ for $0 \leq \theta \leq \varphi$ and for $-90^o \leq \delta_\alpha \leq 90^o$ and the L diffraction coefficient is deduced using (4.67). The results are compared to the analytical expression of the Sommerfeld diffraction coefficients for a wedge with Dirichlet boundary conditions.

Figs. 4.13 and 4.14 show the absolute value of the diffraction coefficient obtained using the SF code (Figs. 4.13a and 4.14a) and with Sommerfeld's analytical expression (Figs. 4.13b and 4.14b) for a wave incident with an angle $\theta_{inc} = 40^o$ on a wedge of angle $\varphi = 160^o$ and for $\theta_{inc} = 240^o$ and $\varphi = 280^o$, respectively.

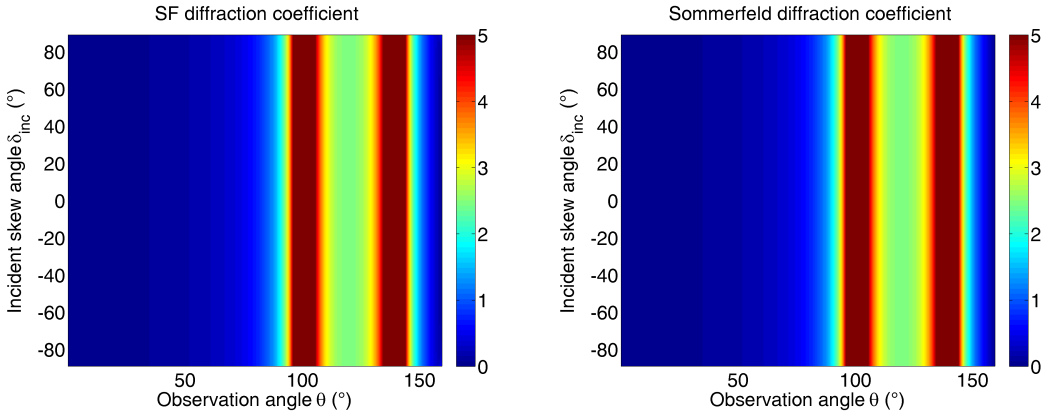

(a) SF diffraction coefficient (b) Sommerfeld diffraction coefficient

Figure 4.13 – Absolute value of the diffraction coefficient computed with the spectral functions and with the Sommerfeld method for a wave incident with an angle $\theta_{inc} = 40^o$ on a wedge of angle $\varphi = 160^o$

In both cases, the diffraction coefficients are computed for various incident skew angles δ_α to check that the SF diffraction coefficient is independent of this parameter, as it should be in the acoustic case. The horizontal axis corresponds to the observation angle θ, the vertical axis corresponds to the incident skew angle δ_α and the magnitude of the diffraction coefficients is represented in color in the (θ, δ_α) plane. For both wedges, the figures representing the SF diffraction coefficients and those representing the Sommerfeld diffraction coefficients appear to be identical and are invariant by vertical translation (meaning that the coefficients do not depend on the angle δ_α). The diffraction coefficients can therefore be plotted for a single skew angle, without loss of generality. This is also the case for the angular phases of the diffraction coefficients, and their plots in the (θ, δ_α) plane are not reproduced here.

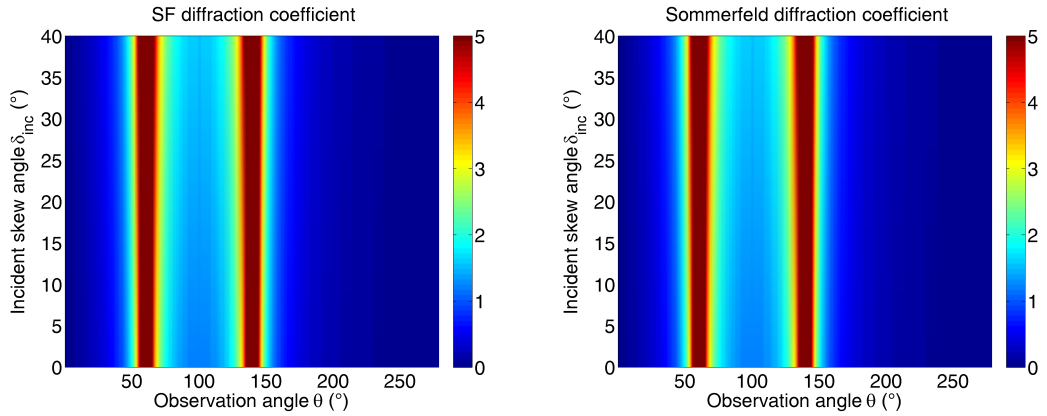

(a) SF diffraction coefficient (b) Sommerfeld diffraction coefficient

Figure 4.14 – Absolute value of the diffraction coefficient computed with the spectral functions and with the Sommerfeld method for a wave incident with an angle $\theta_{inc} = 240^o$ on a wedge of angle $\varphi = 280^o$

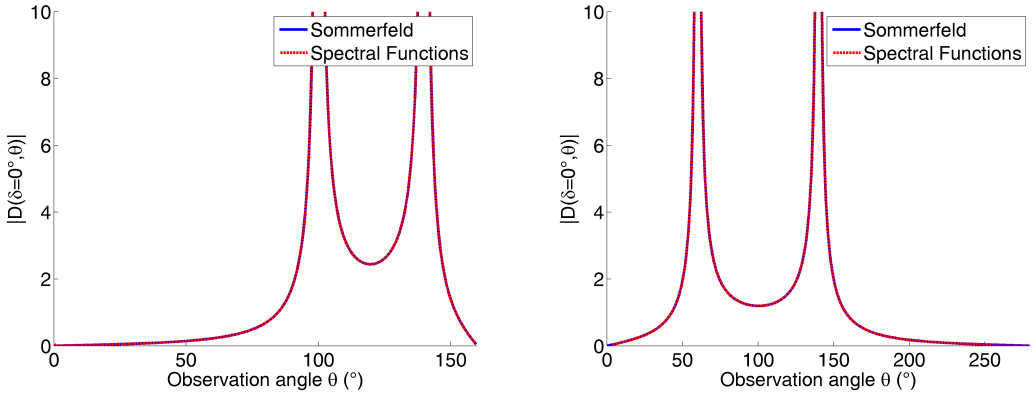

(a) $\varphi = 160^o$, $\theta_{inc} = 40^o$ (b) $\varphi = 280^o$, $\theta_{inc} = 240^o$

Figure 4.15 – Absolute value of the diffraction coefficient computed with the spectral functions and with the Sommerfeld method for $\delta_{inc} = 0^o$.

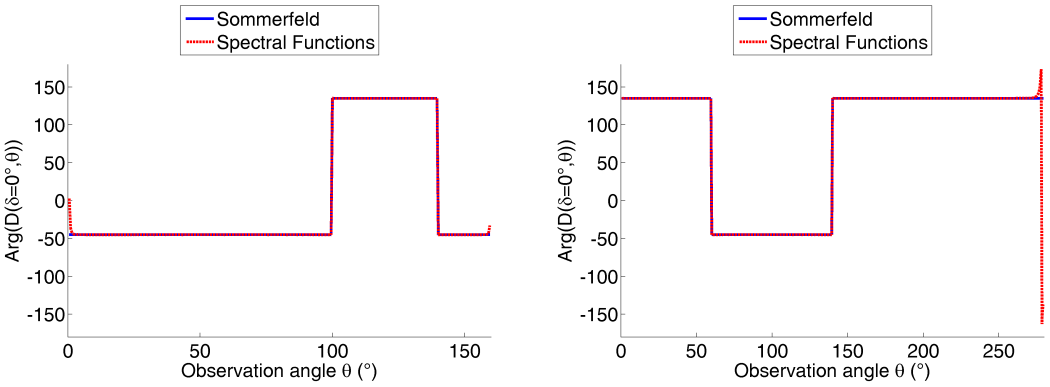

(a) $\varphi = 160^o$, $\theta_{inc} = 40^o$ (b) $\varphi = 280^o$, $\theta_{inc} = 240^o$

Figure 4.16 – Angular phase of the diffraction coefficient computed with the spectral functions and with the Sommerfeld method for $\delta_{inc} = 0^o$.

Figs. 4.15 and 4.16 respectively show the absolute value and the angular phase of the diffraction coefficient, plotted for $\delta_\alpha = 0^o$ for a wave incident with an angle $\theta_\alpha = 40^o$ on a wedge of angle $\varphi = 160^o$ (see Fig. 4.15a) and for a wave incident with an angle $\theta_\alpha = 240^o$ on a wedge of angle $\varphi = 280^o$ (see Fig. 4.15b). In all four figures, the thick blue line is the solution computed using Sommerfeld's analytical expression and the dashed red line is the result obtained using acoustic limit of the 3D SF code. Both lines are perfectly overlapping, except for some discrepancies in the angular phase, for observation directions near the wedge faces.

The "acoustic limit" of the 3D elastic code is thus validated for wedge angles lower and higher than π. This shows that the terms appearing in the evaluation of the spectral functions that depend on $\tilde{\nu}_T$ tend to 0 when transversal wave velocity tends to 0 and that the terms that depend on $\tilde{\nu}_L$ are computed correctly.

4.4.3 Verification of the regular part for an infinite plane

In the case where $\varphi = \pi$, the wedge degenerates into an infinite plane and there is no edge diffracted wave. The regular part of the spectral functions, which is determined by system (4.106) and is the part of the solution corresponding to the diffraction phenomena, vanishes and we should have, for $j = 1, 2$:

$$\|\mathbb{U}_j\| = 0 \tag{4.125}$$

where $\mathbb{U}_j$ is the right-hand side of system (4.106) and is given by (4.110). Verifying that this is the case provides a check on the lengthy computations of the

explicit expressions of operators $\mathbb{D}(\cdot,\cdot)$ and $\mathbb{T}(\cdot,\cdot)$. According to (4.110), the value of $\|\mathbb{U}_j\|$ does not depend on the observation angle θ, therefore in our tests, only the skew incidence angle δ_α varies.

Fig. 4.17 shows $\|\mathbb{U}_j\|$, $j = 1, 2$ for incident L (see Fig. 4.17a), TH (see Fig. 4.17b) and TV (see Fig. 4.17c) waves with an angle $\theta_{inc} = 50^o$ on an infinite plane. The thick blue line represents $\|\mathbb{U}_1\|$ and the dashed red line represents $\|\mathbb{U}_2\|$. In the case of an incident L wave, as expected, $\|\mathbb{U}_1\|$ and $\|\mathbb{U}_2\|$ are very small (of the order of the numerical computation error). For incident T waves, however, when the incident skew angle is higher than the critical angle, $\|\mathbb{U}_1\|$ and $\|\mathbb{U}_2\|$ are suddenly very large, rather than quasi null. Because this is only the case when $\tilde{v}_L \in i\mathbb{R}$, we believe that this is not due to a miscalculation of operators $\mathbb{D}(\cdot,\cdot)$ or $\mathbb{T}(\cdot,\cdot)$ (the corresponding computations are detailed in appendices C and D), which would have produced errors visible in cases where $\tilde{v}_L \in \mathbb{R}$.

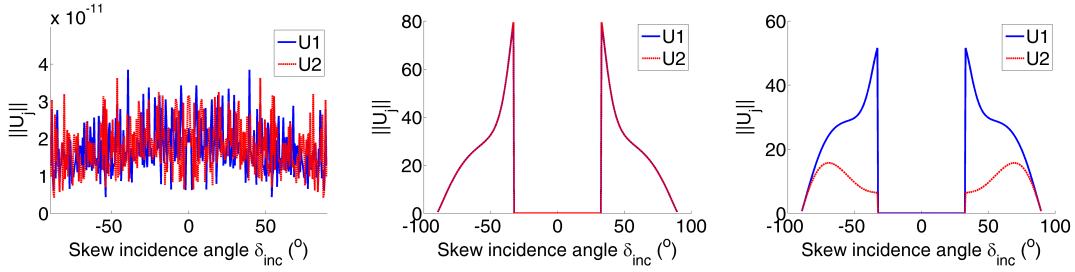

(a) Incident L wave (b) Incident TH wave (c) Incident TV wave

Figure 4.17 – $\|\mathbb{U}_j\|$, $j = 1, 2$ for $\varphi = 180^o$ and $\theta_{inc} = 50^o$

Nonetheless, when $\tilde{v}_L \in i\mathbb{R}$, the code developed according to the theory described in this chapter produces diverging results (see for example Fig. 4.18 showing diffraction coefficients computed with the standard theory of the current chapter). We are not sure what the cause of this error is, and additional work is necessary in order to solve this problem.

Fig. 4.18 shows the absolute value of the diffraction coefficients obtained using the SF code. The L, TH and TV diffraction coefficients are computed using (4.67) for a steel wedge ($c_L = 5700m.s^{-1}$ and $c_T = 3200m.s^{-1}$) of angle $\varphi = 140^o$ illuminated by a TH wave with and angle $\theta_{inc} = 70^o$. The spectral functions are evaluated at $\xi = \tilde{v}_\beta \cos\theta - i10^{-6}$ every $0,5^o$ for $0 \leq \theta \leq \varphi$ and for $-90^o \leq \delta_\alpha \leq 90^o$. The horizontal axis corresponds to the observation angle θ, the vertical axis corresponds to the incident skew angle δ_α and the magnitude of the diffraction coefficient is represented in color in the (θ, δ_α) plane. Fig. 4.18a shows the L diffraction coefficient, Fig. 4.18b shows the TH diffraction coefficient and Fig. 4.18c shows the TV diffraction coefficient. It is clear from these last two figures that the diffraction coefficient abruptly diverges when $\tilde{v}_L \in i\mathbb{R}$.

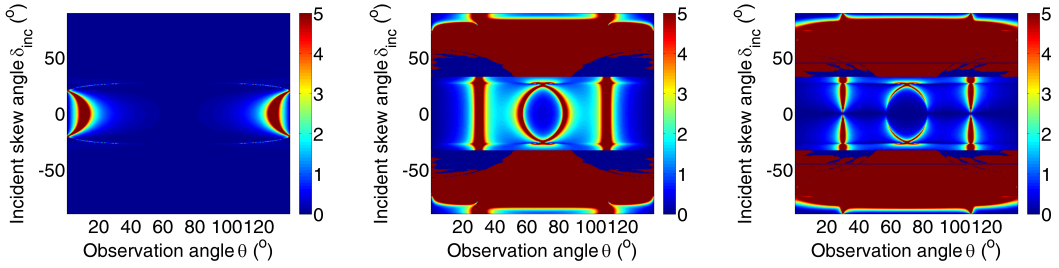

(a) Diffracted L wave (b) Diffracted TH wave (c) Diffracted TV wave

Figure 4.18 – Absolute value of the diffraction coefficient computed in a standard manner (i.e. without approximation (4.126)) for an incident TH wave on a wedge of angle $\varphi = 140^o$ with $\theta_{inc} = 70^o$

The regular part of the spectral functions diverges in cases where $\tilde{\nu}_L \in i\mathbb{R}$ and additionnal work must be done to correct this problem. In the meantime, a new approximation has been proposed in order to obtain a non-diverging diffraction coefficient in these cases. This approximation and its effects are detailed in the following.

4.4.4 Numerical approximation in the case $\tilde{\nu}_L \in i\mathbb{R}$

In the previous subsection, it has been made apparent that the regular part of the spectral functions is miscalculated in the case of an incident T wave with a skew angle higher than the critical angle. The cause of this has not yet been found. In the meantime, in order to obtain physically coherent results, the following approximation is applied (only for incident T waves) :

$$\mathbb{D}(\cdot,\cdot)|_{\delta_\beta > \delta_C} \approx \mathbb{D}(\cdot,\cdot)|_{\delta_\beta = \delta_c - 0.25^o} \tag{4.126a}$$

$$\mathbb{T}(\cdot,\cdot)|_{\delta_\beta > \delta_C} \approx \mathbb{T}(\cdot,\cdot)|_{\delta_\beta = \delta_c - 0.25^o} \tag{4.126b}$$

Fig. 4.19 shows $\|\mathbb{U}_j\|$, $j = 1, 2$ obtained with approximations (4.126) for incident TH (see Fig. 4.19a) and TV (see Fig. 4.19b) waves. with an angle $\theta_{inc} = 50^o$ on an infinite plane. The thick blue line represents $\|\mathbb{U}_1\|$ and the dashed red line represents $\|\mathbb{U}_2\|$. Using approximation (4.126), $\|\mathbb{U}_1\|$ and $\|\mathbb{U}_2\|$ now behave as expected, even when $\tilde{\nu}_L \in i\mathbb{R}$ and are of the order of the numerical computation error.

In order to illustrate the effect of approximation (4.126) in the case where $\tilde{\nu}_L \in i\mathbb{R}$, we provide an example of the effect of this approximation on the resulting diffraction coefficient. To do so, the L, TH and TV diffraction coefficients are

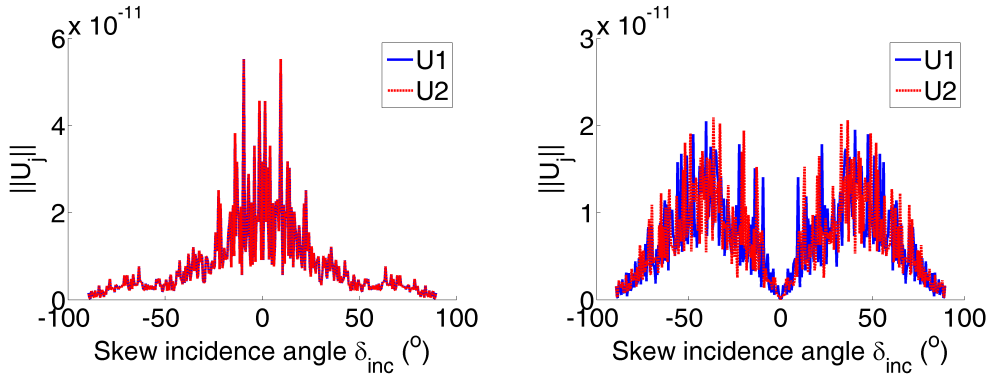

(a) Incident TH wave (b) Incident TV wave

Figure 4.19 – $\|\mathbb{U}_j\|$, $j = 1, 2$ for $\varphi = 180^o$ and $\theta_{inc} = 50^o$

computed using (4.67) for a steel wedge ($c_L = 5700m.s^{-1}$ and $c_T = 3200m.s^{-1}$) of angle $\varphi = 140^o$ illuminated by a TH wave with and angle $\theta_{inc} = 70^o$. The spectral functions are evaluated at $\xi = \tilde{\nu}_\beta \cos\theta - i10^{-6}$ every $0,5^o$ for $0 \leq \theta \leq \varphi$ and for $-90^o \leq \delta_\alpha \leq 90^o$.

Fig. 4.20 shows the absolute value of the diffraction coefficients obtained using the SF code with approximation (4.126). The horizontal axis corresponds to the observation angle θ, the vertical axis corresponds to the incident skew angle δ_α and the magnitude of the diffraction coefficient is represented in color in the (θ, δ_α) plane. Fig. 4.20a shows the TH diffraction coefficient and Fig. 4.20b shows the TV diffraction coefficient. The diffraction coefficients visible in these two figures are no longer divergent when $\tilde{\nu}_L \in i\mathbb{R}$ and their behaviour seems physically coherent. It can be noted that these coefficients seem to diverge when δ_α approaches $\pm 90^o$ (but not for $\delta_\alpha = \pm 90^o$ exactly), meaning when the incidence grazes the wedge edge. In this case, the GTD field diverges because of its proportionality to the factor $(\cos\delta_\beta)^{-1/2}$, see (4.66) and another computation method should be considered.

The diffraction coefficients have been computed using the spectral functions method for a steel wedge of angle $\varphi = 140^o$ illuminated by an incident TH wave with angle $\theta_{inc} = 70^o$ for various incident skew angles. The regular parts of the spectral functions, computed according to the method described in 4.3.3, diverge when $\tilde{\nu}_L \in i\mathbb{R}$. Additional work must be done to find the reason for this instability. In the meantime, a numerical approximation is proposed in order to obtain a diffraction coefficient that only diverges in the directions of specular reflection (as is expected for a GTD diffraction coefficient). These coefficients have yet to be validated numerically or experimentally.

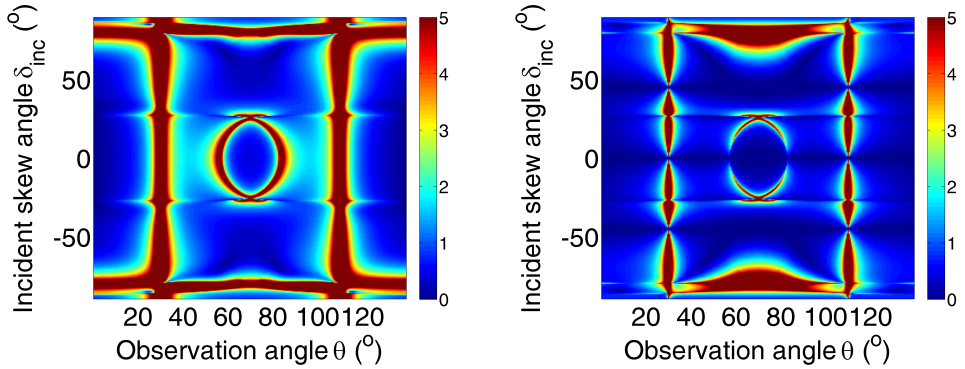

(a) Diffracted TH wave (b) Diffracted TV wave

Figure 4.20 – Absolute value of the diffraction coefficient computed with approximation (4.126) for an incident TH wave on a wedge of angle $\varphi = 140^o$ with $\theta_{inc} = 70^o$

Conclusion

Using the spectral functions method, the elastic wave diffracted by a skew incident plane wave on as stress-free wedge has been studied. In cases where Snell's law of diffraction yields a propagative wave for both longitudinal and transversal diffracted waves, a semi-analytical computation method is developed theoretically and numerically. The corresponding code has been tested in three different manners (by comparison to the 2D elastic code for 2D configurations, by testing the acoustic limit of the code and by computing the regular part in the case of reflection on an infinite plane), yielding promising results, but has yet to be validated (numerically or experimentally) for 3D elastic cases.

In the case of an incident transversal wave, with a skew angle higher than the critical angle in diffraction, Snell's law of diffraction leads only to transversal diffracted waves. This case is also treated theoretically but the corresponding numerical code produces diverging results. Further investigations are necessary in order to solve this problem. In the meantime, an approximate solution is proposed, in order to obtain a less exact, yet physically meaningful result. This approximate solution still remains to be tested.

Conclusion and future work

The aim of this thesis is to propose and validate a generic and reliable elastodynamic diffraction model for infinite stress-free wedges, valid for all wedge angles and for 3D incidences, in order to be applied to high frequency simulation of ultrasonic geometry echoes. This is done by extending a method called the Spectral Functions (SF) method and proposing the corresponding numerical resolution schemes. The principal results of this thesis are summarized in the following.

In the first chapter of this manuscript, a review of high-frequency wedge diffraction models is done. First, the two main non-uniform asymptotic methods are described : Geometrical Elastodynamics (GE), which only model reflected and refracted rays and the Geometrical Theory of Diffraction (GTD), which accounts for diffraction but diverges at observation directions close to specular reflections. Then, some uniform solutions based on these models are presented. The Kirchhoff Approximation (KA), which produces a uniform scattered field but models diffraction inaccurately, the Physical Theory of Diffraction (PTD) which provides a good description of the scattered field in all directions but is computationally expensive for large scatterers, the Uniform Asymptotic Theory (UAT) which also provides a good description of the scattered field but is difficult to implement and finally the Uniform Theory of Diffraction (UTD) which is accurate, simple to implement and computationally cheap. For these reasons, UTD is the preferred uniform asymptotic model to model scattering from structures including wedges. Its accuracy relies on the existence of a reliable GTD wedge diffraction model. With that in mind, the two main existing wedge diffraction models, the Laplace Transform (LT) method and the Sommerfeld Integral (SI) method, are presented briefly. The LT method uses an integral formulation of the components of the displacement field in the entire space to derive a system of functional equations of which the Laplace transform of the displacement field is the solution. The SI method uses Sommerfeld's exact expression of the

elastodynamic potentials in the form of integrals to derive a different system of functional equations. In both cases, the corresponding systems are solved by decomposing the solutions as the sum of a singular function determined analytically and a regular function approached numerically. Neither method has been developed for an elastic wave incident on a wedge of angle higher than π.

In the second chapter of this manuscript, the Spectral Functions (SF) method is developed as a first step in the simpler case of an acoustic wave scattered by a soft (Dirichlet boundary conditions) or hard (Neumann boundary conditions) wedge of arbitrary angle. Similarly to the LT and SI methods, the SF method uses an integral formulation of the solution to derive a system of functional equations which is then solved semi-analytically by decomposing the solution as the sum of a singular function and a regular function. However, as opposed to the LT and SI methods, the SF method is valid for all wedge angles, including those higher than π. This is achieved by introducing a new angular variable $\tilde{\varphi}$ which depends on the wedge angle φ but has a different expression for $\varphi \leq \pi$ and $\varphi > \pi$. In the acoustic version of the SF method, the aforementioned integral formulation of the solution to the scattering problem is derived using a Fourier transform of the Helmoltz equation. This formulation is given with respect to two unknown functions called the spectral functions. A far-field asymptotic evaluation of this integral formulation leads to an expression of the GTD diffraction coefficient as a function of the spectral functions. The integral formulation is then injected into the problem's boundary conditions, yielding an integral system of functional equations of which the spectral functions are the solution. This system is then solved semi-analytically. This means that the spectral functions are decomposed as the sum of two terms : a singular function, which is determined analytically thanks to a recursive algorithm, and a regular function, which is approached numerically thanks to a Galerkin collocation method. Finally, the accuracy of the numerical approximation of the regular part is improved using a technique called the "propagation of the solution". The method is successfully validated by comparing the GTD diffraction coefficients obtained using the semi-analytical spectral functions method to the GTD diffraction coefficients derived from the exact solution given by Sommerfeld. The results obtained using the spectral functions method and those obtained using the analytical formula are almost identical, except for slight discrepancies which appear in certain cases for observation angles close to the wedge faces.

In the third chapter of the manuscript, the spectral functions method is applied to the more complex problem of elastic wave diffraction by a stress-free wedge of arbitrary angle. The main steps of the method are the same as in the previous chapter but the corresponding computations are more complex, since the spectral functions are now two-dimensional vectors and the incident, reflected

and edge-diffracted waves can be polarized longitudinally and transversally. These two propagation modes are coupled by the wedge boundary conditions, meaning that mode conversion occurs. For each given configuration, two diffraction coefficients are therefore computed : one for longitudinal diffracted waves and one for transversal diffracted waves. The absolute values of the diffraction coefficients obtained using the Spectral Functions (SF) code are compared to those obtained using the LT code, for wedge angles lower than π and the results are extremely close. However, the existing LT code is only valid for wedge angles lower than π. For wedge angles higher than π, the absolute values of the diffraction coefficients obtained using the SF code are compared to the diffraction coefficients extracted from the results of a finite elements code. In regions where the diffracted waves do not interfere with other waves and where the GTD evaluation is theoretically valid, both codes give very similar results. Finally, the absolute values and angular phases of the diffraction coefficients computed with the SF code are validated experimentally using the same measurements that were made to validate the LT code and are compared once more to the results of the LT code. The results of both codes are identical, except for a discrepancy near the wedge face in one case, and are very close to the experimental measurements.

In the fourth and final chapter of the manuscript, the spectral functions method is applied to the 3D case of elastic wave diffraction by a stress-free wedge, where the incident wave vector is not necessarily in the the plane normal to the wedge edge. In this case, the incident ray on the wedge edge produces a cone of diffracted rays called Keller's cone of diffraction for each scattered mode. The angle of this cone is determined by Snell's law of diffraction. According to Snell's law of diffraction, when the incident wave is transversal and the incident skew angle (i.e. the angle between the incident wave vector and the plane normal to the wedge edge) is higher than a certain angle called the critical angle, there is no diffracted longitudinal wave. The diffracted field then has imaginary branch points and extra care must be taken in dealing with these. The spectral functions method is developed in detail for the 3D case, for all types of incidences and for wedge angles higher and lower than π. An additional numerical approximation is proposed in order to compute the regular part of the spectral functions in the case of a transversal incident wave with a skew angle higher than the critical angle : the obtained results seem reasonable but have not been tested numerically or experimentally. The 3D spectral functions code is tested successfully in some particular cases. It produces identical results to the 2D code in 2D cases (the skew angle is set to 0) and to the exact solution for the "acoustic limit" (the longitudinal and transversal wave velocities are set to mimic acoustic wave propagation) and the regular part is well evaluated in the case of an infinite plane (the wedge angle is equal to π and there is no diffracted wave),

notably after the critical angle when using the previously mentioned additional approximation.

The spectral functions method provides a high frequency approximation of the waves scattered by a wedge. It is semi-analytical and is therefore applicable to configurations where fully numerical methods such as finite elements or finite differences fail because they are too expensive computationally. It can be used to treat the scattering of acoustic waves as well as elastic longitudinal or transversal waves.

The main advantage of the spectral functions method, as opposed to other GTD wedge-diffraction models, is that it has been developed for wedge angles lower and higher than π. A code developed for elastic waves can be used to treat the simpler case of acoustic waves. Finally, the method is generic and adaptable to more complex problems. However, the method also has some inconvenients. In some cases, it lacks precision for observation angles close to the wedge faces and it is less efficient with very small (i.e. smaller than 80^o in the elastic case) or very large (i.e. larger than 280^o in the elastic case) wedge angles. The Laplace Transform and Sommerfeld Integral methods deal better with small angles and with observation angles close to the wedge faces.

The results obtained during this thesis led to three publications in peer-reviewed journals [8, 9, 2] as well to two communications in international conferences with peer-reviewed proceedings [10, 11].

Some suggestions for future work are given below :

- In the final chapter of this thesis, the regular part of the spectral functions diverges in the case of an incident transversal wave with a skew angle higher than the critical angle for edge diffraction (angle linked to Snell's law of diffraction on the L wave Keller diffraction cone). Further investigations need to be made in order to find the cause of these divergences and a new method of computation could be proposed.

- A thorough numerical and/or experimental validation of the code implemented to treat the case of 3D diffraction of an elastic wave must be conducted and is currently in progress.

- The spectral functions method could be further extended to treat dihedral interfaces between two elastic materials. This would be the continuity of Lucien Rochery's internship, which Michel Darmon and I supervised. During the course of this internship, the theoretical developments concerning the scattering of acoustic and elastic waves by wedges with impedance boundary conditions were launched.

- The UTD model was developed by Audrey Kamta-Djakou [1] using the Sommerfeld Integral (SI) pole propagation algorithm. It should be adapted

to the SF method so it can be applied to 3D incidences. I have begun working on the integration of the 3D SF codes along with a UTD model in the NDT simulation platform CIVA. In order to deal with the finite extension of wedge edges in CIVA, a possibility is to use an incremental model such as the Huygens method or the Incremental Theory of Diffraction (ITD), which I have helped develop and validate in elastodynamics [2].

- The elastodynamic diffraction coefficients present a slight discontinuity at critical angles of reflection (angle linked to Snell's law of reflection on each wedge face), due to the presence of head waves. In the continuity of Fradkin et al. [3] and of Darmon [4], further investigations must be made in order to model the contribution of these waves correctly.

- In the final chapter, it was shown that for transversal incident waves with a skew angle higher than the critical angle for edge diffraction, an evanescent longitudinal wave is produced. The contribution of this wave could be evaluated or modeled.

- Following the ideas of Kamotskii [5], the Spectral Functions method could also be adapted to treat scattering by adjacent wedges for which other methods [6, 7] could also be studied.

APPENDIX A

Steepest Descent Method

The steepest descent method is an integral approximation technique where the integration contour is deformed into a contour γ called the steepest descent contour, which passes near a saddle-point of the integrated function. The method was first published by Debye [79] but the ideas were first suggested by Riemann in an unpublished note [80], which was printed later [81]. A description of the method can be found in English in the translated version of the Encyclopedia of Mathematics [82]. Useful results are stated here without demonstration.

The integral to be estimated is of the form :

$$I(\lambda) = \int_C f(z) e^{\lambda S(z)} \, dz \tag{A.1}$$

where C is the integration contour, S and f are analytical on all $\mathbb{C}^n$, except for eventually at a finite number of points, and $\lambda > 0$. The steepest descent contour γ must verify :

- C and γ must have the same endpoints,
- γ passes through at least one saddle point of S,
- $\mathrm{Im}(S(z))$ is constant on γ.

Le us denote $\mathbf{S_{xx}}(z)$ the hessian matrix of S, defined by :

$$\mathbf{S_{xx}}(z) = \left(\frac{\partial^2 S}{\partial x_i \partial x_j}(z) \right)_{1 \leq i,j \leq n}, \tag{A.2}$$

then z_0 is a non-degenerate saddle point of S if and only if :

$$\begin{cases} \nabla S(z_0) = 0 \\ \det \mathbf{S_{xx}}(z_0) \neq 0 \end{cases} \tag{A.3}$$

The following proposition is then true :

Proposition A.0.1. *Assume*

(i) *f and S are holomorphic on an open, bounded and simply connected subset $W_x \subset \mathbb{C}^n$ such that $I_x = W_x \cap \mathbb{R}^n$ is connected,*

(ii) *$Re(S(z))$ has a single maximum reached at exactly one point $z_0 \in I_x$,*

(iii) *z_0 is a non-degenerate saddle point of S.*

The following asymptotic evaluation then holds :

$$I(\lambda) \underset{\lambda \to +\infty}{=} \left(\frac{2\pi}{\lambda} \right)^{n/2} e^{\lambda S(z_0)} [f(z_0) + \mathcal{O}(\lambda^{-1})] \prod_{j=1}^{n} (-\mu_j)^{-1/2}, \tag{A.4}$$

where $(\mu_j)_{1 \leq j \leq n}$ are the eigen values of $\mathbf{S_{xx}}(z_0)$ and their square roots are defined by

$$|arg \sqrt{-\mu_j}| < \frac{\pi}{4}$$

Note that any if any singularities are crossed during deformation of contour C to contour γ, their contribution to the integral must be correctly taken into account.

APPENDIX B

Some preliminary results for the computation of the regular parts of the spectral functions

Outline of the current chapter

The coefficients of matrices $\mathbb{D}$ and $\mathbb{T}$ depend on the values of two elementary integrals. These values are expressed using two complex functions, rog and sog. Let us therefore begin by defining these new complex functions and giving their analytic properties, before presenting the details of the computation of these two elementary integrals.

B.1 Definition of rog and sog complex functions

Let us introduce $\mathrm{rog}(a)$ and $\mathrm{sog}(a)$ complex functions defined for $a > 1$ as

$$\mathrm{rog}(a) = \int_{-1}^{1} \frac{1}{a(1-x^2)+2ix}\,dx, \tag{B.1}$$

$$\mathrm{sog}(a) = \frac{1}{a}\left(\frac{\pi}{2} - \mathrm{rog}(a)\right) \tag{B.2}$$

These functions are used in the sequel to give an exact expression of the coefficients of matrices $\mathbb{D}(a,b)$ and $\mathbb{T}(a,b)$. Their analytic properties are given hereafter.

Lemma B.1.1. *The function* $\mathrm{rog}(a)$ *defined for* $a > 1$ *by*

$$\mathrm{rog}(a) = \int_{-1}^{1} \frac{1}{a(1-x^2)+2ix}\,dx$$

is holomorphic on $\mathbb{C}\setminus\{-1\}$ *and has the following property :*

For $x \neq \pm 1$,

$$\mathrm{rog}(a) = \frac{1}{\sqrt{a^2-1}} \ln(a + \sqrt{a^2-1}) \tag{B.3}$$

Proof The roots of the polynomial $a(1-x^2)+2ix, a \in \mathbb{C}^*$ are $x_\pm = \frac{1}{a}(i \pm \sqrt{a^2-1})$. When $a \notin \{-1,1\}$, these roots are distinct and formula (B.3) results from a classical integral computation. However, when $a = 1$, (B.1) yields $\mathrm{rog}(1) = 1$ whereas (B.3) presents a singularity. The indetermination is lifted by defining $z = \sqrt{1-1/a^2}$ in (B.3). We then have $a = \frac{1}{\sqrt{1-z^2}}$ (note that the variable change is therefore valid for $a = 1$ and not for $a = -1$) and :

$$\mathrm{rog(a)} = \frac{1}{2\mathrm{az}} \ln\left(\frac{1+\mathrm{z}}{1-\mathrm{z}}\right) \tag{B.4}$$

The Taylor series expansion at $z = 0$ leads to $\mathrm{rog}(1) = 1$. The rog function can therefore be extended to $\mathbb{C}\setminus\{-1\}$.

Lemma B.1.2. *The function* $\mathrm{sog}(x)$ *defined in* (B.2) *for* $x > 1$ *is holomorphic on* $\mathbb{C}\setminus\{-1\}$.

Proof sog function defined in (B.2) depends on the rog function which is holomorphic on $\mathbb{C}\setminus]-\infty,-1]$. To remove the indetermination near $x = 0$, let us define $y = \left(1-x^2\right)^{1/2}$. We then have $x = -i\left(y^2-1\right)^{1/2}$ using the same definition of the square root as in (2.17b). Thus,

$$\mathrm{sog}(x) = -\frac{\pi}{2}\frac{x}{y(y+1)} + \frac{1}{y}\mathrm{rog}(y) \quad \text{with} \quad y \to 1 \tag{B.5}$$

Knowing the analytic properties of functions rog and sog, we can now calculate the integrals $\int_{-1}^{1} \frac{\lambda t+\rho}{Q(t)}\,dt$ and $\int_{-1}^{1} \frac{\eta t+\psi}{P(t)}\,dt$.

B.2 Integral $\int_{-1}^{1} \frac{\lambda t+\rho}{Q(t)}\,dt$

The first elementary integral to compute is the following:

$$\int_{-1}^{1} \frac{\lambda t+\rho}{Q(t)}\,dt = \int_{-1}^{1} \frac{\lambda t}{iat^2+2\nu t-ia}\,dt + \int_{-1}^{1} \frac{\rho}{ia(t-q_+)(t-q_-)}\,dt, \tag{B.6}$$

where q_+, q_- are the roots of the polynomial function Q. They are given by:

$$q_\pm = \frac{1}{a}(i\nu \pm \sqrt{a^2-\nu^2}) \tag{B.7}$$

We have :

$$\begin{aligned}\int_{-1}^{1} \frac{\lambda t+\rho}{Q(t)}\,dt &= \int_{-1}^{1} \frac{\frac{\lambda}{2ia}(2iat+2\nu)}{iat^2+2\nu t-ia}\,dt + (\rho - \frac{\lambda\nu}{ia}) \int_{-1}^{1} \frac{1}{ia(t-q_+)(t-q_-)}\,dt \\ &= \frac{\lambda\pi}{2a} + \frac{1}{q_+-q_-}\left(\frac{\rho}{ia}+\frac{\lambda\nu}{a^2}\right)\int_{-1}^{1}\left(\frac{1}{t-q_+}-\frac{1}{t-q_-}\right)dt\end{aligned} \tag{B.8}$$

$q_\pm$ are substituted by their expression (B.7) :

$$\begin{aligned}\int_{-1}^{1} \frac{\lambda t+\rho}{Q(t)}\,dt &= \frac{\lambda\pi}{2a} + \frac{1}{2\sqrt{a^2-\nu^2}}\left(\frac{\lambda\nu}{a}-i\rho\right)\log\left(\frac{(1-q_+)(1+q_-)}{(1-q_-)(1+q_+)}\right) \\ &= \frac{\lambda\pi}{2a} + \frac{1}{2\sqrt{a^2-\nu^2}}\left(\frac{\lambda\nu}{a}-i\rho\right)\log\left(\frac{-\nu^2-(a-\sqrt{a^2-\nu^2})^2}{-\nu^2-(a+\sqrt{a^2-\nu^2})^2}\right) \\ &= \frac{\lambda\pi}{2a} + \frac{1}{2\sqrt{a^2-\nu^2}}\left(\frac{\lambda\nu}{a}-i\rho\right)\log\left(\frac{-a+\sqrt{a^2-\nu^2}}{-a-\sqrt{a^2-\nu^2}}\right) \\ &= \frac{\lambda\pi}{2a} + \frac{1}{\nu\sqrt{\frac{a^2}{\nu^2}-1}}\left(i\rho-\frac{\lambda\nu}{a}\right)\log\left(\frac{a}{\nu}+\sqrt{\frac{a^2}{\nu^2}-1}\right)\end{aligned} \tag{B.9}$$

Yielding finally :

$$\int_{-1}^{1} \frac{\lambda t+\rho}{Q(t)}\,dt = \frac{\lambda}{\nu}\mathrm{sog}(\frac{a}{\nu}) + i\frac{\rho}{\nu}\mathrm{rog}(\frac{a}{\nu}), \tag{B.10}$$

where the expressions of the complex functions rog and sog are defined by (B.3) and (B.2) respectively.

Note B.2.1. *In the particular case where $a \in]-i\infty, -i]$, $\nu \in i\mathbb{R}_+$, then $\frac{a}{\nu} \in]-\infty, -1]$ and expression (B.10) can not be used, since functions rog and sog are not defined on $]-\infty, -1]$. This issue can simply be avoided by defining $a = -ia'$ and $\nu = i\eta$ and*

noting that :

$$\int_{-1}^{1} \frac{\lambda t+\rho}{2\nu - ia(1-t^2)}\,dt = \int_{-1}^{1} \frac{\lambda t+\rho}{2i\eta - a'(1-t^2)}\,dt = -i\overline{\int_{-1}^{1} \frac{\bar{\lambda} t+\bar{\rho}}{2\eta - ia'(1-t^2)}}, \tag{B.11}$$

where the overline here denotes the complex conjugate. Equation (B.10) *can now be applied (using the definition of* $Q(t)$ *given in* (B.6)*) :*

$$\int_{-1}^{1} \frac{\lambda t+\rho}{2\tilde{\nu} - ia(1-t^2)}\,dt = -i\frac{\lambda}{\eta}\overline{sog(a'/\eta)} - \frac{\rho}{\eta}\overline{rog(a'/\eta)} \tag{B.12}$$

B.3 Integral $\int_{-1}^{1} \frac{\eta t+\psi}{P(t)}\,dt$

The second elementary integral is the following :

$$\begin{aligned}\int_{-1}^{1} \frac{\eta t+\psi}{P(t)}\,dt = &\int_{-1}^{1} \frac{\eta t}{(\nu\sin\tilde{\varphi}-b)t^2 - 2i\nu t\cos\tilde{\varphi} + \nu\sin\tilde{\varphi}+b}\,dt \\ &+ \int_{-1}^{1} \frac{\psi}{(\nu\sin\tilde{\varphi}-b)(t-p_+)(t-p_-)}\,dt,\end{aligned} \tag{B.13}$$

where p_+, p_- are the roots of the polynomial P. Their expression is :

$$p_\pm = \frac{\nu i\cos\tilde{\varphi} \pm \sqrt{b^2-\nu^2}}{\nu\sin\tilde{\varphi}-b} \tag{B.14}$$

We have

$$\begin{aligned}\int_{-1}^{1} \frac{\eta t+\psi}{P(t)}\,dt = &\int_{-1}^{1} \frac{\frac{\eta}{2(\nu\sin\tilde{\varphi}-b)}(2(\nu\sin\tilde{\varphi}-b)t - 2i\nu\cos\tilde{\varphi})}{(\nu\sin\tilde{\varphi}-b)t^2 - 2i\nu t\cos\tilde{\varphi} + \nu\sin\tilde{\varphi}+b}\,dt \\ &+ (\psi + \frac{\eta i\nu\cos\tilde{\varphi}}{\nu\sin\tilde{\varphi}-b})\int_{-1}^{1} \frac{dt}{(\nu\sin\tilde{\varphi}-b)(t-p_+)(t-p_-)} \\ = &\frac{i\eta}{\nu\sin\tilde{\varphi}-b}(\tilde{\varphi}-\frac{\pi}{2}) \\ &+ \frac{1}{p_+-p_-}\left(\frac{\psi}{\nu\sin\tilde{\varphi}-b} + \frac{\eta i\nu\cos\tilde{\varphi}}{(\nu\sin\tilde{\varphi}-b)^2}\right)\int_{-1}^{1}\left(\frac{1}{t-p_+} - \frac{1}{t-p_-}\right)dt\end{aligned} \tag{B.15}$$

$p_\pm$ are substituted by their expression (B.14) :

$$\begin{aligned}
\int_{-1}^{1} \frac{\eta t+\psi}{P(t)}\,dt =& \frac{i\eta}{\nu\sin\tilde{\varphi}-b}(\tilde{\varphi}-\frac{\pi}{2}) + \frac{1}{2\sqrt{b^2-\nu^2}}\left(\psi+\frac{\eta i\nu\cos\tilde{\varphi}}{\nu\sin\tilde{\varphi}-b}\right)\log\left(\frac{(1-p_+)(1+p_-)}{(1-p_-)(1+p_+)}\right)\\
=& \frac{i\eta}{\nu\sin\tilde{\varphi}-b}(\tilde{\varphi}-\frac{\pi}{2})\\
&+\frac{1}{2\sqrt{b^2-\nu^2}}\left(\psi+\frac{\eta i\nu\cos\tilde{\varphi}}{\nu\sin\tilde{\varphi}-b}\right)\log\left(\frac{-\nu^2\cos^2\tilde{\varphi}-(\nu\sin\tilde{\varphi}-b-\sqrt{b^2-\nu^2})^2}{-\nu^2\cos^2\tilde{\varphi}-(\nu\sin\tilde{\varphi}-b+\sqrt{b^2-\nu^2})^2}\right)\\
=& \frac{i\eta}{\nu\sin\tilde{\varphi}-b}(\tilde{\varphi}-\frac{\pi}{2}) + \frac{1}{2\sqrt{b^2-\nu^2}}\left(\psi+\frac{\eta i\nu\cos\tilde{\varphi}}{\nu\sin\tilde{\varphi}-b}\right)\log\left(\frac{b+\sqrt{b^2-\nu^2}}{b-\sqrt{b^2-\nu^2}}\right)\\
=& \frac{i\eta}{\nu\sin\tilde{\varphi}-b}(\tilde{\varphi}-\frac{\pi}{2}) + \frac{1}{\nu\sqrt{\frac{b^2}{\nu^2}-1}}\left(\psi+\frac{\eta i\nu\cos\tilde{\varphi}}{\nu\sin\tilde{\varphi}-b}\right)\log\left(\frac{b}{\nu}+\sqrt{\frac{b^2}{\nu^2}-1}\right)
\end{aligned} \tag{B.16}$$

Yielding finally

$$\int_{-1}^{1} \frac{\eta t+\psi}{P(t)}\,dt = \frac{i\eta}{\nu\sin\tilde{\varphi}-b}[\tilde{\varphi}-\frac{\pi}{2}+\cos\tilde{\varphi}\mathrm{rog}(\frac{b}{\nu})]+\frac{\psi}{\nu}\mathrm{rog}(\frac{b}{\nu}) \tag{B.17}$$

APPENDIX C

Computation details for the coefficients of matrix $\mathbb{D}(a,b)$

Outline of the current chapter

In each chapter of this manuscript, a matrix $\mathbb{D}$ appears, the coefficients of which must be determined analytically. These coefficients are linear combinations of integrals noted I_1^* to I_5^*, $* = L, T$. In this appendix, these integrals are defined and the details of their computation is given. Finally, expressions of the coefficients of matrix $\mathbb{D}$ in the acoustic case and 2D and 3D elastic cases are given, with respect to integrals I_1^* to I_5^*. In all the following, $\tilde{\nu} \in \{1, \nu_T, \tilde{\nu}_L, \tilde{\nu}_T\}$ depending on

whether we are considering the acoustic, 2D or 3D elastic case and whether we are computing the integral for $* = L$ or T (for example, when computing I_1^L for the 2D elastic case, $\tilde{v} = 1$ in the computations detailed in section C.1).

C.1 Integral I_1^*

Integral I_1^* is defined by :

$$I_1^* = \int_{-\infty}^{+\infty} \frac{y}{(y+ib)(y-ia)\sqrt{\tilde{v}^2+y^2}}\,dy \tag{C.1}$$

When $a+b \neq 0$, we have the simple elements decomposition :

$$\frac{y}{(y+ib)(y-ia)} = \frac{1}{a+b}\left(\frac{b}{y+ib} + \frac{a}{y-ia}\right), \tag{C.2}$$

which leads to

$$I_1^* = \frac{1}{a+b}\left(\int_{-\infty}^{+\infty} \frac{b}{(y+ib)\sqrt{\tilde{v}^2+y^2}}\,dy + \int_{-\infty}^{+\infty} \frac{a}{(y-ia)\sqrt{\tilde{v}^2+y^2}}\,dy\right) \tag{C.3}$$

In each of these integrals, the following variable change is applied :

$$\begin{aligned} y &= 2\tilde{v}\frac{t}{1-t^2} \\ \sqrt{\tilde{v}^2+y^2} &= \tilde{v}\left(\frac{1+t^2}{1-t^2}\right) \\ dy &= 2\tilde{v}\frac{1+t^2}{(1-t^2)^2}dt \end{aligned} \tag{C.4}$$

Yielding

$$\int_{-\infty}^{+\infty} \frac{dy}{(y-ia)\sqrt{\tilde{v}^2+y^2}} = \int_{-1}^{1} \frac{2\,dt}{2\tilde{v}t - ia(1-t^2)} \tag{C.5}$$

Finally, formula (B.10) is applied :

$$I_1^* = \frac{2ia}{(a+b)\tilde{v}}\mathrm{rog}(a/\tilde{v}) - \frac{2ib}{(a+b)\tilde{v}}\mathrm{rog}(b/\tilde{v}) \tag{C.6}$$

C.2 Integral I_2^*

Integral I_2^* is defined by :

$$I_2^* = \int_{-\infty}^{+\infty} \frac{y\sqrt{\tilde{\nu}^2 + y^2}}{(y+ib)(y-ia)}\, dy \tag{C.7}$$

Note that

$$I_2^* = \tilde{\nu}^2 \int_{-\infty}^{+\infty} \frac{y}{(y+ib)(y-ia)\sqrt{\tilde{\nu}^2+y^2}}\, dy + \int_{-\infty}^{+\infty} \frac{y^3}{(y+ib)(y-ia)\sqrt{\tilde{\nu}^2+y^2}}\, dy$$
$$I_2^* = \tilde{\nu}^2 I_1^* + I_3^*,$$

where integrals I_1^* and I_3^* are defined by equations (C.1) and (C.8) and their expressions are given by (C.6) and (C.18) respectively.

C.3 Integral I_3^*

Integral I_3^* is defined by :

$$I_3^* = \int_{-\infty}^{+\infty} \frac{y^3}{(y+ib)(y-ia)\sqrt{\tilde{\nu}^2+y^2}}\, dy \tag{C.8}$$

The simple elements decomposition (C.2) leads to

$$I_3^* = \frac{b}{a+b} \int_{-\infty}^{+\infty} \frac{y^2}{(y+ib)\sqrt{\tilde{\nu}^2+y^2}}\, dy + \frac{a}{a+b} \int_{-\infty}^{+\infty} \frac{y^2}{(y-ia)\sqrt{\tilde{\nu}^2+y^2}}\, dy \tag{C.9}$$

Once again, variable change (C.4) is applied

$$\int_{-\infty}^{+\infty} \frac{y^2}{(y-ia)\sqrt{\tilde{\nu}^2+y^2}}\, dy = \int_{-1}^{1} \frac{8\tilde{\nu}^2 t^2}{(1-t^2)^2(2\tilde{\nu}t - ia(1-t^2))}\, dt \tag{C.10}$$

The integrated functions can be decomposed as such :

$$\frac{t^2}{(1-t^2)^2(2\tilde{\nu}t - ia(1-t^2))} = \frac{\alpha}{1-t} + \frac{\beta}{1+t} + \frac{\gamma}{(1-t)^2} + \frac{\delta}{(1+t)^2} + \frac{\lambda t + \rho}{2\tilde{\nu}t - ia(1-t^2)}, \tag{C.11}$$

where the coefficients $\alpha, \beta, \gamma, \delta, \lambda, \rho$ will be determined in the sequel.

To determine γ, (C.11) is multiplied by $(1-t)^2$ and the result is evaluated at $t = 1$. Similarly, δ is determined by multiplying (C.11) by $(1+t)^2$ and evaluating

the result at $t=-1$:

$$\gamma = \frac{1}{8\tilde{\nu}} \tag{C.12a}$$

$$\delta = -\frac{1}{8\tilde{\nu}} \tag{C.12b}$$

The remaining terms are

$$\begin{aligned}
&\frac{\alpha}{1-t} + \frac{\beta}{1+t} + \frac{\lambda t+\rho}{2\tilde{\nu}t - ia(1-t^2)} \\
&= \frac{t^2}{(1-t^2)^2(2\tilde{\nu}t - ia(1-t^2))} - \frac{1}{8\tilde{\nu}(1-t)^2} + \frac{1}{8\tilde{\nu}(1+t)^2} \\
&= \frac{8\tilde{\nu}t^2 - (1+t)^2(2\tilde{\nu}t - ia(1-t^2)) + (1-t)^2(2\tilde{\nu}t - ia(1-t^2))}{8\tilde{\nu}(1-t^2)^2(2\tilde{\nu} - ia(1-t^2))} \\
&= \frac{iat}{2\tilde{\nu}(1-t^2)(2\tilde{\nu}t - ia(1-t^2))}
\end{aligned} \tag{C.13}$$

To determine α, (C.13) is multiplied by $(1-t)$ and the result is evaluated at $t=1$. Similarly, β is determined by multiplying (C.13) by $(1+t)$ and evaluating the result at $t=-1$:

$$\alpha = \frac{ia}{8\tilde{\nu}^2} \tag{C.14a}$$

$$\beta = \frac{ia}{8\tilde{\nu}^2} \tag{C.14b}$$

The remaining term is

$$\begin{aligned}
\frac{\lambda t+\rho}{2\tilde{\nu}t - ia(1-t^2)} &= \frac{iat}{2\tilde{\nu}(1-t^2)(2\tilde{\nu} - ia(1-t^2))} - \frac{ia}{8\tilde{\nu}^2(1-t)} - \frac{ia}{8\tilde{\nu}^2(1+t)} \\
&= \frac{2\tilde{\nu}iat - ia(2\tilde{\nu}t - ia(1-t^2))}{4\tilde{\nu}^2(1-t^2)(2\tilde{\nu}t - ia(1-t^2))} \\
&= \frac{-a^2}{4\tilde{\nu}^2(2\tilde{\nu}t - ia(1-t^2))}
\end{aligned} \tag{C.15}$$

The final coefficients can now be determined by a simple identification of the terms on the left and on the right of the last line of (C.15) :

$$\lambda = 0 \tag{C.16a}$$

$$\rho = -\frac{a^2}{4\tilde{\nu}^2} \tag{C.16b}$$

Finally, equation (B.10) can be applied to the remaining term $\frac{-2a^2}{2\tilde{\nu}t - ia(1-t^2)}$:

$$\int_{-\infty}^{+\infty} \frac{y^2}{(y-ia)\sqrt{\tilde{\nu}^2+y^2}}\,dy = 2ia\log\left(\frac{1+t_{\tilde{\nu}}}{1-t_{\tilde{\nu}}}\right) - 2i\frac{a^2}{\tilde{\nu}}\mathrm{rog}\left(\frac{a}{\tilde{\nu}}\right) \tag{C.17}$$

The value of $\int_{-\infty}^{+\infty} \frac{y^2}{(y+ib)\sqrt{\tilde{\nu}^2+y^2}}\,dy$ can be obtained by taking the complex conjugate of $\int_{-\infty}^{+\infty} \frac{y^2}{(y-ia)\sqrt{\tilde{\nu}^2+y^2}}\,dy$ replacing a with b in the result. The final result can then be obtained using (C.9) an (C.11) :

$$\begin{aligned} I_3^* &= i(a-b)\int_{-1}^{1}\left(\frac{1}{1-t}+\frac{1}{1+t}\right)dt + 2\tilde{\nu}\int_{-1}^{1}\left(\frac{1}{(1-t)^2}-\frac{1}{(1+t)^2}\right)dt \\ &\quad - \frac{2a^3}{a+b}\int_{-1}^{1}\frac{dt}{2\tilde{\nu}t - ia(1-t^2)} - \frac{2b^3}{a+b}\int_{-1}^{1}\frac{dt}{2\tilde{\nu}t + ib(1-t^2)} \end{aligned} \tag{C.18}$$

$$= 2i(a-b)\log\left(\frac{1+t_{\tilde{\nu}}}{1-t_{\tilde{\nu}}}\right) - \frac{2ia^3}{\tilde{\nu}(a+b)}\mathrm{rog}(a/\tilde{\nu}) + \frac{2ib^3}{\tilde{\nu}(a+b)}\mathrm{rog}(b/\tilde{\nu})$$

Note the appearance of the term $\log\left(\frac{1+t_{\tilde{\nu}}}{1-t_{\tilde{\nu}}}\right)$ which diverges when $t_{\tilde{\nu}} \to \pm 1$. This term will be compensated by another in the final expressions (Eqs. (C.37)-(C.38) and (C.40)-(C.43)) of the coefficients of matrix $\mathbb{D}$. In fact, (C.4) leads to :

$$\frac{2t_{\tilde{\nu}}}{1-t_{\tilde{\nu}}^2} = \frac{A}{\tilde{\nu}} \text{ and } A \to +\infty \text{ when } t_{\tilde{\nu}} \to 1 \tag{C.19}$$

and

$$1 - t_{\tilde{\nu}} = \frac{(1-t_{\tilde{\nu}})(1+t_{\tilde{\nu}})}{1+t_{\tilde{\nu}}} \sim \frac{\tilde{\nu}}{A} \tag{C.20}$$

so that, when computing $I_3^L - I_3^T$ (for instance), the following term appears

$$\ln\left(\frac{1+t_{\tilde{\nu}_L}}{1-t_{\tilde{\nu}_L}}\right) - \ln\left(\frac{1+t_{\tilde{\nu}_T}}{1-t_{\tilde{\nu}_T}}\right) \sim \ln\left(\frac{\tilde{\nu}_T}{\tilde{\nu}_L}\right) \tag{C.21}$$

C.4 Integral I_4^*

Integral I_4^* is defined by :

$$I_4^* = \int_{-\infty}^{+\infty} \frac{dy}{(y+ib)(y-ia)\sqrt{\tilde{v}^2+y^2}} \tag{C.22}$$

For $a+b \neq 0$,

$$\frac{1}{(y+ib)(y-ia)} = \frac{-i}{a+b}\left(\frac{1}{y-ia} - \frac{1}{y+ib}\right) \tag{C.23}$$

Substituting the above decomposition in (C.22), we get

$$I_4^* = \frac{i}{a+b}\int_{-\infty}^{+\infty}\left(\frac{1}{(y+ib)\sqrt{\tilde{v}^2+y^2}} - \frac{1}{(y-ia)\sqrt{\tilde{v}^2+y^2}}\right)dy \tag{C.24}$$

These integrals have been computed in section B.2. Using (B.10), we get :

$$I_4^* = \frac{2}{\tilde{v}(a+b)}\left(\mathrm{rog}\,(a/\tilde{v}) + \mathrm{rog}\,(b/\tilde{v})\right) \tag{C.25}$$

C.5 Integral I_5^*

Integral I_5^* is defined by :

$$I_5^* = \int_{-\infty}^{+\infty} \frac{y^2}{(y+ib)(y-ia)\sqrt{\tilde{v}^2+y^2}}\,dy \tag{C.26}$$

Using decomposition (C.23) we get

$$I_5^* = \frac{i}{a+b}\int_{-\infty}^{+\infty}\left(\frac{y^2}{(y+ib)\sqrt{\tilde{v}^2+y^2}} - \frac{y^2}{(y-ia)\sqrt{\tilde{v}^2+y^2}}\right)dy \tag{C.27}$$

These integrals have been computed at section C.3. Applying formula (C.17), we get :

$$I_5^* = 2\log\left(\frac{1+t_{\tilde{v}}}{1-t_{\tilde{v}}}\right) - \frac{2}{\tilde{v}(a+b)}\left[b^2\mathrm{rog}\,(b/\tilde{v}) + a^2\mathrm{rog}\,(a/\tilde{v})\right] \tag{C.28}$$

C.6 Integral I_6^*

Integral I_6^* is defined by :

$$I_6^* = \int_{-\infty}^{+\infty} \frac{\sqrt{\tilde{v}_*^2 + y^2}}{(y - ia)(y + ib)}\, dy \tag{C.29}$$

Note that

$$I_6^* = \tilde{v}_*^2 I_4^* + I_5^* \tag{C.30}$$

where integrals I_4^* and I_5^* are defined by equations (C.22) and (C.26) and their expressions are given by (C.25) and (C.28).

C.7 Continuation and conclusion of the computation of the coefficients of $\mathbb{D}(a, b)$

The final steps of the computation of the coefficients of matrices $\mathbb{D}_{lk}$ are given here. For each physical configuration presented in this manuscript, the coefficients can be expressed as linear combinations of integrals I_1^* to I_5^*. These combinations are given case by case in the following.

C.7.1 Acoustic case

In the second chapter of this manuscript, which deals with the diffraction of an acoustic wave, the expression of operator $\mathcal{D}(a, b)$ depends on whether the wedge is soft (Dirichlet boundary conditions) or hard (Neumann boundary conditions). Let us begin with the case of a soft wedge.

C.7.1.1 Dirichlet boundary conditions

In the case of Dirichlet boundary conditions, the expression of function $\mathcal{D}(a, b)$ is obtained by substituting (2.41) in (2.83) for $a > 1$ and $b > 1$:

$$\mathcal{D}(a, b) = \int_{-\infty}^{+\infty} \frac{1}{y + ib} \frac{1}{y - ia} \frac{1}{\zeta_0^0(iy)}\, dy. \tag{C.31}$$

According to (2.17), the above expression can be simplified using the relation

$$\zeta_0^0(iy) = -\sqrt{1 + y^2}. \tag{C.32}$$

By setting $\tilde{\nu} = 1$ in (C.22), we find :

$$\mathcal{T}(a,b) = -I_4^L \tag{C.33}$$

This integral is computed in section C.4 and its value is given by (C.25).

C.7.1.2 Neumann boundary conditions

In the case of Neumann boundary conditions, the expression of function $\mathcal{D}(a,b)$ is obtained by substituting (2.42) in (2.83) for $a > 1$ and $b > 1$:

$$\mathcal{D}(a,b) = \int_{-\infty}^{+\infty} \frac{dy}{(y+ib)(y-ia)}\, dy. \tag{C.34}$$

The result can be computed directly, by using Cauchy's residue theorem, yielding :

$$\mathcal{D}(a,b) = \frac{2\pi}{a+b} \tag{C.35}$$

C.7.2 2D elastic case

In the third chapter of this manuscript, which deals with the 2D diffraction of an elastic wave, the coefficients of matrix $\mathbb{D}(a,b)$ are linear combinations of integrals I_1^* to I_3^*. These linear combinations are given in the sequel. In all that follows, $\tilde{\nu} = 1$ when $* = L$ and $\tilde{\nu} = \nu_T$ when $* = T$. The first coefficient can be computed using Cauchy's integral formula :

$$\mathcal{D}_1(a,b) = \int_{-\infty}^{+\infty} \frac{dy}{(y+ib)(y-ia)} = \frac{2\pi}{a+b} \tag{C.36}$$

The two other coefficients are linear combinations of I_1^* to I_3^* :

$$\mathcal{D}_2(a,b) = \int_{-\infty}^{+\infty} \frac{-iy(1-2\mu\zeta_L(iy)\zeta_T(iy)+2\mu y^2)}{(y+ib)(y-ia)\zeta_T(iy)}\, dy = iI_1^T - 2i\mu(I_2^L - I_3^T) \tag{C.37}$$

and

$$\mathcal{D}_3(a,b) = \int_{-\infty}^{+\infty} \frac{iy(1-2\mu\zeta_L(iy)\zeta_T(iy)+2\mu y^2)}{(y+ib)(y-ia)\zeta_L(iy)}\, dy = -iI_1^L + 2i\mu(I_2^T - I_3^L) \tag{C.38}$$

This concludes computation of matrix coefficients $\mathbb{D}_{lk}$ for the 2D elastic case.

C.7.3 3D elastic case

In the fourth chapter of this manuscript, which deals with the 3D diffraction of an elastic wave, the coefficients of matrix $\mathbb{D}(a,b)$ are linear combinations of integrals I_1^* and I_6^*. These linear combinations are given in the sequel. In all that follows, $\tilde{\nu} = \tilde{\nu}_L$ when $* = L$ and $\tilde{\nu} = \tilde{\nu}_T$ when $* = T$.

The first coefficient can be computed using Cauchy's integral formula :

$$\mathcal{D}_1(a,b) = \int_{-\infty}^{+\infty} \frac{dy}{(y+ib)(y-ia)} = \frac{2\pi}{a+b} \tag{C.39}$$

The other coefficients are linear combinations of I_1^* to I_6^* :

$$\begin{aligned}\mathcal{D}_2^L(a,b) &= \int_{-\infty}^{+\infty} \frac{iy[1-2\mu(\zeta_L(iy)\zeta_T(iy)-y^2+\tau^2)]}{(y+ib)(y-ia)\zeta_L(iy)}\,dy \\ &= -i(1-2\mu\tau^2)I_1^L + 2i\mu(I_2^T - I_3^L)\end{aligned} \tag{C.40}$$

$$\begin{aligned}\mathcal{D}_2^T(a,b) &= \int_{-\infty}^{+\infty} \frac{iy[1-2\mu(\zeta_L(iy)\zeta_T(iy)-y^2+\tau^2)]}{(y+ib)(y-ia)\zeta_T(iy)}\,dy \\ &= -i(1-2\mu\tau^2)I_1^T + 2i\mu(I_2^L - I_3^T)\end{aligned} \tag{C.41}$$

$$\begin{aligned}\mathcal{D}_3^L(a,b) &= \tau\int_{-\infty}^{+\infty} \frac{1-2\mu(\zeta_L(iy)\zeta_T(iy)-y^2+\tau^2)}{(y+ib)(y-ia)\zeta_L(iy)}\,dy \\ &= -\tau(1-2\mu\tau^2)I_4^L - 2\mu\tau I_5^L + 2\mu\tau I_6^T\end{aligned} \tag{C.42}$$

$$\begin{aligned}\mathcal{D}_3^T(a,b) &= \tau\int_{-\infty}^{+\infty} \frac{1-2\mu(\zeta_L(iy)\zeta_T(iy)-y^2+\tau^2)}{(y+ib)(y-ia)\zeta_T(iy)}\,dy \\ &= -\tau(1-2\mu\tau^2)I_4^T - 2\mu\tau I_5^T + 2\mu\tau I_6^L\end{aligned} \tag{C.43}$$

This concludes computation of matrix coefficients $\mathbb{D}_{lk}$ for the 3D elastic case.

APPENDIX D

Computation details for the coefficients of matrix $\mathbb{T}(a,b)$

Outline of the current chapter

In each chapter of this manuscript, a matrix $\mathbb{T}(a,b)$ appears, the coefficients of which can be determined analytically. These coefficients are linear combinations of integrals J_1^* to J_8^*. In this appendix, these integrals are defined and the details

of their computation is given. Finally, expressions of the coefficients of matrix $\mathbb{T}(a,b)$ in the acoustic case and 2D and 3D elastic cases are given with respect to integrals J_1^* to J_8^*. In all the following, $\tilde{v} \in \{1, v_T, \tilde{v}_L, \tilde{v}_T\}$ depending on whether we are considering the acoustic, 2D or 3D elastic case and whether we are computing the integral for $* = L$ or T (for example, when computing J_1^L for the 2D elastic case, $\tilde{v} = 1$ in the computations detailed in section D.1).

D.1 Integral J_1^*

Integral J_1^* is defined by :

$$\begin{aligned} J_1^* &= \int_{-\infty}^{+\infty} \frac{y(\tilde{v}^2+y^2)}{(y-ia)[b-iy\cos\varphi+\sqrt{\tilde{v}^2+y^2}\sin\tilde{\varphi})]\sqrt{\tilde{v}^2+y^2}}\,dy \\ &= \tilde{v}^2 J_5^* + J_4^* \end{aligned} \tag{D.1}$$

where integral J_4^* and J_5^* are defined by equations (D.18) and (D.26) and their expressions are given (D.25) and (D.29) respectively.

D.2 Integral J_2^*

Integral J_2^* is defined by :

$$J_2 = \int_{-\infty}^{+\infty} \frac{y^2}{(y-ia)[b-iy\cos\tilde{\varphi}+\sqrt{\tilde{v}^2+y^2}\sin\tilde{\varphi})]}\,dy \tag{D.2}$$

Once again, variable change (C.4) is applied

$$J_2 = 8\tilde{v}^3 \int_{-1}^{1} \frac{t^2(t^2+1)}{(1-t^2)^2[b(1-t^2)-2\tilde{v}it\cos\tilde{\varphi}+\sin\tilde{\varphi}\tilde{v}(1+t^2)](2\tilde{v}t-ia(1-t^2))}\,dt \tag{D.3}$$

We have the following simple elements decomposition of the integrand:

$$\frac{t^2(1+t^2)}{(1-t)^2(1+t)^2P(t)Q(t)} = \frac{\alpha_2}{1-t} + \frac{\beta_2}{1+t} + \frac{\gamma_2}{(1-t)^2} + \frac{\delta_2}{(1+t)^2} + \frac{\eta_2 t+\psi_2}{P(t)} + \frac{\lambda_2 t+\rho_2}{Q(t)} \tag{D.4}$$

where $P(t) = b(1-t^2) - 2\tilde{v}it\cos\tilde{\varphi} + \sin\tilde{\varphi}\tilde{v}(1+t^2)$ and $Q(t) = 2\tilde{v}t - ia(1-t^2)$ and the coefficients of the decomposition are determined in the sequel.

The first step is to determine γ_2 by multiplying the above decomposition by $(1-t)^2$ and evaluating the result at $t = 1$. Similarly, δ_2 is determined by

multiplying (D.4) by $(1+t)^2$ and evaluating the result at $t=-1$:

$$\gamma_2 = \frac{e^{i(\pi/2-\tilde{\varphi})}}{8\tilde{v}^2} \tag{D.5a}$$

$$\delta_2 = \frac{e^{i(\pi/2+\tilde{\varphi})}}{8\tilde{v}^2} \tag{D.5b}$$

The remaining terms are

$$\begin{aligned}\frac{\alpha_2}{1-t}+\frac{\beta_2}{1+t}+\frac{\eta_2 t+\psi_2}{P(t)}+\frac{\lambda_2 t+\rho_2}{Q(t)} &= \frac{t^2(1+t^2)}{(1-t)^2(1+t)^2P(t)Q(t)}-\frac{e^{i(\pi/2-\tilde{\varphi})}}{8\tilde{v}^2(1-t)^2}-\frac{e^{i(\pi/2+\tilde{\varphi})}}{8\tilde{v}^2(1+t)^2}\\ &= \frac{2iab\sin\tilde{\varphi}t-\tilde{v}^2 i\sin(2\tilde{\varphi})t-ab\cos\tilde{\varphi}(1+t^2)}{4\tilde{v}^2P(t)Q(t)}\\ &+\frac{(2t\sin\tilde{\varphi}+(1+t^2)i\cos\varphi)(2a\cos\tilde{\varphi}t+ai\sin\tilde{\varphi}(1+t^2)-2bt)}{4\tilde{v}(1-t^2)P(t)Q(t)}\end{aligned} \tag{D.6}$$

α_2 is determined by multiplying the above decomposition by $(1-t)$ and evaluating the result at $t=1$. Similarly, β_2 is determined by multiplying the above equation by $(1+t)$ and evaluating the result at $t=-1$:

$$\alpha_2 = \frac{be^{-2i\tilde{\varphi}}-ae^{-i\tilde{\varphi}}}{8\tilde{v}^3} \tag{D.7a}$$

$$\beta_2 = \frac{ae^{i\tilde{\varphi}}-be^{2i\tilde{\varphi}}}{8\tilde{v}^3} \tag{D.7b}$$

The remaining terms are

$$\begin{aligned}
\frac{\eta_2 t+\psi_2}{P(t)}+\frac{\lambda_2 t+\rho_2}{Q(t)} &= \frac{2iab\sin\tilde{\varphi}t - i\tilde{v}^2\sin(2\tilde{\varphi})t - ab\cos\tilde{\varphi}(1+t^2)}{4\tilde{v}^2P(t)Q(t)} \\
&+ \frac{1}{4(1-t^2)\tilde{v}^3P(t)Q(t)}\Big([2\tilde{v}^2t\sin\tilde{\varphi}+\tilde{v}^2(1+t^2)i\cos\tilde{\varphi}] \\
&\times[2a\cos\tilde{\varphi}t+ai\sin\tilde{\varphi}(1+t^2)-2bt] \\
&-(b\cos(2\tilde{\varphi})t-at\cos\tilde{\varphi}-ib\sin(2\tilde{\varphi})+ia\sin\tilde{\varphi})P(t)Q(t)\Big)
\end{aligned}$$

$$\begin{aligned}
&= -\frac{b\cos(2\tilde{\varphi})t-at\cos\tilde{\varphi}-ib\sin(2\tilde{\varphi})+ia\sin\tilde{\varphi}}{4\tilde{v}^3P(t)Q(t)}[2\tilde{v}bt-iab(1-t^2)-2a\tilde{v}\cos\tilde{\varphi}t \\
&-a\tilde{v}i\sin\tilde{\varphi}(1+t^2)]+\frac{1}{4\tilde{v}(1-t^2)P(t)Q(t)}\Big([2t\sin\tilde{\varphi}+(1+t^2)i\cos\tilde{\varphi}][2a\cos\tilde{\varphi}t \\
&+ai\sin\tilde{\varphi}(1+t^2)-2bt]-(b\cos(2\tilde{\varphi})t-at\cos\tilde{\varphi}-ib\sin(2\tilde{\varphi})+ia\sin\tilde{\varphi}) \\
&\times(2\sin\tilde{\varphi}t(1+t^2)-4i\cos\tilde{\varphi}t^2)\Big)+\frac{2iab\sin\tilde{\varphi}t-i\tilde{v}^2\sin(2\tilde{\varphi})-ab\cos\tilde{\varphi}(1+t^2)}{4\tilde{v}^2P(t)Q(t)} \\
&= -\frac{b\cos(2\tilde{\varphi})t-at\cos\tilde{\varphi}-ib\sin(2\tilde{\varphi})+ia\sin\tilde{\varphi}}{4\tilde{v}^3P(t)Q(t)}[2\tilde{v}bt-iab(1-t^2)-2a\tilde{v}\cos\tilde{\varphi}t \\
&-a\tilde{v}i\sin\tilde{\varphi}(1+t^2)]+\frac{2iab\sin\tilde{\varphi}t-i\tilde{v}^2\sin(2\tilde{\varphi})t-ab\cos\tilde{\varphi}(1+t^2)}{4\tilde{v}^2P(t)Q(t)} \\
&+\frac{2ia\cos^2\tilde{\varphi}t-a\cos\tilde{\varphi}\sin\tilde{\varphi}(1+t^2)+2b\sin\tilde{\varphi}\cos(2\tilde{\varphi})t^2-2ib\cos\tilde{\varphi}\cos(2\tilde{\varphi})t}{4\tilde{v}P(t)Q(t)}
\end{aligned} \tag{D.8}$$

The last step is to determine constants $\eta_2, \psi_2, \lambda_2, \rho_2$. The method used is detailed in the sequel.

Let us note $N(t)$ a third degree polynomial and assume we have:

$$\frac{\eta t+\psi}{P(t)}+\frac{\lambda t+\rho}{Q(t)}=\frac{N(t)}{P(t)Q(t)} \tag{D.9}$$

The roots of polynomial P are $p_\pm$ and have been defined by equation (B.14). The roots of polynomial Q are $q_\pm$ and are defined by equation (B.7). Multiplying (D.9) by $P(t)$ and evaluating the result at $t=p_+$ and $t=p_-$ leads to the following

system

$$\begin{cases} \eta p_+ + \psi = \frac{N(p_+)}{Q(p_+)} \\ \eta p_- + \psi = \frac{N(p_-)}{Q(p_-)} \end{cases} \tag{D.10}$$

solved by

$$\begin{cases} \eta = \frac{1}{p_+ - p_-}\left[\frac{N(p_+)}{Q(p_+)} - \frac{N(p_-)}{Q(p_-)}\right] \\ \psi = \frac{N(p_+)}{Q(p_+)} - \eta p_+ \end{cases} \tag{D.11}$$

By symmetry of the roles of P and Q, we also have :

$$\begin{cases} \lambda = \frac{1}{q_+ - q_-}\left[\frac{N(q_+)}{P(q_+)} - \frac{N(q_-)}{P(q_-)}\right] \\ \rho = \frac{N(q_+)}{P(q_+)} - \lambda q_+ \end{cases} \tag{D.12}$$

In the present case, numerator N is given by equation (D.8) and coefficients $\eta_2, \psi_2, \lambda_2, \rho_2$ are deduced using (D.11) and (D.12).

Finally, using (B.10) and (B.17) :

$$\begin{aligned} J_2 =& 2i\cos\tilde{\varphi} A + 2i(a\sin\tilde{\varphi} - b\sin(2\tilde{\varphi}))\ln\left(\frac{1+t_{\tilde{\nu}}}{1-t_{\tilde{\nu}}}\right) \\ &+ \frac{8i\eta_2\tilde{\nu}^2}{b/\tilde{\nu} - \sin\tilde{\varphi}}\left(\frac{\pi}{2} - \tilde{\varphi} - \cos\tilde{\varphi}\,\mathrm{rog}(\frac{b}{\tilde{\nu}})\right) + 8\tilde{\nu}^2\psi_2\mathrm{rog}(\frac{b}{\tilde{\nu}}) \\ &+ 8\tilde{\nu}^2\left(\lambda_2\mathrm{sog}(a/\tilde{\nu}) + i\rho_2\mathrm{rog}(a/\tilde{\nu})\right), \end{aligned} \tag{D.13}$$

with $A \to +\infty$ and $t_{\tilde{\nu}} \to 1$. These diverging terms will be compensated in the final computation of matrix $\mathbb{T}$, as seen in section C.3.

D.3 Integral J_3^*

Integral J_3^* is defined by

$$J_3 = \int_{-\infty}^{+\infty} \frac{1}{(y - ia)[b - iy\cos\tilde{\varphi} + \sqrt{\tilde{\nu}^2 + y^2}\sin\tilde{\varphi}]}\, dy \tag{D.14}$$

Variable change (C.4) is applied

$$J_3 = 2\tilde{\nu}\int_{-1}^{1} \frac{1+t^2}{(2\tilde{\nu}t - ia(1-t^2))(b(1-t^2) - 2i\tilde{\nu}t\cos\tilde{\varphi} + \tilde{\nu}\sin\tilde{\varphi}(1+t^2))}\, dt \tag{D.15}$$

We have the following simple elements decomposition

$$\frac{1+t^2}{P(t)Q(t)} = \frac{\eta_3 t + \psi_3}{P(t)} + \frac{\lambda_3 t + \rho_3}{Q(t)} \tag{D.16}$$

The coefficients of the decomposition are obtained using (D.9), (D.11) and (D.12). Finally :

$$\begin{aligned} J_3 =& \frac{2i\eta_3}{b/\tilde{v} - \sin\tilde{\varphi}}\left(\frac{\pi}{2} - \tilde{\varphi} - \cos\tilde{\varphi}\,\mathrm{rog}(\frac{b}{\tilde{v}})\right) + 2\psi_3 \mathrm{rog}(\frac{b}{\tilde{v}}) \\ &+ 2\left(\lambda_3 \mathrm{sog}(a/\tilde{v}) + i\rho_3 \mathrm{rog}(a/\tilde{v})\right) \end{aligned} \tag{D.17}$$

D.4 Integral J_4^*

Integral J_4^* is defined by

$$J_4 = \int_{-\infty}^{+\infty} \frac{y^3}{(y-ia)\sqrt{y^2+\tilde{v}^2}(b - iy\cos\tilde{\varphi} + \sqrt{\tilde{v}^2+y^2}\sin\tilde{\varphi})}\,dy \tag{D.18}$$

Variable change (C.4) is applied

$$J_4 = 16\tilde{v}^3 \int_{-1}^{1} \frac{t^3}{(2\tilde{v}t - ia(1-t^2))(1-t^2)^2(b(1-t^2) - 2i\tilde{v}t\cos\tilde{\varphi} + \tilde{v}(1+t^2)\sin\tilde{\varphi})}\,dt \tag{D.19}$$

We have the following simple elements decomposition

$$\frac{t^3}{(1-t^2)^2 P(t)Q(t)} = \frac{\alpha_4}{1-t} + \frac{\beta_4}{1+t} + \frac{\gamma_4}{(1-t)^2} + \frac{\delta_4}{(1+t)^2} + \frac{\eta_4 t + \psi_4}{P(t)} + \frac{\lambda_4 t + \rho_4}{Q(t)} \tag{D.20}$$

The first step is to determine γ_4 by multiplying the above decomposition by $(1-t)^2$ and evaluating the result at $t = 1$. Similarly, δ_4 is determined by multiplying (D.20) by $(1+t)^2$ and evaluating the result at $t = -1$:

$$\gamma_4 = \frac{e^{i(\pi/2-\tilde{\varphi})}}{16\tilde{v}^2} \tag{D.21a}$$

$$\delta_4 = \frac{e^{i(\tilde{\varphi}-\pi/2)}}{16\tilde{v}^2} \tag{D.21b}$$

The remaining terms are

$$\frac{\alpha_4}{1-t}+\frac{\beta_4}{1+t}+\frac{\eta_4 t+\psi_4}{P(t)}+\frac{\lambda_4 t+\rho_4}{Q(t)}=\frac{8\tilde{\nu}^2t^3-[\sin\tilde{\varphi}(1+t^2)+2i\cos\tilde{\varphi}t]P(t)Q(t)}{8\tilde{\nu}^2(1-t^2)^2P(t)Q(t)}$$

$$\begin{aligned}=&\frac{\sin\tilde{\varphi}(1+t^2)+2i\cos\tilde{\varphi}t}{8\tilde{\nu}^2(1-t^2)P(t)Q(t)}\Big(a\tilde{\nu}(2\cos\tilde{\varphi}t+i\sin\tilde{\varphi}(1+t^2))-b(2\tilde{\nu}t-ia(1-t^2))\Big)\\&+\frac{4t^3-(\sin\tilde{\varphi}(1+t^2)+2i\cos\tilde{\varphi}t)(\sin\tilde{\varphi}t(1+t^2)-2i\cos\tilde{\varphi}t^2)}{4(1-t^2)^2P(t)Q(t)}\end{aligned}$$

$$\begin{aligned}=&\frac{2ait^2-b\sin\tilde{\varphi}t(1+t^2)-2ib\cos\tilde{\varphi}t^2}{4\tilde{\nu}(1-t^2)P(t)Q(t)}\\&+\frac{a\tilde{\nu}i\sin^2\tilde{\varphi}(1-t^2)+iab\sin\tilde{\varphi}(1+t^2)-2ab\cos\tilde{\varphi}t}{8\tilde{\nu}^2P(t)Q(t)}-\frac{\sin^2\tilde{\varphi}.t}{4P(t)Q(t)}\end{aligned}\tag{D.22}$$

α_4 is determined by multiplying the above decomposition by $(1-t)$ and evaluating the result at $t=1$. Similarly, β_4 is determined by multiplying the above equation by $(1+t)$ and evaluating the result at $t=-1$:

$$\alpha_4=\frac{be^{-2i\tilde{\varphi}}-ae^{-i\tilde{\varphi}}}{16\tilde{\nu}^3}\tag{D.23a}$$

$$\beta_4=\frac{be^{2i\tilde{\varphi}}-ae^{i\tilde{\varphi}}}{16\tilde{\nu}^3}\tag{D.23b}$$

The remaining terms are

$$\begin{aligned}\frac{\eta_4 t+\psi_4}{P(t)}+\frac{\lambda_4 t+\rho_4}{Q(t)} =& \frac{a\tilde{\nu} i\sin^2\tilde{\varphi}(1-t^2)+iab\sin\tilde{\varphi}(1+t^2)-2ab\cos\tilde{\varphi}t-2\tilde{\nu}^2\sin^2\tilde{\varphi}t}{8\tilde{\nu}^2P(t)Q(t)}\\ &+\frac{2ait^2-b\sin\tilde{\varphi}t(1+t^2)-2ib\cos\tilde{\varphi}t^2}{4\tilde{\nu}(1-t^2)P(t)Q(t)}\\ &-\frac{[b\cos(2\tilde{\varphi})-a\cos\tilde{\varphi}-bit\sin(2\tilde{\varphi})+ait\sin\tilde{\varphi}]P(t)Q(t)}{8\tilde{\nu}^3(1-t^2)P(t)Q(t)}\end{aligned}$$

$$\begin{aligned}=&\frac{a\tilde{\nu} i\sin^2\tilde{\varphi}(1-t^2)+iab\sin\tilde{\varphi}(1+t^2)-2ab\cos\tilde{\varphi}t-2\tilde{\nu}^2\sin^2\tilde{\varphi}}{8\tilde{\nu}^2P(t)Q(t)}\\ &+\frac{b\cos(2\tilde{\varphi})-a\cos\tilde{\varphi}-bit\sin(2\tilde{\varphi})+ait\sin\tilde{\varphi}}{8\tilde{\nu}^3P(t)Q(t)}\Big(2a\tilde{\nu}\cos\tilde{\varphi}t+\tilde{\nu}ai\sin\tilde{\varphi}(1+t^2)\\ &-2\tilde{\nu}bt-iab(1-t^2)\Big)+\frac{1}{4\tilde{\nu}(1-t^2)P(t)Q(t)}[2ait^2-b\sin\tilde{\varphi}t(1+t^2)-2ib\cos\tilde{\varphi}t^2\\ &-(b\cos(2\tilde{\varphi})-a\cos\tilde{\varphi}-bit\sin(2\tilde{\varphi})+ait\sin\tilde{\varphi})\Big(\sin\tilde{\varphi}t(1+t^2)-2it^2\cos\tilde{\varphi}\Big)]\end{aligned}$$

$$\begin{aligned}=&\frac{a\tilde{\nu} i\sin^2\tilde{\varphi}(1-t^2)+iab\sin\tilde{\varphi}(1+t^2)-2ab\cos\tilde{\varphi}t-2\tilde{\nu}^2\sin^2\tilde{\varphi}t}{8\tilde{\nu}^2P(t)Q(t)}\\ &+\frac{b\cos(2\tilde{\varphi})-a\cos\tilde{\varphi}-bit\sin(2\tilde{\varphi})+ait\sin\tilde{\varphi}}{8\tilde{\nu}^3P(t)Q(t)}\Big(2a\tilde{\nu}\cos\tilde{\varphi}t+\tilde{\nu}ai\sin\tilde{\varphi}(1+t^2)\\ &-2\tilde{\nu}bt+iab(1-t^2)\Big)\\ &+\frac{ai\sin^2\tilde{\varphi}t^2+a\cos\tilde{\varphi}\sin\tilde{\varphi}t-b\sin(2\tilde{\varphi})\cos\tilde{\varphi}t-ib\sin\tilde{\varphi}\sin(2\tilde{\varphi})t^2}{4\tilde{\nu}P(t)Q(t)}\end{aligned} \tag{D.24}$$

The final coefficients are deduced using (D.9), (D.11) and (D.12). Finally

$$\begin{aligned}J_4 =&2A\sin\tilde{\varphi}+2(b\cos(2\tilde{\varphi})-a\cos\tilde{\varphi})\ln\left(\frac{1+t_{\tilde{\nu}}}{1-t_{\tilde{\nu}}}\right)\\ &+\frac{16i\eta_4\tilde{\nu}^2}{b/\tilde{\nu}-\sin\tilde{\varphi}}\left(\frac{\pi}{2}-\tilde{\varphi}-\cos\tilde{\varphi}\,\mathrm{rog}(\frac{b}{\tilde{\nu}})\right)+16\tilde{\nu}^2\psi_4\mathrm{rog}(\frac{b}{\tilde{\nu}})\\ &+16\tilde{\nu}^2(\lambda_4\mathrm{sog}(a/\tilde{\nu})+i\rho_4\mathrm{rog}(a/\tilde{\nu}))\end{aligned} \tag{D.25}$$

D.5 Integral J_5^*

Integral J_5^* is defined by

$$J_5 = \int_{-\infty}^{+\infty} \frac{y}{(y-ia)\sqrt{\tilde{\nu}^2+y^2}[b-(iy\cos\tilde{\varphi}+\zeta(iy)\sin\tilde{\varphi})]}\,dy \tag{D.26}$$

Variable change (C.4) is applied :

$$J_5 = 4\tilde{\nu}\int_{-1}^{1} \frac{t}{P(t)Q(t)}\,dt \tag{D.27}$$

We have the following simple elements decomposition

$$\frac{t}{P(t)Q(t)} = \frac{\eta_5 t+\psi_5}{P(t)} + \frac{\lambda_5 t+\rho_5}{Q(t)} \tag{D.28}$$

Coefficients $\eta_5, \psi_5, \lambda_5, \rho_5$ are determined using (D.9), (D.11) and (D.12). Finally

$$\begin{aligned} J_5 =& \frac{4i\eta_5}{b/\tilde{\nu}-\sin\tilde{\varphi}}\left(\frac{\pi}{2}-\tilde{\varphi}-\cos\tilde{\varphi}\,\mathrm{rog}(\frac{b}{\tilde{\nu}})\right)+4\psi_5\mathrm{rog}(\frac{b}{\tilde{\nu}}) \\ &+4(\lambda_5\mathrm{sog}(a/\tilde{\nu})+i\rho_5\mathrm{rog}(a/\tilde{\nu})) \end{aligned} \tag{D.29}$$

D.6 Integral J_6^*

Integral J_6^* is defined by

$$J_6 = \int_{-\infty}^{+\infty} \frac{y}{(y-ia)[b-(iy\cos\tilde{\varphi}+\zeta(iy)\sin\tilde{\varphi})]}\,dy \tag{D.30}$$

Variable change (C.4) is applied

$$J_6 = 4\tilde{\nu}^2\int_{-1}^{1} \frac{t(1+t^2)}{(1-t^2)P(t)Q(t)}\,dt \tag{D.31}$$

We have the following simple elements decomposition

$$\frac{t(1+t^2)}{(1-t^2)P(t)Q(t)} = \frac{\alpha_6}{1-t}+\frac{\beta_6}{1+t}+\frac{\eta_6 t+\psi_6}{P(t)}+\frac{\lambda_6 t+\rho_6}{Q(t)} \tag{D.32}$$

α_6 is determined by multiplying the above decomposition by $(1-t)$ and evaluating the result at $t=1$. Similarly, β_6 is determined by multiplying the above

equation by $(1+t)$ and evaluating the result at $t=-1$:

$$\alpha_6 = \frac{e^{i(\pi/2-\tilde{\varphi})}}{4\tilde{\nu}^2} \tag{D.33a}$$

$$\beta_6 = \frac{e^{-i(\pi/2-\tilde{\varphi})}}{4\tilde{\nu}^2} \tag{D.33b}$$

The remaining terms are

$$\begin{aligned}
\frac{\eta_6 t+\psi_6}{P(t)} + \frac{\lambda_6 t+\rho_6}{Q(t)} &= \frac{2\tilde{\nu}^2 t(1+t^2) - (\sin\tilde{\varphi} + i\cos\tilde{\varphi}\, t)P(t)Q(t)}{2\tilde{\nu}^2(1-t^2)P(t)Q(t)} \\
&= -\frac{\sin\tilde{\varphi} + i\cos\tilde{\varphi}\, t}{2\tilde{\nu}^2 P(t)Q(t)}\Big(b(2\tilde{\nu}t - ia(1-t^2)) - a\tilde{\nu}(2\cos\tilde{\varphi}\, t + i\sin\tilde{\varphi}(1+t^2))\Big) \\
&+ \frac{1}{(1-t^2)P(t)Q(t)}\Big(t(1+t^2) - (\sin\tilde{\varphi} + i\cos\tilde{\varphi}\, t)(\sin\tilde{\varphi}\, t(1+t^2) - 2it^2\cos\tilde{\varphi})\Big) \\
&= -\frac{(\sin\tilde{\varphi} + i\cos\tilde{\varphi}\, t)}{2\tilde{\nu}^2 P(t)Q(t)}\Big(b(2\tilde{\nu}t - ia(1-t^2)) - a\tilde{\nu}(2\cos\tilde{\varphi}\, t + i\sin\tilde{\varphi}(1+t^2))\Big) \\
&+ \frac{\cos^2\tilde{\varphi}.t + i\sin\tilde{\varphi}\cos\tilde{\varphi}.t^2}{P(t)Q(t)}
\end{aligned} \tag{D.34}$$

The final coefficients are determined using (D.9), (D.11) and (D.12). Finally

$$\begin{aligned}
J_6 =& 2\sin\tilde{\varphi}\ln\left(\frac{1+t_{\tilde{\nu}}}{1-t_{\tilde{\nu}}}\right) \\
&+ \frac{4i\eta_6\tilde{\nu}}{b/\tilde{\nu} - \sin\tilde{\varphi}}\left(\frac{\pi}{2} - \tilde{\varphi} - \cos\tilde{\varphi}\,\mathrm{rog}(\frac{b}{\tilde{\nu}})\right) + 4\tilde{\nu}\psi_6\mathrm{rog}(\frac{b}{\tilde{\nu}}) \\
&+ 4\tilde{\nu}\,(\lambda_6\mathrm{sog}(a/\tilde{\nu}) + i\rho_6\mathrm{rog}(a/\tilde{\nu}))
\end{aligned} \tag{D.35}$$

D.7 Integral J_7^*

Integral J_7^* is defined by

$$J_7 = \int_{-\infty}^{+\infty} \frac{y^2}{(y-ia)\sqrt{\tilde{\nu}^2+y^2}[b - (iy\cos\tilde{\varphi} + \zeta(iy)\sin\tilde{\varphi})]}\, dy \tag{D.36}$$

Variable change (C.4) is applied

$$J_7 = 8\tilde{\nu}^2 \int_{-1}^{1} \frac{t^2}{(1-t^2)P(t)Q(t)}\, dt \tag{D.37}$$

We have the following simple elements decomposition

$$\frac{t^2}{(1-t^2)P(t)Q(t)} = \frac{\alpha_7}{1-t} + \frac{\beta_7}{1+t} + \frac{\eta_7 t + \psi_7}{P(t)} + \frac{\lambda_7 t + \rho_7}{Q(t)} \tag{D.38}$$

α_7 is determined by multiplying the above decomposition by $(1-t)$ and evaluating the result at $t = 1$. Similarly, β_7 is determined by multiplying the above equation by $(1+t)$ and evaluating the result at $t = -1$:

$$\alpha_7 = \frac{e^{i(\frac{\pi}{2}-\tilde{\varphi})}}{8\tilde{\nu}^2} \tag{D.39a}$$

$$\beta_7 = \frac{e^{i(\frac{\pi}{2}+\tilde{\varphi})}}{8\tilde{\nu}^2} \tag{D.39b}$$

The remaining terms are

$$\begin{aligned}
\frac{\eta_7 t + \psi_7}{P(t)} + \frac{\lambda_7 t + \rho_7}{Q(t)} &= \frac{8\tilde{\nu}^2 t^2 - 2(i\cos\tilde{\varphi} + \sin\tilde{\varphi} t)P(t)Q(t)}{8\tilde{\nu}^2(1-t^2)P(t)Q(t)} \\
&= -\frac{(i\cos\tilde{\varphi} + \sin\tilde{\varphi} t)}{4\tilde{\nu}^2 P(t)Q(t)}[b(2\tilde{\nu}t - ia(1-t^2)) - a\tilde{\nu}(2\cos\tilde{\varphi} t + i\sin\tilde{\varphi}(1+t^2))] \\
&+ \frac{\sin^2\tilde{\varphi} t^2 - i\cos\tilde{\varphi}\sin\tilde{\varphi} t}{2P(t)Q(t)}
\end{aligned} \tag{D.40}$$

The final coefficients are determined using (D.9), (D.11) and (D.12). Finally

$$\begin{aligned}
J_7 = {} & 2i\cos\tilde{\varphi}\log\left(\frac{1+t_{\tilde{\nu}}}{1-t_{\tilde{\nu}}}\right) \\
& \frac{8i\eta_7\tilde{\nu}}{b/\tilde{\nu} - \sin\tilde{\varphi}}\left(\frac{\pi}{2} - \tilde{\varphi} - \cos\tilde{\varphi}\,\mathrm{rog}(\frac{b}{\tilde{\nu}})\right) + 8\tilde{\nu}\psi_7\mathrm{rog}(\frac{b}{\tilde{\nu}}) \\
& + 8\tilde{\nu}\,(\lambda_7\mathrm{sog}(a/\tilde{\nu}) + i\rho_7\mathrm{rog}(a/\tilde{\nu}))
\end{aligned} \tag{D.41}$$

D.8 Integral J_8^*

Integral J_8^* is defined by

$$J_8 = \int_{-\infty}^{+\infty} \frac{dy}{(y-ia)\sqrt{\tilde{\nu}^2+y^2}[b-(iy\cos\tilde{\varphi}+\zeta(iy)\sin\tilde{\varphi})]} \tag{D.42}$$

Variable change (C.4) is applied

$$J_8 = 2\int_{-1}^{1} \frac{1-t^2}{P(t)Q(t)}\,dt \tag{D.43}$$

We have the following simple elements decomposition

$$\frac{1-t^2}{P(t)Q(t)} = \frac{\eta_8 t+\psi_8}{P(t)} + \frac{\lambda_8 t+\rho_8}{Q(t)} \tag{D.44}$$

The final coefficients are determined using (D.9), (D.11) and (D.12). Finally

$$\begin{aligned} J_8 =& \frac{2i\eta_8}{b-\tilde{\nu}\sin\tilde{\varphi}}\left(\frac{\pi}{2}-\tilde{\varphi}-\cos\tilde{\varphi}\,\mathrm{rog}(\frac{b}{\tilde{\nu}})\right)+2\frac{\psi_8}{\tilde{\nu}}\mathrm{rog}(\frac{b}{\tilde{\nu}}) \\ &+\frac{2}{\tilde{\nu}}\left(\lambda_8\,\mathrm{sog}(a/\tilde{\nu})+i\rho_8\,\mathrm{rog}(a/\tilde{\nu})\right) \end{aligned} \tag{D.45}$$

D.9 Continuation and conclusion of the computation of the coefficients of $\mathbb{T}(a,b)$

The final steps of the computation of the coefficients of matrices $\mathbb{T}_{lk}$ are given here. For each physical configuration presented in this manuscript, the coefficients can be expressed as linear combinations of integrals J_1^* to J_8^*. These combinations are given case by case in the following.

D.9.1 Acoustic case

In the second chapter of this manuscript, which deals with the diffraction of an acoustic wave, the expression of operator $\mathcal{T}(a,b)$ depends on whether the wedge is soft (Dirichlet boundary conditions) or hard (Neumann boundary conditions). Let us begin with the case of a soft wedge.

D.9.1.1 Dirichlet boundary conditions

In the case of Dirichlet boundary conditions, the expression of function $\mathcal{T}(a,b)$ is obtained by substituting (2.44) in (2.85) for $a>1$ and $b>1$:

$$\mathcal{T}(a,b)=\int_{-\infty}^{+\infty}\frac{1}{b-iy\cos 2\varphi+|\sin 2\varphi|\sqrt{1+y^2}}\,\frac{1}{y-ia}\,\frac{1}{\zeta_0^0(iy)}\,dy. \tag{D.46}$$

According to (2.17), the above expression can be simplified using the relation

$$\zeta_0^0(iy)=-\sqrt{1+y^2}. \tag{D.47}$$

By setting $\tilde{\nu}=1$ in (D.42), we find :

$$\mathcal{T}(a,b)=-J_8^1 \tag{D.48}$$

This integral is computed in section D.8 and its value is given by (D.45).

D.9.1.2 Neumann boundary conditions

In the case of Neumann boundary conditions, the expression of function $\mathcal{T}(a,b)$ is obtained by substituting (2.45) in (2.85) for $a>1$ and $b>1$:

$$\mathcal{T}(a,b)=\int_{-\infty}^{+\infty}\frac{iy\sin\varphi-\epsilon\zeta_0^0(iy)\cos\varphi}{b-iy\cos 2\varphi+|\sin 2\varphi|\sqrt{1+y^2}}\,\frac{1}{y-ia}\,\frac{1}{\zeta_0^0(iy)}\,dy. \tag{D.49}$$

where $\epsilon=\operatorname{sgn}\sin\varphi$. Once again, the expression above can be simplified using (D.47). By setting $\tilde{\nu}=1$ in (D.14) and (D.26), we find :

$$\mathcal{T}(a,b)=-\epsilon\cos\varphi J_3^1-i\sin\varphi J_5^1 \tag{D.50}$$

Integrals J_3^1 and J_5^1 are computed in sections D.3 and D.5 respectively. Their values are given by (D.17) and (D.29).

D.9.2 2D elastic case

In the third chapter of this manuscript, which deals with the 2D diffraction of an elastic wave, the coefficients of matrix $\mathbb{T}(a,b)$ are linear combinations of integrals J_1^* to J_5^*. These linear combinations are given in the sequel. In all that follows, $\tilde{\nu}=1$ when $*=L$ and $\tilde{\nu}=\nu_T$ when $*=T$.

D.9.2.1 L terms

We begin by computing terms derived from $\mathbf{tm}_L$, defined by (3.57).

$$\begin{aligned}\mathcal{T}_1^L(a,b) &= \int_{-\infty}^{+\infty} \frac{iy[2i\epsilon\cos(2\varphi).y\zeta_L(iy)+\sin(2\varphi)(y^2+\zeta_L^2(iy))]}{(y-ia)\zeta_L(iy)[b-(iy\cos\tilde{\varphi}+\zeta_L(iy)\sin\tilde{\varphi})]}\,dy \\ &= -2\epsilon\cos(2\varphi)J_2^L - i\sin(2\varphi)J_1^L - i\sin(2\varphi)J_4^L \end{aligned} \tag{D.51}$$

$$\begin{aligned}\mathcal{T}_2^L(a,b) &= \int_{-\infty}^{+\infty} \frac{2i\cos(2\varphi).y\zeta_L(iy)+\epsilon\sin(2\varphi)(y^2+\zeta_L^2(iy))}{(y-ia)[b-(iy\cos\tilde{\varphi}+\zeta_L(iy)\sin\tilde{\varphi})]}\,dy \\ &= -2i\cos(2\varphi)J_1^L + 2\epsilon\sin(2\varphi)J_2^L + \epsilon\sin(2\varphi)J_3^L \end{aligned} \tag{D.52}$$

$$\begin{aligned}\mathcal{T}_3^L(a,b) &= 2\int_{-\infty}^{+\infty} \frac{(1-\nu_T^2/2)iy+iy[i\epsilon\sin(2\varphi).y\zeta_L(iy)-\zeta_L^2(iy)\cos^2\varphi+y^2\sin^2\varphi]}{(y-ia)\zeta_L(iy)[b-(iy\cos\varphi+\zeta_L(iy)\sin\tilde{\varphi})]}\,dy \\ &= i(\nu_T^2-2\sin^2\varphi)J_5^L - 2\epsilon\sin(2\varphi)J_2^L + 2i\cos(2\varphi)J_4^L \end{aligned} \tag{D.53}$$

$$\begin{aligned}\mathcal{T}_4^L(a,b) &= 2\int_{-\infty}^{+\infty} \frac{(1-\nu_T^2/2)\epsilon+i\sin(2\varphi).y\zeta_L(iy)-\epsilon\zeta_L^2(iy)\cos^2\varphi+\epsilon y^2\sin^2\varphi}{(y-ia)[b-(iy\cos\varphi+\zeta_L(iy)\sin\tilde{\varphi})]}\,dy \\ &= \epsilon(2\sin^2\tilde{\varphi}-\nu_T^2)J_3^L - 2i\sin(2\varphi)J_1^L - 2\epsilon\cos(2\varphi)J_2^L \end{aligned} \tag{D.54}$$

D.9.2.2 T terms

Let us now compute terms derived from $\mathbf{tm}_T$, defined by (3.58).

$$\begin{aligned}\mathcal{T}_1^T(a,b) &= \int_{-\infty}^{+\infty} \frac{-2i\sin(2\varphi).y\zeta_T(iy)+\epsilon\cos(2\varphi)(y^2+\zeta_T^2(iy))}{(y-ia)[b-(iy\cos\varphi+\zeta_T(iy)\sin\tilde{\varphi})]}\,dy \\ &= 2i\sin(2\varphi)J_1^T + 2\epsilon\cos(2\varphi)J_2^T + \epsilon\nu_T^2\cos(2\varphi)J_3^T \end{aligned} \tag{D.55}$$

$$\begin{aligned}\mathcal{T}_2^T(a,b) &= \int_{-\infty}^{+\infty} \frac{iy[2i\epsilon\sin(2\varphi).y\zeta_T(iy)-\cos(2\varphi)(y^2+\zeta_T^2(iy))]}{(y-ia)\zeta_T(iy)[b-(iy\cos\tilde{\varphi}+\zeta_T(iy)\sin\tilde{\varphi})]}\,dy \\ &= -2\epsilon\sin(2\varphi)J_2^T + i\cos(2\varphi)J_1^T + i\cos(2\varphi)J_4^T \end{aligned} \tag{D.56}$$

$$\begin{aligned}\mathcal{T}_3^T(a,b) &= \int_{-\infty}^{+\infty} \frac{2i\cos(2\varphi).y\zeta_T(iy) + \epsilon\sin(2\varphi)(y^2+\zeta_T^2(iy))}{(y-ia)[b-(iy\cos\varphi+\zeta_T(iy)\sin\tilde{\varphi})]}\,dy \\ &= -2i\cos(2\varphi)J_1^T + 2\epsilon\sin(2\varphi)J_2^T + \epsilon\nu_T^2\sin(2\varphi)J_3^T \end{aligned} \tag{D.57}$$

$$\begin{aligned}\mathcal{T}_4^T(a,b) &= \int_{-\infty}^{+\infty} \frac{-iy[2i\epsilon\cos(2\varphi).y\zeta_T(iy) + \sin(2\varphi)(y^2+\zeta_T^2(iy))]}{(y-ia)\zeta_T(iy)[b-(iy\cos\tilde{\varphi}+\zeta_T(iy)\sin\tilde{\varphi})]}\,dy \\ &= 2\epsilon\cos(2\varphi)J_2^T + i\sin(2\varphi)J_1^T + i\sin(2\varphi)J_4^T \end{aligned} \tag{D.58}$$

This concludes computation of coefficients of matrix $\mathbb{T}_{kl}$ in the 2D elastic case. It has been verified that all diverging terms $\log\left(\frac{1+t_{\tilde{\nu}}}{1-t_{\tilde{\nu}}}\right)$ that appear in integrals J_1^* to J_5^* compensate each other when the L and T terms are summed, as explained in C.3.

D.9.3 3D elastic case

In the fourth chapter of this manuscript, which deals with the 3D diffraction of an elastic wave, the coefficients of matrix $\mathbb{T}(a,b)$ are linear combinations of integrals J_1^* to J_8^*. These linear combinations are given in the sequel. In all that follows, $\tilde{\nu} = \tilde{\nu}_L$ when $* = L$ and $\tilde{\nu} = \tilde{\nu}_T$ when $* = T$.

D.9.3.1 L terms

We begin by computing the terms derived from $\mathbf{tm}_L$, defined by (4.79).

$$\begin{aligned}\mathcal{T}_1^L(a,b) &= \mu\int_{-\infty}^{+\infty} \frac{iy[2i\epsilon\cos(2\varphi).y\zeta_L(iy) + \sin(2\varphi)(y^2+\zeta_L^2(iy))]}{(y-ia)\zeta_L(iy)[b-(iy\cos\varphi+\zeta_L(iy)\sin\tilde{\varphi})]}\,dy \\ &= -2\epsilon\mu\cos(2\varphi)J_2^L - i\mu\sin(2\varphi)(J_1^L + J_4^L) \end{aligned} \tag{D.59}$$

$$\begin{aligned}\mathcal{T}_2^L(a,b) &= \mu\int_{-\infty}^{+\infty} \frac{2i\cos(2\varphi).y\zeta_L(iy) + \epsilon\sin(2\varphi)(y^2+\zeta_L^2(iy))}{(y-ia)[b-(iy\cos\varphi+\zeta_L(iy)\sin\tilde{\varphi})]}\,dy \\ &= -2i\mu\cos(2\varphi)J_1^L + \epsilon\mu\sin(2\varphi)(2J_2^L + \tilde{\nu}_L^2 J_3^L) \end{aligned} \tag{D.60}$$

$$\begin{aligned}\mathcal{T}_3^L(a,b) &= \mu\tau\int_{-\infty}^{+\infty} \frac{2i\epsilon\cos(2\varphi).y\zeta_L(iy) + \sin(2\varphi)(y^2+\zeta_L^2(iy))}{(y-ia)\zeta_L(iy)[b-(iy\cos\varphi+\zeta_L(iy)\sin\tilde{\varphi})]}\,dy \\ &= \mu\tau[2i\epsilon\cos(2\varphi)J_6^L - \sin(2\varphi)(2J_7^L + \tilde{\nu}_L^2 J_8^L)] \end{aligned} \tag{D.61}$$

$$\begin{aligned}\mathcal{T}_4^L(a,b) &= (2\mu-1)\int_{-\infty}^{+\infty}\frac{iy}{(y-ia)\zeta_L(iy)[b-(iy\cos\varphi+\zeta_L(iy)\sin\tilde{\varphi})]}\,dy\\ &\quad+2\mu\int_{-\infty}^{+\infty}\frac{iy[i\epsilon\sin(2\varphi).y\zeta_L(iy)-\zeta_L^2(iy)\cos^2\varphi+y^2\sin^2\varphi]}{(y-ia)\zeta_L(iy)[b-(iy\cos\varphi+\zeta_L(iy)\sin\tilde{\varphi})]}\,dy\\ &= i(1-2\mu)J_5^L+2i\mu\cos^2\varphi J_1^L-2\epsilon\mu\sin(2\varphi)J_2^L-2i\mu\sin^2\varphi J_4^L\end{aligned}\tag{D.62}$$

$$\begin{aligned}\mathcal{T}_5^L(a,b) &= (2\mu-1)\int_{-\infty}^{+\infty}\frac{\epsilon}{(y-ia)[b-(iy\cos\varphi+\zeta_L(iy)\sin\tilde{\varphi})]}\,dy\\ &\quad+2\mu\int_{-\infty}^{+\infty}\frac{i\sin(2\varphi).y\zeta_L(iy)-\epsilon\cos^2\varphi\zeta_L^2(iy)+\epsilon\sin^2\varphi y^2}{(y-ia)[b-(iy\cos\varphi+\zeta_L(iy)\sin\tilde{\varphi})]}\,dy\\ &= \epsilon(2\mu-1-2\mu\tilde{v}_L^2\cos^2\varphi)J_3^L-2i\mu\sin(2\varphi)J_1^L-2\epsilon\mu\cos(2\varphi)J_2^L\end{aligned}\tag{D.63}$$

$$\begin{aligned}\mathcal{T}_6^L(a,b) &= \int_{-\infty}^{+\infty}\frac{\tau(2\mu-1)}{(y-ia)\zeta_L(iy)[b-(iy\cos\varphi+\zeta_L(iy)\sin\tilde{\varphi})]}\,dy\\ &\quad+2\mu\tau\int_{-\infty}^{+\infty}\frac{i\epsilon\sin(2\varphi).y\zeta_L(iy)-\cos^2\varphi\zeta_L^2(iy)+\sin^2\varphi y^2}{(y-ia)\zeta_L(iy)[b-(iy\cos\varphi+\zeta_L(iy)\sin\tilde{\varphi})]}\,dy\\ &= \tau(\lambda+2\mu\tilde{v}_L^2\cos^2\varphi)J_8^L+2\mu\tau[i\epsilon\sin(2\varphi)J_6^L+\cos(2\varphi)J_7^L]\end{aligned}\tag{D.64}$$

$$\begin{aligned}\mathcal{T}_7^L(a,b) &= -2\mu\tau\int_{-\infty}^{+\infty}\frac{\epsilon iy\zeta_L(iy)\cos\varphi+y^2\sin\varphi}{(y-ia)\zeta_L(iy)[b-(iy\cos\varphi+\zeta_L(iy)\sin\tilde{\varphi})]}\,dy\\ &= -2\mu\tau(\sin\varphi J_7^L-i\epsilon\cos\varphi J_6^L)\end{aligned}\tag{D.65}$$

$$\begin{aligned}\mathcal{T}_8^L(a,b) &= -2\mu\tau\int_{-\infty}^{+\infty}\frac{i\epsilon y\sin\varphi-\zeta_L(iy)\cos\varphi}{(y-ia)[b-(iy\cos\varphi+\zeta_L(iy)\sin\tilde{\varphi})]}\,dy\\ &= -2\mu\tau[i\epsilon\sin\varphi J_6^L+\cos\varphi(J_7^L+\tilde{v}_L^2J_8^L)]\end{aligned}\tag{D.66}$$

$$\begin{aligned}\mathcal{T}_9^L(a,b) &= 2\mu\tau^2\int_{-\infty}^{+\infty}\frac{iy\sin\varphi-\epsilon\zeta_L(iy)\cos\varphi}{(y-ia)\zeta_L(iy)[b-(iy\cos\varphi+\zeta_L(iy)\sin\tilde{\varphi})]}\,dy\\ &= 2\mu\tau^2[i\sin\varphi J_5^L+\epsilon\cos\varphi J_3^L]\end{aligned}\tag{D.67}$$

D.9.3.2 TH terms

Let us now compute terms derived from $\mathbf{tm}_{TH}$, defined by (4.80).

$$\begin{aligned}\mathcal{T}_1^{TH}(a,b) &= \mu\left(1+\frac{\tau^2}{\tilde{\nu}_T^2}\right)\int_{-\infty}^{+\infty}\frac{-2i\sin(2\varphi).y\zeta_T(iy)+\epsilon\cos(2\varphi)(y^2+\zeta_T^2(iy))}{(y-ia)[b-(iy\cos\varphi+\zeta_T(iy)\sin\tilde{\varphi})]}\,dy\\ &= \mu\left(1+\frac{\tau^2}{\tilde{\nu}_T^2}\right)[2i\sin(2\varphi)J_1^T+\epsilon\cos(2\varphi)(2J_2^T+\tilde{\nu}_T^2J_3^T)] \qquad \text{(D.68)}\end{aligned}$$

$$\begin{aligned}\mathcal{T}_2^{TH}(a,b) &= \mu\left(1+\frac{\tau^2}{\tilde{\nu}_T^2}\right)\int_{-\infty}^{+\infty}\frac{iy[2i\epsilon\sin(2\varphi).y\zeta_T(iy)-\cos(2\varphi)(y^2+\zeta_T^2(iy))]}{(y-ia)\zeta_T(iy)[b-(iy\cos\varphi+\zeta_T(iy)\sin\tilde{\varphi})]}\,dy\\ &= \mu\left(1+\frac{\tau^2}{\tilde{\nu}_T^2}\right)[-2\epsilon\sin(2\varphi)J_2^T+i\cos(2\varphi)(J_1^T+J_4^T)] \qquad \text{(D.69)}\end{aligned}$$

$$\begin{aligned}\mathcal{T}_4^{TH}(a,b) &= \mu\left(1+\frac{\tau^2}{\tilde{\nu}_T^2}\right)\int_{-\infty}^{+\infty}\frac{2i\cos(2\varphi).y\zeta_T(iy)+\epsilon\sin(2\varphi)(y^2+\zeta_T^2(iy))}{(y-ia)[b-(iy\cos\varphi+\zeta_T(iy)\sin\tilde{\varphi})]}\,dy\\ &= \mu\left(1+\frac{\tau^2}{\tilde{\nu}_T^2}\right)[-2i\cos(2\varphi)J_1^T+\epsilon\sin(2\varphi)(2J_2^T+\tilde{\nu}_TJ_3^T)] \qquad \text{(D.70)}\end{aligned}$$

$$\begin{aligned}\mathcal{T}_5^{TH}(a,b) &= \mu\left(1+\frac{\tau^2}{\tilde{\nu}_T^2}\right)\int_{-\infty}^{+\infty}\frac{-iy[2i\epsilon\cos(2\varphi).y\zeta_T(iy)+\sin(2\varphi)(y^2+\zeta_T^2(iy))]}{(y-ia)\zeta_T(iy)[b-(iy\cos\varphi+\zeta_T(iy)\sin\tilde{\varphi})]}\,dy\\ &= \mu\left(1+\frac{\tau^2}{\tilde{\nu}_T^2}\right)[2\epsilon\cos(2\varphi)J_2^T+i\sin(2\varphi)(J_1^T+J_4^T)] \qquad \text{(D.71)}\end{aligned}$$

$$\begin{aligned}\mathcal{T}_7^{TH}(a,b) &= \mu\tau\left(1+\frac{\tau^2}{\tilde{\nu}_T^2}\right)\int_{-\infty}^{+\infty}\frac{\sin\varphi\zeta_T(iy)+i\epsilon\cos\varphi.y}{(y-ia)[b-(iy\cos\varphi+\zeta_T(iy)\sin\tilde{\varphi})]}\\ &= -\mu\tau\left(1+\frac{\tau^2}{\tilde{\nu}_T^2}\right)[i\epsilon\cos\varphi J_6^T-\sin\varphi(J_7^T+\tilde{\nu}_T^2J_8^T)] \qquad \text{(D.72)}\end{aligned}$$

$$\mathcal{T}_8^{TH}(a,b) = \mu\tau\left(1+\frac{\tau^2}{\tilde{v}_T^2}\right)\int_{-\infty}^{+\infty}\frac{\cos\varphi.y^2 - i\epsilon\sin\varphi.y\zeta_T(iy)}{(y-ia)\zeta_T(iy)[b-(iy\cos\varphi+\zeta_T(iy)\sin\tilde{\varphi})]}$$
$$= \mu\tau\left(1+\frac{\tau^2}{\tilde{v}_T^2}\right)[i\epsilon\sin\varphi J_6^T + \cos\varphi J_7^T] \tag{D.73}$$

In addition, we have

$$\mathcal{T}_3^{TH} = \mathcal{T}_6^{TH} = \mathcal{T}_9^{TH} = 0$$

D.9.3.3 TV terms

Finally, we compute terms derived from $\mathbf{tm}_{TV}$, defined by (4.81).

$$\mathcal{T}_1^{TV}(a,b) = \mu\frac{\tau^2}{\tilde{v}_T^2}\int_{-\infty}^{+\infty}\frac{iy[2i\epsilon\cos(2\varphi).y\zeta_T(iy)+\sin(2\varphi)(y^2+\zeta_T^2(iy))]}{(y-ia)\zeta_T(iy)[b-(iy\cos\varphi+\zeta_T(iy)\sin\tilde{\varphi})]}dy$$
$$= -\mu\frac{\tau^2}{\tilde{v}_T^2}[2\epsilon\cos(2\varphi)J_2^T + i\sin(2\varphi)(J_1^T+J_4^T)] \tag{D.74}$$

$$\mathcal{T}_2^{TV}(a,b) = \mu\frac{\tau^2}{\tilde{v}_T^2}\int_{-\infty}^{+\infty}\frac{2i\cos(2\varphi).y\zeta_T(iy)+\epsilon\sin(2\varphi)(y^2+\zeta_T^2(iy))}{(y-ia)[b-(iy\cos\varphi+\zeta_T(iy)\sin\tilde{\varphi})]}dy$$
$$= \mu\frac{\tau^2}{\tilde{v}_T^2}[-2i\cos(2\varphi)J_1^T + \epsilon\sin(2\varphi)(2J_2^T+\tilde{v}_T^2J_3^T)] \tag{D.75}$$

$$\mathcal{T}_3^{TV}(a,b) = -\mu\tau\int_{-\infty}^{+\infty}\frac{2i\epsilon\cos(2\varphi).y\zeta_T(iy)+\sin(2\varphi)(y^2+\zeta_T^2(iy))}{(y-ia)\zeta_L(iy)[b-(iy\cos\varphi+\zeta_T(iy)\sin\tilde{\varphi})]}dy$$
$$= \mu\tau[\sin(2\varphi)(2J_7^T+\tilde{v}_T^2J_8^T) - 2i\epsilon\cos(2\varphi)J_6^T] \tag{D.76}$$

$$\mathcal{T}_4^{TV}(a,b) = 2\mu\frac{\tau^2}{\tilde{v}_T^2}\int_{-\infty}^{+\infty}\frac{iy[i\epsilon\sin(2\varphi).y\zeta_T(iy)-\zeta_T^2(iy)\cos^2\varphi+y^2\sin^2\varphi]}{(y-ia)\zeta_T(iy)[b-(iy\cos\varphi+\zeta_T(iy)\sin\tilde{\varphi})]}dy$$
$$= 2\mu\frac{\tau^2}{\tilde{v}_T^2}[i\cos^2\varphi J_1^T - \epsilon\sin(2\varphi)J_2^T - i\sin^2\varphi J_4^T] \tag{D.77}$$

$$\mathcal{T}_5^{TV}(a,b) = 2\mu\frac{\tau^2}{\tilde{\nu}_T^2}\int_{-\infty}^{+\infty}\frac{i\sin(2\varphi).y\zeta_T(iy) - \epsilon\cos^2\varphi\zeta_T^2(iy) + \epsilon\sin^2\varphi y^2}{(y-ia)[b-(iy\cos\varphi+\zeta_T(iy)\sin\tilde{\varphi})]}\,dy$$
$$= -2\mu\frac{\tau^2}{\tilde{\nu}_T^2}[i\sin(2\varphi)J_1^T + \epsilon\cos(2\varphi)J_2^T + \tilde{\nu}_T^2\cos^2\varphi J_3^T] \tag{D.78}$$

$$\mathcal{T}_6^{TV}(a,b) = -2\mu\tau\int_{-\infty}^{+\infty}\frac{i\epsilon\sin(2\varphi).y\zeta_T(iy) - \cos^2\varphi\zeta_T^2(iy) + \sin^2\varphi y^2}{(y-ia)\zeta_T(iy)[b-(iy\cos\varphi+\zeta_T(iy)\sin\tilde{\varphi})]}\,dy$$
$$= -2\mu\tau[\tilde{\nu}_T^2\cos^2\varphi J_8^T + i\epsilon\sin(2\varphi)J_6^T + \cos(2\varphi)J_7^T] \tag{D.79}$$

$$\mathcal{T}_7^{TV}(a,b) = \mu\tau\left(1-\frac{\tau^2}{\tilde{\nu}_T^2}\right)\int_{-\infty}^{+\infty}\frac{i\epsilon\cos\varphi.y\zeta_T(iy) + \sin\varphi y^2}{(y-ia)\zeta_T(iy)[b-(iy\cos\varphi+\zeta_T(iy)\sin\tilde{\varphi})]}\,dy$$
$$= -\mu\tau\left(1-\frac{\tau^2}{\tilde{\nu}_T^2}\right)[i\epsilon\cos\varphi J_6^T - \sin\varphi J_7^T] \tag{D.80}$$

$$\mathcal{T}_8^{TV}(a,b) = \mu\tau\left(1-\frac{\tau^2}{\tilde{\nu}_T^2}\right)\int_{-\infty}^{+\infty}\frac{\cos\varphi.\zeta_T(iy) - i\epsilon\sin\varphi y}{(y-ia)[b-(iy\cos\varphi+\zeta_T(iy)\sin\tilde{\varphi})]}\,dy$$
$$= \mu\tau\left(1-\frac{\tau^2}{\tilde{\nu}_T^2}\right)[\cos\varphi(J_7^T + \tilde{\nu}_T^2 J_8^T) + i\epsilon\sin\varphi J_6^T] \tag{D.81}$$

$$\mathcal{T}_9^{TV}(a,b) = -\mu(\tilde{\nu}_T^2-\tau^2)\int_{-\infty}^{+\infty}\frac{\epsilon\cos\varphi.\zeta_T(iy) - i\sin\varphi y}{(y-ia)\zeta_T(iy)[b-(iy\cos\varphi+\zeta_T(iy)\sin\tilde{\varphi})]}\,dy$$
$$= \mu(\tilde{\nu}_T^2-\tau^2)[\epsilon\cos\varphi J_3^T + i\sin\varphi J_5^T] \tag{D.82}$$

This concludes computation of coefficients of matrix $\mathbb{T}_{kl}$ in the 3D elastic case. It has been verified that all diverging terms that appear in integrals J_1^* to J_8^* compensate each other when the L, TH and TV terms are summed.

Bibliography

[1] A. Kamta-Djakou. "Modélisation des effets de diffraction pour le calcul des échos de géométrie en CND par ultrasons". PhD thesis. Université du Maine, 2016.

[2] M. Darmon, A. Kamta-Djakou, S. Chehade, C. Potel, and L. Fradkin. "Two Elastodynamic Incremental Models: The Incremental Theory of Diffraction and a Huygens Method". In: *IEEE Transactions on Ultrasonics, Ferroelectrics, and Frequency Control* 66.5 (2019), pp. 998–1005.

[3] L. J. Fradkin, M. Darmon, S. Chatillon, and P. Calmon. "A semi-numerical model for near-critical angle scattering". In: *Journal of the Acoustical Society of America* 139.1 (2016), pp. 115–127.

[4] M. Darmon. "Modeling of propagation and scattering of ultrasonic waves for non-destructive material testing". Habilitation thesis. Université Paris-Sud, 2015.

[5] V. V. Kamotskii. "Application of the spectral function method to the problem of scattering on two wedges". In: *Journal of Mathematical Sciences* 138.2 (2006), pp. 5514–5523.

[6] J. M. L. Bernard. "A spectral approach for scattering by impedance polygons". In: *The Quarterly Journal of Mechanics and Applied Mathematics* 59.4 (2006), pp. 517–550.

[7] V. A. Borovikov and B. Ye. Kinber. *Geometrical theory of diffraction*. Institution of electrical engineers, 1994.

[8] S. Chehade, A. Kamta-Djakou, M. Darmon, and G. Lebeau. "The spectral functions method for acoustic wave diffraction by a stress-free wedge : theory and validation". In: *Journal of Computational Physics* 377 (2018), pp. 200–218. URL: https://doi.org/10.1016/j.jcp.2018.10.040.

[9] S. Chehade, M. Darmon, and G. Lebeau. "2D elastic plane-wave diffraction by a stress-free wedge of arbitrary angle". In: *Journal of Computational Physics* 394 (2019), pp. 532–558. URL: https://doi.org/10.1016/j.jcp.2019.06.016.

[10] S. Chehade, M. Darmon, G. Lebeau, and L. Fradkin. "The spectral functions method for elastic plane wave diffraction by a wedge". In: *2018 Days on Diffraction*. 2018.

[11] S. Chehade, M. Darmon, and G. Lebeau. "The spectral functions method for elastic plane wave diffraction by a wedge". In: *Journal of Physics: Conference Series AFPAC 2018*. 2019.

[12] A. K. Gautesen and L. J. Fradkin. "Diffraction by a Two-Dimensional Traction-Free Elastic Wedge". In: *SIAM Journal of Applied Mathematics* 70 (Jan. 2010), pp. 3065–3085.

[13] M. Darmon, N. Leymarie, S. Chatillon, and S. Mahaut. "Modelling of scattering of ultrasounds by flaws for NDT". In: *UltrasonicWave Propagation in Non Homogeneous Media*. Springer Proceedings in Physics, 2009.

[14] J. B. Keller. "Geometrical Theory of Diffraction*". In: *J. Opt. Soc. Am.* 52.2 (Feb. 1962), pp. 116–130. URL: http://www.osapublishing.org/abstract.cfm?URI=josa-52-2-116.

[15] J. D. Achenbach and A. K. Gautesen. "Geometrical Theory of diffraction for three-D elastodynamics". In: *Journal of the Acoustical Society of America* 62.2 (1977), pp. 413–421. URL: http://asa.scitation.org/doi/10.1121/1.381332.

[16] J. D. Achenbach, A. K Gautesen, and H. McMaken. *Ray methods for waves in elastic solids: with applications to scattering by cracks*. Pitman advanced publishing program, 1982.

[17] B. B. Baker and E. T. Copson. *The Mathematical Theory of Huygens' Principle*. Oxford University Press, 1950.

[18] L. Schmerr and S.-J. Song. *Ultrasonic nondestructive evaluation systems*. Springer, 2007.

[19] V. Dorval, S. Chatillon, B. Lu, M. Darmon, and S. Mahaut. "A general Kirchhoff approximation for echo simulation in ultrasonic NDT". In: *AIP Conference Proceedings-American Institute of Physics* 143 (2012).

[20] P.Y. Ufimtsev. *Fundamentals of the Physical Theory of Diffraction*. John Wiley & Sons, 2007.

[21] V. Zernov, L. Fradkin, and M. Darmon. "A refinement of the Kirchhoff approximation to the scattered elastic fields". In: *Ultrasonics* 52.7 (2012), pp. 830–835. URL: http://www.sciencedirect.com/science/article/pii/S0041624X11002149.

[22] M. Darmon, V. Dorval, A. Kamta-Djakou, L. J. Fradkin, and S. Chatillon. "A system model for ultrasonic NDT based on the Physical Theory of Diffraction (PTD)". In: *Ultrasonics* 64 (2016), pp. 115–127.

[23] A. Kamta-Djakou, M. Darmon, L. J. Fradkin, and C. Potel. "The Uniform geometrical Theory of Diffraction for elastodynamics: Plane wave scattering from a half-plane". In: *The Journal of the Acoustical Society of America* 138 (Nov. 2015), pp. 3272–3281.

[24] Y. Rahmat-Samii. "GTD, UTD, UAT, and STD: a historical revisit and personal observations". In: *IEEE Antennas and Propagation Magazine* 55.3 (2013), pp. 29–40.

[25] J. J Bowman, T. B. Senior, and P.L. Uslenghi. *Electromagnetic and acoustic scattering by simple shapes*. Tech. rep. DTIC, 1970.

[26] R. M. Lewis. "Physical optics inverse diffraction". In: *Antennas and Propagation, IEEE Transactions on Antennas and Propagation* 17.3 (1969), pp. 308–314.

[27] R. K. Chapman. *Ultrasonic scattering from smooth flat cracks : an elastodynamic Kirchhoff theory*. Tech. rep. North western Region NDT Applications Center, 1982.

[28] R.M. Lewis and J. Boersma. "Uniform asymptotic theory of edge diffraction". In: *Journal of Mathematical Physics* 10.12 (1969), pp. 2291–2305.

[29] D. Ahluwalia. "Uniform Asymptotic Theory of Diffraction by the Edge of a Three-Dimensional Body". In: *SIAM Journal on Applied Mathematics* 18.2 (1970), pp. 287–301.

[30] S.-W. Lee and G. A. Deschamps. "A Uniform Asymptotic Theory of Electromagnetic Diffraction by a Curved Wedge". In: *IEEE Transactions on Antennas and Propagation* 24.1 (1976), pp. 25–34.

[31] D. Bouche, F. Molinet, and R. Mittra. *Asymptotic Methods in Electromagnetics*. Springer, 1997.

[32] F. Molinet. *Acoustic high-frequency diffraction theory*. New York: Momentum Press, 2011.

[33] R. G. Kouyoumjian and P. H. Pathak. "A uniform geometrical theory of diffraction for an edge in a perfectly conducting surface". In: *Proceedings of the IEEE* 62.11 (Nov. 1974), pp. 1448–1461. ISSN: 0018-9219.

[34] P. H. Pathak and R. G. Kouyoumjian. *The dyadic diffraction coefficient for a perfectly conducting wedge*. Tech. rep. DTIC, 1970.

[35] R. K. Chapman, S. F. Burch, N. J. Colett, and L. J. Fradkin. "Ultrasonic inspection of tilted defects using the 'corner effect' – modelling and experimental validation". In: *Insight - Non-Destructive Testing and Condition Monitoring* 50 (Feb. 2008), pp. 66–69.

[36] B. V. Budaev. *Diffraction by Wedges*. Longman Scientific & Technical ; Wiley, 1995.

[37] B. V. Budaev. "Diffraction of elastic waves by a free wedge. Reduction to a singular integral equation". In: *Journal of Soviet Mathematics* 57.3 (1991), pp. 3087–3092.

[38] B. V. Budaev. "Elastic wave diffraction by a wedge-shaped inclusion". In: *Journal of Mathematical Sciences* 73.3 (1995), pp. 330–341.

[39] B. V. Budaev and D. B. Bogy. "Rayleigh wave scattering by a wedge". In: *Wave Motion* 22.3 (1995), pp. 239–257. URL: http://www.sciencedirect.com/science/article/pii/016521259500023C.

[40] B. V. Budaev and D. B. Bogy. "Rayleigh wave scattering by a wedge II". In: *Wave Motion* 24.3 (1996), pp. 307–314.

[41] B. V. Budaev and D. B. Bogy. "Errata to the paper 'Rayleigh wave scattering by a wedge. II' [Wave Motion 24 (1996) 307–317]". In: *Wave Motion* 35.3 (2002).

[42] V. V. Kamotski, L. Ju. Fradkin, B. A. Samokish, V. A. Borovikov, and V. M. Babich. "On Budaev and Bogy's Approach to Diffraction by the 2D Traction-Free Elastic Wedge". In: *SIAM Journal on Applied Mathematics* 67.1 (2006), pp. 235–259. URL: https://doi.org/10.1137/050637297.

[43] A. A. Sommerfeld. "Asymtotische Darstellung von Formeln aus Beugungstehorie des Lichtes". In: *Journal für die reine und angewandte Mathematik.* 158 (1928), pp. 199–208.

[44] V. M. Babich, M. A. Lyalinov, and V. E. Girkurov. *Diffraction theory: Sommerfeld-Malyuzhinets technique.* Alpha Science, 2008, p. 215.

[45] A. K. Gautesen. "Scattering of a Rayleigh wave by an elastic wedge whose angle is less than 180°". In: *Wave Motion* 36.4 (2002), pp. 417–424. URL: http://www.sciencedirect.com/science/article/pii/S0165212502000331.

[46] A. K. Gautesen. "Scattering of a Rayleigh Wave by an Elastic Wedge Whose Angle is Greater Than 180 Degrees". In: *Journal of Applied Mechanics* 68.3 (2000), pp. 476–479. URL: http://dx.doi.org/10.1115/1.1365156.

[47] A. K. Gautesen. "Scattering of a Rayleigh Wave by an Elastic Quarter Space". In: *Journal of Applied Mechanics* 52.3 (1985), pp. 664–668.

[48] A. K. Gautesen. "Scattering of an obliquely incident Rayleigh wave in an elastic quarterspace". In: *Wave Motion* 8.1 (1986), pp. 27–41.

[49] A. K. Gautesen. "Scattering of a Rayleigh wave by an elastic quarter space - revisited". In: *Wave Motion* 35.1 (2002), pp. 91–98.

[50] A. K. Gautesen. "Scattering of a plane longitudinal wave by an elastic quarter space". In: *Wave Motion* 7.6 (1985), pp. 557–568.

[51] M. Lax. "Multiple scattering of waves II. The effective field in dense systems". In: *Physical Review* 85.4 (1952), pp. 621–629.

[52] J.-P. Croisille and G. Lebeau. *Diffraction by an Immersed Elastic Wedge*. Vol. 1723. Springer, Jan. 2000, p. 134.

[53] V. V. Kamotski and G. Lebeau. "Diffraction by an elastic wedge with stress-free boundary: existence and uniqueness". In: *Proceedings of the Royal Society of London A: Mathematical, Physical and Engineering Sciences* 462.2065 (2006), pp. 289–317. URL: http://rspa.royalsocietypublishing.org/content/462/2065/289.

[54] H. M. Macdonald. *Electric waves : being an Adams prize essay in the University of Cambridge*. Cambridge, 1902. URL: http://hdl.handle.net/2027/hvd.32044080810880.

[55] B. Lu, M. Darmon, L. J. Fradkin, and C. Potel. "Numerical comparison of acoustic wedge models, with application to ultrasonic telemetry". In: *Ultrasonics* 65 (2016), pp. 5–9. URL: http://www.sciencedirect.com/science/article/pii/S0041624X15002644.

[56] L.P. Castro and D. Kapanadze. "Wave diffraction by wedges having arbitrary aperture angle". In: *Journal of Mathematical Analysis and Applications* 421.2 (2015), pp. 1295–1314. URL: http://www.sciencedirect.com/science/article/pii/S0022247X14007355.

[57] K. Klem-Musatov. *Theory of seismic diffractions*. Society of Exploration Geophysicists, 1994.

[58] A. M. Aizenberg and A. A. Ayzenberg. "Feasible fundamental solution of the multiphysics wave equation in inhomogeneous domains of complex shape". In: *Wave Motion* 53 (2015), pp. 66–79. ISSN: 0165-2125. DOI: https://doi.org/10.1016/j.wavemoti.2014.11.006. URL: http://www.sciencedirect.com/science/article/pii/S0165212514001589.

[59] A. A. Ayzenberg. "Transmission-propagation operator theory and tip-wave superposition method for sub-salt shadow wavefield description". PhD thesis. Norwegian University of Science and Technology, Oct. 2015.

[60] M. Darmon, V. Dorval, A. Kamta Djakou, L. Fradkin, and S. Chatillon. "A system model for ultrasonic NDT based on the Physical Theory of Diffraction (PTD)". In: *Ultrasonics* 64 (2016), pp. 115–127.

[61] L. J. Fradkin and R. Stacey. "The high-frequency description of scatter of a plane compressional wave by an elliptic crack". In: *Ultrasonics* 50 (2010), pp. 529–538.

[62] P. C. Clemmow. "Some extensions to the method of integration by steepest descents". In: *The Quarterly Journal of Mechanics and Applied Mathematics* 3.2 (1950), pp. 241–256. URL: http://dx.doi.org/10.1093/qjmam/3.2.241.

[63] V. H. Aristizabal, F. J. Velez, and J. D. Jaramillo. "Efficient solution for the diffraction of elastic SH waves by a wedge: Performance of various exact, asymptotic and simplified solutions". In: *Soil Dynamics and Earthquake Engineering* 95 (2017), pp. 9–16. URL: http://www.sciencedirect.com/science/article/pii/S026772611730091X.

[64] A. K Gautesen. "On scattering of an SH-wave by a corner comprised of two different elastic materials". In: *Mechanics of Materials* 35.3 (2003), pp. 407–414.

[65] B. V. Budaev. "Diffraction of elastic waves by a free wedge. Reduction to a singular integral equation". In: *Journal of Soviet Mathematics* 57.3 (1991), pp. 3087–3092. URL: http://link.springer.com/10.1007/BF01098973.

[66] B. V. Budaev. "Elastic wave diffraction by a wedge-shaped inclusion". In: *Journal of Mathematical Sciences* 73.3 (1995), pp. 330–341. URL: http://link.springer.com/10.1007/BF02362817.

[67] A. Imperiale, S. Chatillon, M. Darmon, N. Leymarie, and E. Demaldent. "UT Simulation using a fully automated 3D hybrid model: application to planar backwall breaking defects inspection". In: *44th Review of Progress in Quantitative Nondestructive Evaluation*. 2017.

[68] V. A. Borovikov. *Uniform Stationary Phase method*. Institution of electrical engineers, 1994.

[69] D. Gridin. "High-frequency asymptotic description of head waves and boundary layers surrounding the critical rays in an elastic half space". In: *Journal of the Acoustical Society of America* 104.3 (1998), pp. 1188–1197.

[70] V. V. Kamotski. "The incidence of the plane wave on an elastic wedge at a critical angle". In: *St. Petersburg Math. Journal* 15.3 (2004), pp. 419–436.

[71] V. Zernov, L. Fradkin, A. Gautesen, M. Darmon, and P. Calmon. "Wedge diffraction of a critically incident Gaussian beam". In: *Wave Motion* 50.4 (2013), pp. 708–722.

[72] H. S. Carslaw. "Diffraction of Waves by a Wedge of any Angle". In: *Proceedings of the London Mathematical Society* s2-18.1 (1920), pp. 291–306.

[73] A. D. Rawlins. *Spherical wave diffraction by a rational wedge*. Tech. rep. Department of Mathematics and Statistics, Brunel University, 1986.

[74] R. G. Rojas. "Electromagnetic diffraction of an obliquely incident plane wave field by a wedge with impedance faces". In: *IEEE Transactions on Antennas and Propagation* 36.7 (1988), pp. 956–970.

[75] J.-M. Bernard. "On the diffraction of an electromagnetic skew incident wave by a non perfectly conducting wedge". In: *Annales Des Télécommunications* 45.1-2 (1990), pp. 30–39.

[76] V. Daniele. "The Wiener-Hopf Technique for Impenetrable Wedges Having Arbitrary Aperture Angle". In: *SIAM Journal on Applied Mathematics* 63.3 (2003), pp. 1442–14460.

[77] V. G. Daniele and G. Lombardi. "Wiener-Hopf Solution for Impenetrable Wedges at Skew Incidence". In: *IEEE Transactions on Antennas and Propagation* 54.9 (2006), pp. 2472–2485.

[78] A. K. Gautesen. "A note on the diffraction coefficients for elastodynamic diffraction by sharp edges". In: *Wave Motion* 47.5 (2010), pp. 327–332.

[79] P. Debye. "Näherungsformeln für die Zylinderfunktionen für grosse Werte des Arguments und unbeschränkt veranderliche Werte des Index". In: *Mathematische Annalen* 67 (1909), pp. 535–558.

[80] B. Riemann. "Sullo svolgimento del quoziente di due serie ipergeometriche in frazione continua infinita". 1863.

[81] B. Riemann. *Mathematische Werke*. Dover, 1953.

[82] M.V. Fedoryuk. "Saddle point method". In: *Encyclopedia of Mathematics*. 1977. URL: http://www.encyclopediaofmath.org/index.php?title=Saddle_point_method&oldid=14602.

université PARIS-SACLAY
ÉCOLE DOCTORALE
Physique et ingénierie : électrons, photons, sciences du vivant (EOBE)

Titre : Modélisation de la diffusion 3D d'ondes élastiques par des structures complexes pour le calcul des échos de géométrie. Application à la simulation des CND par ultrasons.

Mots clés : Elastodynamique, Diffraction, Méthodes asymptotiques

Résumé : Le sujet de la thèse s'inscrit dans le cadre du développement de modèles pour la simulation du contrôle non-destructif (CND) par ultrasons. L'objectif à long terme est la mise au point, par une méthode de rayons, d'un outil complet de simulation des échos issus de la géométrie (surfaces d'entrée, de fond...) ou des structures internes des pièces inspectées. La thèse vise plus précisément à intégrer le phénomène de diffraction par les dièdres à un modèle existant dérivant de l'acoustique géométrique et qui prend uniquement en compte les réflexions sur les faces.
Pour cela, la méthode dite des fonctions spectrales, développée initialement pour le cas d'un dièdre immergé, est développée et validée dans un premier temps dans le cas des ondes acoustiques pour des conditions aux limites de type Dirichlet ou Neumann. La méthode est ensuite étendue à la diffraction des ondes élastiques par des dièdres infinis à faces libres et d'angles quelconques, pour une incidence 2D puis pour une incidence 3D. Cette méthode est semi-analytique puisque les solutions recherchées s'écrivent sous la forme d'une somme d'une fonction singulière, qui est déterminée analytiquement à l'aide d'un algorithme récursif, et d'une fonction régulière, qui est approchée numériquement.
Les codes correspondants sont validés par comparaison à une solution exacte dans le cas acoustique et par comparaison à d'autres codes (semi-analytiques et numériques) dans le cas élastique. Des validations expérimentales du modèle élastodynamique sont également proposées.

Title : Modelling of the 3D scattering of elastic waves by complex structures for specimen echoes calculation. Application to ultrasonic NDT simulation.

Keywords : Elastodynamics, Diffraction, Asymptotic Methods

Abstract : This thesis falls into the framework of model development for simulation of ultrasonic non-destructive testing (NDT). The long-term goal is to develop, using ray methods, a complete simulation tool of specimen echoes (input, back-wall surfaces...) or echoes of inner structures of inspected parts. The thesis aims more specifically to integrate the phenomenon of diffraction by wedges to an existing model derived from geometrical acoustics, which only accounts for reflections on the wedge faces.
To this end, a method called the spectral functions method, which was initially developed for immersed wedges, is developed and validated as a first step in the case of acoustic waves with Dirichlet or Neumann boundary conditions. The method is then extended to elastic wave diffraction by infinite stress-free wedges of arbitrary angles, for 2D and 3D incidences. This method is semi-analytic since the unknown solutions are expressed as the sum of a singular function, determined analytically using a recursive algorithm, and a regular function which is approached numerically.
The corresponding codes are validated by comparison to an exact solution in the acoustic case and by comparison to other codes (semi-analytic and numerical) in the elastic case. Experimental validations of the elastodynamic model are also proposed.

Université Paris-Saclay
Espace Technologique / Immeuble Discovery
Route de l'Orme aux Merisiers RD 128 / 91190 Saint-Aubin, France